UNIVERSIDAD COMPLUTENSE DE MADRID

FACULTAD DE CIENCIAS QUÍMICAS

Departamento de Ciencia de los Materiales e Ingeniería Metalúrgica

HIGH STRAIN-RATE BEHAVIOR OG MAGNESIUM ALLOYS (COMPORTAMIENTO MECÁNICO A ALTA VELOCIDAD DE DEFORMACIÓN DE ALEACIONES DE MAGNESIO)

MEMORIA PARA OPTAR AL GRADO DE DOCTOR
PRESENTADA POR

Nathamar Valenthina Dudamel Caballero

Bajo la dirección de los doctores

María Teresa Pérez-Prado
Francisco Gálvez Díaz-Rubio

Madrid, 2013

UNIVERSIDAD COMPLUTENSE DE MADRID
FACULTAD DE CIENCIAS QUÍMICAS
DEPARTAMENTO DE CIENCIAS DE LOS MATERIALES E INGENIERÍA METALÚRGICA

HIGH STRAIN-RATE BEHAVIOR OF MAGNESIUM ALLOYS

(COMPORTAMIENTO MECÁNICO A ALTA VELOCIDAD DE DEFORMACIÓN DE ALEACIONES DE MAGNESIO)

A thesis submitted in fulfillment of the requirements for the degree of "Doctor por la Universidad Complutense de Madrid". –European Mention-

NATHAMAR VALENTHINA DUDAMELL CABALLERO

SUPERVISED BY:

DRA. MARÍA TERESA PÉREZ-PRADO
PROF. FRANCISCO GÁLVEZ DÍAZ-RUBIO

Departamento de Ciencia de Materiales
Universidad Politécnica de Madrid
E.T.S.I. de Caminos, Canales y Puertos

imdea materials

Madrid, julio 2012

UNIVERSIDAD COMPLUTENSE DE MADRID
FACULTAD DE CIENCIAS QUÍMICAS
DEPARTAMENTO DE CIENCIAS DE LOS MATERIALES E INGENIERÍA METALÚRGICA

HIGH STRAIN-RATE BEHAVIOR OF MAGNESIUM ALLOYS

(COMPORTAMIENTO MECÁNICO A ALTA VELOCIDAD DE DEFORMACIÓN DE ALEACIONES DE MAGNESIO)

A thesis submitted in fulfillment of the requirements for the degree of "Doctor por la Universidad Complutense de Madrid". –European Mention-

NATHAMAR VALENTHINA DUDAMELL CABALLERO

SUPERVISED BY:

DRA. MARÍA TERESA PÉREZ-PRADO
PROF. FRANCISCO GÁLVEZ DÍAZ-RUBIO

Madrid, julio 2012

Lo importante es no

dejar de hacerse preguntas...

(The important thing is

not to stop questioning...)

(Albert Einstein, 1879-1955)

A Christophe,
mi mayor fortaleza.
Mi compañero de aventuras.

A mis hermanas
y a mi familia,
mi gran apoyo.

A mis sobrinos y a mis
pequeñas Hilda y María T.
para que este logro les
sirva de ejemplo de que, a
pesar de las adversidades,
con esfuerzo podemos lograr
nuestras metas.

A mi madre,
con nostalgia.

A mi padre, con cariño.

AGRADECIMIENTOS

Antes de iniciar el desarrollo de mi trabajo de investigación quisiera extender mi más profundo agradecimiento a las siguientes personas e instituciones:

- A mis tutores, Dra. María Teresa Pérez-Prado y Prof. Francisco Gálvez Díaz-Rubio, por su apoyo absoluto, por su gran calidad profesional, por todo el conocimiento que me han trasmitido, por sus consejos durante todo el desarrollo de este trabajo y sobre todo, por el entusiasmo y las palabras de ánimo que me brindan en todo momento. Para mí ha sido un gran honor tenerlos de tutores.

- Al Prof. Javier Llorca por abrirme las puertas del Instituto Madrileño de Estudios Avanzados de Materiales (IMDEA Materiales) y por darme la oportunidad de iniciar mi carrera de investigación en este excelente instituto.

- Al departamento de Ciencia de Materiales de la ETSI Caminos Canales y Puertos, especialmente a la Ing. María Jesús Pérez y a la Ing. Noemí García Lepetit por toda su colaboración técnica en el desarrollo de esta tesis doctoral.

- Al Dr. Gaspar González-Doncel, al Ing. Jesús Reales y al Ing. Marcos Angulo-Martin del Centro Nacional de Investigaciones Metalúrgicas (CENIM). A todos ellos mil gracias por su gran colaboración en el desarrollo experimental de esta investigación.

- Al grupo de profesores del programa de doctorado “Ciencia y Tecnología de Materiales” de la Facultad de Ciencias Químicas de

la Universidad Complutense de Madrid, por sus aportes y enseñanzas.

- Al Dr. Dietmar Letzig, al Dr. Jan Bohlen, y al Dr. Sangbong Yi del *Magnesium Innovation Centre (MagIC),* de Helmholtz-Zemtrum Geesthacht (Alemania) por los conocimientos transmitidos, por abrirme las puertas de su prestigioso instituto y ofrecerme la oportunidad de una estancia que ha significado para mi una gran experiencia profesional y personal.

- Al Dr. Ibai Ulacia, de la Universidad de Mondragón por el apoyo científico.

- A mis compañeros de IMDEA Materiales por estos excelentes años y por el buen ambiente de trabajo.

- A Dios porque en él todo lo puedo.

- Desde el plano personal, quisiera agradecer muy especialmente a mis hermanas Nathaly, Marialberth y a Yadira por su apoyo incondicional. Al Ing. Miguel Ángel Contreras y a la Dra. Aurora Medina por facilitarme el camino. Además, de forma especial a: Christophe Ortiz, Yvonne Boutillier, Juan Ortiz, Katia Tamargo, Ana Fernández, Antoine Jérusalem, Juan Carlos Rubalcaba, Nora Cueto, Vanesa Martínez, Enrique Martínez, Berta Herrero, Eva Moreno, Teresa Pérez-Prado, Inés Leiva, Vanessa Fernández, Mariana Huerta, Eduardo Ciudad-Real, Lester López, Laura Castro, Patricia Ávila, Silvia Henández, Yinett Quesada y Lorena Andreu, por todos los momentos compartidos, por las alegrías en las buenas y el apoyo en las malas, por marcar la diferencia, por hacer que fuera de mi país, las cosas sigan siendo sencillas. Por ser mis amigos con todo lo que ello conlleva. ¡Gracias Chicos!

TABLE OF CONTENTS

PAG.

1. PRÓLOGO Y OBJETIVO DEL TRABAJO 11

2. INTRODUCCIÓN. ALEACIONES DE MAGNESIO 15

2.1. Características generales 16

2.2. Ventajas y desventajas 19

2.3. Aplicaciones 20

2.4. Estructura cristalina 22

2.5. Textura cristalina 24

2.6. Mecanismos de deformación 26

2.6.1. Mecanismos de deformación a bajas temperaturas 29

2.6.1.1. Policristal orientado al azar 29

2.6.1.2. Chapas laminadas 29

2.6.1.3. Barras extruidas 31

2.6.2. Mecanismos de deformación a alta temperatura 32

2.6.3. Mecanismos de deformación en aleaciones de magnesio con tierras raras (Mg-RE) 35

2.7. Aleaciones de magnesio procesadas mediante colada por inyección a alta presión 37

2.8. Objetivo de la investigación 38

3. RESEARCH PAPERS 43

3.1. Mechanical behavior and microstructural evolution of a Mg AZ31 sheet at dynamic strain rates 44

3.2. Twinning and grain subdivision during dynamic deformation of Mg AZ31 sheet alloy at room temperature 56

3.3. Influence of texture on the recrystallization mechanisms in an AZ31 Mg sheet alloy at dynamic rates 71

PAG.

4. COMPLEMENTARY STUDIES 80

4.1. Complementary Study I. Mechanical Behavior at quasi-static and dynamic rates of a magnesium alloy containing neodymium 81

4.1.1. Introduction. 82

4.1.2. Materials and Experimental Procedure 82

4.1.2.1. Material: initial microstructure 82

4.1.2.2. Mechanical testing 83

4.1.2.3. Microstructure examination 84

4.1.3. Results and Discussion 85

4.1.3.1. As-extruded and heat treated material 85

4.1.3.2. Mechanical behavior at quasi-static rates 86

4.1.3.3. Mechanical behavior at dynamic rates 94

4.1.3.4. Microstructural evolution under quasi-static and dynamic conditions 96

4.1.4. Conclusions 108

4.2. Complementary Study II. Dynamic deformation of high pressure die-cast Mg alloys 110

4.2.1. Introduction 111

4.2.2. Materials and Experimental Procedure 111

4.2.3. Results and Discussion 112

4.2.4. Conclusions 118

5. GENERAL DISCUSSION 120

5.1. Strain rate sensitivity of the yield stress in the Mg AZ31 alloy. 121

5.2. Strain rate dependence of the critical resolved shear stress of non-basal slip systems and of tensile twinning in the Mg AZ31 alloy. 122

PAG.

5.3. Influence of strain rate on the twinning activity. 123

5.4. Influence of the strain rate on grain subdivision. 126

5.5. Dynamic recrystallization at high strain rates. 127

5.6. Influence of Rare Earth (RE) atoms in the incidence of basal slip and twinning at quasi-static rates. 130

5.7. Influence of Rare Earth (RE) atoms in the incidence of basal slip and twinning under dynamic deformations. 132

6. CONCLUSIONS (ENGLISH VERSION) 135

CONCLUSIONES (SPANISH VERSION) 138

7. FURTHER WORK 142

8. REFERENCES 144

9. APPENDICES 158

LIST OF FIGURES 178

LIST OF TABLES 187

PARTE I
PRÓLOGO Y OBJETIVO

1. PRÓLOGO Y OBJETIVO DEL TRABAJO.

En la última década las aleaciones de magnesio se han estudiado profundamente ya que, debido a su baja densidad, se perfilan como materiales con gran potencial para reducir el peso de los vehículos. Esto conllevaría una disminución en el consumo de los combustibles fósiles y, a su vez, una reducción en la emisión de CO_2.

Sin embargo, para que las aleaciones de magnesio puedan ser ampliamente comercializadas, es necesario aumentar su resistencia mecánica y su ductilidad, disminuir su anisotropía para mejorar su capacidad para ser conformadas y aumentar su resistencia a la corrosión. Así mismo, es vital conocer sus propiedades mecánicas a velocidades de impacto, especialmente si se quiere fabricar con ellas determinados componentes estructurales de los automóviles.

En la actualidad son muchos los trabajos que explican el comportamiento mecánico de las aleaciones de magnesio a velocidades de deformación cuasi-estáticas. Esta investigación pretende llenar la laguna conceptual existente en cuanto al comportamiento mecánico de estas aleaciones a alta velocidad de deformación.

Por tanto, esta tesis doctoral, que se presenta con la finalidad de obtener el título de Doctor en Ciencia y Tecnología de los Materiales, tiene como **objetivo** principal estudiar el comportamiento mecánico así como los mecanismos de deformación y de recristalización en condiciones dinámicas de una chapa laminada de la aleación comercial Mg-3%$_p$Al-1%$_p$Zn (AZ31), de una barra extruida de una aleación de magnesio con tierras raras de última generación (Mg-1%$_p$Nd-1%$_p$Mn, MN11) y de las aleaciones comerciales Mg-6%$_p$Al-0.5%$_p$Mn (AM60B) y Mg-9%$_p$Al-1%$_p$Zn (AZ91D) procesadas mediante colada por inyección. Con este propósito se realizaron ensayos de tensión y compresión en

una barra Hopkinson a una velocidad de deformación de aproximadamente 10^3 s^{-1} y a temperaturas comprendidas entre 25ºC y 400ºC. También se realizaron ensayos de compresión a velocidades cuasi-estáticas ($5x10^{-4}$ s^{-1}, $5x10^{-3}$ s^{-1} y $5x10^{-2}$ s^{-1}) con la finalidad de comparar los resultados obtenidos en ambos regímenes de deformación. Los resultados de este trabajo están recogidos en los siguientes 3 artículos publicados en revistas internacionales de elevado índice de impacto:

- Acta Materialia. Vol. *58, Issue 8*, *Mayo 2010*, *Pag. 2988-2998.*
- Acta Materialia. Vol. *59, Issue 18*, *October 2011*, *Pag. 6949-6962.*
- Materials Science and Engineering*: A*,Vol. *532*,*Issue15, January 2012*, *Pag. 528-535.*

La estructura de este trabajo es la siguiente: primero se introduce el tema en el apartado 2. A continuación, en el apartado 3, se presentan los artículos de investigación que componen el cuerpo de esta tesis doctoral. En el apartado 4 se presentan dos estudios complementarios donde se recogen resultados adicionales obtenidos en esta investigación pero que no se encuentran recopilados en los artículos de investigación del apartado 3. Estos dos estudios complementarios darán lugar a sendos artículos científicos, que se encuentran en fase de preparación. En el apartado 6 se exponen las conclusiones más relevantes de este trabajo, el cual ha permitido establecer los mecanismos de deformación y recristalización predominantes durante la deformación de las aleaciones de magnesio estudiadas en condiciones dinámicas. Estos resultados son de gran utilidad para la industria de la automoción, ya que proporcionan información acerca de la aplicabilidad de este material en componentes que podrían estar sometidos a impacto. En el apartado 7 se presenta el trabajo futuro. En la sección 8 se enumeran las referencias utilizadas para escribir este trabajo de investigación. Por último, en el apartado 9 se presenta, a manera de apéndice, una base de datos de propiedades mecánicas de aleaciones de magnesio que

consideramos de gran utilidad tanto para la industria automotriz como para trabajos futuros.

PARTE II

INTRODUCCIÓN. ALEACIONES DE MAGNESIO

2. INTRODUCCIÓN. ALEACIONES DE MAGNESIO.

2.1. Características Generales.

El magnesio es un elemento químico que pertenece al Grupo IIa de la tabla periódica, es decir, forma parte de los metales alcalinotérreos. Su número atómico es 12 y su masa atómica es 24.3050 uma. Es el octavo elemento más abundante de la corteza terrestre. De hecho, el planeta Tierra contiene aproximadamente 2.5% en peso de este metal. En estado natural nunca se encuentra como metal puro ya que fácilmente reacciona con otros elementos para formar compuestos. Las principales fuentes de magnesio en la naturaleza son la magnesita, la dolomita y la carnalita. La magnesita es una mezcla de carbono, oxígeno y magnesio tal y como se puede observar en su fórmula química $MgCO_3$. La dolomita está constituida por calcio, carbono, oxígeno y magnesio y su fórmula química es $CaMg(CO_3)_2$. La carnalita es un mineral compuesto de cloruro doble de potasio y de magnesio ($KMgCl_3 \cdot 6H_2O$). Además, los océanos poseen gran cantidad de magnesio; cada kilogramo de agua de mar contiene 1.2 gramos de magnesio [1].

Las dos vías más utilizadas para obtener magnesio metálico mediante su separación del mineral son:

- **La reducción térmica:** El mineral se calienta hasta alrededor de los 1600 ºC con reductores como aleaciones de hierro y silicio (ferrosilicio), carbono, CaC_2, etc. Luego el magnesio se convierte en gas. Cuando el gas se enfría se transforma en magnesio líquido y posteriormente en magnesio sólido [1].
- **La electrólisis**: Esta técnica utiliza corriente eléctrica para separar el magnesio de su mineral. Consiste en promover la

electrólisis del cloruro de magnesio en mezclas de sales fundidas [1].

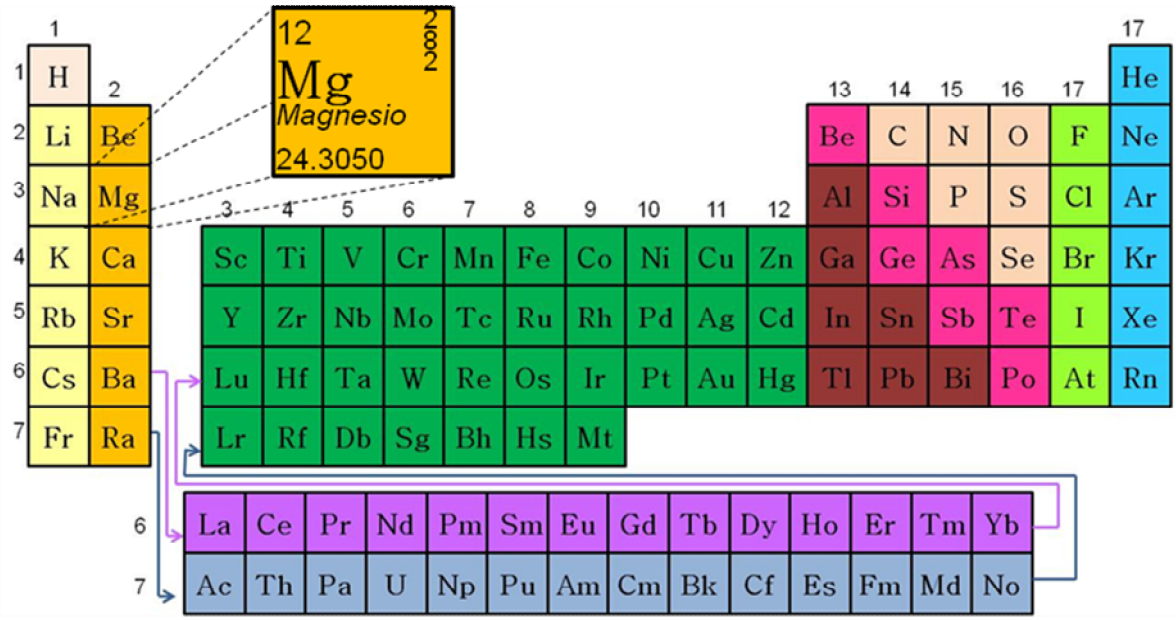

Figura 2.1. Tabla periódica de los elementos.

En su forma más pura el magnesio es un metal blanco plateado. Cuando se encuentra en forma de polvo es altamente reactivo y como sólido puede reaccionar, aunque muy lentamente, con el agua y oxidarse con el aire. En la gran mayoría de sus aplicaciones el magnesio se encuentra aleado con otros elementos tales como, por ejemplo, aluminio, cinc, manganeso, entre otros, para obtener materiales con propiedades mecánicas más atractivas.

En comparación con otros metales estructurales de gran uso, como el acero y el aluminio, el magnesio tiene muy baja densidad (1.74 g/cm^3) (Ver figura 2.2). Esta característica ha sido el motor que ha impulsado los estudios realizados en aleaciones de magnesio en la última década, ya que se ha considerado su gran potencial para contribuir en la reducción de peso en vehículos y otras estructuras [2,3]. Los materiales ligeros, como el Mg, tienen especial relevancia en una era como la actual en la que se sabe que los recursos energéticos de origen fósil son

limitados. La demanda de este tipo de materiales pretende reducir el consumo energético y, a la vez, disminuir el impacto medioambiental [4]. Introducir piezas de magnesio en el mercado requiere, dependiendo de su aplicación específica, mejorar su resistencia a la corrosión, incrementar su resistencia mecánica y su ductilidad y, a la vez, disminuir su anisotropía con la finalidad de mejorar su conformabilidad [5]. Además, es importante optimizar el comportamiento de las aleaciones de magnesio en condiciones de impacto [2], (es decir, a altas velocidades de deformación) especialmente cuando se diseñan piezas de magnesio para ser utilizadas en automóviles como componentes de seguridad crítica.

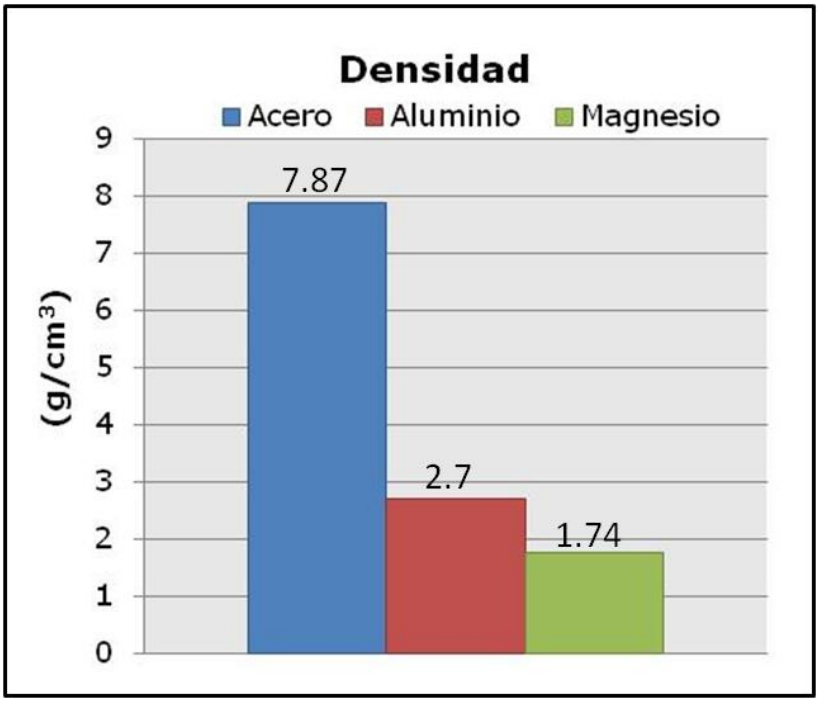

Figura 2.2. Densidades de algunos metales estructurales.

La tabla 2.1 recopila algunas de las propiedades físicas del magnesio y, a su vez, las compara con las de otros metales de gran uso estructural.

Tabla 2.1. Comparación de las propiedades físicas del Mg puro con las de otros metales estructurales [6].

	Gravedad Específica	Punto de Fusión (ºC)	Punto de Ebullición (ºC)	Calor latente de fusión (kJ/kg.K; J/cm³.K)	Calor específico (kJ/kg; J/cm³)	Coeficiente de expansión lineal x10⁶	Resistencia a la tracción (MPa)	Elongación (%)	Dureza (HB)
Mg	1.74	650	1110	368; 640	1.05; 1.84	25.5	98	5	30
Al	2.74	660	2486	398; 1088	0.88; 2.43	23.9	88	45	23
Fe	7.86	1535	2754	272; 213	0.46; 3.68	11.7	265	45	67

2.2. Ventajas y desventajas.

A continuación se enumeran algunas de las principales ventajas del Mg y sus aleaciones [3,6]:

- Baja densidad. Es el metal estructural más ligero. Su densidad es 2/3 la del aluminio y 1/4 la del hierro.
- Alta resistencia específica.
- Buenas características de colabilidad. Es apto para colada por inyección a alta presión.
- Buena soldabilidad en atmósfera controlada.
- Abundancia tanto en la corteza terrestre como en los océanos.
- Alta reciclabilidad además de bajo consumo de energía durante el proceso.
- Capacidad de amortiguación de las vibraciones.
- Buena capacidad para ser mecanizado.
- Baja toxicidad en humanos.
- Capacidad para inhibir ondas electromagnéticas
- Si se compara con los materiales poliméricos:
  - Mejores propiedades mecánicas.

- Mejor conductividad eléctrica.
- Mejor conductividad térmica.

Por otra parte, el magnesio también tiene algunos inconvenientes que han limitado su comercialización. Estos han sido y son objeto de muchas investigaciones cuyo desafío es superar, en lo posible, dichos inconvenientes. A continuación se presenta una lista de algunas de las desventajas más significativas [3,6]:

- Bajo módulo elástico.
- Baja tenacidad y baja ductilidad a temperatura ambiente. Esto va en detrimento de su aptitud para ser trabajado en frío.
- Resistencia mecánica limitada a altas temperaturas.
- Baja resistencia a la fluencia.
- Alto porcentaje de grietas de contracción durante la solidificación.
- Alta reactividad química.
- Resistencia a la corrosión limitada (dependiendo de la aplicación).

2.3 Aplicaciones.

Las aleaciones de magnesio son de gran interés tanto en el sector automovilístico como en el sector aeronáutico. En automoción, por ejemplo, al disminuir el peso de los coches se disminuye la cantidad de combustible necesario para ponerlo en marcha y, a la vez, los niveles de CO_2 que se expulsan a la atmósfera también decrecen considerablemente [3,6].

La figura 2.3 muestra algunos componentes de automóviles que se fabrican ya en la actualidad con aleaciones de magnesio: la armadura del volante, la parte interna de puerta del maletero, la estructura interna de la puerta, la estructura del asiento, la carcasa de la caja de

transmisión, el colector de admisión, la carcasa de los cilindros y la columna de la dirección [6].

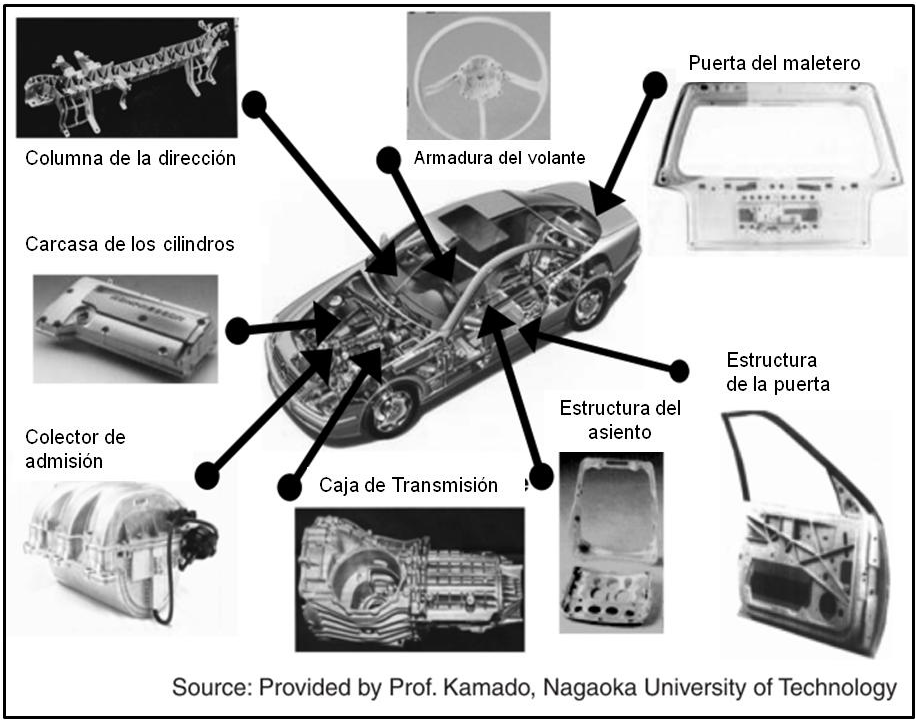

Figura 2.3. Aplicaciones de las aleaciones de magnesio en automóviles [6].

Sin embargo, las aplicaciones de las aleaciones de magnesio van más allá de las mencionadas anteriormente. Por ejemplo, en el área de los biomateriales ya se ha avanzado mucho en la fabricación de extensores coronarios biodegradables a partir de aleaciones de Mg. Estos componentes se introducen en el interior de una arteria coronaria obstruida con el fin de que se produzca la dilatación de la misma para así facilitar el flujo sanguíneo. La ventaja de utilizar Mg en este tipo de aplicaciones es que el cuerpo humano posee magnesio naturalmente por lo que es muy improbable que se produzca una infección debido a sus productos de corrosión [7].

El magnesio se utiliza también para fabricar material deportivo y dispositivos electrónicos. En el área deportiva encontramos, por

ejemplo, marcos de bicicletas, raquetas, patines, gafas, binoculares, entre otros. En el área electrónica se pueden mencionar, por ejemplo, carcasas de portátiles, de móviles, de cámaras fotográficas y de video. La Figura 2.4 muestra algunas de estas aplicaciones.

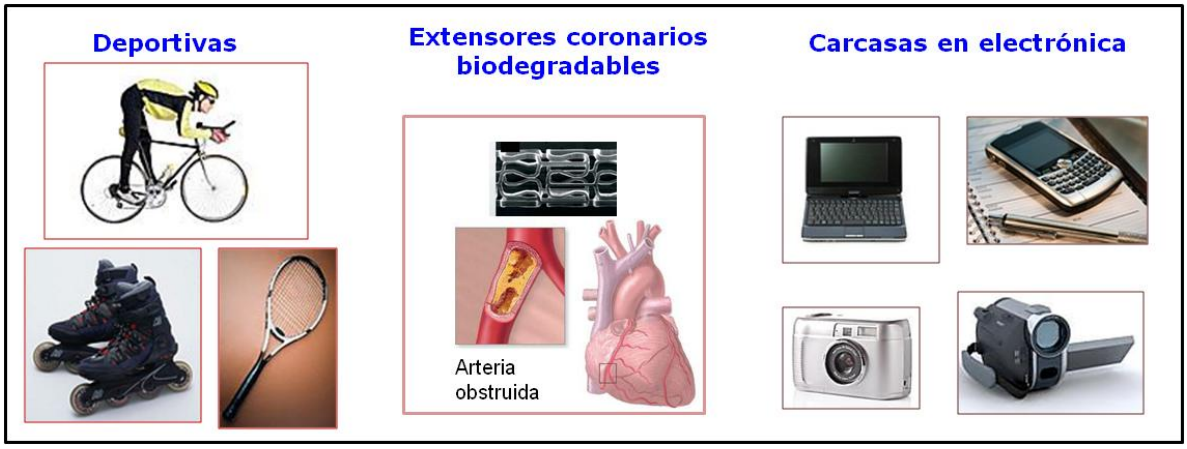

Figura 2.4. Aplicaciones de las aleaciones de magnesio para la fabricación de dispositivos biomédicos, electrónicos y material deportivo.

2.4. Estructura cristalina.

La estructura cristalina del magnesio puro, en condiciones de presión atmosférica y temperatura ambiente es hexagonal compacta (*HCP*) [8]. La figura 2.5 muestra una representación, mediante esferas reducidas, de la celdilla unidad *HCP*. En dicha figura se puede observar que las bases superior e inferior (planos basales) son hexágonos regulares con un átomo en cada vértice y otro en el centro. Los planos perpendiculares a los basales reciben el nombre de planos prismáticos. Además, hay otro plano que provee tres átomos adicionales a la celdilla unidad y está ubicado entre los planos basales. Cada celda unitaria *HCP* tiene 6 átomos: cada átomo de los 12 vértices superiores e inferiores contribuye a la celda unidad con 1/6 de átomo mientras que los tres átomos del plano central contribuyen enteramente. En la figura

II.5 también se observa que “c” y “a” son las dimensiones de la celda unitaria. La relación c/a ideal es de 1.633; no obstante, para la mayoría de los metales *HCP* esta relación se desvía de la idealidad. Los valores de los parámetros de red del magnesio son c=0.52105 nm y a=0.32095 [8]. Esto quiere decir que la relación c/a para el magnesio a temperatura ambiente es 1.6235; por ello se le podría considerar un metal con estructura hexagonal muy próxima a la ideal. Los vértices a_1, a_2, a_3 (separados entre sí 120º) y el eje C, son los índices de Miller que permiten definir los planos de las celda (a_1, a_2, a_3, C), cumpliéndose la regla de que $a_1+a_2=-a_3$ [8-10].

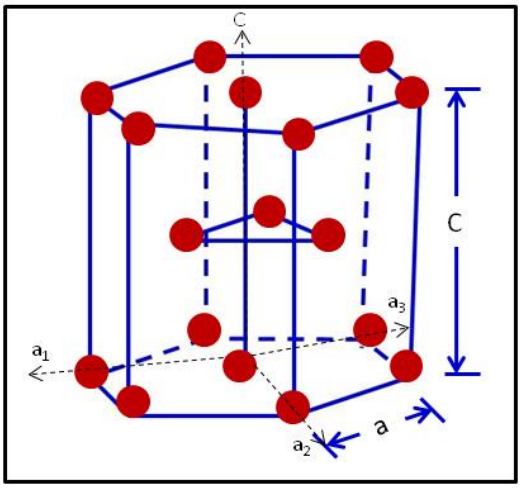

Figura 2.5. Estructura cristalina hexagonal compacta (HCP): representación de la celdilla unidad mediante esferas reducidas.

Ahora, en este contexto, se hace necesario introducir el concepto de textura cristalina (o cristalográfica), ya que debido a la baja disponibilidad de sistemas de deslizamiento independientes para cada modo de deslizamiento (este aspecto se tratará en detalle en el apartado 2.6), la deformación de las aleaciones de magnesio es altamente dependiente de la textura [11-12].

2.5 Textura cristalina.

Se entiende por textura cristalina la distribución de las orientaciones cristalográficas de un metal policristalino. Atendiendo a su textura, los materiales pueden clasificarse en:

- Sin Textura: Cuando los cristales están orientados completamente al azar.
- Con textura: Cuando existen una o varias orientaciones preferentes (componentes de la textura). Dependiendo de la fracción de volumen de material que está orientada según las distintas componentes se dice que éste tiene textura débil, moderada o fuerte.

Debido a que la orientación preferente de los granos es un fenómeno bastante común, la textura cristalina juega un rol fundamental en el comportamiento mecánico y físico del material. La textura evoluciona durante el procesado (colada, forja, laminación, extrusión, etc.), la soldadura y los tratamientos térmicos. Durante la deformación de un material policristalino el flujo plástico produce una reorientación de la red de cada grano y esto da lugar a la estabilización de orientaciones preferentes. La mayoría de los principios que gobiernan el desarrollo de una determinada textura durante los procesos convencionales de conformado han sido ampliamente estudiados y por tanto, en la actualidad es posible predecir la textura que tendrá un material fabricado mediante un determinado proceso [13,14]. La figura 2.6 muestra algunos ejemplos de las texturas que se desarrollan en las aleaciones de magnesio en tres procesos de fabricación distintos: la colada, la laminación y la extrusión.

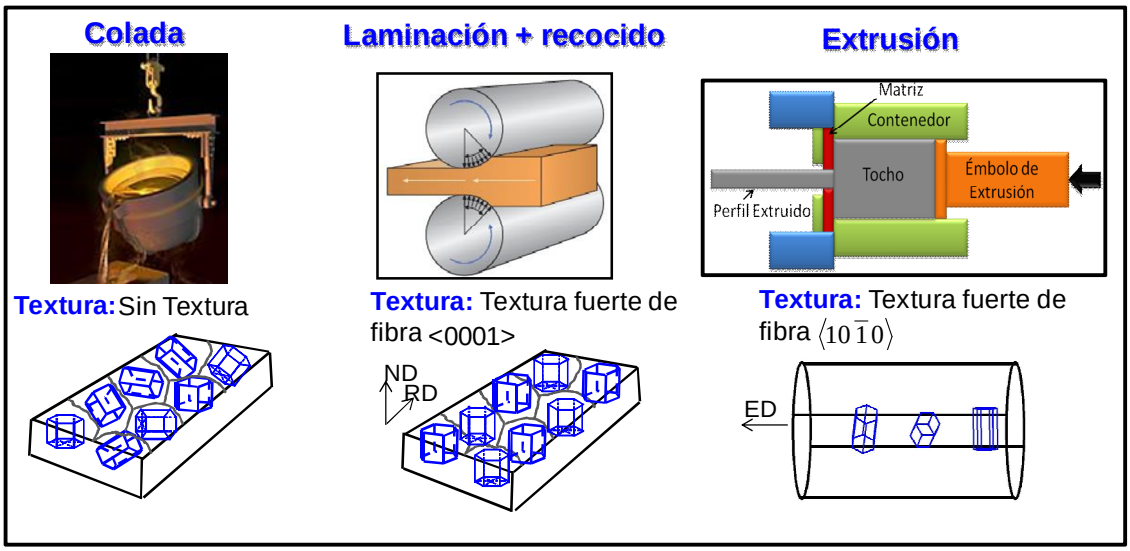

Figura 2.6. Tipos de textura que se desarrollan en los materiales procesados mediante tres procesos de fabricación: colada, laminación más un recocido posterior y extrusión.

Como se puede observar en la figura anterior, el tipo de procesado influye en la textura del material. Así, por ejemplo, durante un proceso de colada los granos cristalinos se orientan al azar. En cambio, el flujo plástico generado durante un proceso de laminación seguido de un tratamiento de recocido favorece el desarrollo de una textura fuerte de fibra en la que los hexágonos se encuentran con el eje "c" perpendicular al plano de laminación. Finalmente, en las barras extruidas de magnesio también se genera una textura fuerte en la cual la dirección $\langle 10\bar{1}0 \rangle$ de la celda cristalina se alinea con el eje de extrusión.

La red cristalina *HCP*, altamente anisótropa, confiere a las aleaciones de magnesio unas propiedades mecánicas particulares. Esto es así porque el número de sistemas de deslizamiento equivalentes es limitado. Así, las aleaciones de magnesio texturadas (esto es, cuyos granos no están orientados al azar), como es el caso de las aleaciones forjadas, presentan una fuerte anisotropía mecánica, una asimetría tensión-compresión en el límite elástico y baja ductilidad.

En la sección que se presenta a continuación se describirán los principales mecanismos de deformación del magnesio para distintas aleaciones con diversas texturas y se discutirán las condiciones bajo las cuales se activan unos u otros.

2.6. Mecanismos de deformación.

Los metales con estructura cristalina *HCP* tienen un número menor de sistemas de deslizamiento independientes para cada modo de deformación que los que poseen los metales con estructura cúbica centrada en el cuerpo (*BCC*) y cúbica centrada en las caras (*FCC*) [15,16].

En el caso particular del magnesio y sus aleaciones, los mecanismos de deformación que operan a bajas velocidades de deformación han sido exhaustivamente investigados en los últimos años [11-12,17-44]. Existen evidencias experimentales que muestran que en las aleaciones de Mg el deslizamiento de dislocaciones o *"slip"* puede producirse a lo largo de la dirección $\langle 11\bar{2}0\rangle$, también llamada dirección $\langle a\rangle$, tanto en los planos basales ($\{0001\}$) como en los planos no basales (en los prismáticos $\{10\bar{1}0\}$, y en los piramidales $\{10\bar{1}1\}$). Además, se ha observado deslizamiento a lo largo de la dirección $\langle c+a\rangle$ en planos piramidales $\{10\bar{1}1\}$ y $\{11\bar{2}2\}$ [34].

La figura 2.7 muestra los principales sistemas de deslizamiento que se pueden activar en las aleaciones de magnesio. Los mecanismos de deformación que operan a velocidades de deformación dinámicas aún no han sido estudiados en profundidad.

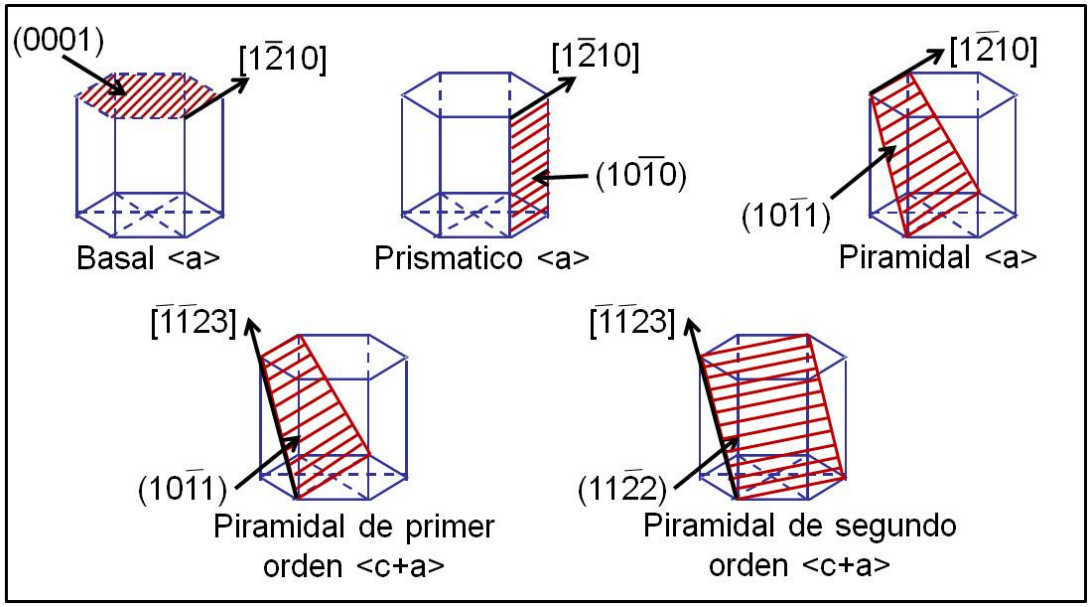

Figura 2.7. Sistemas de deslizamiento de las aleaciones de magnesio.

La deformación también pude tener lugar mediante la activación del maclado, principalmente a lo largo de los planos $\{10\bar{1}2\}$ y $\{10\bar{1}1\}$ y $\{10\bar{1}3\}$. Éste juega un papel importante durante la deformación de aleaciones de magnesio, y lo hace muy particularmente a bajas temperaturas [21,26,29,32,34,44] y altas velocidades de deformación. El maclado es un mecanismo polar [45]. Por ejemplo, el maclado $\{10\bar{1}2\}$ (también llamado maclado de extensión) se activa en un grano sólo cuando las condiciones de deformación son tales que se produce la extensión del eje C de la red cristalográfica hexagonal [38]. Análogamente, el maclado $\{10\bar{1}1\}$, o maclado de compresión se activa cuando la deformación aplicada promueve la compresión del eje C de la red HCP [46]. La figura 2.8 muestra los dos tipos de maclado más comunes en las aleaciones de magnesio.

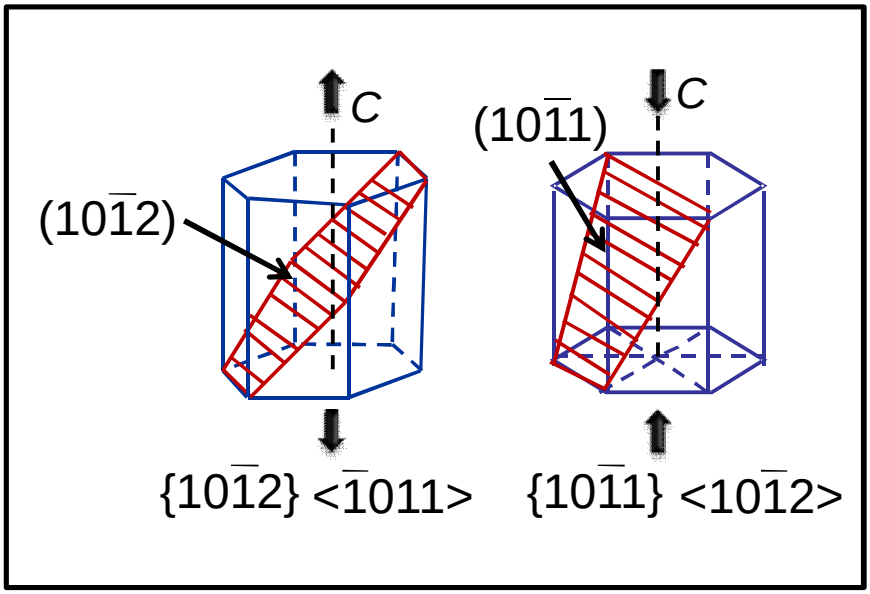

Figura 2.8. Sistemas de maclado más comunes en las aleaciones de magnesio.

La tensión de cizalladura crítica resuelta o *"Critical Resolved Shear Stress" (CRSS)* se define como el esfuerzo cortante mínimo que se debe aplicar sobre un plano de deslizamiento específico a lo largo de una dirección de deslizamiento concreta para que se produzca el deslizamiento cristalográfico. La *CRSS* varía considerablemente para cada uno de los sistemas de deslizamiento [16]. A pesar de que se ha publicado un amplio intervalo de valores de tensión de cizalladura crítica resuelta para los diferentes sistemas de deslizamiento y maclado [21, 26, 29, 32,34 ,44], se acepta generalmente que:

$$CRSS_{Basal} < CRSS_{Maclado} < CRSS_{Prismático} < CRSS_{Piramidal}$$

En [47] se recoge un resumen de las *CRSS* obtenidas de experimentos en monocristales, aunque los valores absolutos aún son un tema de debate [48].

2.6.1. Mecanismos de deformación a bajas temperaturas.

2.6.1.1. Policristal orientado al azar.

Durante la deformación uniaxial de policristales de magnesio, orientados al azar, con tamaño de grano convencional (~10-50 μm), a baja velocidad de ensayo y a temperatura ambiente, el deslizamiento en planos basales y el maclado de extensión $\{10\bar{1}2\}$ son los principales mecanismos de deformación [17-22]. En estas condiciones también se activa el deslizamiento no basal, pero en una proporción mucho menor [31,34,36].

2.6.1.2. Chapas laminadas.

Como se explicó anteriormente, las chapas laminadas poseen una textura basal, esto es, en la mayoría de los granos el eje C es paralelo a la dirección normal de laminación (*ND*). Cuando se comprime una placa de magnesio a lo largo de *ND*, es decir, cuando el eje de compresión es paralelo al eje C para la mayoría de los granos, el deslizamiento basal y el deslizamiento prismático y el maclado $\{10\bar{1}2\}$ no están favorecidos (ya que su factor de Schmid es prácticamente cero) y, por esta razón, el deslizamiento piramidal [34] y el maclado $\{10\bar{1}1\}$ se activan desde los primeros estadios de deformación [36]. El maclado se produce mayoritariamente en los planos $\{10\bar{1}1\}$, causando una reorientación de la red de aproximadamente 56º alrededor del eje $\langle 11\bar{2}0\rangle$. Ocasionalmente, áreas que han sufrido maclado de contracción se encuentran en una orientación favorable para un subsecuente maclado de extensión. Cuando ocurren de forma consecutiva estos dos mecanismos de maclado, se produce lo que se conoce como mecanismo de maclado secundario [46]. El ángulo de desorientación de las fronteras de macla que rodean un área con maclado secundario es de

aproximadamente 38º alrededor del eje $\langle 11\bar{2}0 \rangle$. La importancia del maclado de contracción y del maclado secundario para promover la compresión del eje C en aleaciones de Mg no se conoce con certeza. De hecho, las evidencias experimentales disponibles sugieren que su contribución neta a la deformación total no es muy importante. En particular, se ha afirmado que el maclado de contracción y el maclado secundario se activan en monocristales de magnesio ensayados con el eje de tensión paralelo al plano basal [49-51]. Sin embargo, los estudios en monocristales fueron llevados a cabo hace varias décadas y mayoritariamente utilizando exclusivamente microscopía óptica. Además, los indicios de esos mecanismos han sido hallados solamente en regiones muy localizadas (por ejemplo, muy cerca de la superficie de fractura o de la misma superficie de la muestra). Finalmente, la ductilidad de los monocristales raras veces excede el 2% y, por lo tanto, no queda muy claro si este mecanismo puede ser responsable de las elevadas deformaciones a fractura que son típicamente observadas en policristales de magnesio. Algunos estudios recientes han mostrado también la activación del maclado de contracción y del maclado secundario en aleaciones de magnesio policristalinas durante la compresión del eje C [12,36,52-54]. Sin embargo, nuevamente, los indicios de estos tipos de maclado son observados únicamente en regiones muy pequeñas, con frecuencia muy cerca de las superficies de fractura. Por todo ello, en la actualidad se acepta de forma general que el deslizamiento cristalográfico piramidal acomoda la mayoría de la deformación de compresión a lo largo del eje C [29,55]. Algunos autores han destacado el papel de las maclas de compresión en el endurecimiento por deformación (strain hardening) de las aleaciones de Mg [55].

Los sistemas de deslizamiento prismáticos se activan cuando se realizan ensayos de tracción a lo largo de la dirección de laminación *(RD)* o a lo largo de la dirección transversal a la de laminación *(TD)*

[34,36]. Por el contrario, si a temperatura ambiente se comprime una lámina de magnesio a lo largo de *RD*, es decir, de tal manera que el eje de compresión es perpendicular al eje "c" en la mayoría de los granos, entonces es el maclado $\{10\bar{1}2\}$ el que predomina desde las primeras etapas de la deformación, dando lugar a una rotación de la red cristalina de los granos de aproximadamente 86º, de forma que el eje "c" gira hasta casi alinearse con *ND.* Cuando un número suficiente de granos se ha orientado así, comienza a predominar el deslizamiento piramidal y el maclado $\{10\bar{1}1\}$, como se explicó anteriormente. Como consecuencia, se produce un importante endurecimiento por deformación debido a las interacciones dislocación–dislocación y macla–dislocación. La actividad de los distintos mecanismos de deformación debido a los diferentes ángulos entre la dirección de carga y el eje "c" genera una asimetría en el límite elástico [33,43,44].

2.6.1.3. Barras extruidas.

En barras de magnesio extruidas, en las cuales el eje C se alinea con la dirección radial (perpendicular al eje de extrusión) durante el procesado, el maclado de extensión predomina cuando se aplica una carga de compresión en la dirección de extrusión. Si una barra extruida se deforma en tracción a lo largo del eje de extrusión los mecanismos predominantes son el deslizamiento prismático y, en menor medida, el piramidal.

En los últimos años algunos estudios han investigado el comportamiento mecánico dinámico de aleaciones de magnesio obtenidas mediante procesos de conformado, como extrusión o laminación [56-66]. Estos trabajos analizan el efecto del incremento de la velocidad de deformación en el límite elástico, la tensión máxima, y la elongación a fractura, así como en los mecanismos de deformación que

se activan. Se ha sugerido que, en condiciones dinámicas, tiene lugar un incremento de la sensibilidad a la velocidad de deformación, de la ductilidad y de la capacidad de absorción de energía. También se ha observado un aumento de la actividad del maclado de extensión con la velocidad de deformación y se sugiere que este mecanismo opera incluso a temperaturas bastante elevadas, a las cuales no se encuentra activo en condiciones de ensayo cuasi-estáticas. Sin embargo, en general, los mecanismos de deformación predominantes a velocidades de impacto en aleaciones de Mg son todavía poco conocidos.

2.6.2. Mecanismos de deformación a alta temperatura.

A medida que aumenta la temperatura, a bajas velocidades de deformación y en aleaciones con tamaños de grano convencional (d~5-50 μm), la *CRSS* del deslizamiento basal y la del maclado de extensión $\{10\bar{1}2\}$ permanecen constantes [32], pero las de los sistemas de deslizamiento no basales y la del maclado de contracción disminuyen gradualmente [32]. De esta forma, a altas temperaturas la actividad de estos sistemas de deslizamiento no basal aumenta, facilitando la compatibilidad intergranular [20, 23, 34, 35,37,42]. En la figura 2.9 se muestra la variación de la *CRSS* de los distintos modos de deformación con la temperatura, según un modelo ideado por Barnett [32]. Las curvas fueron calculadas utilizando las ecuaciones que se presentan en la tabla 2.2, donde Z es el parámetro de Zener-Hollomon, $Z = \dot{\varepsilon}\exp\left(\frac{147000}{RT}\right)$, R es la constante de los gases ideales y T, la temperatura**.**

Tabla 2.2 Valores de la *CRSS* para los diferentes sistemas de deslizamiento y maclado en Mg según Barnett [32]**.**

Parámetro	Valor
$CRSS_{basal}$	$5MPa$
$CRSS_{prismatic}$	$2.5\ln(Z)-38MPa$
$CRSS_{\langle c+a\rangle}$	$2.1\ln(Z)-32MPa$
$CRSS_{twinning}$	$32MPa$
Twinning Region	$Z > 7x10^{12}\,s^{-1}$

A temperaturas mayores que 250ºC la *CRSS* de los sistemas no basales se hace finalmente menor que la del maclado de extensión y comparable con la del deslizamiento basal. A temperaturas ligeramente superiores (T > ≈300ºC) la *CRSS* para el maclado de compresión también disminuye significativamente, aunque sigue manteniendo valores más altos que los de los otros modos de deformación. Como resultado, con el incremento de temperatura, la deformación se va acomodando progresivamente por deslizamiento múltiple [34,67,68]. Algunos autores han resaltado también la importancia del deslizamiento de fronteras de grano a temperaturas superiores a los 300ºC [39,42]. Debido a la activación de un mayor número de modos de deformación, la ductilidad aumenta y el comportamiento mecánico de las aleaciones de magnesio, incluso las de textura fuerte, se vuelve más isótropo.

La deformación cuasi-estática a alta temperatura de aleaciones de magnesio con tamaño de grano convencional viene acompañada usualmente por recristalización dinámica (*DRX*). Hasta la fecha se han llevado a cabo bastantes estudios con el propósito de dilucidar el mecanismo de *DRX* predominante a distintas temperaturas y velocidades de deformación [69,70-82]. Ion et al. [70] publicaron en

1982 un estudio pionero en esta materia, en el cual observaron que la *DRX* era altamente dependiente de la temperatura de deformación. A T > 300-350ºC predominaría la recristalización dinámica discontinua (*DDRX)* [83,84,85], es decir, la nucleación de granos libres de deformación y el crecimiento de los mismos a expensas de las regiones deformadas mediante la migración a larga distancia de las fronteras de grano de ángulo alto. Esto ha sido confirmado, por ejemplo, en [76]. A temperaturas inferiores prevalecerían procesos de tipo continuo (*CDRX*), que consisten en la formación de límites de subgrano por acumulación de dislocaciones y el aumento gradual de la desorientación de éstos (θ) con la deformación [83,84]. Numerosos estudios han descrito la presencia de procesos continuos a temperaturas moderadas [69,74-75,77-78,80-82]. Más recientemente, las condiciones específicas bajo las cuales predominan la *DDRX* y la *CDRX*, han sido asociadas con determinados valores críticos del parámetro de Zener-Hollomon (Z), así como con la velocidad de deformación que también desempeña un papel importante (opuesto al de la temperatura) [28]. Dependiendo de la composición del material y de las características microestructurales, la *DDRX* y la *CDRX* pueden coexistir en un amplio intervalo de valores de Z.

Los mecanismos de deformación y recristalización de aleaciones de magnesio a velocidades de deformación de impacto (~10^3 s^{-1}) todavía no se conocen, ya que se han llevado a cabo muy pocos estudios en este área [56-62].

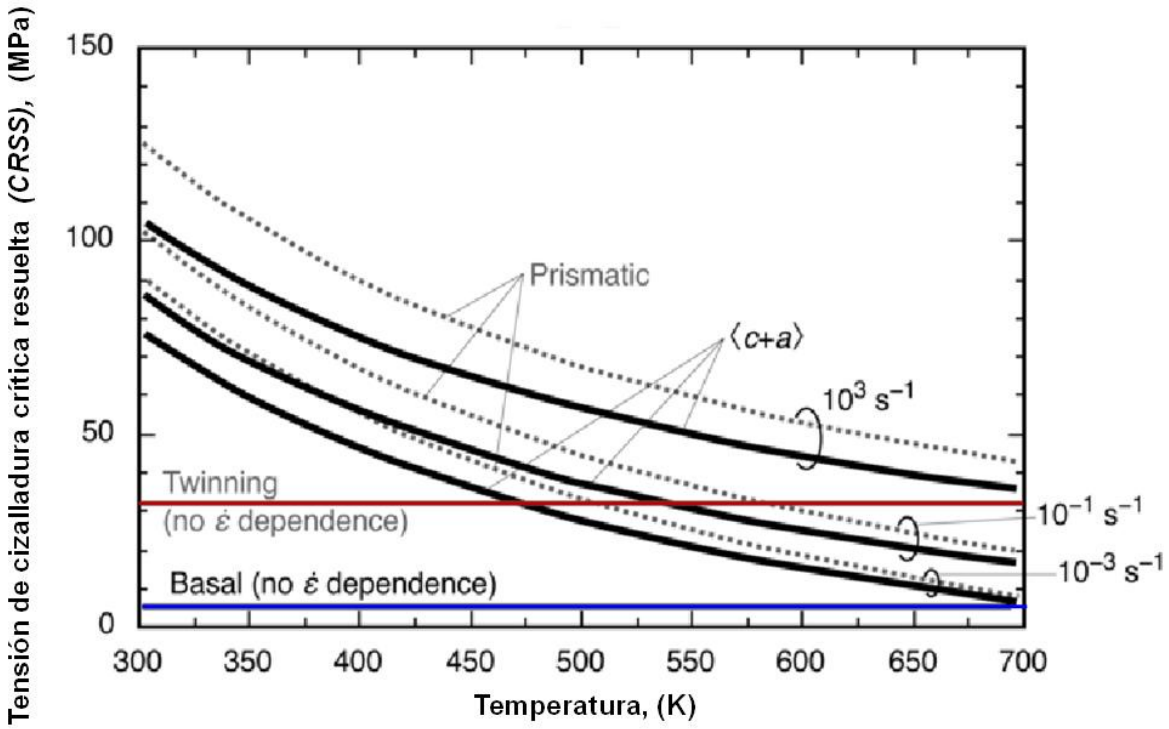

Figure 2.9. Variación de la *CRSS* de los distintos sistemas de deslizamiento y maclado con la temperatura [32,58].

2.6.3. Mecanismos de deformación en aleaciones de magnesio con tierras raras (Mg-RE).

Uno de los obstáculos a la entrada masiva de aleaciones de Mg en el mercado automovilístico es su baja capacidad para ser conformadas que, como habíamos mencionado anteriormente, viene originada por la gran anisotropía mecánica presente en las aleaciones comerciales convencionales. Recientemente se ha descubierto que esta anisotropía se puede reducir en gran medida mediante la aleación de Mg con elementos de tierras raras (*RE*), puesto que estas aleaciones poseen texturas de extrusión y laminado significativamente débiles [86-99]. A pesar de los grandes esfuerzos puestos en los últimos años en investigar aleaciones de Mg-*RE*, aún no se conoce claramente el origen de esta textura débil. Tampoco se conocen las contribuciones relativas a la deformación de los diferentes sistemas de deslizamiento y maclado en

aleaciones de Mg-*RE* a velocidades cuasi-estáticas. Algunos estudios han sugerido que la actividad del deslizamiento no basal aumenta debido a la interacción de elementos de tierras raras con las dislocaciones [87,88,96,98,99], lo que hace que los valores de la *CRSS* en el deslizamiento basal y no basal se encuentran mucho más próximos entre sí que en el caso de las aleaciones de Mg que no contienen *RE*. Otra prueba de la interacción entre los átomos de soluto de *RE* y las dislocaciones es la observación del fenómeno de envejecimiento dinámico por deformación en varias aleaciones de Mg-*RE* [93,94,97,100-101]. Los mecanismos de deformación que operan a velocidades dinámicas en estas aleaciones todavía no han sido investigados.

Como se había mencionado anteriormente, hasta la fecha se han llevado a cabo muchos estudios con la finalidad de elucidar los mecanismos de recristalización dinámica (*DRX*) en aleaciones de magnesio convencionales [70-82]. Sin embargo, los mecanismos de recristalización predominantes en aleaciones de Mg-*RE* no se conocen todavía. Se ha demostrado que los elementos de tierras raras debilitan drásticamente las texturas de recristalización. Esto fue inicialmente atribuido al fenómeno de "*particle stimulated nucleation"* (*PSN*) [43]. Sin embargo, después se ha mostrado que adiciones muy pequeñas de elementos de tierras raras, que no resultan en la precipitación de partículas de segunda fase, también pueden alterar notablemente las texturas de recristalización [86,93,102]. Se ha propuesto que la segregación de átomos de tierras raras en las fronteras de grano puede influir en las texturas de recristalización modificando la movilidad relativa de las fronteras [95,103]. Es necesario llevar a cabo estudios con mayor profundidad para clarificar estos aspectos. Los mecanismos de recristalización dinámica que operan a velocidades de deformación de impacto nunca han sido investigados.

2.7. Aleaciones de magnesio procesadas mediante colada por inyección a alta presión.

La colada por inyección a alta presión ("*high pressure die casting*", *HPDC*) es una de las técnicas más ampliamente extendidas para la fabricación de componentes de las aleaciones de Mg para aplicaciones automovilísticas debido a su bajo coste y a que permite fabricar grandes volúmenes de productos semi-terminados [10]. Las aleaciones AZ91 (Mg-9%$_p$Al-1%$_p$Zn) y AM60 (Mg-6%$_p$Al-0.5%$_p$Mn) son las que se utilizan habitualmente para fabricar piezas mediante moldeo por inyección; la primera posee excelentes propiedades de colabilidad y resistencia y la segunda está dotada de una ductilidad y una capacidad de absorción de energía extraordinarias. Muchos estudios se han centrado en relacionar la microestructura con el comportamiento mecánico de las aleaciones de Mg obtenidas mediante *HPDC*, en especial las de las series AZ y AM, a bajas velocidades de deformación [104-113].

Las propiedades mecánicas de las piezas de Mg obtenidas mediante *HPDC* son menos predecibles que las de piezas procesadas mediante procesos de conformado ya que parámetros microestructurales clave como la distribución de segundas fases y su fracción de volumen, el tamaño de grano y, la forma y distribución de los poros depende fuertemente de las condiciones de solidificación [114-115], las cuales cambian durante el procesado y son, de este modo, difíciles de reproducir y controlar.

Para que los componentes de Mg obtenidos mediante moldeo por inyección se puedan utilizar de forma masiva en aplicaciones estructurales en la industria del automóvil, éstos deben cumplir estrictos requisitos de absorción de energía frente a condiciones de impacto. Sin embargo, el comportamiento mecánico a alta velocidad de deformación de las aleaciones de Mg moldeadas por inyección no se

conoce con certeza [116].

2.8. Objetivo de la investigación.

El comportamiento de las aleaciones de Mg a altas velocidades de deformación (rango dinámico (~10^3 s^{-1})) aún no ha sido investigado en profundidad. En particular, la influencia de la temperatura y de la textura en los mecanismos de deformación y de recristalización, en las propiedades mecánicas y en las anisotropías del límite elástico y de la tensión máxima todavía no ha sido suficientemente estudiado.

Los estudios en condiciones dinámicas llevados a cabo hasta la fecha han versado principalmente sobre aleaciones de Mg de las series AZ y AM, procesadas por extrusión o por colada, y los ensayos se han realizado predominantemente en compresión [56-,57,58,60,63,66,117-123]. Estos han concluido que la ductilidad aumenta con la velocidad de deformación [60,118-,119,120,121] debido a que en condiciones dinámicas es mayor la sensibilidad a la velocidad de deformación. Asimismo, se ha observado que el maclado contribuye significativamente a la deformación inclusive a altas temperaturas, a las cuales es mayoritariamente suprimido a velocidades de deformación cuasi-estáticas [56-57,58,117]. También se ha mostrado que la tensión de flujo, o tensión máxima, en ensayos a alta velocidad de deformación es muy poco sensible a las variaciones de temperatura [56,57]. Solamente un estudio ha analizado el comportamiento mecánico dinámico de una aleación AZ31 laminada mediante ensayos de compresión a temperatura ambiente [66].

El propósito de esta tesis doctoral es contribuir a clarificar tanto el comportamiento mecánico, como los mecanismos de deformación y de recristalización de las aleaciones de Mg a velocidades de impacto. En

particular, se ha estudiado una chapa laminada de una aleación comercial (Mg-3%$_p$Al-1%$_p$Zn, AZ31), una barra extruida de una aleación con tierras raras (Mg-1%$_p$Mn-1%$_p$Nd, MN11) y varias piezas de las aleaciones comerciales Mg-9%$_p$Al-1%$_p$Zn (AZ91) y Mg-6%$_p$Al-0.5%$_p$Mn (AM60) obtenidas mediante colada por inyección.

Los resultados de este trabajo de investigación se han publicado en 3 artículos en revistas internacionales de SCI (Science Citation Index), los cuales constituyen el cuerpo de este escrito. A continuación se describe el contenido científico de cada uno de ellos.

En el primer artículo (*Ulacia I., N.V Dudamell, F. Gálvez, S. Yi, M.T. Pérez-Prado, I. Hurtado. Acta Materialia 58 (2010), 2988-2998*) se ha estudiado el comportamiento mecánico en compresión a lo largo de RD y ND de una lámina de la aleación AZ31 a alta velocidad de deformación (~10^3 s^{-1}) y en un amplio rango de temperaturas (de 25 ºC a 400 ºC) y éste se ha comparado con el observado tanto en estudios previos realizados a alta velocidad en tracción a lo largo de RD y TD como a bajas velocidades de deformación en tracción y en compresión a lo largo de RD, TD, y ND. Con este propósito se han realizado dos tipos de ensayos de compresión en muestras extraídas de una lámina de la aleación AZ31: por una parte, en una barra Hopkinson a temperaturas entre 25 ºC y 400 ºC a ~10^3 s^{-1} y, por otra, en una máquina convencional de ensayos Instron a 25 ºC, 200 ºC y 400 ºC y a velocidades de deformación de 5x10^{-4} s^{-1}, 5x10^{-3} s^{-1} y 5x10^{-2} s^{-1}. La anisotropía tanto del límite elástico como de la tensión máxima fuera del plano (esto es, comparando los valores correspondientes a ensayos de compresión realizados a lo largo de *RD* y *ND*) y la asimetría tensión-compresión se han evaluado en función de la temperatura. Estos datos han permitido investigar los mecanismos de deformación y recristalización predominantes y analizar la variación de la CRSS con la temperatura a alta velocidad de deformación.

En el segundo artículo de investigación (*N.V. Dudamell, I. Ulacia, F. Gálvez, S. Yi, J. Bohlen, D. Letzig, I. Hurtado, M.T Pérez-Prado. Acta Materialia 59 (2011), 6949-6962*) se ha estudiado la evolución de la microestructura y de la textura de una chapa de aleación de Mg AZ31, laminada y recocida, durante deformación dinámica a temperatura ambiente en función de la deformación y de la orientación de la carga aplicada. En particular, las condiciones analizadas incluyen, por una parte, compresión tanto a lo largo de la dirección de laminación (*RD*) como en la dirección normal (*ND)* y, por otra, tensión a lo largo de *RD*. Se realizaron ensayos en una barra Hopkinson controlando la deformación máxima alcanzada con el fin de evaluar la actividad de los distintos mecanismos de deformación y recristalización a medida que aumenta la deformación. La microestructura de las muestras, antes y después de deformar, fue caracterizada exhaustivamente mediante microscopía óptica, mediante difracción de electrones retrodispersados ("*electron backscatter difraction"* EBSD) y mediante difracción de neutrones. Se ha prestado especial atención a la actividad de diferentes modos de maclado y a la evolución de la distribución de la desorientación de los límites de grano, los cuales dan información valiosa sobre la presencia de mecanismos de restauración. La evolución microestructural a temperatura ambiente de esta aleación laminada de magnesio AZ31 a altas velocidades de deformación se ha comparado con aquéllas que se producen a velocidades de deformación cuasiestáticas.

En el tercer artículo de investigación (*N.V. Dudamell, I. Ulacia, F. Gálvez, S. Yi, J. Bohlen, D. Letzig, I. Hurtado, M.T Pérez-Prado. et al. Materials Science and Engineering A 532 (2012), 528-535*), se han investigado los mecanismos de *DRX* que predominan durante la deformación a alta temperatura y a velocidades de deformación dinámicas en una chapa laminada de la aleación AZ31 en función del modo de carga y de la orientación relativa entre el eje de carga y el eje C del agregado

policristalino. Con este propósito se ha examinado la evolución de la microestructura, la textura y la distribución de la desorientación de las fronteras de grano con la deformación a 250ºC en una chapa laminada de AZ31 comprimida a lo largo de las direcciones de laminación (*RD*) y normal (*ND*) y también ensayada en tensión a lo largo de la *RD*. La microestructura de las muestras, antes y después de deformar, fue caracterizada exhaustivamente mediante microscopía óptica, mediante difracción de electrones retrodispersados (EBSD) y mediante difracción de neutrones. El comportamiento mecánico, la evolución de la microestructura y la textura y los mecanismos de *DRX* se han comparado con los que prevalecen a velocidades de deformación cuasi-estáticas a temperaturas similares.

Además, en el apartado 4 se presentan dos estudios complementarios a los incluidos en los artículos descritos anteriormente. En el primero (apartado 4.1) se ha analizado el comportamiento mecánico, a temperaturas comprendidas entre 25ºC y 400ºC, tanto a velocidades cuasi-estáticas como dinámicas, de una barra extruida de una aleación de última generación de Mg con adición de tierras raras (Mg-1%$_p$Mn-1%$_p$Nd (MN11)). Los ensayos se han realizado a lo largo de la dirección paralela al eje de extrusión y de una perpendicular a esta con la finalidad de evaluar la anisotropía mecánica. La evolución de la microestructura y de la textura se caracterizaron exhaustivamente mediante microscopía óptica y mediante difracción de electrones retrodispersados (EBSD) durante la deformación con el propósito de elucidar los mecanismos de deformación y recristalización predominantes. Los resultados se comparan con los obtenidos en la aleación comercial AZ31.

Finalmente, se presenta un segundo estudio complementario (sección 4.2.) en el que se describe el comportamiento mecánico de las aleaciones comerciales de Mg moldeadas por inyección AZ91D y AM60B

cuando se deforman a en el régimen dinámico en un amplio intervalo de temperaturas, en tensión y en compresión. Se ha estudiado la influencia de la velocidad de deformación en el límite elástico, en la tensión máxima, y en la elongación a fractura. Además, se describe la variabilidad de las propiedades mecánicas. Se ha realizado una comparación entre las propiedades obtenidas a alta y a baja velocidad de deformación.

PART III

RESEARCH PAPERS

Important Note: Figures and tables are numbered as 1, 2, 3... inside each research paper, but they are labeled in the list of figures and tables with their corresponding article number, following the notation: chapter.article.figure(or table). For example, the figure 3.1.4 corresponds to the fourth figure of the first research paper located in chapter 3. Similarly, the table 3.2.1 corresponds to the first table of the second research paper located in chapter 3.

3.1. Mechanical behavior and microstructural evolution of a Mg AZ31 sheet at dynamic strain rates.

Acta Materialia 58 (2010) 2988-2998

I. Ulacia[a], N.V. Dudamell[b], F. Gálvez[c], S. Yi[d],
M.T. Pérez-Prado[b], I. Hurtado[a]

[a] Mondragon Goi Eskola Politeknikoa, Mondragon Unibertsitatea, 20500 Mondragón, Spain
[b] Madrid Institute for Advanced Studies in Materials, IMDEA Materials, C/Profesor Aranguren s/n, 28040 Madrid, Spain
[c] ETS Ingenieros de Caminos, Universidad Politécnica de Madrid, 28040 Madrid, Spain
[d] GKSS Research Center, 21502 Geesthacht, Germany

Received 10 December 2009; received in revised form 19 January 2010; accepted 19 January 2010
Available online 17 February 2010

Available online at www.sciencedirect.com
ScienceDirect
Acta Materialia 58 (2010) 2988–2998
Acta MATERIALIA
www.elsevier.com/locate/actamat

Mechanical behavior and microstructural evolution of a Mg AZ31 sheet at dynamic strain rates

I. Ulacia [a], N.V. Dudamell [b], F. Gálvez [c], S. Yi [d], M.T. Pérez-Prado [b,*], I. Hurtado [a]

[a] Mondragon Goi Eskola Politeknikoa, Mondragon Unibertsitatea, 20500 Mondragón, Spain
[b] Madrid Institute for Advanced Studies in Materials, IMDEA Materials, Cl Profesor Aranguren s/n, 28040 Madrid, Spain
[c] ETS Ingenieros de Caminos, Universidad Politécnica de Madrid, 28040 Madrid, Spain
[d] GKSS Research Center, 21502 Geesthacht, Germany

Received 10 December 2009; received in revised form 19 January 2010; accepted 19 January 2010
Available online 17 February 2010

Abstract

The mechanical behavior of an AZ31 Mg sheet has been investigated at high strain rate ($10^3\ s^{-1}$) and compared with that observed at low rates ($10^{-3}\ s^{-1}$). Dynamic tests were carried out using a Hopkinson bar at temperatures between 25 and 400 °C. Tensile tests were carried out along the rolling and transverse directions and compression tests along the rolling and the normal directions in both strain rate ranges. The tension–compression yield asymmetry as well as the yield and flow stress in-plane and out-of-plane anisotropies were investigated. The microstructure of the initial and tested samples was examined by electron backscatter diffraction. The dynamic mechanical behavior is characterized by the following observations. At high temperatures the yield asymmetry and the yield anisotropies remain present and twinning is highly active. The rate of decrease in the critical resolved shear stress of non-basal systems with temperature is smaller than at quasi-static rates. Rotational recrystallization mechanisms are activated.

Keywords: AZ31; High strain rate; Twinning; Slip; Anisotropy

1. Introduction

Magnesium alloys have been the subject of numerous studies in the last decade due to their low density ($1.7\ g\ cm^{-3}$) and thus their potential to contribute to weight reduction in vehicles and other structures [1,2]. Bringing Mg parts to the market requires, depending upon the specific application, increasing their mechanical strength and ductility, decreasing their anisotropy in order to improve formability or enhancing their corrosion resistance [3]. It is also crucial to optimize the behavior of Mg alloys under crash conditions [1], i.e. at high strain rates, especially when Mg parts are designed to be used in some critical automobile components.

The deformation mechanisms of Mg and Mg alloys that are operative at low strain rates have been extensively investigated over the past years [4–33]. Slip in hexagonal close packed (hcp) metals may take place along the $\langle 1\ 1\ -2\ 0\rangle$($\langle a\rangle$) direction on basal and non-basal ($\{1\ 0\ -1\ 0\}$-prismatic, $\{1\ 0\ -1\ 1\}$-pyramidal) planes. Additionally, second order pyramidal $\langle c+a\rangle$ slip has also been observed along $\{1\ 1\ -2\ 2\}$ planes [22]. Deformation is accommodated also by twinning, mainly along $\{1\ 0\ -1\ 2\}$ and $\{1\ 0\ -1\ 1\}$ planes. However, the deformation mechanisms operative at dynamic strain rates are still widely unknown.

The activity of the different deformation modes has been shown to be highly dependent on temperature [34]. Although widely spread values have been reported for the critical resolved shear stress (CRSS) in the different slip and twinning systems [8,13,16,19,22,33], it is generally accepted that $CRSS_{basal} < CRSS_{twinning} < CRSS_{prismatic} \leqslant CRSS_{pyramidal}$. In agreement with this trend, earlier studies reported that slip on basal planes and $\{1\ 0\ -1\ 2\}$ twinning (so called extension twinning) are the main deformation mechanisms during uniaxial deformation at low temperatures and low strain

* Corresponding author.
E-mail address: teresa.perez.prado@imdea.org (M.T. Pérez-Prado).

1359-6454/$36.00 © 2010 Acta Materialia Inc. Published by Elsevier Ltd. All rights reserved.
doi:10.1016/j.actamat.2010.01.029

rates in randomly oriented Mg polycrystals of conventional grain sizes (~10–50 μm) [4–9]. Non-basal slip systems are also active, albeit to a lesser extent [18,22,24]. The CRSS for basal slip and {1 0 −1 2} twinning are believed to be temperature independent [34]. However, the CRSS of prismatic and pyramidal systems decrease with increasing temperature even to smaller levels than the CRSS of {1 0 −1 2} twinning. Thus, at high temperatures the activity of these non-basal slip systems increases, facilitating intergranular compatibility and, therefore, that of twinning decreases [7,10,22,23,25,31]. Some studies have also suggested an increasing contribution of grain boundary sliding (GBS) at high temperatures, even in materials with conventional grain sizes [12,23,27,31]. At temperatures higher than about 200 °C dynamic recrystallization (DRX) takes place simultaneously [35–39]. The activation of these additional mechanisms results in enhanced ductility with increasing temperature.

Due to the low availability of independent slip systems for each slip mode, the deformation of Mg alloys is highly dependent on texture [20,28]. This anisotropy is further accentuated by the polarity of {1 0 −1 2} twinning, which only allows shear in one direction (as opposed to the possibility of forward and backward shear characteristic of deformation by slip) [40]. The effect of texture is more pronounced when investigating extruded or rolled alloys, as in these cases strong ⟨1 0 −1 0⟩ and ⟨0 0 0 1⟩ fibers, respectively, develop. For example, when compression is carried out along the rolled sheet normal direction (ND), i.e. the compression axis is parallel to the *c*-axes of most grains, both basal slip and {1 0 −1 2} twinning are not favored and thus non-basal slip [22] and {1 0 −1 1} twinning are activated at the early stages of deformation [24]. Non-basal slip systems are also activated when tension tests are carried out along the rolling direction (RD) or the transverse direction (TD) [22,24]. On the contrary, when a Mg sheet is compressed at room temperature along RD, i.e. the compression axis is perpendicular to the *c*-axes in most grains, {1 0 −1 2} twinning predominates at the early stages of deformation, causing grains to rotate ~86° and thus the *c*-axes to become closely aligned to the ND. Significant strain hardening ensues due to both dislocation–dislocation and twin-dislocation interactions. The operation of different deformation mechanisms due to the different angles between the loading direction and the *c*-axis causes an asymmetry in the yield stress [21,32,33].

The deformation of Mg alloys at dynamic strain rates (10^3 s^{-1}) has not been thoroughly investigated yet. In particular, the influence of temperature and texture on the deformation mechanisms and on the yield stress and flow stress anisotropies is still unknown. The studies carried out to date have dealt mostly with AZ and AM alloys, processed by extrusion or by casting, and testing has been performed predominantly in compression [41–53]. It has been concluded that ductility increases with increasing strain rate [41–45] due to an increase in the strain rate sensitivity. Additionally, twinning has been observed to contribute significantly to deformation even at high temperatures, at which it is mostly suppressed at quasi-static strain rates [46,47,50,53]. The flow stress in high strain rate tests has been observed to be very insensitive to temperature [46,47]. Only one study has analyzed the dynamic mechanical behavior of an AZ31 sheet, by means of room temperature compression tests [52].

The aim of this work was to analyze the mechanical behavior of an AZ31 sheet under dynamic conditions (10^3 s^{-1}) and to compare it with that observed at low strain rates. With that purpose AZ31 sheets have been tested in tension and in compression using a Hopkinson bar apparatus at temperatures ranging from 25 to 400 °C. The tension–compression yield asymmetry and the yield stress and flow stress in-plane and out-of-plane anisotropies have been evaluated as a function of temperature. Detailed microstructure and texture examination by EBSD and neutron diffraction has been carried out in selected samples in order to elucidate the predominant deformation and recrystallization mechanisms.

2. Experimental procedure

2.1. Material: initial microstructure

The material under study was the Mg alloy AZ31-O. Two rolled and annealed sheets, 1 and 3 mm in thickness, were purchased from Magnesium Elektron.

The microstructure and the texture of the as received material was analyzed by electron backscatter diffraction (EBSD) using the EDAX-OIM™ software in a Zeiss Ultra 55™ FEG-SEM scanning electron microscope. Sample preparation for EBSD included grinding with 4000 SiC paper, mechanical polishing with a 0.05 μm silica suspension and final electro-chemical polishing for 90 s at 33 V using the AC2™ commercial electrolyte. The microstructure is represented by EBSD orientation maps and the texture by pole figures recalculated from the EBSD orientation data. Since EBSD only allows examination of the local texture, macrotexture measurements were also performed by neutron diffraction in the STRESS-SPEC instrument at the Forschungs-Neutronenquelle Heinz Maier-Leibnitz (FRM II) of the Munich Technical University (Germany). The area examined had a diameter of ~5 mm. A Ge monochromator with an associated wavelength of 1.65 Å was used.

The initial microstructures of the two AZ31 sheets of 1 and 3 mm thickness were formed of equiaxed grains, with average sizes of 10 and 13 μm, respectively. As generally observed in annealed AZ31 sheets, both have a characteristic strong texture, formed by the ⟨0 0 0 1⟩ fiber (*c*-axes parallel to ND). Fig. 1 illustrates the microstructure and the texture of the 1 mm sheet, measured by EBSD. It can be seen that the ⟨0 0 0 1⟩ fiber is not perfect, as some spreading of the (0 0 0 1) poles toward the RD is present. Macrotexture measurements by neutron diffraction were consistent with the EBSD measurements. Due to the fact

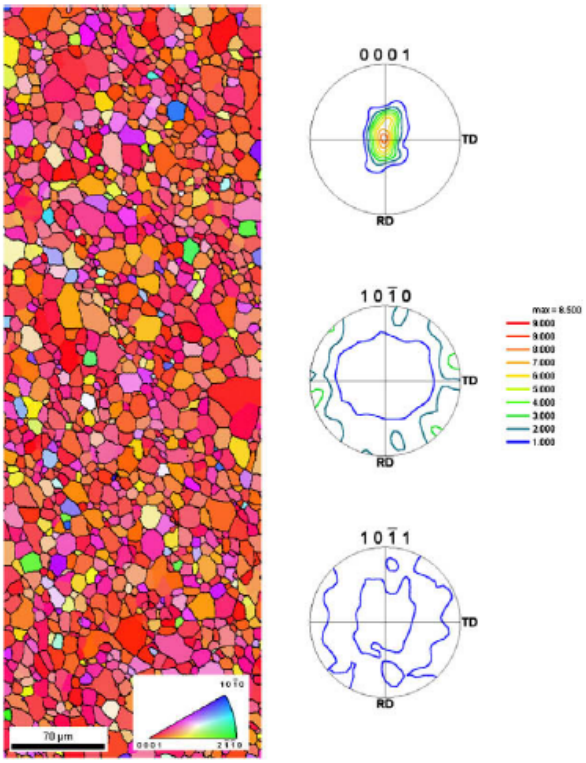

Fig. 1. Microstructure and texture of the a received Mg AZ31-O alloy measured by EBSD. The color code corresponds to the ND inverse pole figure.

that the microstructures and textures of both sheets were almost identical, the data corresponding to the 3 mm sheet will not be shown here for the sake of brevity.

2.2. Mechanical testing

An exhaustive testing campaign was performed in order to compare the mechanical behavior of the AZ31-O sheet at dynamic ($\dot{\varepsilon}\sim10^{3}\ s^{-1}$) and low ($\dot{\varepsilon}\sim10^{-3}\ s^{-1}$) strain rates. In particular, the tension–compression asymmetry of the yield and flow stresses, as well as the in-plane and the out-of-plane anisotropies of the yield and flow stresses were evaluated with increasing temperature at both strain rates. It will be assumed that the results from the tests carried out in samples machined out of the two AZ31 sheets are comparable for the following two reasons. Firstly, previous studies have shown that the uniaxial mechanical behavior of Mg sheets is not affected by thickness (in the range considered here) [33]. Secondly, although grain size has been found to influence the mechanical behavior of Mg alloys [21,33], the small difference in grain sizes of the sheets investigated here is not considered significant for the purpose of this study.

Tensile tests were performed in the 1 mm thick sheet. The reader is referred to Ulacia et al. [54] for a more detailed description of the testing procedures. High strain rate tests (HSR) ($10^{3}\ s^{-1}$) were carried out using a tensile split Hopkinson bar, furnished with a radiant furnace and a high speed camera. Tests were performed along the RD and TD at temperatures ranging from 25 to 300 °C in dumbbell-shaped tensile specimens with a gage length of 12.5 mm and a width of 1.75 mm. Tensile tests at low strain rates (LSR) ($10^{-3}\ s^{-1}$) were also performed along the RD and TD using a conventional electromechanical Instron 4206 testing machine at temperatures ranging from 25 to 250 °C. The specimens tested at LSR were machined according to a sample geometry defined by ASTM E8 M-00.

Compression testing was carried out on the 3 mm thick sheet. HSR compression tests were performed using also a Hopkinson bar at $10^{3}\ s^{-1}$, while LSR compression tests were carried out at $10^{-3}\ s^{-1}$. At both high and low strain rates tests were performed along the RD and ND in order to investigate the out-of-plane anisotropy and the testing temperatures ranged from room temperature to 400 °C. The specimens compressed along RD were $3 \times 3 \times 4.5$ mm prisms and the samples compressed along ND were $3 \times 3 \times 3$ mm cubes.

Fig. 2 is a schematic that summarizes the relative orientation between the tension and compression axes and the *c*-axes with respect to the sheet reference system (RD, TD, ND) corresponding to all the tests (at high and low strain rates) performed. As illustrated in this figure, the nomenclature adopted in the remainder of the paper for the different tests is as follows: RD-T (tension along RD); RD-C (compression along RD); TD-T (tension along TD); ND-C (compression along ND).

The microstructure and texture of the samples deformed in tension were examined by EBSD in order to evaluate the deformation and recrystallization mechanisms. Neutron diffraction was also utilized to measure the macrotexture of the deformed specimens, as it gives a better statistical description of the orientations. Microstructural analysis could not be performed in the samples deformed in compression because the specimens were smashed during testing.

3. Results

3.1. Mechanical behavior of the AZ31-O Mg sheet at high strain rates

Fig. 3 illustrates the stress–strain curves corresponding to HSR tests carried out at room temperature and at

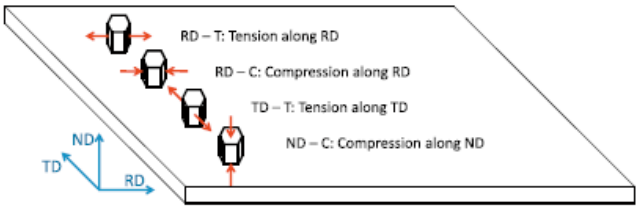

Fig. 2. Schematic illustrating the relative orientation of the tension and compression axes with respect to the *c*-axes and the sheet reference system (RD, TD, ND) for all the tests carried out in the present investigation.

250 °C. Specifically, Fig. 3a compares the curves corresponding to the AZ31-O alloy deformed in tension and compression along RD (RD-T vs. RD-C). The shapes of the curves at room temperature were similar to those observed at low strain rates (concave down under tensile loading and concave up under compressive loading). These distinct shapes are consistent with the predominance of crystallographic slip in tension and of {1 0 −1 2} twinning followed by rapid strain hardening in compression [21,32,33]. Asymmetry in the yield stress can thus also be clearly seen at these high strain rates. Furthermore, this asymmetry remains present at 250 °C and, in fact, at all the temperatures investigated here. Concave up curves have been obtained when testing in compression along RD at temperatures as high as 400 °C. This is consistent with the activation of {1 0 −1 2} twinning at high temperatures during dynamic deformation, as suggested by other authors [46,47,50,53]. Fig. 3a reveals a significant decrease in the flow stress with temperature.

Fig. 3b illustrates the stress–strain curves corresponding to tensile tests along RD and TD (RD-T vs. TD-T) at room temperature and at 250 °C. Both curves had a concave down shape, due to the predominant operation of crystallographic slip under these two testing conditions. In-plane anisotropy in the yield stress can be observed. This anisotropy remains present at 250 °C and, in fact, at all the temperatures investigated.

Fig. 3c depicts the stress–strain curves corresponding to tests carried out in compression along RD and ND (RD-C vs. ND-C) at room temperature and at 250 °C. The RD-C curves had a concave up shape, due to the operation of {1 0 −1 2} twinning, while the ND-C curves had a concave down shape, reflecting the predominant operation of crystallographic slip. Firstly, clear out-of-plane yield stress anisotropy can be observed at both temperatures. This anisotropy remained present under dynamic conditions at all the temperatures investigated. Secondly, a significant decrease in the maximum flow stress with increasing testing temperature was apparent. Finally, it is important to remark that none of the tests performed at high strain rate showed any softening with increasing strain, whereas at LSR softening was observed at moderate temperatures (~200 °C).

3.1.1. Yield stress

The yield stress (σ_y) is related to the CRSS of the various operating deformation mechanisms as $\sigma_y = m\tau_0 + mkd^{-1/2}$, where m is the Taylor factor, τ_0 is the CRSS for the operative slip systems and k is the microstructural shear stress intensity characterizing the average grain boundary resistance to plasticity spreading between the grains. Thus, analyzing the variation of σ_y with strain rate and temperature allows approximate inference of the sensitivity of the CRSS of the operative deformation modes to $\dot{\varepsilon}$ and temperature.

3.1.1.1. Yield stress tension–compression asymmetry. Fig. 4a depicts the variation in $\sigma_{0.005}$ with temperature during tensile and compressive loading along the RD (RD-T vs. RD-C) in HSR (closed symbols) and LSR (open symbols) tests. In dynamic tests it is difficult to measure the true yield stress at the nominal strain rate, since in the early stages of deformation the strain rate increases gradually. Thus, $\sigma_{0.005}$ is used in the present study as a best approximation to this material property. In RD-T tests non-basal (mainly prismatic) systems were activated, since basal planes are unfavorably oriented for slip in many grains [22,24]. (Basal slip, however, is also activated to some extent). In RD-C tests, however, {1 0 −1 2} twinning predominated during the first stages of deformation.

It is apparent in Fig. 4a that the tensile yield stress was higher at HSR than at LSR at all the temperatures investigated. This can mainly be attributed to the strain rate dependency of the CRSS of non-basal slip systems, since the CRSS for basal slip has been shown to be independent of strain rate [34]. However, compression yield stresses did not show any dependence on the strain rate, confirming

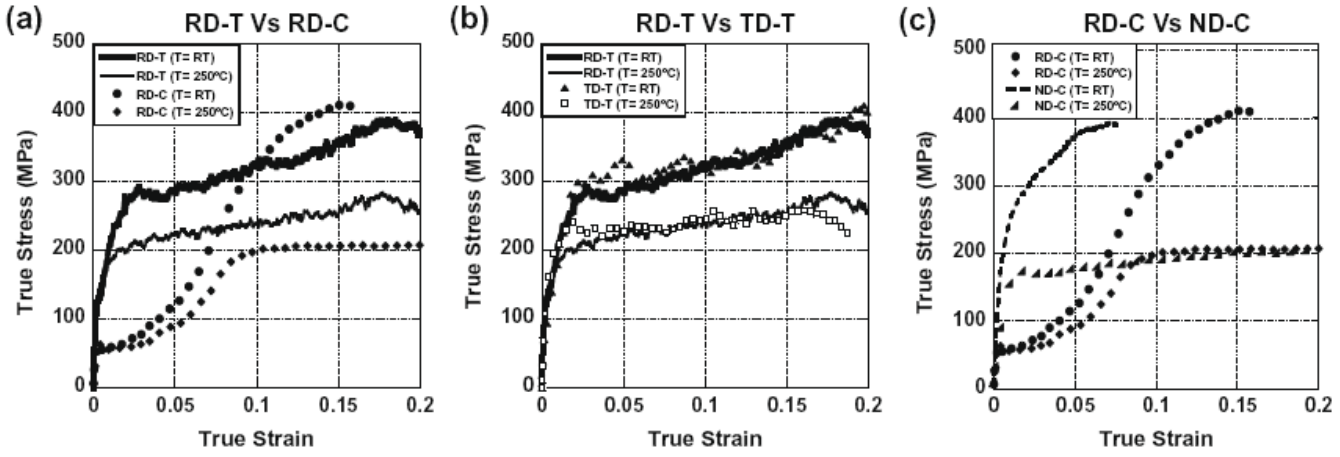

Fig. 3. True stress–true strain curves corresponding to HSR (10^3 s^{-1}) tests performed at room temperature and at 250 °C: (a) RD-T vs. RD-C; (b) RD-T vs. TD-T; and (c) RD-C vs. ND-C.

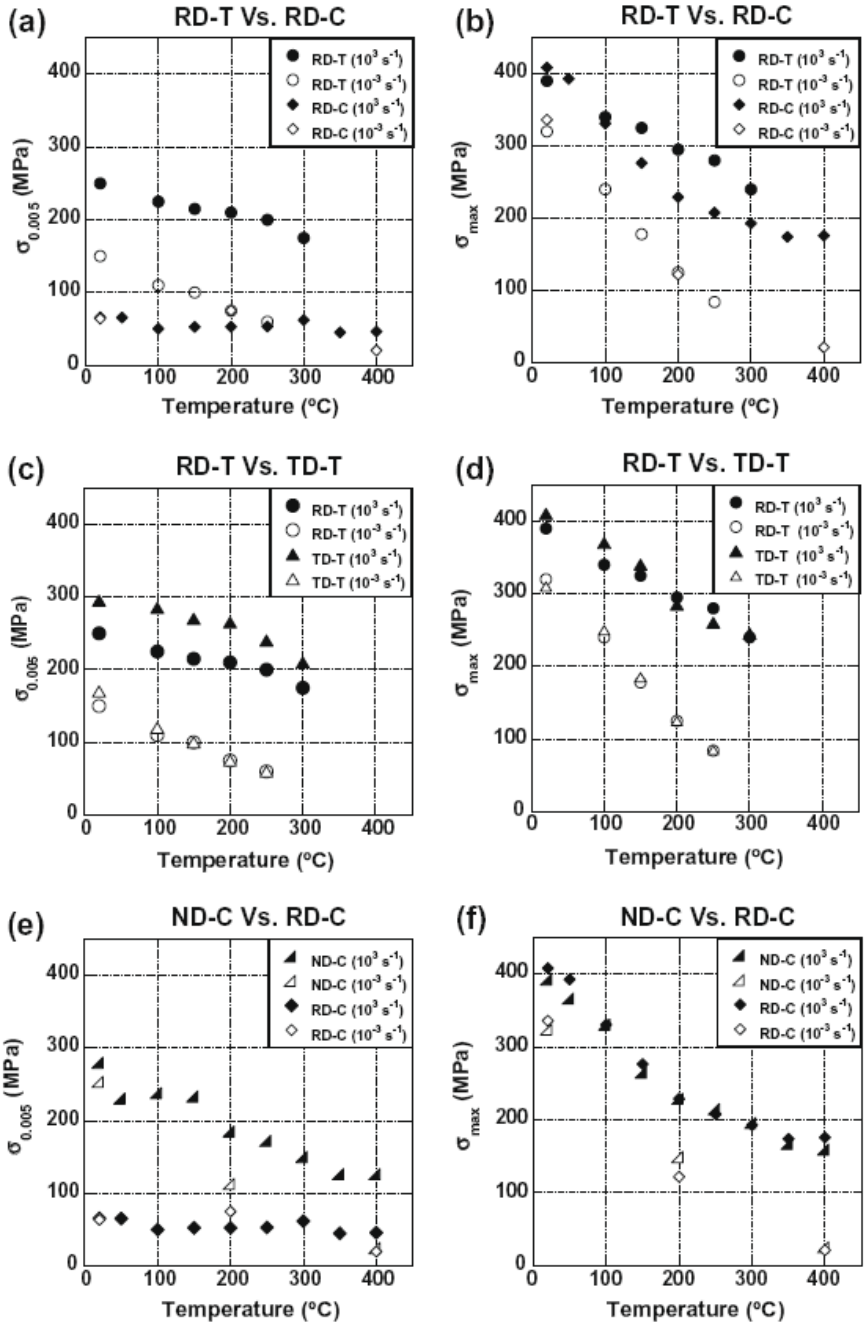

Fig. 4. Variation of the true stress at $\varepsilon = 0.005$ ($\sigma_{0.005}$) and of the flow stress (σ_{max}) with temperature during HSR (10^3 s^{-1}, closed symbols) and LSR (10^{-3} s^{-1}, open symbols) strain rate tests.

that the CRSS for {1 0 −1 2} twinning is strain rate independent. Moreover, under both strain rate regimes the tensile yield stress decreased with temperature, while the compression yield stress remained constant. These two observations can be explained, respectively, by the decrease in the CRSS of non-basal slip systems with increasing temperature [7,10,22,23,25,31] and the temperature independence of the CRSS for {1 0 −1 2} twinning [34]. The decrease in the compressive yield stress at 400 °C in LSR tests is due to a change in the predominant deformation mechanism from {1 0 −1 2} twinning to crystallographic slip, which is caused by a decrease in the CRSS of non-basal slip systems below that of twinning at approximately 200 °C [34].

In Fig. 5a the yield stress tension–compression asymmetry ($\sigma_{0.005(RD\text{-}T)}/\sigma_{0.005(RD\text{-}C)}$) has been plotted as a function of temperature for both HSR and LSR. The tension–compression asymmetry was significantly larger at HSR than at LSR (3.84 and 2.59 at room temperature and 2.7 and 1 at 300 °C, respectively). The tension–compression asymmetry

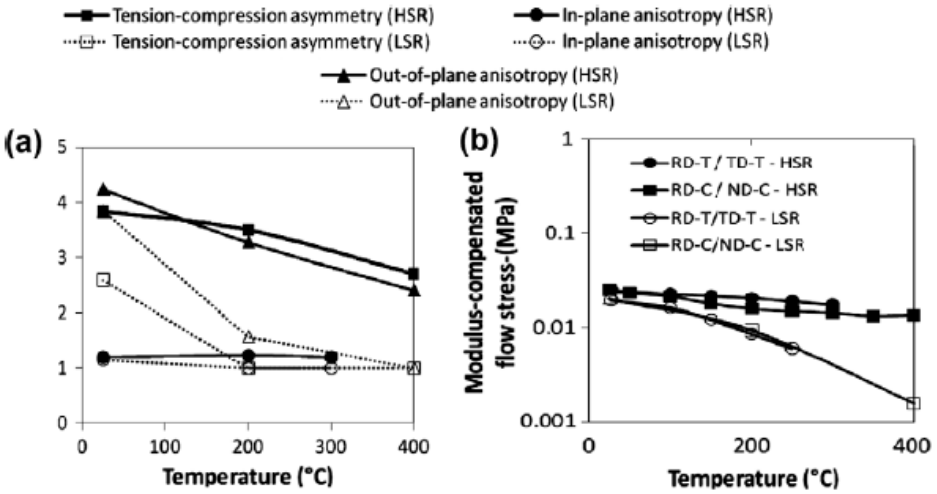

Fig. 5. (a) Variation in the yield stress tension–compression asymmetry ($\sigma_{0.005(RD\text{-}T)}/\sigma_{0.005(RD\text{-}C)}$), the yield stress in-plane anisotropy ($\sigma_{0.005(TD\text{-}T)}/\sigma_{0.005(RD\text{-}T)}$) and the yield stress out-of-plane anisotropy ($\sigma_{0.005(ND\text{-}C)}/\sigma_{0.005(RD\text{-}C)}$) with temperature at both high strain rates (HSR) and low strain rates (LSR). (b) Modulus-compensated flow stress (σ_{max}/G) as a function of temperature corresponding to tests performed in tension along in-plane directions (RD-T/TD-T) and in compression along RD and ND (RD-C and ND-C) at both high strain rate (HSR) and low strain rate (LSR).

decreased gradually with temperature in both strain rate ranges, but the rate of decrease was smaller under dynamic conditions. This suggests that the decrease in the CRSS of non-basal (mainly prismatic) slip with temperature is less pronounced at HSR than at LSR.

3.1.1.2. Yield stress in-plane and out-of-plane anisotropies. Fig. 4c presents the variation in $\sigma_{0.005}$ as a function of temperature during tensile loading along the RD and TD (RD-T vs. TD-T) at HSR and LSR. Under these loading conditions the activation of basal slip was limited and non-basal (mainly prismatic) slip played an important role, as explained above. At room temperature the yield stress along the TD was higher than that obtained along the RD for both strain rate regimes. This is related to the slight spread of the basal fiber towards the RD in the initial material, which allows relatively easier activation of basal slip by tensile loading along the RD [22,33]. In both RD-T and TD-T tests the yield stress decreased with temperature at both strain rates. However, the decrease was more pronounced at low strain rates. This, again, suggests that the decrease in the CRSS of non-basal slip with temperature is less pronounced at HSR than at LSR. The variation of the in-plane yield anisotropy ($\sigma_{0.005(TD\text{-}T)}/\sigma_{0.005(RD\text{-}T)}$) with temperature is illustrated in Fig. 5a for both strain rates. At room temperature this parameter was only slightly higher at HSR than at LSR (1.20 and 1.16, respectively). It remained constant with temperature at high strain rate, while it becomes 1 at ~200 °C at low strain rates.

Fig. 4e shows the evolution with temperature of $\sigma_{0.005}$ during compression tests along the RD and ND (RD-C vs. ND-C) at high and low strain rates. The RD-C tests were explained above. In ND-C tests basal planes were mostly perpendicular to the compression axis and prismatic planes were predominantly parallel to it. Additionally, {1 0 −1 2} twinning was not favored, also for geometrical reasons. Thus, pyramidal slip was the predominant deformation mechanism in ND-C tests. At room temperature the yield stress of HSR ND-C tests was only slightly higher than that of the low strain rate tests, suggesting that the CRSS for pyramidal slip is not very dependent on the strain rate. The yield stress in ND-C tests decreased with increasing temperature, mostly attributed to the temperature dependence of the CRSS of pyramidal slip systems. The decrease was more pronounced in low strain rate tests. This observation further confirmed that at HSR the temperature decrease in the CRSS for pyramidal slip is less pronounced than at LSR.

Fig. 5a illustrates the variation in the out-of-plane anisotropy ($\sigma_{0.005(ND\text{-}C)}/\sigma_{0.005(RD\text{-}C)}$) with temperature at HSR and LSR. This parameter was significantly larger at HSR than at LSR (4.23 and 3.84 at room temperature and 2.40 and 1 at 400 °C, respectively). The out-of-plane yield anisotropy decreased gradually with temperature at both strain rates, but the rate of decrease was smaller under dynamic conditions.

3.1.2. Flow stress

Fig. 4b, d, and f illustrates the variation in σ_{max} with increasing temperature corresponding to all tests performed. Similar maximum flow stress values were obtained for tension tests along the RD and TD and for compression tests along the RD and ND. The flow stress at HSR was always higher that at LSR, due to a greater degree of work hardening. At both strain rates σ_{max} decreased with temperature. Fig. 5b illustrates the variation of the normalized flow stress (σ_{max}/G) with temperature for tests performed in tension along in-plane directions and in compression along the RD and ND at both HSR and LSR. Since the flow stresses in tension and in compression are independent of the testing direction, a single value was used for both RD and TD tension tests and for both RD and ND compression tests. G

has been assumed to vary with temperature as G (GPa) = 18.46–0.0082T(K) [50]. It can be seen that the normalized σ_{max} at HSR decreased significantly less than at LSR. This is consistent with the occurrence of dynamic recrystallization at low strain rates, as explained below, and suggests that diffusion controlled processes are limited at HSR, as reported previously for dynamically tested extruded and cast Mg samples [46,47,50].

3.2. Microstructural evolution of the AZ31-O Mg sheet during deformation at high strain rates

Fig. 6 illustrates the microstructure (EBSD orientation map) and the texture (pole figures recalculated from EBSD data) of the AZ31 sheet deformed under dynamic conditions at room temperature in tension along the RD (Fig. 6a) and TD (Fig. 6b) and at 250 °C along the RD (Fig. 6c). Fig. 6a and b reveals that at room temperature grains elongated along the tensile axis as a consequence of the operation of crystallographic slip. The initial basal fiber texture ($\langle 0\,0\,0\,1\rangle$ directions parallel to the ND) was substituted by a single component texture, in which the basal planes remained approximately parallel to the ND and the $\langle 1\,0\,-1\,0\rangle$ directions were aligned with the tensile axis. The intensity of the $\langle 1\,0\,-1\,0\rangle$ pole was higher in the tests performed along the TD. Spread of the central basal pole towards the in-plane direction perpendicular to the tensile axis can also be appreciated. This spread was much more pronounced in the TD tests. The same texture has been observed previously after low strain rate uniaxial tensile deformation of Mg–Al sheets along the in-plane directions [22,55–57] and has been attributed to the prominent role of prismatic slip. Similar textures were also obtained during rolling of Ti and Zr alloys [58,59], in which prismatic slip is the predominant deformation mechanism. In the present work the observation that this particular texture component was more pronounced in TD tests, where basal slip is more difficult, further supports the argument that prismatic slip is mainly responsible for texture formation and that, thus, carries a large amount of the total strain.

The prominent role of prismatic slip in the room temperature deformation of Mg has been emphasized by several authors [18,55,22,24]. Armstrong and Walley [60] and Koike et al. [18] reported its occurrence mainly near grain boundaries, in order to maintain intergranular compatibility between deforming grains. Other authors claim prismatic slip actually carries a significant amount of the total strain, especially when basal planes are not favorably oriented for slip [22,24]. Our results further demonstrate that prismatic slip also plays a significant role during uniaxial deformation under dynamic conditions in an AZ31 sheet tensile tested along the in-plane directions.

Fig. 6 also illustrates that although twinning is not the main deformation mechanism when testing under dynamic conditions along the RD and TD at room temperature, some twins were present in the microstructure. It is apparent in the (0 0 0 1) pole figures that a newly developed texture component, marked by dotted circles, appeared. This new texture component was associated with $\{1\,0\,-1\,2\}$ twins. Neutron diffraction measurements also confirmed the presence of some $\{1\,0\,-1\,2\}$ twinning.

Fig. 6c corresponds to a sample deformed under dynamic conditions at 250 °C in tension along the TD. The microstructure now consisted mainly of two types of grains: large ones elongated in the direction of the tensile axis (RD) and small, equiaxed, recrystallized grains of ~1 μm diameter. Additionally, some twins could also be detected. The texture component was the same as that developed when testing at room temperature, i.e. the $\langle 0\,0\,0\,1\rangle$ directions tend to be parallel to the ND, whereas the prismatic $\langle 1\,0\,-1\,0\rangle$ directions are parallel to the tensile axis (RD). However, the texture intensity corresponding to the maximum in the (1 0 −1 0) pole figure was clearly smaller. The texture component at the edges of the (0 0 0 1) pole figure was visible, as was the case in the samples deformed at room temperature, confirming the activation of $\{1\,0\,-1\,2\}$ twinning, to some extent, under these deformation conditions. Fig. 6d shows the Kernel average misorientation (KAM) map corresponding to the same area as Fig. 6c. A KAM map illustrates the local misorientation degree between neighboring measuring points, such that the local deformation energy and recrystallized grains can be depicted. It is clear in Fig. 6d that most small grains had large internal misorientations, i.e. a large density of dislocations. For comparison, the microstructure and the texture of the sample deformed in tension at LSR and 250 °C is illustrated in Fig. 7. A fully recrystallized structure is present, with equiaxed grains of ~7 μm diameter that are strain free (as revealed by the corresponding KAM map). The distribution of basal poles in the (0 0 0 1) pole figure is symmetric and prismatic poles are homogeneously distributed along the edges of the pole figures. This texture is typical of recrystallized Mg sheets [23,31].

4. Discussion

It is well known that the crystalline structure influences the strain rate response of metallic materials [61]. For body-centered cubic (bcc) metals the strain rate sensitivity reflects the yield stress dependence, whereas for face-centered cubic (fcc) metals it mainly reflects strain hardening [60]. In the latter, the yield stress is virtually independent of the strain rate and of temperature. Metals with an hcp structure are known to follow either bcc or fcc behavior. In particular, magnesium alloys with a random texture have been reported to follow the fcc pattern [60].

Our results show that the strain rate sensitivity of the yield stress of this AZ31 alloy may follow the fcc or the bcc patterns depending on the initial relative orientation between the loading axis and the crystallographic c-axes. A close look at the room temperature data in Fig. 4a, c, and e reveals that the yield strength does indeed not vary with strain rate when testing the material in compression along the RD (RD-C) due to the preferential activation of twinning, whose CRSS is strain rate insensitive, or when

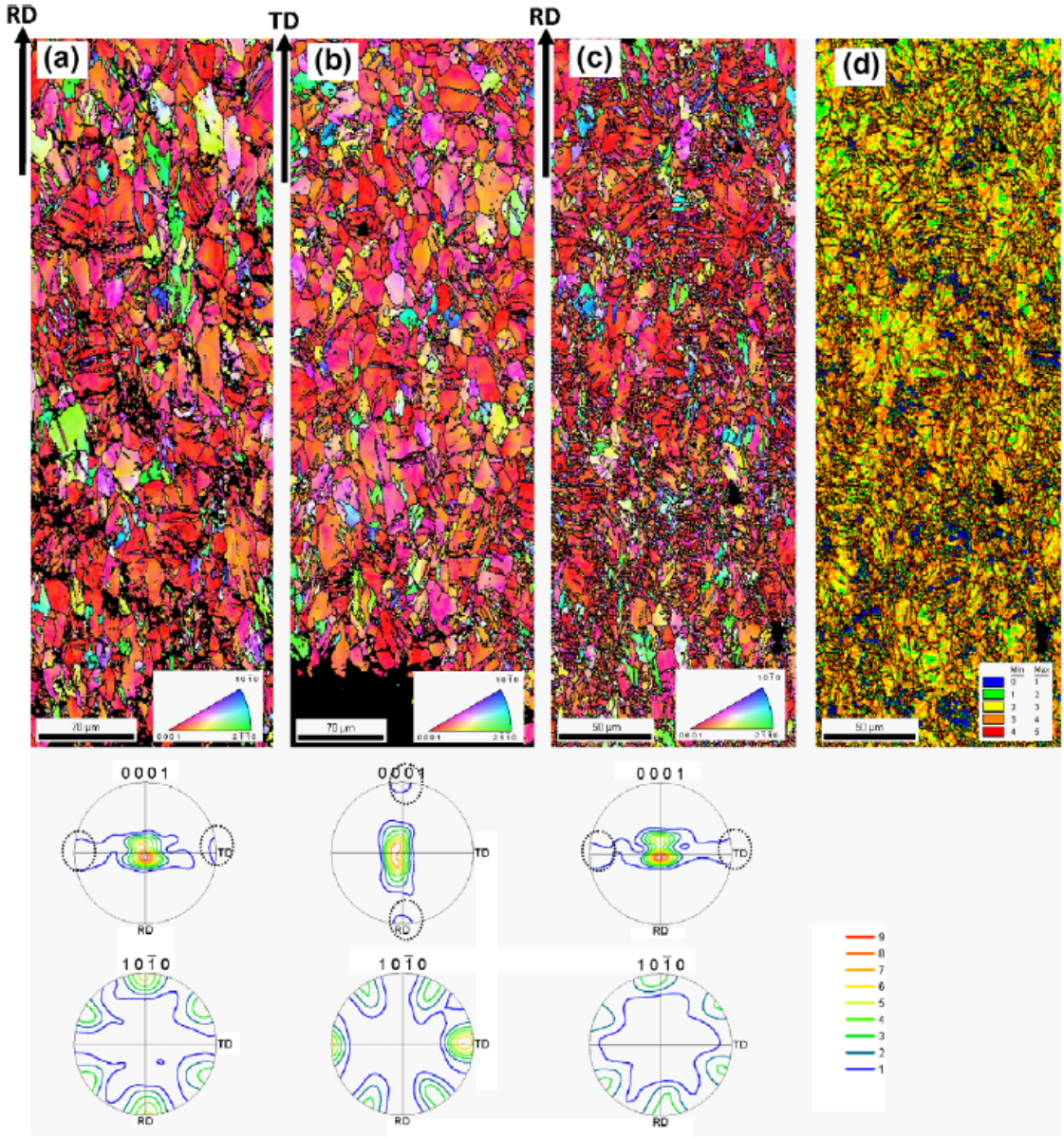

Fig. 6. EBSD inverse pole figure maps in the ND and textures measured in the samples loaded in tension at HSR under the following conditions: (a) room temperature, tension along RD; (b) room temperature, tension along TD; (c) 250 °C, tension along RD. The color coding of the three EBSD maps represents the orientation of the ND. (d) Kernel average misorientation map at the area (c).

testing the material in compression along the ND (ND-C), where pyramidal slip and tensile twinning play major roles (fcc pattern). However, there is significant variation in the yield strength with strain rate when testing the material in tension along the in-plane directions (RD-T and TD-T), where prismatic and basal slip predominate (bcc pattern).

4.1. The CRSS of non-basal slip systems and of {1 0 −1 2} twinning under dynamic conditions

The present study reveals, firstly, that at room temperature the strain rate dependency of the CRSS of prismatic slip is higher than that of pyramidal slip (refer, for example, to the TD-T and ND-C tests, respectively). Consistent with earlier findings, twinning is seen to be strain rate independent. Secondly, it appears that the temperature dependence of the CRSS of non-basal slip systems is significantly less pronounced at dynamic strain rates than at quasi-static strain rates. Barnett [34] calculated the evolution of the CRSS of several deformation mechanisms in Mg as a function of the Zener–Hollomon parameter (Z). His model predicts that $CRSS_{prismatic} = 2.5\ \ln(Z) - 38$ MPa and that $CRSS_{pyramidal} = 2.1\ \ln(Z) - 32$ MPa and considers that $CRSS_{basal} = 2.5$ MPa and $CRSS_{twinning} = 32$ MPa over the whole temperature and strain rate ranges. The model shows good correlation with experimental data for values of Z between

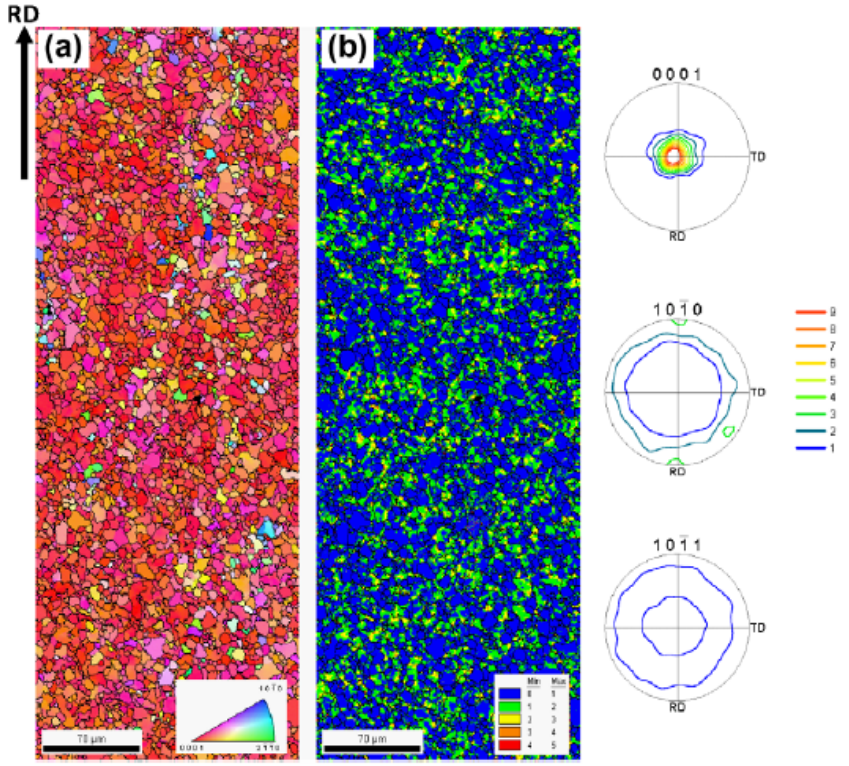

Fig. 7. Microstructure and microtexture of the AZ31 sheet deformed in tension along RD at 10^{-3} s^{-1} and 250 °C. (a) EBSD inverse pole figure maps in the ND and (b) Kernel average misorientation map of the same area.

10^9 and 10^{14} s^{-1} [34], i.e. for temperatures between ~180 and 380 °C at 10^{-3} s^{-1} and higher than 380 °C at 10^3 s^{-1}. Although this model does not cover the whole strain rate/temperature conditions investigated in the present work, it does point towards greater variation in the CRSS of non-basal slip systems at lower strain rates. Thirdly, at dynamic strain rates the CRSS for {1 0 −1 2} twinning seems to remain constant with temperature up to 400 °C.

From Fig. 5a it is obvious that under dynamic conditions the tension–compression asymmetry and the out-of-plane anisotropy of the yield stress remained high up to 400 °C. This suggests that the CRSS of non-basal slip systems remains higher than that of twinning, even at these high temperatures. Also, the in-plane yield stress anisotropy did not change with temperature, revealing that the CRSS of non-basal slip remains higher than that of basal slip up to temperatures as high as 400 °C. Both observations are in full agreement with Barnett's model prediction [34].

4.2. Dynamic recrystallization mechanisms

The dynamic recrystallization (DRX) mechanisms observed in Mg alloys can be either discontinuous (DDRX), consisting of the nucleation of new grains and their growth, or continuous (CDRX), in which new high angle boundaries are formed as a consequence of local lattice rotations by dislocation accumulation [35–39]. Rotational dynamic recrystallization (RDRX) is a variation of the latter in which new grains are formed near grain boundaries due to increased dislocation activity as a consequence of intergranular strain incompatibilities [62–64]. Rotational dynamic recrystallization has also been observed in minerals and its occurrence is enhanced at low temperatures, high strain rates and high stresses [65]. Investigations of the microstructural evolution during dynamic deformation of metals [66,67] have also emphasized the importance of rotational dynamic recrystallization mechanisms at high strain rates.

When analyzing recrystallization mechanisms in Mg alloys two main difficulties arise. First, differentiating DDRX and RDRX mechanisms can be challenging, as in both cases the new grains usually develop near grain boundaries. Second, the recrystallization processes are highly dependent on alloy composition, grain size, deformation conditions, and initial texture [35–39,62–64]. However, for the particular case of rolled sheets of Mg AZ alloys it has been reported that recrystallized grains nucleated by DDRX usually possess a basal fiber texture (*c*-axes parallel to the ND) [22,23,31], whereas those formed by RDRX tend to have orientations in which the *c*-axes are tilted away from the ND [64]. Our results confirmed that when testing the AZ31 alloy in tension at 250 °C at low strain rates (Fig. 7) DDRX took place, as revealed by the development of a basal fiber texture accompanying the formation of the small, strain free, recrystallized grains. However, clear divergences from this behavior have been observed when testing the AZ31 alloy at high strain rates

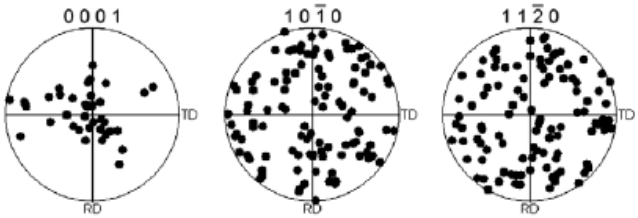

Fig. 8. Discrete orientations of the recrystallized grains in the sample deformed at high strain rates (RD-T at $10^3\ s^{-1}$ and 250 °C).

and 250 °C (Fig. 6c). Two observations suggest an increasing contribution of rotational recrystallization (RDRX) in this strain rate regime. Firstly, the KAM map in Fig. 6d reveals that some small grains were not strain free. Secondly, in some small grains the *c*-axes were rotated away from the ND. This can be seen in Fig. 8, where the orientation of several recrystallized grains has been plotted using discrete pole figures. Due to the limited time for diffusion, recrystallized grains may thus be formed by a combination of both DDRX and RDRX.

5. Conclusions

The aim of this work was to investigate the mechanical behavior and the microstructural evolution of a rolled and recrystallized AZ31-O sheet alloy tested at high strain rates ($10^3\ s^{-1}$). With this purpose, tension tests along the rolling and transverse directions and compression tests along the rolling and normal directions were carried out at temperatures between 25 and 400 °C. EBSD and neutron diffraction have been utilized to examine the microstructure and texture of the samples deformed in tension. The results of this investigation have been compared with the mechanical behavior and microstructural evolution of the AZ31-O sheet alloy at low strain rates. The main conclusions of this study are listed below.

1. Tensile twinning is enhanced at high strain rates and remains the predominant deformation mechanism during the early stages of deformation in compression tests along the RD even at very high temperatures (400 °C). At low strain rates a transition between twin and slip-dominated flow occurs at approximately 200 °C.
2. During tension tests along the in-plane directions at both high and low strain rates prismatic slip is the main deformation mechanism, leading to alignment of the $\langle 1\,0\,-1\,0\rangle$ directions with the tensile axis and to a spread of the basal pole toward the in-plane direction perpendicular to the tensile axis.
3. It is well known that at low strain rates the yield stress asymmetry as well as the in-plane and out-of-plane yield stress anisotropies disappear with increasing temperature. Thus, the material becomes isotropic at ~200 °C. However, at high strain rates these three magnitudes retain relatively high values even at the highest temperature investigated (400 °C).
4. The rate of decrease in the CRSS of non-basal slip systems with temperature is much smaller at high strain rates than at low strain rates. The CRSS of non-basal systems is still significantly higher than that of twinning and of basal systems at 400 °C. At room temperature the strain rate dependency of the CRSS of pyramidal slip systems seems to be higher than that of prismatic slip systems.
5. Diffusion-based phenomena are severely restricted at high strain rates. Only a small fraction of recrystallized grains is still apparent when testing in tension at 250 °C, whereas at low strain rates the microstructure is fully recrystallized at 200 °C. Rotational recrystallization appears to play a more predominant role with increasing strain rate.

Acknowledgements

The authors would like to thank the vehicle interior manufacturer, Grupo Antolin Ingenieria, S.A., within the framework of the project MAGNO2008-1028-CENIT funded by the Spanish Ministry. Funding from Konauto Manufacturing 0,0 (within the Etortek Programme), MAT 2006-11202, CCG07-CSIC/MAT-2270, and MAT 2009-14547-C02-01 is acknowledged. Neutron diffraction measurements were supported by the EC under the sixth FP through the Key Action: Strengthening the ERA, Research Infrastructures, contract no. RII3-CT-2003-505925. The help provided by G. Arruebarrena, U. Garbe, P. Spalthoff, W. Gan and C. Randau is gratefully acknowledged. Assistance from J. Reales and G. González Doncel and N. García-Lepetit with the mechanical testing and from V. Kree with the EBSD analysis was appreciated. Prof. Ron Armstrong and Antoine Jerusalem are sincerely thanked for stimulating discussions.

References

[1] Easton M, Beer A, Barnett M, Davies C, Dunlop G, Durandet Y, et al. JOM 2008;60:57.
[2] Mordike BL, Ebert T. Mater Sci Eng 2001;302:37.
[3] Bamberger M, Dehm G. Annu Rev Mater Res 2008;38:505.
[4] Couling SL, Pashak JF, Sturkey L. Trans ASM 1959;51:94.
[5] Kocks UF, Westlake DG. Trans AIME 1967;239:1107.
[6] Kelley EW, Hosford WF. Trans AIME 1968;242:654.
[7] Couret A, Caillard D. Acta Metal 1985;33:1455.
[8] Chin GY, Mammel WL. Metall Trans 1970;1:357.
[9] Yoo MH. Metall Trans 1981;12A:409.
[10] Vagarali SS, Langdon TG. Acta Metall 1981;29:1969.
[11] Zelin MG, Yang HS, Valiev RZ, Mukherjee AK. Metall Trans 1992;23:3135.
[12] Munroe N, Tan X. Scripta Mater 1997;36:1383.
[13] Agnew SR, Yoo MH, Tomé CN. Acta Mater 2001;49:4277.
[14] Watanabe H, Tsutsui H, Mukai T, Kohzu M, Tanabe S, Higashi K. Int J Plasticity 2001;17:387.
[15] Barnett MR. J Light Metals 2001;1:167.
[16] Agnew SR, Tomé CN, Brown DW, Holden TM, Vogel SC. Scripta Mater 2003;48:1003.
[17] Galiyev A, Sitdikov O, Kaibyshev R. Mater Trans 2003;44:426.

[18] Koike J, Kobayashi T, Mukai T, Watanabe H, Suzuki M, Maruyama K, et al. Acta Mater 2003;51:2055.
[19] Barnett MR. Metall Mater Trans 2003;34:1799.
[20] Gehrmann R, Frommert MM, Gottstein G. Mater Sci Eng 2005;395:338.
[21] Barnett MR, Keshavarz Z, Beer AG, Atwell D. Acta Mater 2004;52:5093.
[22] Agnew SR, Duygulu Ö. Int J Plasticity 2005;21:1161.
[23] Del Valle JA, Pérez-Prado MT, Ruano OA. Metall Mater Trans 2005;36:1427.
[24] Keshavarz Z, Barnett MR. Scripta Mater 2006;55:915.
[25] Meza-García E, Dobroň P, Bohlen J, Letzig D, Chmelik F, Lukáč P, et al. Mater Sci Eng 2007;462:297.
[26] Barnett MR. Mater Sci Eng 2007;464:1.
[27] Del Valle JA, Ruano OA. Acta Mater 2007;55:455.
[28] Al-Samman T, Gottstein G. Mater Sci Eng 2008;488:406.
[29] Chino Y, Kimura K, Mabuchi M. Mater Sci Eng 2008;486:481.
[30] Jain A, Duygulu O, Brown DW, Tomé CN, Agnew SR. Mater Sci Eng 2008;486:545.
[31] Hutchinson B, Barnett MR, Ghaderi A, Cizek P, Sabirov I. Int J Mat Res 2009;100:556.
[32] Ball EA, Prangnell PB. Scripta Metall Mater 1994;31:111.
[33] Lou XY, Li M, Boger RK, Agnew SR, Wagoner RH. Int J Plasticity 2007;23:44.
[34] Barnett MR. Metall Mater Trans 2003;34A:1799.
[35] Kaibyshev R, Sokolov B, Galiyev A. Textures Microstruct 1999;32:47.
[36] Galiyev A, Kaibyshev R, Gottstein G. Acta Mater 2001;49:1199.
[37] Del Valle JA, Ruano OA. Mater Sci Eng 2008;487:473.
[38] Myshlyaev MM, McQueen HJ, Mwembela A, Konopleva E. Mater Sci Eng 2002;337:121.
[39] Al-Samman T, Gottstein G. Mater Sci Eng 2008;490:411.
[40] Christian JW, Mahajan S. Prog Mater Sci 1995;39:1.
[41] Mukai T, Mohri T, Mabuchi M, Nakamura M, Ishikawa K, Higashi K. Scripta Mater 1998;39:1249.
[42] Mukai T, Yamanoi M, Higashi K. Mater Sci Forum 2000;350–351:97.
[43] Yokohama T. Strain 2003;39:167.
[44] El-Magd E, Abouridouane M. J Phys IV France 2003;110:15.
[45] Shu DW, Zhou W, Ma GW. Key Eng Mater 2007;340–341:247.
[46] Ishikawa K, Watanabe H, Mukai T. Mater Lett 2005;59:1511.
[47] Ishikawa K, Watanabe H, Mukai T. J Mater Sci 2005;40:1577.
[48] El-Magd E, Abouridouane M. Int J Impact Eng 2006;32:741.
[49] Rittel D, Wang ZG. Mech Mater 2008;40:629.
[50] Watanabe H, Ishikawa K, Mukai T. Key Eng Mater 2007;340–341:107.
[51] Li B, Joshi S, Azevedo K, Ma E, Ramesh KT, Figueiredo RB, et al. Mater Sci Eng 2009;517:24.
[52] Tucker MT, Horstemeyer MF, Gullett PM, El Kadiri H, Whittington WR. Scripta Mater 2009;60:182.
[53] Watanabe H, Ishikawa K. Mater Sci Eng 2009;523:304.
[54] Ulacia I, Salisbury CP, Hurtado I, Worswick MJ. submitted for publication.
[55] Koike J, Ohyama R. Acta Mater 2005;53:1963.
[56] Yi S, Bohlen J, Heinemann F, Letzig D. Acta Mater 2010;58:592.
[57] Del Valle JA, Ruano OA. Mater Lett 2009;63:1551.
[58] Tenckhoff E. Deformation mechanisms, texture, and anisotropy in zirconium and zircaloy. ASTM Special Technical Publication STP 966; 1988.
[59] Jiang L, Pérez-Prado MT, Gruber PA, Arzt E, Ruano OA, Kassner ME. Acta Mater 2008;56:1228.
[60] Armstrong RW, Walley SM. Int Mater Rev 2008;53:105.
[61] Meyers MA. Dynamic behavior of materials. New York: John Wiley & Sons; 1994.
[62] Ion SE, Humphreys FJ, White SH. Acta Metal 1982;30:1909.
[63] Yi SB, Zaefferer S, Brokmeier HG. Mater Sci Eng 2006;424:275.
[64] Del Valle JA, Pérez-Prado MT, Ruano CA. Mater Sci Eng 2003;355:68.
[65] Humphreys FJ, Hatherly M. Recrystallization and related annealing phenomena. Oxford: Pergamon; 1995.
[66] Andrade U, Meyers MA, Vecchio KS, Chokshi AH. Acta Metall Mater 1994;42:3183.
[67] Murr LE, Pizaña C. Metall Mater Trans 2007;38:2611.

3.2. Twinning and grain subdivision during dynamic deformation of Mg AZ31 sheet alloy at room temperature

Acta Materialia 59 (2011) 6949-6962

N.V. Dudamell[a], I. Ulacia[b], F. Gálvez[c], S. Yi[d], J. Bohlen[d], D. Letzig[d], I. Hurtado[b], M.T. Pérez-Prado[a],

[a] Madrid Institute for Advanced Studies in Materials, IMDEA Materials, C/Profesor Aranguren s/n, 28040 Madrid, Spain
[b] Mondragon Goi Eskola Politeknikoa, Mondragon Unibertsitatea, 20500 Mondragón, Spain
[c] ETS Ingenieros de Caminos, Universidad Politécnica de Madrid, 28040 Madrid, Spain
[d] Magnesium Innovation Centre. Helmholtz-Zentrum Geesthacht, 21502 Geesthacht, Germany

Received 1 June 2011; received in revised form 19 July 2011; accepted 21 July 2011
Available online 29 August 2011

Available online at www.sciencedirect.com
SciVerse ScienceDirect
Acta Materialia 59 (2011) 6949–6962
Acta MATERIALIA
www.elsevier.com/locate/actamat

Twinning and grain subdivision during dynamic deformation of a Mg AZ31 sheet alloy at room temperature

N.V. Dudamell [a], I. Ulacia [b], F. Gálvez [c], S. Yi [d], J. Bohlen [d], D. Letzig [d], I. Hurtado [b], M.T. Pérez-Prado [a,*]

[a] Madrid Institute for Advanced Studies in Materials, IMDEA Materials, 28040 Madrid, Spain
[b] Mondragon Goi Eskola Politeknikoa, Mondragon Unibertsitatea, 20500 Mondragón, Spain
[c] ETS Ingenieros de Caminos, Universidad Politécnica de Madrid, 28040 Madrid, Spain
[d] Magnesium Innovation Centre, Helmholtz-Zentrum Geesthacht, 21502 Geesthacht, Germany

Received 1 June 2011; received in revised form 19 July 2011; accepted 21 July 2011
Available online 29 August 2011

Abstract

The microstructural evolution of an AZ31 rolled sheet during dynamic deformation at strain rates of $\sim 10^3\ s^{-1}$ has been investigated by electron backscatter diffraction, X-ray and neutron diffraction. The influence of orientation on the predominant deformation mechanisms and on the recovery processes taking place during deformation has been systematically examined. The results have been compared with those corresponding to the same alloy tested quasi-statically under equivalent conditions. It has been found that strain rate enhances the activation of $\{10\bar{1}2\}$ extension twinning dramatically, while contraction and secondary twinning are not significantly influenced. The polarity of $\{10\bar{1}2\}$ extension twinning is even reversed in some grains under selected testing conditions. Significant grain subdivision by the formation of geometrically necessary boundaries (GNBs) takes place during both quasi-static and dynamic deformation of this AZ31 alloy. It is remarkable that GNBs of high misorientations form even at the highest strain rates. The phenomenon of recovery has been found to be orientation dependent.

Keywords: Magnesium; AZ31; High strain rate; Twinning; Slip

1. Introduction

Magnesium alloys are light metals ($\rho \sim 1.7\ g\ cm^{-3}$) that have been studied profusely over the last decade due to their potential in the transportation and aerospace industries, among others [1–3]. The deformation and dynamic recrystallization mechanisms of Mg alloys at low strain rates are now well known [4–33]. Slip may take place along the $\langle 11\bar{2}0\rangle$ ($\langle a\rangle$) direction on basal and non-basal ($\{10\bar{1}0\}$-prismatic, $\{10\bar{1}1\}$-pyramidal) planes. Additionally, $\langle c+a\rangle$ slip has also been observed along $\{11\bar{2}2\}$ second-order pyramidal planes [22]. The predominance of a specific slip system is dependent on the deformation temperature, as well as on the crystallographic texture [4–33].

Twinning, mainly on $\{10\bar{1}2\}$, $\{10\bar{1}1\}$ and $\{10\bar{1}3\}$ planes, plays a key role during deformation of Mg alloys, particularly at low temperatures [8,13,16,19,22,33]. Twinning is a polar mechanism [34]. For example, extension twinning in $\{10\bar{1}2\}$ planes is active in a grain only when the deformation conditions are such that an extension along the *c*-axis takes place [26]. This mechanism is especially important in strongly textured wrought Mg alloys. It is well known that rolled Mg sheets have a strong basal-type texture (the *c*-axes are parallel to the normal direction, ND), and thus extension twinning is the predominant deformation mechanism during the first stages of deformation when compressive loading is applied in a direction parallel to the rolling plane. In extruded Mg rods,

* Corresponding author.
E-mail address: teresa.perez.prado@imdea.org (M.T. Pérez-Prado).

1359-6454/$36.00
doi:10.1016/j.actamat.2011.07.047

in which the *c*-axes align with the radial directions during processing, extension twinning predominates when a compressive stress is applied in the extrusion direction. In both cases twinning leads to a reorientation of the lattice of 86° in such a way that, after about 4–6% of strain, the *c*-axes of most grains become parallel to the applied stress. Tensile twinning is favored at high strain rates and low temperatures [34]. In randomly oriented polycrystals basal slip and $\{10\bar{1}2\}$ twinning are the predominant deformation mechanisms in selected grains, and are favorably oriented for these deformation modes.

When the *c*-axis of a Mg grain is placed under compression, both contraction twinning and non-basal slip might be activated. Twinning under such conditions takes place mostly in $\{10\bar{1}1\}$ planes, causing a lattice reorientation of approximately 56° around the $\langle 11\bar{2}0\rangle$ axis. Occasionally, areas that have undergone contraction twinning are in a suitable orientation for subsequent extension twinning. The consecutive occurrence of these two twinning mechanisms gives rise to the so-called secondary twinning mechanism [35]. The misorientation angle of the twin boundary surrounding a secondary-twinned area is approximately 38° around the $\langle 11\bar{2}0\rangle$ axis. The significance of contraction and secondary twinning in accommodating *c*-axis compression in Mg alloys is still not clear. In fact, the experimental evidence available suggests that their net contribution to the total deformation is not very significant. In particular, contraction and secondary twinning have been claimed to operate in Mg single crystals tested with the tensile axis parallel to the basal plane [36–38]. However, single crystal studies were carried out several decades ago and rely mostly on optical microscopy. Furthermore, traces of these mechanisms have only been found in very localized regions (e.g. close to the fracture surface or to the sample surface itself). Finally, the ductility of the single crystals rarely exceeds 2%, and thus it remains unclear from these experiments whether these mechanisms can be responsible for the larger fracture strains typically observed in Mg polycrystals. Some studies have recently reported the occurrence of contraction and secondary twinning in polycrystalline Mg alloys during *c*-axis compression [24,28,39–41]. However, again, traces of these types of twins are only observed in very small regions, often very close to the fracture surfaces. Thus, it is now widely accepted that pyramidal slip accommodates most of the compression strain along the *c*-axis [16,42]. Some authors have highlighted the role of compression twins in the strain hardening of Mg alloys [42].

While twinning in Mg alloys at quasi-static strain rates has been extensively studied, the occurrence of this mechanism at dynamic strain rates has still not been thoroughly explored. It is known that, in this strain rate range, twinning is active even at temperatures as high as 400 °C [43–47], at which it is mostly suppressed at quasi-static strain rates. However, the effect of strain rate on the activity of the different twinning modes is still unknown.

In a recent study [43] the present authors analyzed in detail the mechanical response of the Mg alloy AZ31 under dynamic loading conditions. In particular, the temperature dependencies of the tension–compression yield asymmetry, the yield strength anisotropy and the critical resolved shear stress (CRSS) of the various slip systems at those high strain rates were thoroughly investigated. However, the microstructural evolution of Mg alloys with strain under dynamic conditions and, more specifically, the dependence, if any, of the grain size, grain boundary distributions and restoration mechanisms on the straining direction have still not been studied.

In this work we describe the microstructure and microtexture evolution of a Mg AZ31 rolled sheet during dynamic deformation at room temperature as a function of the strain and the orientation of the applied stress. In particular, the conditions analyzed include compression along the rolling and normal directions (RD and ND) and tension along the RD. Special attention is paid to the activity of the various twinning modes and to the evolution of the grain boundary distributions, which give very valuable information regarding the presence of any restoration mechanisms. The room temperature microstructural evolution of this rolled Mg AZ31 alloy at high strain rates is compared to that taking place at quasi-static strain rates.

2. Experimental procedure

2.1. Material: initial microstructure

The material under study is the Mg alloy AZ31 (Mg–3% Al–1% Zn). Two rolled and annealed sheets, 1 and 3 mm in thickness, were purchased from Magnesium Elektron. The initial microstructures of the two AZ31 sheets consist of equiaxed grains, with average sizes of 10 and 13 μm, respectively. As generally observed in annealed AZ31 sheets, both have a characteristic strong basal-type texture with a spread of the (0001) poles toward the RD (Fig. 1). In the following both sheets will be referred to as "the AZ31 alloy", as their microstructure and mechanical behavior are basically identical. Further considerations about the similarity of the two materials can be found in Ref. [43].

2.2. Mechanical testing

Room temperature high strain rate ($\sim 10^3\ s^{-1}$) mechanical tests were performed in the AZ31 alloy up to failure and up to several intermediate strains using a Hopkinson bar furnished with a high-speed camera. In the compression tests the specimens were dynamically loaded to a predefined strain level, using a stop-ring technique that limits the displacement of the incident Hopkinson bar. Ring stoppers of specific heights were machined out of an F522 steel. In the tension tests, momentum-trapping fixtures were used in order to interrupt testing and obtain samples deformed at different strains.

Compression tests along the RD were performed in $3 \times 3 \times 4.5\ mm^3$ specimens and compression tests along

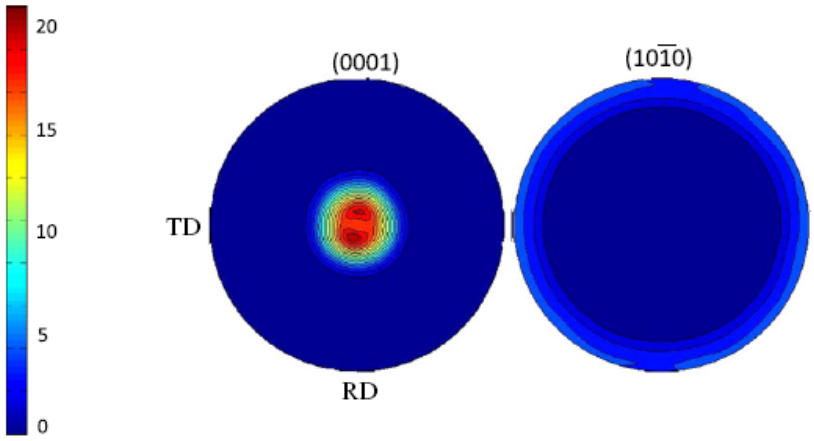

Fig. 1. Texture of the as-received AZ31 sheet alloy.

the ND were carried out in $3 \times 3 \times 3$ mm^3 cubes. Tensile tests along the RD were performed in dogbone-shaped tensile specimens with a gage length of 12.5 mm and a width of 1.75 mm. The reader is referred to Ref. [48] for a more detailed description of the testing procedures.

Quasi-static tests were also carried out until failure and up to some intermediate strains along the same directions in order to compare the variations in the microstructural evolution with the strain rate. These tests were carried out in a conventional universal testing machine (Instron) using the same specimen geometries described above.

2.3. Microstructure examination

The microstructure and texture of a number of samples compressed along the RD and ND and tensile tested along the RD at room temperature up to various strain levels were analyzed by electron backscatter diffraction (EBSD) using the TSL-OIM™ software in a Zeiss Ultra 55™ FEG-SEM. Sample preparation for EBSD investigations included grinding with 4000 SiC paper, mechanical polishing with a 0.05 μm silica suspension and final electrochemical polishing for 90 s at 33 V using the AC2™ commercial electrolyte. The microstructure is represented by EBSD orientation maps and the texture by pole figures recalculated from the EBSD orientation data. In order to investigate the operative deformation and restoration mechanisms, the nature of the grain boundaries present in all the samples was analyzed from the EBSD data. Special attention was paid to the presence of twin boundaries and to the misorientation distribution histograms. Additionally, the grain size of various samples was calculated by the linear intercept method in the EBSD orientation maps using only grain boundaries with misorientations higher than 15°.

Since EBSD only allows examining the local texture, macrotexture measurements were also performed in selected samples by neutron diffraction using the STRESS-SPEC instrument at the research reactor FRM II, Munich Technical University, Germany. The area examined had a diameter of approximately 5 mm. A Ge monochromator with an associated wavelength of 1.65 Å was used. The macrotexture of some samples was also measured by the Schulz reflection method in a Philips Ẋpert-Pro Panalytical X-ray diffractometer furnished with a PW3050/60 goniometer, located at the CAI X-ray Diffraction of the Complutense University in Madrid, Spain. The radiation used was β-filtered Cu$K\alpha$. The surface area examined was about 2 mm^2. The polar angle ranged from 0 to 75° in steps of 3°. The irradiation time at each step was 2 s. The measured incomplete pole figures were corrected for background and defocusing using the Philips Ẋpert software. The orientation distribution function (ODF) and the complete pole figures were calculated using the MTex software [49]. This software was also utilized to calculate the volume fraction of specific texture components. A spread of 30° around the ideal component was allowed. The notation utilized to name specific texture components was {rolling plane normal}⟨rolling direction⟩. Sample preparation for texture measurement included grinding with increasingly finer SiC papers, whose grit size ranged from 320 to 2000.

3. Results

3.1. Mechanical behavior

Fig. 2 illustrates the stress–strain curves corresponding to room temperature tests carried out until failure under compression along the RD (Fig. 2a), tension along the RD (Fig. 2b) and compression along the ND (Fig. 2c). Tests carried out at dynamic rates (10^3 s^{-1}) and under quasi-static conditions (5×10^{-3} s^{-1} in the compression tests and 10^{-3} s^{-1} in the tension test) are compared. Images illustrating the three tested samples after macroscopic fracture (i.e. after the complete test) under dynamic conditions, captured in situ by a high-speed camera, have been added to the corresponding stress–strain curves. These images show the resulting adiabatic shear failure, a dynamic fracture mechanism that develops in the vast majority of ductile materials subjected to impact loading. Adiabatic

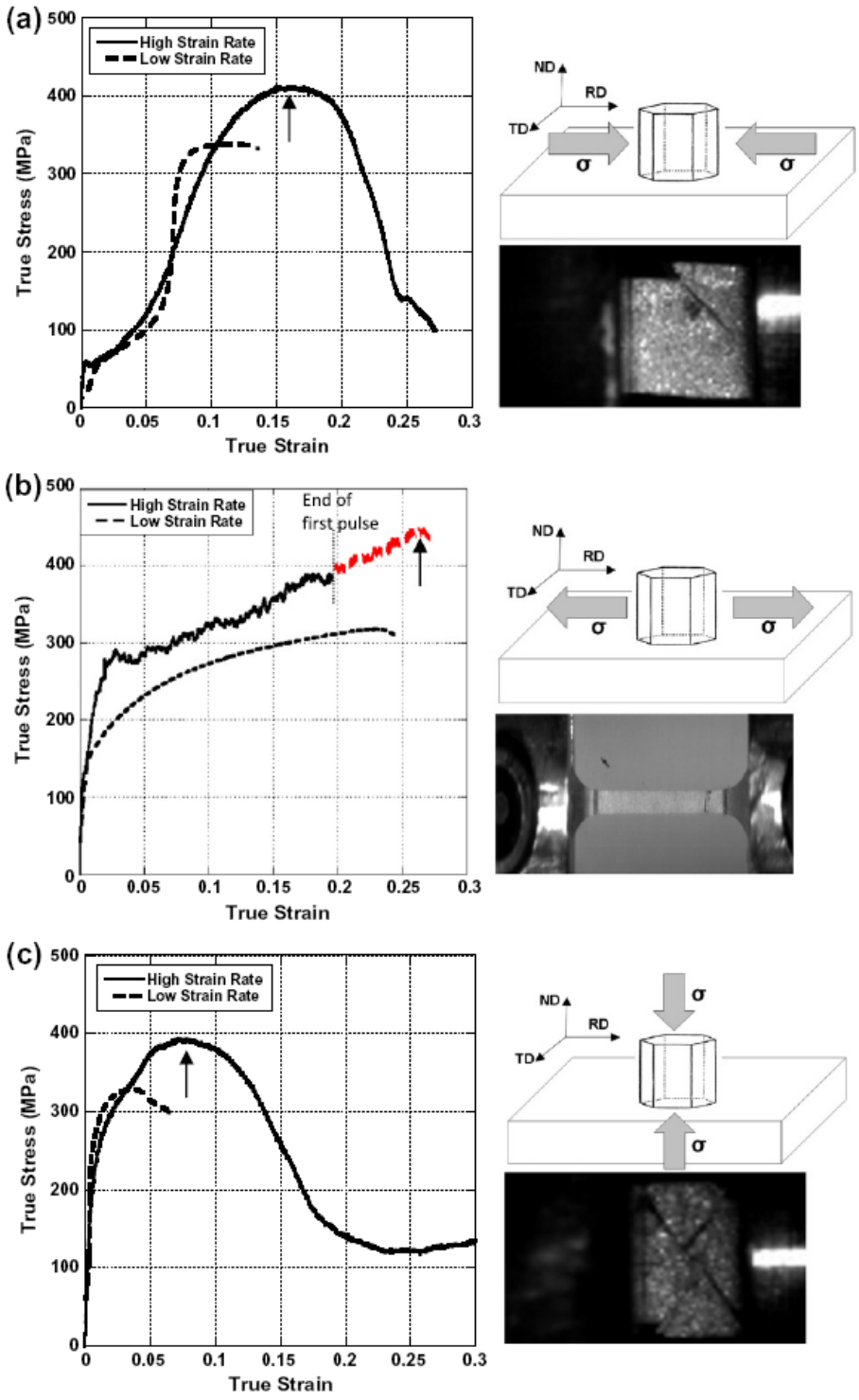

Fig. 2. Room temperature stress–strain curves corresponding to the AZ31 alloy deformed at a high strain rate (10^3 s^{-1}) and at a quasi-static strain rate in (a) compression along the RD; (b) tension along the RD; and (c) compression along the ND. Images of the specimen after fracture, taken in real time with a high-speed camera, are included next to each plot. The strains to failure corresponding to each tests, ε_f, are indicated by arrows.

shear bands (ASB) are regions in which very high local strains and very high temperatures develop, leading to uncontrolled failure [50]. At strains lower than those at which ASBs form, homogeneous deformation takes place throughout the specimen; at higher strains the deformation is highly localized in the bands, the rest of the material remaining basically in the deformation state corresponding to the instant prior to strain localization.

The occurrence of ASBs in dynamically deformed materials has been extensively investigated [50,51]. The classical model for the prediction of the onset of ASB formation (Zener–Hollomon) [52] relies on the competition between strain hardening and thermal softening of the material, and it predicts that the onset of the bands coincides with the strain at which the material loses its hardening capacity. The curves corresponding to the dynamic compression tests along RD and ND (Figs. 2a and 2c) show significant strain hardening followed by pronounced softening. A note must be made about the curve corresponding to dynamic tension along the RD (Fig. 2b). The maximum loading duration with the current apparatus set up, governed by the maximum length of the striker, is 200 μs. This limited duration of the loading pulse was not enough to cause the fracture of the specimen. The fracture strain (approximately 0.27) is achieved by a subsequent pulse loading. We have nevertheless included, in red, the portion of the curve corresponding to the second pulse, for reference. According to the Zener–Hollomon criterion, the strains, ε_f, at which ASBs form during the three tests investigated here (compression along the RD (Fig. 2a), tension along the RD (Fig. 2b) and compression along the ND (Fig. 2c)) were 0.16, 0.27 and 0.07, respectively. These strains are indicated by arrows in Fig. 2. The dynamic fracture energies for the three tests are 3.9×10^7, $\sim 7.4 \times 10^7$ and 2.2×10^7 J m^{-3}, respectively. These values are clearly dependent on the test mode (tension vs. compression) and on the loading direction with respect to the *c*-axes of the polycrystalline aggregate, as different deformation mechanisms are activated in each of the three tests investigated. Rittel et al. [53] suggested that the onset of ASBs could start at lower strains than those predicted by the Zener–Hollomon model, since in their view ASBs form by early dynamic recrystallization before ε_f. Determining the exact strain at which ASB formation starts would then require a thorough investigation by transmission electron microscopy, which is beyond the scope of the present paper and would constitute a separate study by itself. Since we are interested in analyzing the dynamic deformation mechanisms during homogeneous deformation of the AZ31 alloy, we will consider that, as long as clear bulk microstructural changes take place in the specimen with straining, we will be examining samples deformed to strains lower than those required for ASB formation since, once ASBs form, strain localization in these narrow regions leads to the freezing of the microstructure elsewhere. During homogeneous dynamic straining, the temperature rise during testing is below about 30 K [53].

It can be seen in Fig. 2 that dynamic tests exhibit higher flow stresses than the corresponding quasi-static tests. The elongations to failure, ε_f, are also larger under dynamic conditions. The differences in the mechanical behavior with strain rate will be rationalized on the light of the microstructural evolution during testing, which will be described in the following section.

3.2. Microstructural evolution

Each of the three dynamic tests investigated was carried out to failure (Fig. 2) and also stopped at various intermediate true strains in order to analyze the microstructure evolution of the AZ31 alloy under high strain rate conditions. In compression along the RD (Fig. 2a), tests were interrupted at strains of 0.05, 0.10 and 0.13. All of these strain values are lower than ε_f (0.16), the value at which ASBs form according to the Zener–Hollomon criterion [52]. In tension along the RD (Fig. 2b), tests were stopped at strains of 0.10 and 0.20. Again, these two strain values are lower than ε_f (0.27). The compression tests along the ND (Fig. 2c) were stopped at strains of 0.05 and 0.10. The latter is higher than the corresponding ε_f (0.07), and therefore it is expected that the homogeneous strain accumulated in this sample is lower than 0.10.

3.2.1. Compression along the RD

Fig. 3 illustrates the EBSD inverse pole figure maps in the ND and the microtextures of the samples deformed at 5×10^{-3} s^{-1} in compression along the RD up to strains of 0.05 and 0.13. As is well known [21,26,43], extension twinning takes place during the first stages of deformation (Fig. 3a), leading to an 86° rotation of the *c*-axes, which brings them into alignment with the RD (compression axis). A single texture component develops, with $\langle 10\bar{1}0 \rangle$ directions parallel to the ND (Fig. 3a). The main texture component would thus be $\{10\bar{1}0\}\langle 0001 \rangle$. Extension twins nucleate and propagate quickly, often encompassing the entire grain [42]. The area fraction of extension twinned material at a strain of 0.05 is 68%, and increases to 85% at a strain of 0.13 (Fig. 3b). The volume fraction, estimated from the X-ray ODF, is approximately 72% at a strain of 0.13. These values are consistent with previous studies [54]. A significant fraction of extension twin boundaries, plotted in red in Fig. 3c, are thus still present in the microstructure even at the largest strains investigated here. Contraction and secondary twins, plotted in green and yellow in Fig. 3c, respectively, are basically absent. The grain size, measured counting only high angle boundaries ($\theta > 15°$), including twin boundaries, is equal to 6 μm at a strain of 0.05 and to 8.5 μm at a strain of 0.13. The reduction in grain size (from a value of 13 μm in the as-received material) is mainly attributed to the presence of the twin boundaries. In the twinned grains pyramidal slip becomes the dominant deformation mechanism, together with basal slip [21,43]. The single component texture described above is retained until failure. Grain subdivision by the formation of GNBs also takes place during the last stages of deformation. It can be seen in Fig. 3c that newly formed boundaries (in gray), lying perpendicular to the compression axis, traverse the original grains. Some of these new boundaries are indicated by white arrows.

Figs. 4a–c illustrates the EBSD inverse pole figure maps in the ND and the microtextures of the samples deformed

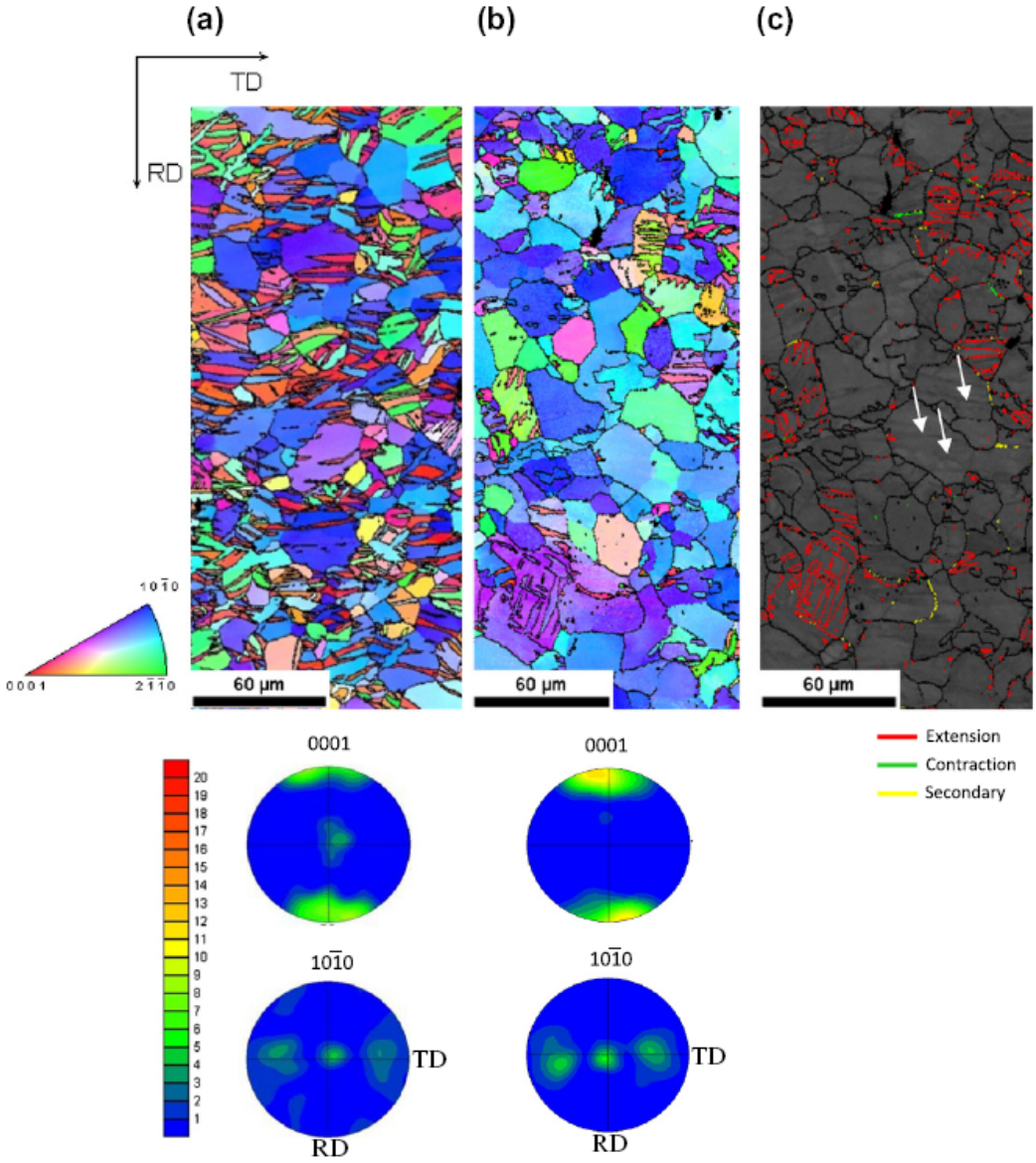

Fig. 3. EBSD inverse pole figure maps in the ND and microtextures measured in the samples deformed quasi-statically at room temperature in compression along the RD up to strains of (a) 0.05 and (b) 0.13. (c) Twin boundary map corresponding to the sample strained up to 0.13. Extension twin boundaries are colored in red, contraction twin boundaries are colored in green and secondary twin boundaries are colored in yellow. White arrows indicate the low and medium angle boundaries formed as a consequence of grain subdivision. (For interpretation of the references to color in this figure legend, the reader is referred to the web version of this article.)

at a high strain rate ($\sim 10^3\ s^{-1}$) in compression along the RD up to strains of 0.05, 0.10 and 0.13. These three strains are included within the hardening region of the stress–strain curve. A clear microstructural evolution with strain can be observed. Significant extension twinning activity takes place at the early stages of deformation. At $\varepsilon = 0.05$ the fraction of twinned material, calculated from the EBSD data, is 81% (compared with 68% at low strain rates) and the grain size is 9 μm (compared with 6 μm at low strain rate). Together, these data reveal that the nucleation and propagation of extension twins are significantly enhanced at dynamic strain rates. Twinning at high rates leads to the development of the same single component texture described above for quasi-static strain rates ($\langle 0001 \rangle$ directions parallel to the RD and $\langle 10\bar{1}0 \rangle$ directions parallel to the ND, i.e. $\{10\bar{1}0\}\langle 0001 \rangle$). The volume fraction of twinned material increases to 98% at $\varepsilon = 0.10$. The texture intensity increases slightly from $\varepsilon = 0.05$ to $\varepsilon = 0.10$ due to the increase in the volume fraction of twins, then remains basically constant. This is consistent with the operation of pyramidal and basal slip during the last stages of deformation. The intragranular kernel average misorientation (KAM) parameter, which is an average of the whole calculated KAM values, increased from 1 at $\varepsilon = 0.05$ to 1.3 at $\varepsilon = 0.10$ and to 1.2 at $\varepsilon = 0.13$, consistent with the higher slip activity during the later stages of deformation.

N.V. Dudamell et al. / Acta Materialia 59 (2011) 6949–6962

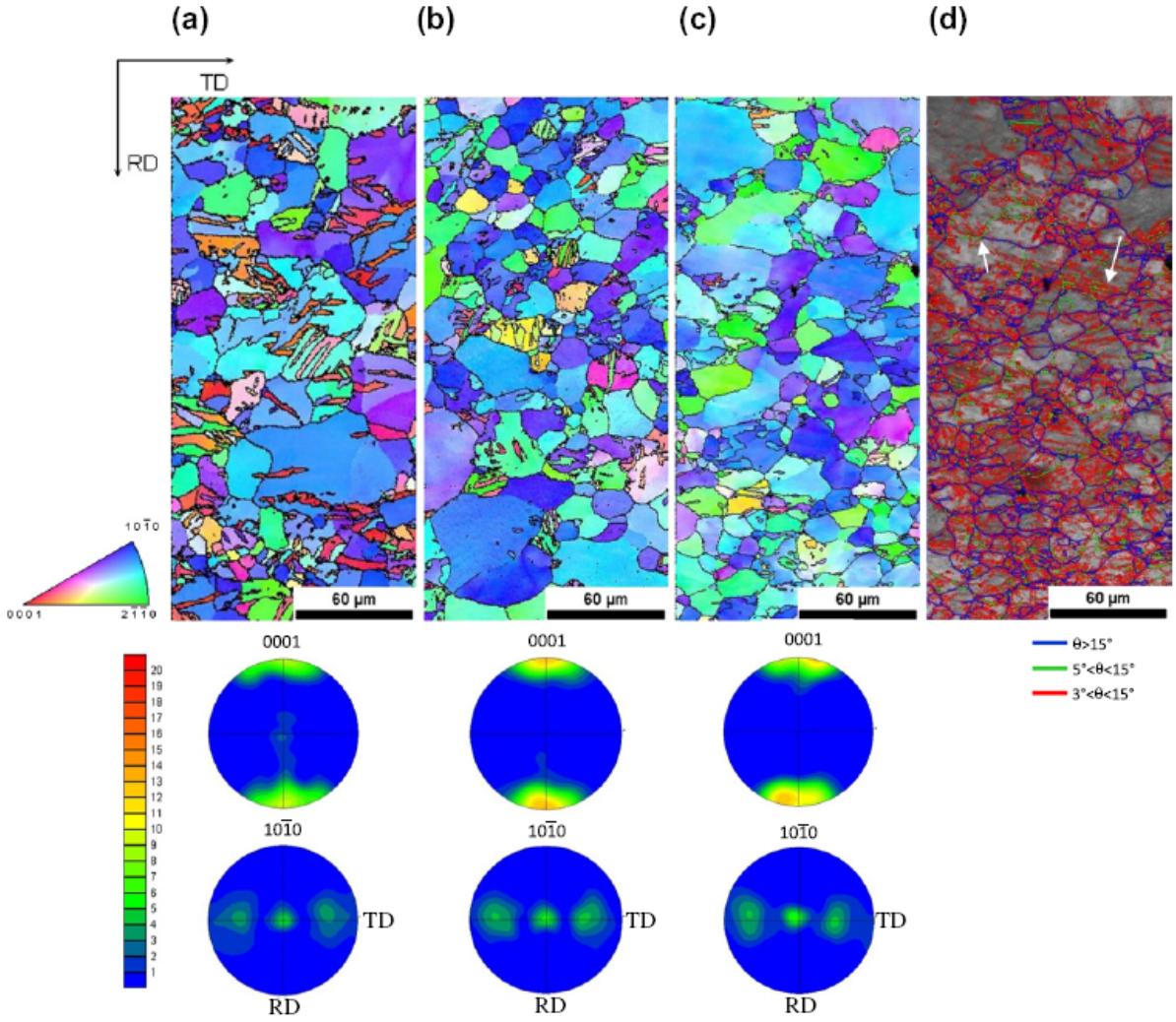

Fig. 4. EBSD inverse pole figure maps in the ND and microtextures measured in the samples dynamically loaded at room temperature in compression along the RD up to strains of (a) 0.05, (b) 0.10 and (c) 0.13. (d) Boundary map corresponding to the sample strained up to 0.13. High angle boundaries ($\theta > 15°$) are colored in blue, moderately misoriented boundaries ($5° < \theta < 15°$) are colored in green and low angle boundaries ($3° < \theta < 5°$) are colored in red. White arrows indicate boundaries transitioning from being low to medium angle or from medium to high angle. (For interpretation of the references to color in this figure legend, the reader is referred to the web version of this article.)

Fig. 4d presents the EBSD boundary map of the sample deformed to $\varepsilon = 0.13$. It can be clearly seen that grain subdivision by the formation of GNBs has taken place. We have observed that low to medium angle boundaries, mostly lying perpendicular to the applied stress, in fact start forming during the early stages of deformation ($\varepsilon = 0.05$) by dislocation accumulation in the twinned grains, where crystallographic slip takes place. With increasing strain, the misorientation of these boundaries increases, leading ultimately to high angle boundaries. Some examples of boundaries transitioning from a low to a moderate misorientation angle and, from the latter, to a high angle boundary are indicated by arrows in Fig. 4d. Further evidence of this phenomenon can be found in Fig. 5, which illustrates the misorientation distribution histograms corresponding to the samples deformed up to $\varepsilon = 0.05$, 0.10 and 0.13 at dynamic strain rates. Boundaries with $\theta > 5°$ are included. It can be clearly seen that extension twin boundaries ($\theta = 86°$) are predominant at low strains and that the fraction of boundaries with misorientations between 5 and 50° increase with strain. As a result, the grain size remains basically constant until failure ($d = 9.5$ μm at $\varepsilon = 0.10$ and $d = 10$ μm at $\varepsilon = 0.13$). The grain size corresponding to the sample deformed at a low strain rate up to $\varepsilon = 0.13$ is 8.5 μm. This difference can be attributed to the higher fraction of twin boundaries in the latter. We could not detect any significant differences in the process of grain subdivision between samples deformed at low and high strain rates (Figs. 3 and 4).

The above results allow the differences in the mechanical behavior of this AZ31 alloy at low and high strain rates under compression along the RD to be explained (Fig. 2a). First, since the CRSS of twinning is strain rate independent [43], both samples yield at approximately the

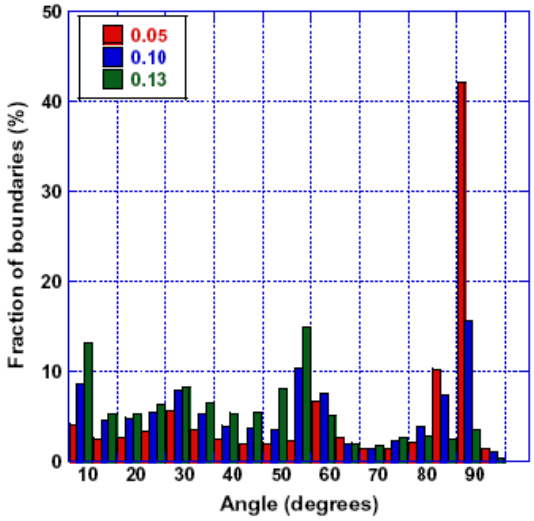

Fig. 5. Misorientation distribution histograms corresponding to AZ31 compressed at dynamic strain rates along the RD at room temperature up to strains of 0.05, 0.10 and 0.13.

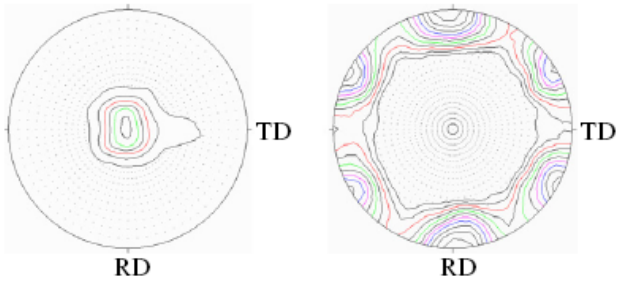

Fig. 6. Texture of the AZ31 alloy deformed to failure at room temperature in tension along the RD at a strain rate of 10^{-3} s^{-1}. Direct pole figures, measured by neutron diffraction.

same stress level and exhibit similar hardening rates during the first stages of deformation ($\varepsilon < 0.03$). However, extension twins propagate faster at a high strain rate and thus crystallographic slip (pyramidal and basal) becomes the predominant deformation mechanism at small strains (~0.03). Since the CRSS of pyramidal slip is higher than that of twinning at room temperature [43], at a strain of, for example, 0.05, the flow stress is higher in the sample that is dynamically deformed. For $\varepsilon > 0.03$, the hardening rate in samples deformed dynamically corresponds mainly to dislocation–dislocation interactions, as very few twin boundaries remain present. In contrast, in the low strain rate regime crystallographic slip becomes predominant at higher strains (~0.06). Since the volume fraction of twinned areas saturates at a value in the range of 72–85%, the amount of twin boundaries that remains present is larger than in the microstructure deformed at high strain rate. Thus, the hardening rate is higher than in the dynamic case due to the presence of dislocation–twin boundary interactions, in addition to the dislocation–dislocation interactions.

3.2.2. Tension along the RD

It is well known that, at low strain rate, deformation in tension along the RD takes place mainly by prismatic slip, together with basal slip [22,24,33,43]. Fig. 6 shows the pole figures, measured by neutron diffraction in order to get a good statistical description of the macrotexture, corresponding to the AZ31 alloy deformed at 10^{-3} s^{-1} up to failure. With increasing deformation, a single component texture develops, in which c-axes remain mostly parallel to the ND and $\langle 10\bar{1}0\rangle$ directions become aligned with the tensile axis (RD) ($\{0001\}\langle 10\bar{1}0\rangle$).

Fig. 7 illustrates the EBSD inverse pole figure maps in the ND and the direct pole figures, measured by neutron diffraction, corresponding to the AZ31 alloy deformed dynamically in tension along the RD. Data corresponding to strains of 0.10 (Fig. 7a) and 0.20 (Fig. 7b) are presented. A clear evolution of the microstructure can be observed in the two samples investigated. First, the same deformation texture described above for quasi-static tests ($\langle 0001\rangle$ directions parallel to the ND and $\langle 10\bar{1}0\rangle$ directions aligned with the tensile axis (RD)) develops during dynamic straining. The intensity of this texture has been found to be similar at dynamic and quasi-static rates (Figs. 6 and 7). Second, an additional texture component can be detected, which reveals the alignment of c-axes perpendicular to the tensile axis (parallel to the TD). This component is associated with extension twinning. Its intensity increases with strain. Neutron diffraction pole figures are shown in order to prove that the presence of extension twins is an important contributor to deformation, not merely an accommodation mechanism, as has been suggested for low strain rate deformation under the same conditions [16]. Extension twinning is thus clearly enhanced at high strain rates, taking place in grains that would otherwise not be suitably oriented for the activation of this mechanism at low strain rates. Once formed, extension twins are stable under this loading condition, as they are not favorably oriented either for detwinning or for basal slip. They thus must deform by non-basal slip, as the rest of the material.

Fig. 7c shows the twin boundary map corresponding to the sample deformed to a strain of 0.20. A significant fraction of extension twin boundaries is indeed present. It must be noted that extension twin boundaries are not straight, as is commonly observed. Instead, their morphology is wavy (see arrows in Fig. 7c), revealing that twin boundary propagation is sluggish under the current deformation conditions. This is not surprising since extension twinning is somehow forced in grains that would otherwise not twin at a low strain rate, presumably by the large amount of energy accumulated during impact loading.

Fig. 8 illustrates the boundary maps corresponding to the AZ31 alloy deformed at a high strain rate up to strains of 0.10 (Fig. 8a) and 0.20 (Fig. 8b), and at a low strain rate up to failure (the strain is approximately 0.23) (Fig. 8c).

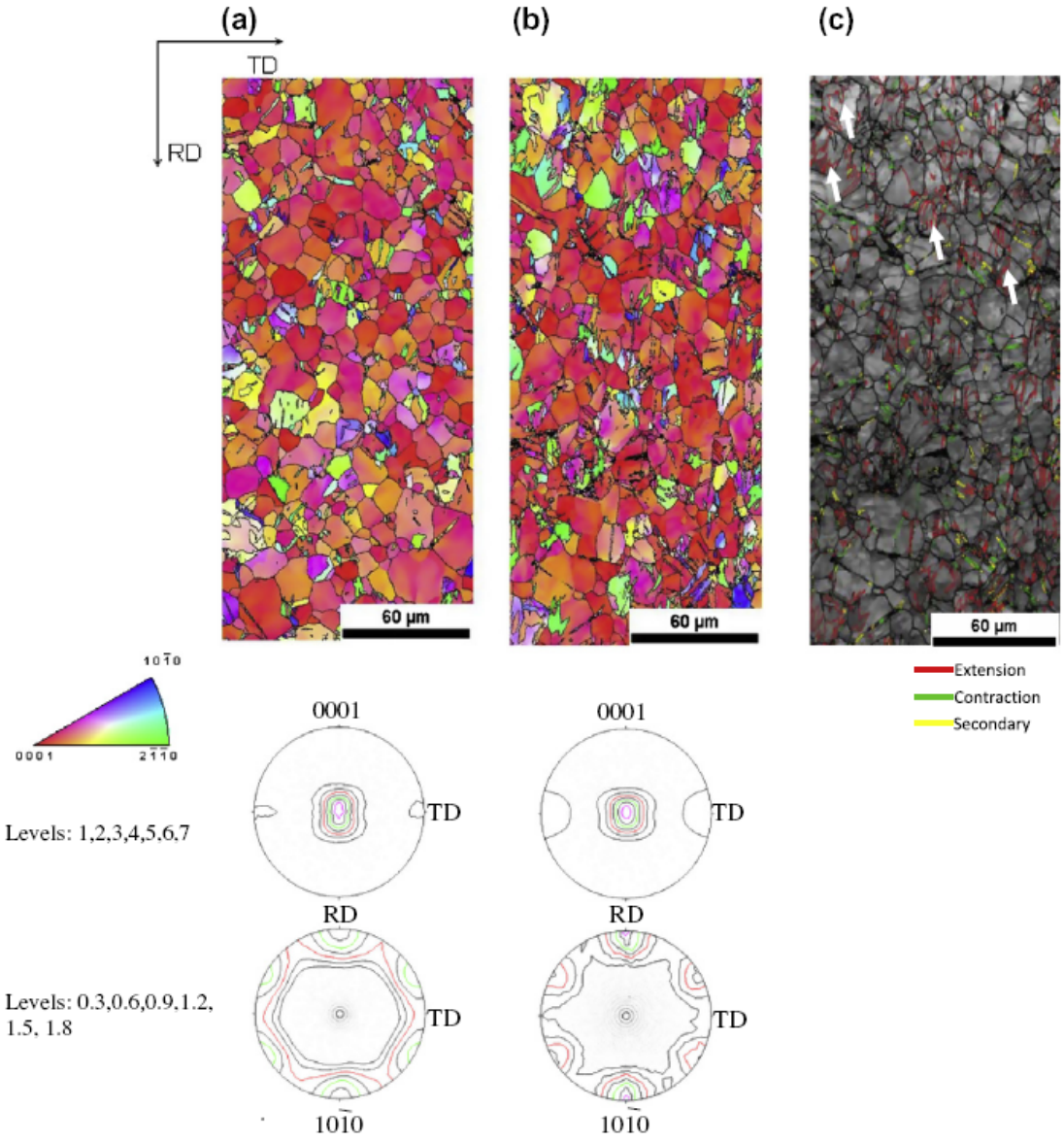

Fig. 7. EBSD inverse pole figure maps in the ND and direct pole figures, measured by neutron diffraction, corresponding to the samples dynamically loaded at room temperature in tension along the RD up to strains of (a) 0.10 and (b) 0.20. (c) Twin boundary map corresponding to the sample deformed to 0.20. Extension twin boundaries are colored in red, contraction twin boundaries are colored in green and secondary twin boundaries are colored in yellow. (For interpretation of the references to color in this figure legend, the reader is referred to the web version of this article.)

Fig. 8d shows the twin boundary map corresponding to the low strain rate sample. It can be seen, first, that the amount of low to medium angle boundaries (red and green in Figs. 8a and 8b), formed by dislocation interactions, increases with strain during dynamic deformation. Second, the grain size, measured counting only high angle boundaries, decreases from 10 μm in the initial material to 7.1 μm at a dynamic strain of 0.10 (Fig. 8a) and to 7.2 μm at a dynamic strain of 0.20 (Fig. 8b). This decrease is mainly attributed to the twin boundaries created during high strain rate deformation. Third, in the sample deformed at a low strain rate (Figs. 8c and 8d) the grain size reduction is much more pronounced ($d \sim 2.5$ μm). The presence of extension twins in this sample is significantly lower than at an equivalent dynamic strain (Fig. 7c), although it seems contraction and secondary twins are more abundant. However, the increase in contraction and secondary twin boundaries is not large enough to justify the significant decrease in grain size. Therefore, the significant decrease in grain size observed at low strain rates must be attributed mainly to the larger degree of grain subdivision caused by the formation of GNBs. Our results thus suggest that this process of grain refinement is more pronounced at low strain rates.

If the curves of Fig. 2b are compared, it can be seen that the yield stress at dynamic rates is higher than at low strain rates. This can be attributed to the higher CRSS of prismatic systems at higher strain rates [43]. The hardening rate

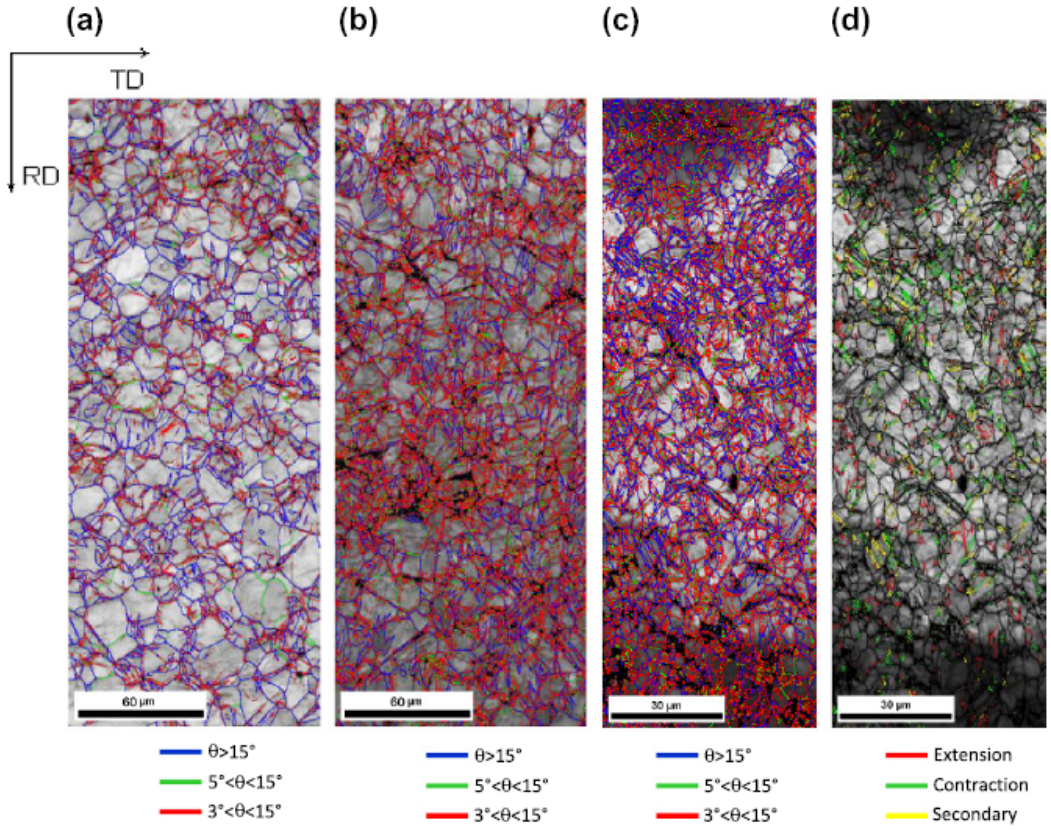

Fig. 8. Boundary maps corresponding to the AZ31 alloy deformed in tension along the RD: (a) at a high strain rate up to a strain of 0.10; (b) at a high strain rate up to a strain of 0.20; (c) at a low strain rate up to failure (failure strain approximately equal to 0.20). High angle boundaries ($\theta > 15°$) are colored in blue, moderately misoriented boundaries ($5° < \theta < 15°$) are colored in green and low angle boundaries ($3° < \theta < 5°$) are colored in red. (d) Twin boundary map corresponding to the sample deformed at a low strain rate until failure. Extension twin boundaries are colored in red, contraction twin boundaries are colored in green and secondary twin boundaries are colored in yellow. Note that the maps in (c) and (d) are taken at a higher magnification. (For interpretation of the references to color in this figure legend, the reader is referred to the web version of this article.)

under dynamic conditions tends to remain constant or increases with strain, while at low strain rates it decreases gradually, as is commonly observed in polycrystalline materials [55]. This difference in the hardening behavior is attributed to the higher degree of recovery present at low strain rate, which results in the formation of a larger fraction of GNBs.

3.2.3. Compression along the ND

Under these conditions the predominant deformation mechanisms at low strain rates are pyramidal and basal slip [16,42]. Some compression twinning is also activated in localized regions.

Fig. 9 illustrates the EBSD inverse pole figure maps in the ND as well as the macrotexture (measured by X-ray diffraction) and the microtexture (EBSD) corresponding to the samples deformed at high strain rates up to strains of 0.05 (Fig. 9a) and 0.10 (Fig. 9c). The latter strain is higher than the Zener–Hollomon failure strain (0.07), which implies that the total homogeneous strain accumulated in the sample plotted in Fig. 9b is probably closer to 0.07 than to 0.10. Fig. 9b is the twin boundary map corresponding to Fig. 9a. Significant microstructural changes take place during dynamic straining. First, surprisingly, a large number of extension twins are clearly visible after a strain of 0.05. The fraction of extension twinned area, calculated from EBSD data, is 17%. The presence of extension twinning is reflected in the intensity maximum that appears at orientations tilted 90° to the ND in the macro- and micro-(0001) direct pole figures of Fig. 9a. We have included the macrotexture in order to demonstrate that the occurrence of extension twinning is not a local effect. It must be emphasized that these twins appear in grains that are unfavorably oriented for this mechanism to be activated, i.e. which have *c*-axes parallel to the compression axis. This is surprising as it is well known that twinning is a polar mechanism and that extension twins are only predicted to occur in grains in which an extension along the *c*-axis takes place. Our data confirm that the polarity of twinning is inverted in some grains under dynamic compression along the ND. This is yet further evidence of how high strain rates stimulate extension twinning. We have not observed a similar effect for compression twins, which are scarce (Fig. 9b) despite most grains being oriented favorably for this mechanism to be activated. The extension twins formed are very soft regions in comparison

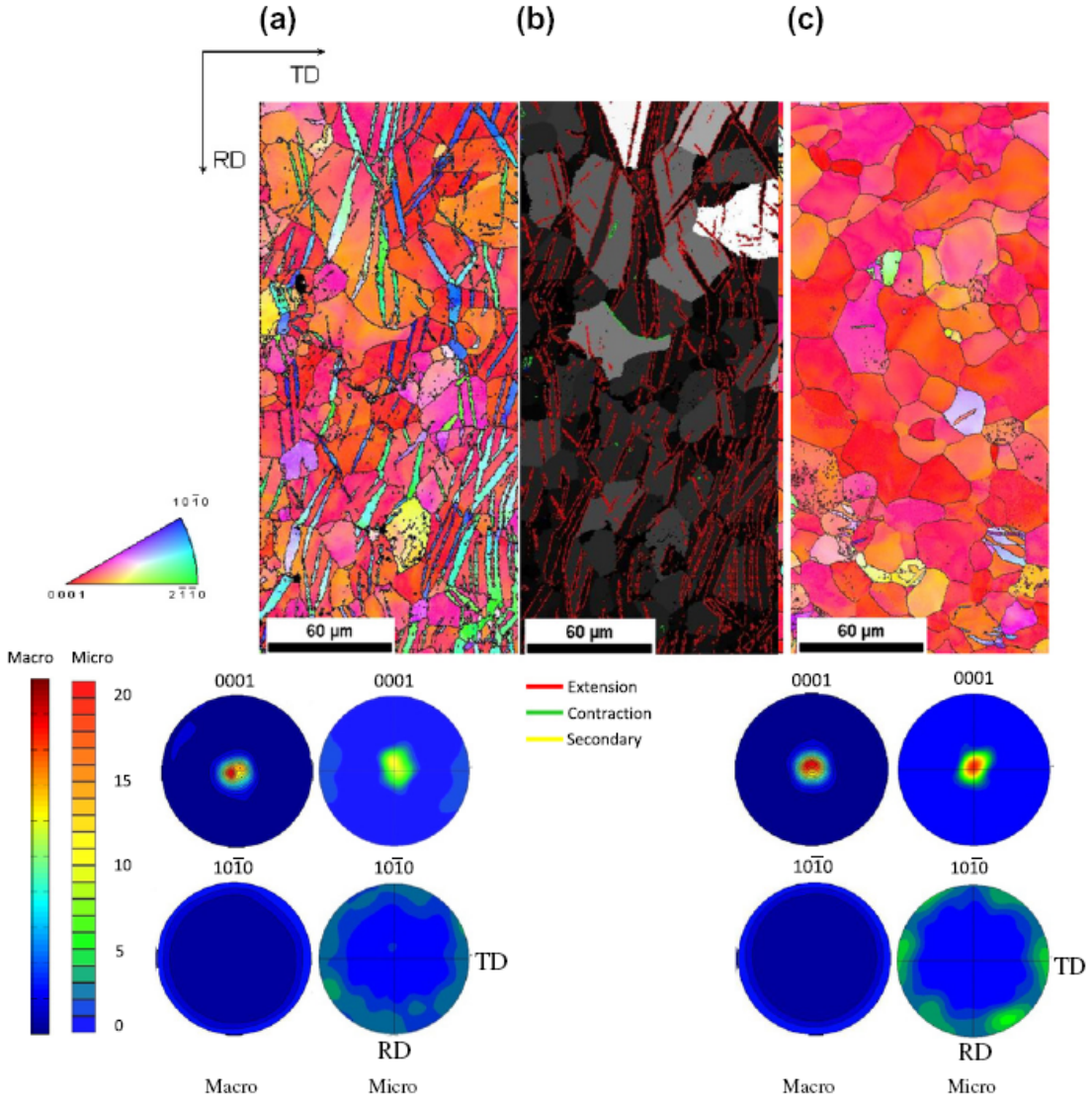

Fig. 9. (a) EBSD inverse pole figure map in the ND, macrotexture (X-ray) and microtexture (EBSD) corresponding to the AZ31 alloy dynamically loaded at room temperature in compression along the ND up to a strain of 0.05; (b) twin boundary map corresponding to the same sample (extension twin boundaries are colored in red, contraction twin boundaries are colored in green and secondary twin boundaries are colored in yellow); (c) EBSD inverse pole figure map in the ND, macrotexture (X-ray) and microtexture (EBSD) corresponding to the AZ31 alloy dynamically loaded at room temperature in compression along the ND up to a strain of 0.10. (For interpretation of the references to color in this figure legend, the reader is referred to the web version of this article.)

with the remaining of the material, which has a basal texture. Thus, it is expected that, under compression along the ND, detwinning takes place. Indeed, both the macro- and microtexture data in Fig. 9c reveal that extension twins revert back to their original orientation (*c*-axes aligned with the ND) at higher strains. EBSD (micro-)pole figures show a preferential alignment of $\langle 10\bar{1}0 \rangle$ directions with TD after detwinning, but this is considered a local effect, as macrotexture data suggest the presence of a perfect basal fiber.

The grain size after dynamic compression along the ND up to a strain of 0.05 decreases from 13 μm (initial material) to 10 μm, due to the presence of the extension twin boundaries. With increasing deformation, after detwinning the grain size increases again, reaching a value of 16 μm. This high value suggests that no significant grain subdivision by the formation of GNBs has taken place under these deformation conditions. This seems reasonable, as the strains investigated are significantly lower than those undergone by the samples deformed in compression and in tension along the RD (Sections 3.2.1 and 3.2.2).

The present results suggest that the increase in ductility with strain rate (Fig. 2c) might be due to the activation of additional deformation mechanisms, such as twinning and detwinning. Finally, since the extension twins formed at intermediate strains are very soft regions, they might constitute favorable locations for the nucleation of adiabatic shear bands.

4. Discussion

4.1. Influence of strain rate on the twinning activity

It is now well known that twinning is enhanced in Mg alloys during dynamic deformation to such an extent that it is present even at very high temperatures (400 °C) [34,43–47], at which it is absent at low strain rates. A profuse twinning activity at dynamic rates has also been reported in other hexagonal close-packed metals, such as Ti and Zr [56–58]. The current work additionally reveals that the influence of the strain rate on the AZ31 alloy consists of the enhancement of extension twinning, but that compression and double twinning are not only not enhanced, but are even hindered under dynamic conditions. In particular, it has been observed that the strain rate enhances extension twin propagation in grains that are favorably oriented for this mechanism to operate, and that it promotes the nucleation of extension twins even in grains that would not be favorably oriented for extension twinning at low strain rates.

The enhancement of extension twinning at high strain rates can be rationalized as follows. Arguments based on variations in the CRSS for twinning with strain rate must be ruled out, as it is well known that this parameter is strain rate and temperature insensitive [19,34,43]. The choice of twin systems was classically based on the criterion of minimum shear put forward by Jaswon and Dove [59] (see also Ref. [34]). This model assumes that the atoms in the twinned area reach their final positions exclusively by pure shear, which excludes atomic translations (shuffles). The twinning shears associated to extension and compression twinning in Mg (s) are −0.1289 and 0.1377, respectively [34]. These values are very similar, but usually extension twins are abundant and thick, while the compression twins are often observed only in localized regions. Furthermore, this criterion does not explain why extension twinning is preferentially enhanced at high strain rates, since shear is not diffusion assisted. A more sophisticated model for determining the operative twin systems was proposed by Bilby and Crocker [60] (see also Ref. [34]). This model considers twinning as a combination of shear plus individual atomic shuffles. The latter are dependent on both temperature and strain rate [61]. Bilby and Crocker suggested that, besides having a small shear, the operative twin mode should require only simple shuffles. In their theory, the "simplicity" of the atomic shuffles is related to a positive integer parameter (q) associated with each twinning mode, which is the number of lattice invariant planes (K_1) of spacing d traversed by the primitive lattice vector in the shear direction (η_2) [34]. The lower the value of q, the simpler the shuffles involved. For extension twinning $q = 4$, while for $\{10\bar{1}1\}$ contraction twinning $q = 8$ [34]. Thus, contraction twinning involves more complicated atom shuffling. Since atomic translations (shuffling) are activated thermally, an increase in the strain rate would hinder these atomic movements – and even more so if they are complex. Therefore contraction twinning is expected to be less favored than extension twinning at high strain rates. This is consistent with our observations.

The enhancement of extension twinning under dynamic conditions is especially dramatic during compression along the ND, where the polarity of twinning is reversed in a rather large number of grains. It is remarkable that an inversion of the polarity of tensile twinning is preferred to an enhancement of compression twinning in grains in which the c-axes are being compressed. The reason for this surprising phenomenon is not entirely clear. Twin polarity is explained in the following way. The shear associated to a specific twinning system (s) is calculated as the ratio between the modulus of the corresponding twinning dislocation (b_{TD}) and the step height, h ($s = b_{TD}/h$) [34]. For twinning modes with q higher than 2, $s \sim 2b_{TD}/q$ [34]. b_{TD}, and therefore s, may also be expressed as a function of the c/a ratio (γ). For $\{10\bar{1}2\}$ twins, $s = (2b_{TD}/q) = (\gamma^2 - 3)/3^{1/2}\gamma$. The shear thus changes dramatically with the c/a ratio. In Mg, γ is equal to 1.624 and the resulting shear is negative. This makes this twinning mode a tension twin [9,34]. Within this framework, the observation of $\{10\bar{1}2\}$ twins during c-axis compression at dynamic rates implies that the associated twinning shear adopts a positive value. This could only be achieved if the c/a ratio were to increase by approximately 5% during elastic deformation, which is not observed experimentally, or if a different mechanism (other than the propagation of the above-mentioned twinning dislocation) would dominate $\{10\bar{1}2\}$ twinning under the mentioned conditions. Some controversy does indeed exist regarding the fundamental mechanism responsible for $\{10\bar{1}2\}$ twinning in Mg alloys [62,63].

4.2. Influence of strain rate on dynamic recovery

It is well known that the dislocations generated during shock loading in high stacking fault energy materials arrange in ordered cell structures whose size and misorientation angle depend on the applied pressure and pulse time [50]. Since dislocation reorganization into cell structures requires some thermal activation, usually cells become better developed as the strain rate decreases. In low stacking fault energy metals, however, dislocation rearrangement during dynamic deformation is more sluggish and thus homogeneous dislocation distributions develop.

It has been observed that significant dislocation rearrangement to form new boundaries subdividing the original grains takes place when the AZ31 alloy is tested both at quasi-static and dynamic rates (Figs. 3, 4 and 8). However, the misorientation of these GNBs can reach very high angles in AZ31, in some cases exceeding 15°, whereas the typical misorientation of a cell boundary is rarely higher than 1 or 2°. Such highly misoriented GNBs have been observed only in rare cases, such as when deforming severely ($\varepsilon = 1$) pure Al by equal channel angular pressing [64]. It is remarkable that dislocation rearrangement can take place to such an extent at dynamic rates, where

Table 1
Comparison of the stacking fault energies corresponding to non-basal and basal dislocations in Mg with those of other metals.

	Mg-pyramidal $\langle c+a \rangle$	Mg-prismatic $\langle 1\,0\,-1\,0 \rangle$	Mg-basal	Ag	Al	Cu	Ni
γ (mJ m^{-2})	452 [65]	354 [65] 265 [66]	<50 [66]	22 [67]	200 [67]	78 [67]	128 [67]

thermal activation is very limited. The explanation for this phenomenon might be related to the very high values of the stacking fault energies corresponding to both $\langle c+a \rangle$ and prismatic $\langle 1\,0\,\bar{1}\,0 \rangle$ dislocations in Mg alloys, which are activated under all the conditions investigated here, as described in the previous sections. These values are compared in Table 1 to those corresponding to other metals [65–67].

The phenomenon of grain subdivision is most pronounced in the sample deformed quasi-statically in tension along the RD, resulting in a large reduction of the grain size with increasing deformation (from 13 to 2.5 μm). This can be rationalized as follows. First, the predominant deformation mechanism is the slip of prismatic dislocations, which have high stacking fault energy [66]. Second, prismatic slip predominates during all the deformation stages, and thus carries a large amount of the total strain (not all, as basal slip also takes place to some extent). This is not the case of the compression test along the RD, where twinning carries quite a large portion of the strain during the first stages of deformation, and pyramidal $\langle c+a \rangle$ slip, also with a high stacking fault energy [66], becomes predominant only in the latter stages of deformation. This is not the case of the compression test along ND, since the total strain to failure is small (0.07). The dynamic fracture energy corresponding to the tension test along the RD is higher than that corresponding to the other two tests (see Section 3.1). This energy is presumably employed in the formation of a larger fraction of GNBs. Finally, grain subdivision is more pronounced in the test in tension along the RD at quasi-static rates than at dynamic rates due to the easier thermal activation in the former case.

5. Conclusions

The microstructural evolution during dynamic deformation (strain rate of $\sim 10^3$ s^{-1}) of an AZ31 Mg rolled sheet with a typical basal fiber texture and an equiaxed grain size around 13 μm has been investigated and the following conclusions have been drawn from the present work:

1. $\{10\bar{1}2\}$ extension twin nucleation and propagation are dramatically enhanced at dynamic rates. Contraction and secondary twinning, however, are not favored at such high rates. The choice of $\{10\bar{1}2\}$ twinning at 10^3 s^{-1} may be attributed to the simpler atom shuffles involved.
2. The polarity of twinning may be inverted at dynamic rates. In particular, $\{10\bar{1}2\}$ twinning, which is well known to be an extension twin in the AZ31 alloy, has been observed to take place in grains in which the c-axes are compressed during dynamic compression along the normal direction.
3. Grain subdivision by the formation of GNBs occurs readily in the AZ31 alloy during both quasi-static and dynamic deformation. Dislocation accumulation and rearrangement takes place with increasing deformation in both strain rate regimes, leading to a gradual increase in the misorientation of the newly formed boundaries, which may eventually become high angle boundaries. The process of grain subdivision is more pronounced at low strain rates due to the easiness of thermal activation, which favors dislocation rearrangement.
4. The extent to which grain subdivision takes place depends on the relative orientation between the applied stress and the c-axes of the crystallites. This phenomenon is most pronounced in the sample tested in tension along the RD since prismatic dislocations, which have high stacking fault energy, carry most of the strain up until failure.

Acknowledgements

The authors would like to thank the vehicle interior manufacturer, Grupo Antolin Ingenieria, S.A., within the framework of the project MAGNO2008-1028-CENIT funded by the Spanish Ministry. Funding from the Basque Government through the Manufacturing 0,0 project (within the Etortek Programme) is acknowledged. Neutron diffraction measurements were supported by the EC under the sixth FP through the Key Action: Strengthening the ERA, Research Infrastructures, contract no. RII3-CT-2003-505925. The help provided by G. Arruebarrena, U. Garbe, P. Spalthoff, W. Gan and C. Randau is gratefully acknowledged. The assistance of María Jesús Pérez (UPM, Madrid) and Jesús Reales (CENIM, Madrid) with the mechanical testing and of Yu Kyung Shin and V. Kree (HZG, Germany) with the EBSD analysis is appreciated. The technicians at the CAI Difracción de Rayos X of UCM are acknowledged for their help with the macrotexture measurements. Prof. Daniel Rittel (Technion, Israel) is sincerely thanked for stimulating discussions.

References

[1] Easton M, Beer A, Barnett M, Davies C, Dunlop G, Durandet Y, et al. JOM 2008;60:57.
[2] Mordike BL, Ebert T. Mater Sci Eng 2001;302:37.
[3] Bamberger M, Dehm G. Annu Rev Mater Res 2008;38:505.

[4] Couling SL, Pashak JF, Sturkey L. Trans ASM 1959;51:94.
[5] Kocks UF, Westlake DG. Trans AIME 1967;239:1107.
[6] Kelley EW, Hosford WF. Trans AIME 1968;242:654.
[7] Couret A, Caillard D. Acta Metall 1985;33:1455.
[8] Chin GY, Mammel WL. Metall Trans 1970;1:357.
[9] Yoo MH. Metall Trans 1981;12A:409.
[10] Vagarali SS, Langdon TG. Acta Metall 1981;29:1969.
[11] Zelin MG, Yang HS, Valiev RZ, Mukherjee AK. Metall Trans 1992;23:3135.
[12] Munroe N, Tan X. Scripta Mater 1997;36:1383.
[13] Agnew SR, Yoo MH, Tomé CN. Acta Mater 2001;49:4277.
[14] Watanabe H, Tsutsui H, Mukai T, Kohzu M, Tanabe S, Higashi K. Int J Plasticity 2001;17:387.
[15] Barnett MR. J Light Met 2001;1:167.
[16] Agnew SR, Tomé CN, Brown DW, Holden TM, Vogel SC. Scripta Mater 2003;48:1003.
[17] Galiyev A, Sitdikov O, Kaibyshev R. Mater Trans 2003;44:426.
[18] Koike J, Kobayashi T, Mukai T, Watanabe H, Suzuki M, Maruyama K, et al. Acta Mater 2003;51:2055.
[19] Barnett MR. Metall Mater Trans 2003;34:1799.
[20] Gehrmann R, Frommert MM, Gottstein G. Mater Sci Eng 2005;395:338.
[21] Barnett MR, Keshavarz Z, Beer AG, Atwell D. Acta Mater 2004;52:5093.
[22] Agnew SR, Duygulu Ö. Int J Plasticity 2005;21:1161.
[23] Del Valle JA, Pérez-Prado MT, Ruano OA. Metall Mater Trans 2005;36:1427.
[24] Keshavarz Z, Barnett MR. Scripta Mater 2006;55:915.
[25] Meza-García E, Dobroň P, Bohlen J, Letzig D, Chmelik F, Lukáč P, et al. Mater Sci Eng 2007;462:297.
[26] Barnett MR. Mater Sci Eng 2007;464:1.
[27] Del Valle JA, Ruano OA. Acta Mater 2007;55:455.
[28] Al-Samman T, Gottstein G. Mater Sci Eng 2008;488:406.
[29] Chino Y, Kimura K, Mabuchi M. Mater Sci Eng 2008;486:481.
[30] Jain A, Duygulu O, Brown DW, Tomé CN, Agnew SR. Mater Sci Eng 2008;486:545.
[31] Hutchinson B, Barnett MR, Ghaderi A, Cizek P, Sabirov I. Int J Mater Res 2009;100:556.
[32] Ball EA, Prangnell PB. Scripta Metall Mater 1994;31:111.
[33] Lou XY, Li M, Boger RK, Agnew SR, Wagoner RH. Int J Plasticity 2007;23:44.
[34] Christian JW, Mahajan S. Prog Mater Sci 1995;39:1.
[35] Barnett MR. Mater Sci Eng 2007;464:8.
[36] Wonsiewizc BC, Backofen WA. Trans AIME 1967;239:1422.
[37] Hartt WH, Reed-Hill RE. Trans AIME 1968;242:1127.
[38] Hartt WH, Reed-Hill RE. Trans AIME 1968;239:1511.
[39] Nave MD, Barnett MR. Scripta Mater 2004;51:881.
[40] Barnett MR, Nave MD, Bettles CJ. Mater Sci Eng 2004;386:205.
[41] Cizek P, Barnett MD. Scripta Mater 2008;59:959.
[42] Knezevic M, Levinson A, Harris R, Mishra RK, Doherty RD, Kalidindi SR. Acta Mater 2010;58:6230.
[43] Ulacia I, Dudamell NV, Gálvez F, Yi S, Pérez-Prado MT, Hurtado I. Acta Mater 2010;58:2988.
[44] Ishikawa K, Watanabe H, Mukai T. Mater Lett 2005;59:1511.
[45] Ishikawa K, Watanabe H, Mukai T. J Mater Sci 2005;40:1577.
[46] Watanabe H, Ishikawa K, Mukai T. Key Eng Mater 2007;340–341:107.
[47] Watanabe H, Ishikawa K. Mater Sci Eng 2009;523:304.
[48] Ulacia I, Salisbury CP, Hurtado I, Worswick MJ. J Mater Process Tech 2011;211:830.
[49] Mtex Software, Hielscher R, Chemnitz TU, Germany.
[50] Meyers MA. Dynamic behavior of materials. New York: John Wiley & Sons; 1994. p. 448.
[51] Bai YL, Dodd B. Adiabatic shear localization – occurrence, theories and applications. New York: Pergamon Press; 1992.
[52] Zener C, Hollomon JH. J Appl Phys 1944;15:22.
[53] Rittel D, Landau P, Venkert A. Phys Rev Lett 2008;101:165501.
[54] Fernández A, Pérez-Prado MT, Wei Y, Jérusalem A. Int J Plasticity 2011, in press.
[55] Kocks UF, Mecking H. Prog Mater Sci 2003;48:171.
[56] Padilla HA, Smith CD, Lambros J, Beaudoin AJ, Robertson IM. Metall Mater Trans 2007;38A:2916.
[57] Gurao NP, Kapoor R, Suwas S. Acta Mater 2011;59:3431.
[58] Nemat-Nasser S, Guo WG, Cheng JY. Acta Mater 1999;47:3705.
[59] Jaswon MA, Dove DB. Acta Crystallogr 1956;9:621.
[60] Bilby BA, Crocker AG. Proc Roy Soc 1965;288:240.
[61] Serra A, Bacon DJ. Mater Sci Eng 2005;400-401:496.
[62] Li B, Ma E. Phys Rev Lett 2009;113:035503.
[63] Serra A, Bacon DJ, Pond RC. Phys Rev Lett 2010;104:029603.
[64] Cabibbo M, Blum W, Evangelista E, Kassner ME, Meyers MA. Metall Trans 2008;39:181.
[65] Wen L, Chen P, Tong ZF, Tang BY, Peng LM, Ding WJ. Eur Phys J B 2009;72:397.
[66] Smith AE. Surface Sci 2007;601:5762.
[67] Murr LE. Interfacial phenomena in metals and alloys. Reading MA: Addison-Wesley; 1975.

3.3. Influence of texture on the recrystallization mechanisms in an AZ31 Mg sheet alloy at dynamic rates

Materials Science and Engineering A 532 (2012) 528-535

N.V. Dudamell[a], I. Ulacia[b], F. Gálvez[c], S. Yi[d], J. Bohlen[d], D. Letzig[d], I. Hurtado[b], M.T. Pérez-Prado[a],

[a] IMDEA Materials Institute, C/Profesor Aranguren s/n, 28040 Madrid, Spain
[b] Mondragon Goi Eskola Politeknikoa, Mondragon Unibertsitatea, 20500 Mondragón, Spain
[c] ETS Ingenieros de Caminos, Universidad Politécnica de Madrid, 28040 Madrid, Spain
[d] Magnesium Innovation Centre. Helmholtz-Zentrum Geesthacht, 21502 Geesthacht, Germany

Received 19 August 2011; received in revised form 2 November 2011; accepted 3 November 2011
Available online 11 November 2011

Materials Science and Engineering A 532 (2012) 528–535

Contents lists available at SciVerse ScienceDirect

Materials Science and Engineering A

journal homepage: www.elsevier.com/locate/msea

Influence of texture on the recrystallization mechanisms in an AZ31 Mg sheet alloy at dynamic rates

N.V. Dudamell[a,*], I. Ulacia[b], F. Gálvez[c], S. Yi[d], J. Bohlen[d], D. Letzig[d], I. Hurtado[b], M.T. Pérez-Prado[a]

[a] IMDEA Materials Institute, C/Profesor Aranguren,s/n, 28040 Madrid, Spain
[b] Mondragon Goi Eskola Politeknikoa, Mondragon Unibertsitatea, 20500 Mondragón, Spain
[c] ETS Ingenieros de Caminos, Universidad Politécnica de Madrid, 28040 Madrid, Spain
[d] Magnesium Innovation Centre, Helmholtz-Zentrum Geesthacht, 21502 Geesthacht, Germany

ARTICLE INFO

Article history:
Received 19 August 2011
Received in revised form 2 November 2011
Accepted 3 November 2011
Available online 11 November 2011

Keywords:
Magnesium
AZ31
High strain rate
Dynamic recrystallization
Twinning

ABSTRACT

An AZ31 rolled sheet alloy has been tested at dynamic strain rates ($\dot{\varepsilon}\sim10^3\ s^{-1}$) at 250 °C up to various intermediate strains before failure in order to investigate the predominant deformation and restoration mechanisms. In particular, tests have been carried out in compression along the rolling direction (RD), in tension along the RD and in compression along the normal direction (ND). It has been found that dynamic recrystallization (DRX) takes place despite the limited diffusion taking place under the high strain rates investigated. The DRX mechanisms and kinetics depend on the operative deformation mechanisms and thus vary for different loading modes (tension, compression) as well as for different relative orientations between the loading axis and the *c*-axes of the grains. In particular, DRX is enhanced by the operation of ⟨c + a⟩ slip, since cross-slip and climb take place more readily than for other slip systems, and thus the formation of high angle boundaries is easier. DRX is also clearly promoted by twinning.

1. Introduction

Light magnesium alloys have been widely investigated over the last decade due to their potential to replace heavier metals in transport vehicles [1–3]. The deformation mechanisms predominant in Mg alloys at low temperatures and low strain rates are now known rather well and have been reviewed in several occasions [4–6]. Possible deformation modes include basal ((0 0 0 1)⟨a⟩), prismatic ({10–10}⟨a⟩) and pyramidal ({10–11}⟨a⟩ and {11–22}⟨c + a⟩) slip, as well as {10–12} extension and {10–11} and {10–13} contraction twinning. The critical resolved shear stresses (CRSS) of all these deformation modes differ widely at room temperature. A summary of the CRSS obtained from single crystal experiments can be found in [7]. These values are of the order of 5 MPa for basal slip, 10 MPa for extension twinning, 20 MPa for prismatic slip, 40 MPa for pyramidal slip and 70–80 MPa for contraction twinning. Thus, in the highly textured alloys resulting from conventional rolling or extrusion processes the predominant mechanisms will depend strongly on the loading mode (tension or compression) as well as on the loading direction with respect to the *c*-axes of the polycrystalline aggregate [4–6,8]. In summary, the mechanical behavior and the microstructural evolution during room temperature quasi-static deformation of strongly textured Mg alloys is highly anisotropic.

With increasing temperature, at low strain rates and in alloys with conventional grain sizes ($d\sim5$–$50\ \mu m$), the CRSS of basal slip and extension twinning remain constant, but that of non-basal slip systems and contraction twinning decrease gradually [9]. In particular, at $T>250$ °C the CRSS values of non-basal slip become eventually lower than that of extension twinning. At slightly higher temperatures ($\sim T>300$ °C) the CRSS for compression twinning also decreases significantly, albeit retaining higher values than the other deformation modes. As a result, with increasing temperature, deformation becomes progressively accommodated by multiple slip [4,10,11]. Some authors have also highlighted the important role of grain boundary sliding at $T>300$ °C [12,13]. Due to the operation of a larger number of deformation modes, ductility increases and the mechanical behavior of Mg alloys, even if strongly textured, becomes more isotropic.

High temperature quasi-static deformation of Mg alloys of conventional grain sizes is usually accompanied by dynamic recrystallization (DRX). Several studies have been carried out to date with the aim of elucidating the predominant DRX mechanisms [6,14–26]. Ion et al. [14] published in 1982 a pioneer study on the subject, in which they reported that DRX was strongly dependent on the deformation temperature. At $T>300$–350 °C, discontinuous DRX (DDRX) [27,28], i.e., the nucleation of strain free grains and subsequent growth of these at the expense of deformed regions,

* Corresponding author. Tel.: +34 91 549 34 22; fax: +34 91 550 30 47.
E-mail address: nathamar.dudamell@imdea.org (N.V. Dudamell).

0921-5093/$ – see front matter © 2011 Elsevier B.V. All rights reserved.
doi:10.1016/j.msea.2011.11.018

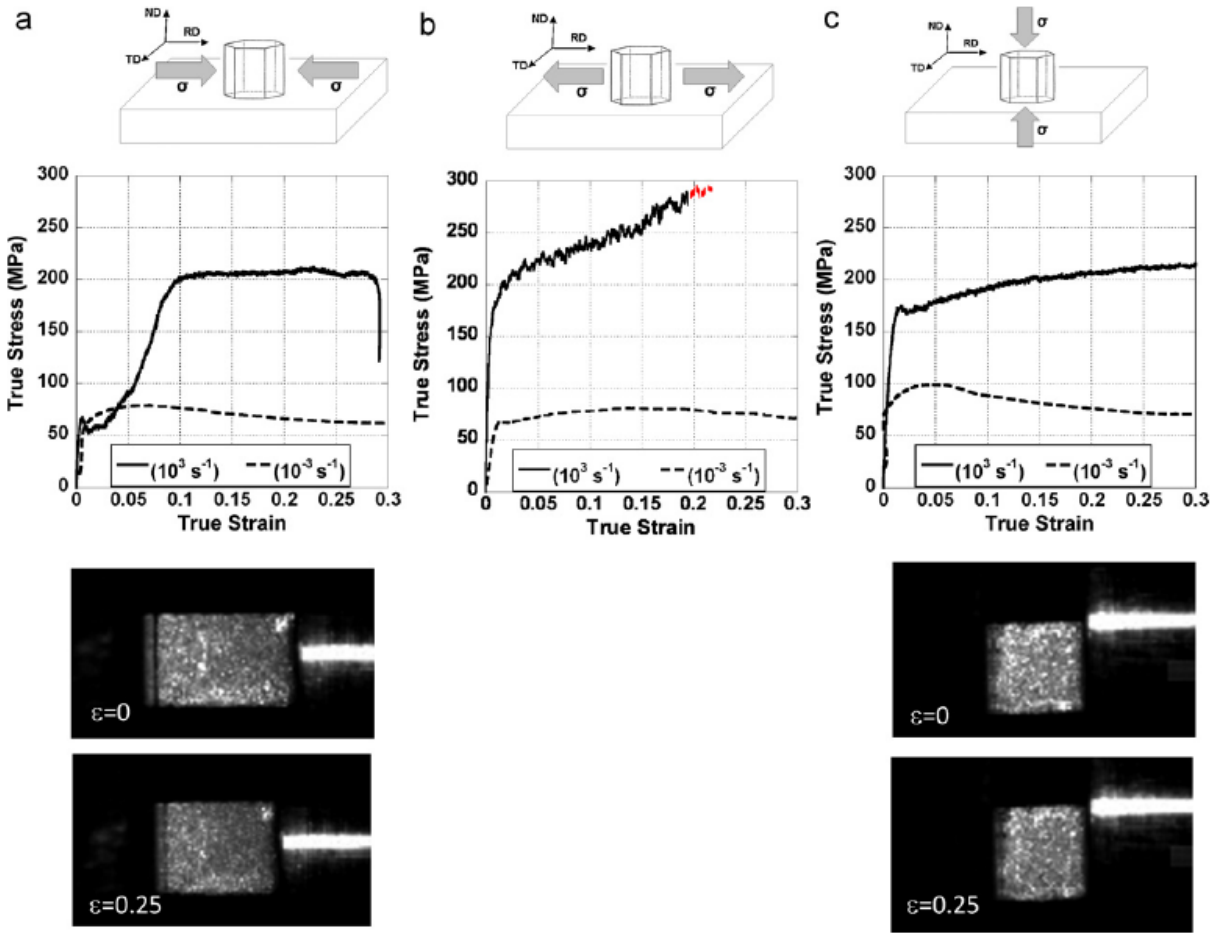

Fig. 1. Stress–strain curves corresponding to the Mg AZ31 alloy deformed at high strain rate (10^3 s^{-1}, solid line) and at quasi-static strain rates (10^{-3} s^{-1}, dotted line) at 250 °C in (a) compression along RD; (b) tension along RD; and (c) compression along ND. In (b), the black line indicates the part of the test corresponding to the first pulse. The red part is included here only to clarify that fracture took place shortly after the first pulse. The images below each graph show the corresponding specimen before testing (upper image) and after dynamic deformation up to a true strain of approximately 0.25 (lower image). (For interpretation of the references to color in this figure legend, the reader is referred to the web version of the article.)

would predominate. This has been confirmed, for example, in [20]. At lower temperatures, continuous type processes (CDRX), consisting on the formation of subgrain boundaries by dislocation accumulation and the gradual increase of their misorientation (θ) with strain [27,28], would prevail. Numerous studies have reported the occurrence of continuous processes at moderate temperatures [6,18,19,21,22,24–26]. More recently, the specific domains under which DDRX and CDRX predominate, have been associated to critical values of the Zener–Hollomon parameter (Z), as strain rate also plays a significant role (opposite to that of temperature) [29]. Depending on the material composition and microstructural characteristics, DDRX and CDRX may coexist in wide Z ranges.

The high temperature deformation and recrystallization mechanisms of Mg alloys at impact strain rates ($\sim 10^3$ s^{-1}) are currently not well understood, as significantly fewer studies have been carried out in this area [5,30–36]. It is known that the CRSS of non-basal systems decreases more slowly with temperature than under quasi-static conditions [5] and, thus, twinning is operative even at $T > 400$ °C [5,30–33]. Therefore strongly textured Mg alloys remain mechanically anisotropic at such high temperatures [5]. Dynamically recrystallized grains have been observed in Mg alloys, such as AZ91 and AZ31, after impact loading at high temperatures [30–32]. However, the DRX mechanisms operative under these extreme conditions are not known.

The aim of the present work is to investigate the DRX mechanisms predominant in a rolled AZ31 sheet alloy at dynamic strain rates as a function of the loading mode and of the relative orientation between the loading axis and the c-axes of the polycrystalline aggregate. With that purpose, the evolution of the microstructure, the texture, and the grain boundary distribution with strain is examined when the rolled AZ31 sheet is compressed along the rolling (RD) and normal (ND) directions and tensile tested along the RD. The dynamic deformation and DRX mechanisms will be compared to those prevalent at quasi-static strain rates.

2. Experimental procedure

2.1. Material: initial microstructure

The material under study is a Mg alloy AZ31 (Mg–3%Al–1%Zn). Two rolled and annealed sheets, 1 and 3 mm in thickness, were purchased from Magnesium Elektron. The initial microstructures of the two AZ31 sheets with 1 and 3 mm thickness are formed by equiaxed grains, with average sizes of 10 and 13 μm, respectively. Both have a characteristic strong basal texture. In the following we will refer to both sheets as "the AZ31 alloy", as their microstructure and mechanical behavior are basically identical. Further considerations about the similarity of the two materials can be found in [5].

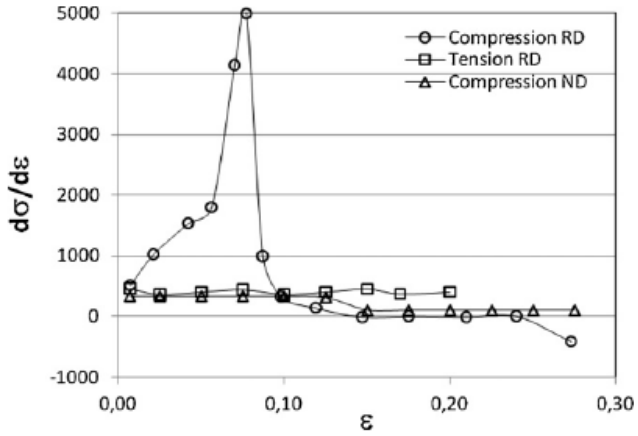

Fig. 2. Work hardening behavior corresponding to the AZ31 sheet alloy deformed at 250 °C and 10^3 s^{-1}.

2.2. Mechanical testing

High strain rate ($\dot{\varepsilon}\sim10^3$ s^{-1}) tension and compression tests were performed in the AZ31 alloy at 250 °C up to failure and up to several intermediate strains using a Hopkinson bar furnished with a high speed camera. Samples were heated at 10 °C/min and they remained at this temperature during half an hour in order to achieve the temperature stabilization. In the compression tests the specimens were dynamically loaded to a predefined strain level, using a stop-ring technique which limits the displacement of the incident Hopkinson bar. Ring stoppers of specific heights were machined out of an F522 steel. Two nickel superalloy (RENE-41) bars, 1 m in length and 19 and 10 mm in diameter, respectively, were machined for this purpose. In the tension tests, momentum trapping fixtures were used in order to interrupt testing and obtain samples deformed at different strains. The incident and transmitted bars in tension tests were made of aluminum AA6061-T6 with 15.87 mm diameter and 1.44 min length. Aluminum bars were used in order to minimize the impedance difference between the bars and specimen and also to increase the signal/noise ratio. The maximum loading duration with the current apparatus setup is 200 μs as governed by the maximum length of the striker. Compression tests were performed along the RD in 3 mm × 3 mm × 4.5 mm specimens and along the ND in 3 mm × 3 mm × 3 mm cubes. Tensile tests along the RD were performed in dog-bone shaped tensile specimens with a gage length of 12.5 mm and a width of 1.75 mm. After the tests, samples were quickly removed from the machine and put on metallic surface with the purpose of accelerate the cooling of the small samples. In order to reduce friction, solid graphite was used as lubricant. As Hopkinson bar has works in the elastic regime, dynamic stress–strain curves were calculated using the elastic modulus of the bars.

Quasi-static tests at a strain rate of 10^{-3} s^{-1} were also carried out until failure along the same directions in order to compare the variations in the microstructural evolution with the strain rate. These tests were carried out in a conventional universal testing

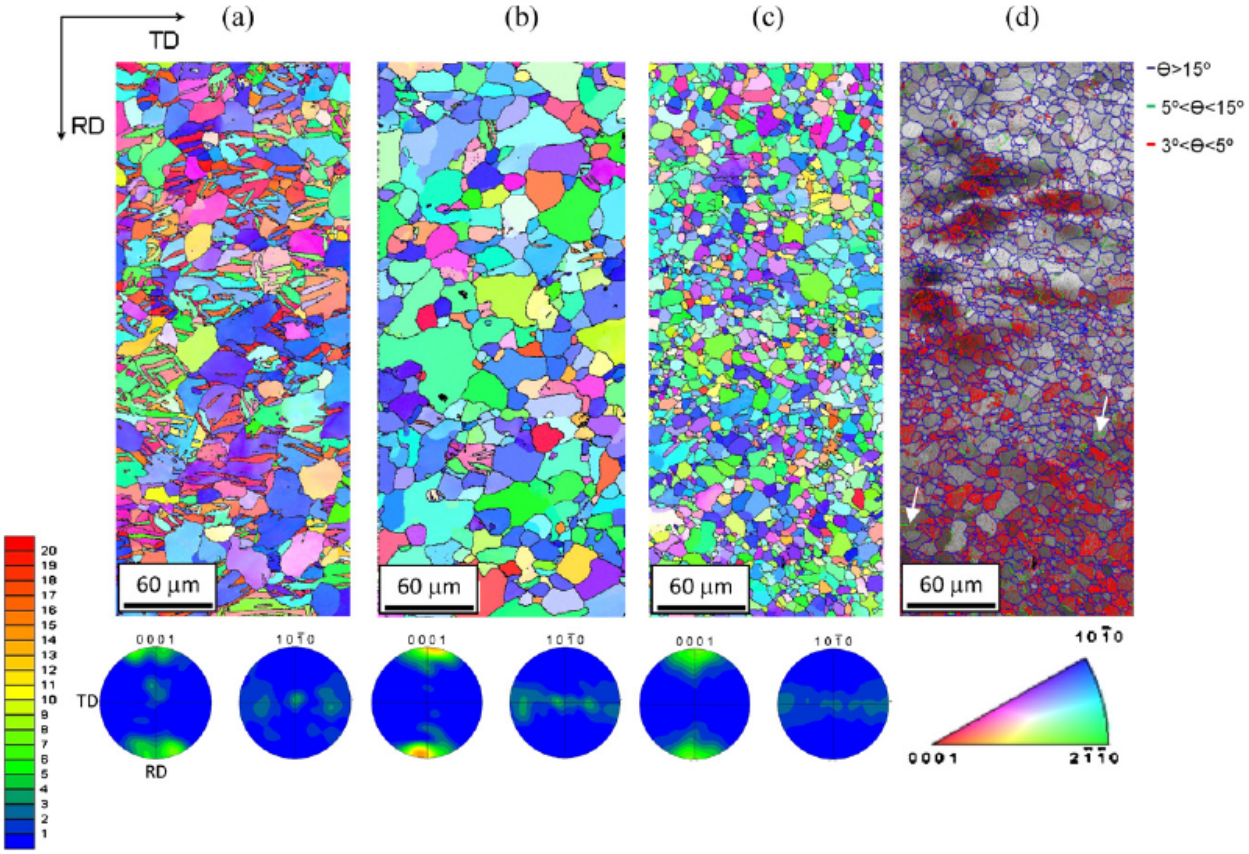

Fig. 3. EBSD inverse pole figure maps in the ND and microtextures corresponding to samples dynamically loaded at 250 °C in compression along RD up to strains of (a) 0.06, (b) 0.10, and (c) 0.15. (d) Boundary map corresponding to the sample strained up to 0.15. High angle boundaries (misorientation, $\theta > 15°$) are colored in blue, moderately misoriented boundaries ($5° < \theta < 15°$) in green and low angle boundaries ($3° < \theta < 5°$) in red. White arrows indicate the presence of some (very few) moderately misoriented boundaries, perpendicular to the applied stress, resulting from dislocation interactions. (For interpretation of the references to color in this figure legend, the reader is referred to the web version of the article.)

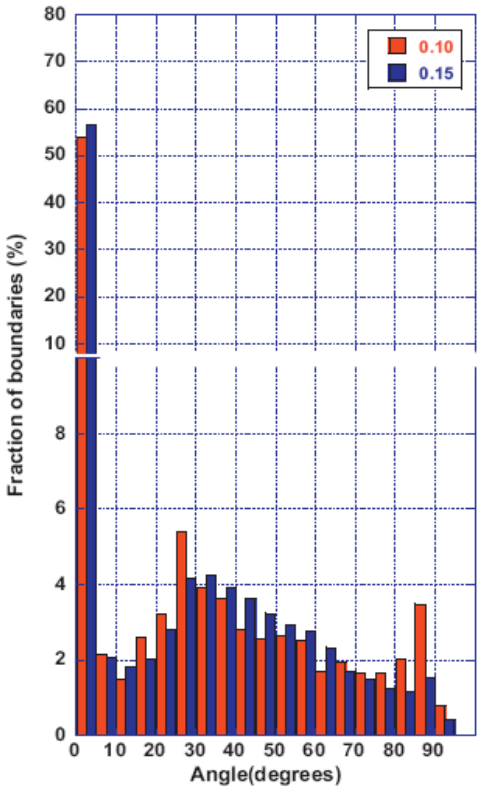

Fig. 4. Misorientation distribution histograms corresponding to the AZ31 sheet alloy compressed along RD at $10^3\,s^{-1}$ and 250 °C up to strains of 0.10 and 0.15.

machine (Instron) using the same specimen geometries, heating procedure and lubricant described above. To calculate quasi-static stress–strain curves, the stiffness of the Instron machine was taken into account. Tests were found very reproducible as in dynamic as quasi-static tests.

2.3. Microstructure examination

The microstructure and the texture of a number of samples compressed along the RD and the ND and tensile tested along the RD at 250 °C up to various strain levels were analyzed by electron backscatter diffraction (EBSD) using the TSL-OIM™ software in a Zeiss Ultra 55™ FEG-SEM. Sample preparation for EBSD investigations included grinding with 4000 SiC paper, mechanical polishing with a 0.05 μm silica suspension and final electro-chemical polishing for 90 s at 33 V using the AC2™ commercial electrolyte. The microstructure is represented by EBSD orientation maps and the texture by pole figures recalculated from the EBSD orientation data. In order to investigate the operative deformation and DRX mechanisms, the nature of the grain boundaries present in all the samples was analyzed from the EBSD data. Additionally, the grain size of various samples was calculated by the linear intercept method in the EBSD orientation maps using only grain boundaries with misorientations higher than 15°. The volume fraction of material oriented as specific texture components was calculated using the EBSD software.

3. Results

Fig. 1 illustrates the stress–strain curves corresponding to the AZ31 samples deformed at 250 °C at dynamic ($10^3\,s^{-1}$) and at quasi-static ($10^{-3}\,s^{-1}$) rates in compression along the RD (Fig. 1a), in tension along the RD (Fig. 1b) and in compression along the ND (Fig. 1c). Images of the samples deformed in compression right before testing and after a true strain of 0.25 have been added. At quasi-static strain rates, in all three cases, the stress–strain curves have a "concave-down" shape, indicative of the operation of crystallographic slip. The presence of softening during high temperature deformation of an AZ31 sheet is consistent with the observations of other authors [e.g. 4, 18, 25] and it has been attributed to the occurrence of dynamic recrystallization [18,25]. The peak strains are 0.06 in compression along the RD, 0.14 in tension along the RD and 0.05 in compression along the ND. Ductility values exceeding 0.4 (strain at which the compression tests were interrupted) can be obtained in all cases.

At high strain rates the yield and maximum stresses are significantly higher than those measured at quasi-static rates, but the elongation to failure is smaller in all three testing conditions. Fig. 2 illustrates the work hardening rates for the three tests. Significant differences can be found between the three curves. The one corresponding to the compression test along the RD (Fig. 1a) exhibits first a "concave-up" stage, indicative of the presence of twinning, which is known to occur at high temperatures under dynamic conditions [5,30–33]. This is followed by significant strain hardening up to a strain of approximately 0.08 and, subsequently, a stage of practically zero hardening until fracture at a strain of 0.28. The curve corresponding to the tension test along the RD (Fig. 1b) has a "concave-down" shape, characteristic of the predominance of crystallographic slip, and exhibits work hardening until fracture. Finally, the curve corresponding to compression along the ND also has also a "concave-down" shape and the strength increases monotonously with strain. The work hardening rate is positive, but smaller than the one observed in tension along the RD. The ductility values obtained are approximately 0.28 in compression along the RD, 0.22 in tension along the RD and 0.38 in compression along the ND.

Fig. 3 illustrates the evolution of the microstructure and the texture during compression along the RD. EBSD inverse pole figure maps in the ND and the corresponding pole figures are shown for samples deformed up to strains of 0.06 (Fig. 3a), 0.10 (Fig. 3b), and 0.15 (Fig. 3c). A significant amount of extension twinning has indeed taken place at a strain of 0.06. It is well known that extension twins propagate rapidly in AZ31 at low temperatures and quasi-static rates [37]. It is also remarkable that a similar effect can be observed at the current testing conditions, which involve high temperatures and very high strain rates. The volume fraction of twinned material is 72%. This value is slightly lower than that observed for similar strains at low strain rates and room temperature (86%, [38]), but still very high. Twinning results in a lattice rotation of 86° around the ⟨11–20⟩ axis, giving rise to a characteristic texture, formed by two maxima parallel to the RD in the (0 0 0 1) pole figure and to a maximum parallel to the ND in the (10–10) pole figure. The grain size at this strain is 6 μm. The decrease in grain size with respect to the as-received material is attributed mainly to the presence of a significant amount of twin boundaries. With increasing deformation extension twins propagate even further. At a strain of 0.10 (Fig. 3b) the twinned volume fraction is 93%. Accordingly, the grain size increases to 12 μm, as twin propagation has now basically encompassed the entire grains and very few twin boundaries remain. It is well known that the twinned regions, in which the compression axis is parallel to the *c*-axes, pyramidal ⟨c + a⟩ and basal slip are the predominant deformation mechanisms [39,40]. As shown in Figs. 1a and 2a, for strains higher than 0.10, the work hardening rate decreases practically to zero. This is accompanied by a dramatic change in the microstructure. In particular, at a strain of 0.15 (Fig. 3c), the microstructure is formed by equiaxed grains, 6 μm in size, and a fiber texture, with the ⟨0 0 0 1⟩ axis parallel to the RD, develops. These two observations are consistent with the occurrence of dynamic recrystallization. Fig. 4 shows the

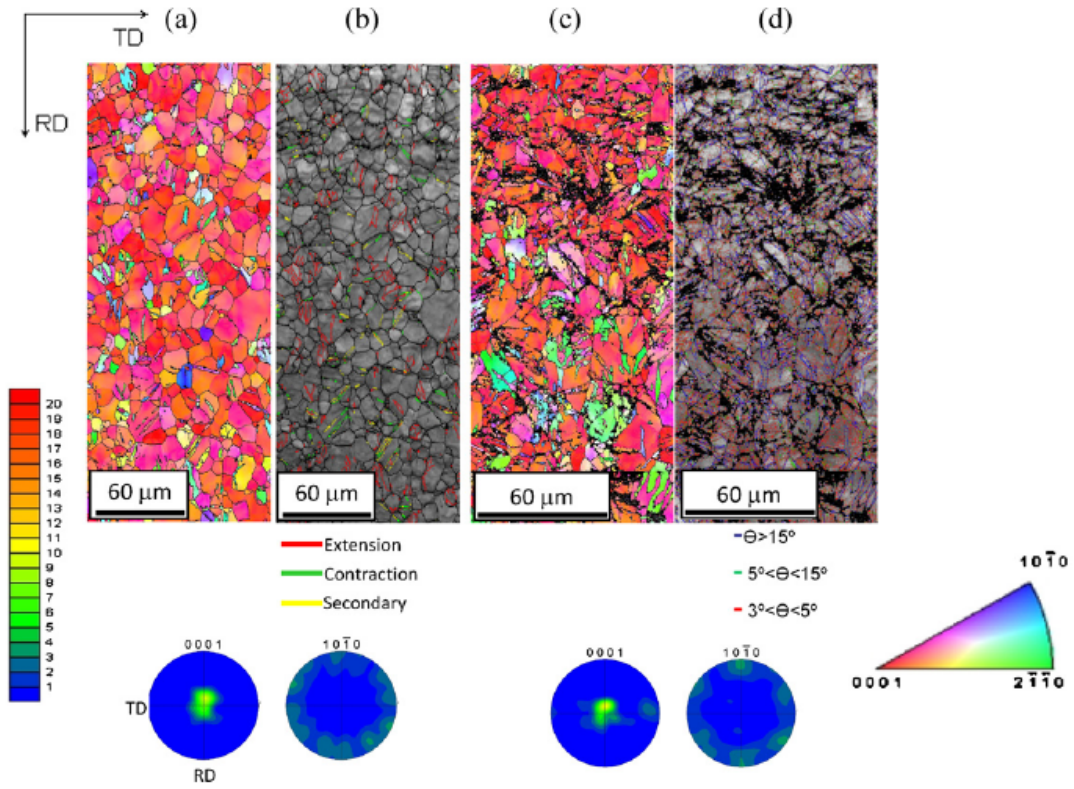

Fig. 5. EBSD inverse pole figure maps in the ND and microtextures corresponding to samples dynamically loaded at 250 °C in tension along RD up to strains of (a) 0.10, and (c) 0.20. (b) Twin boundary map corresponding to the sample deformed up to a strain of 0.10. Extension twin boundaries are colored in red, contraction twin boundaries are colored in green and secondary twin boundaries are colored in yellow. (d) Boundary map corresponding to the sample strained up to 0.20. High angle boundaries (misorientation, $\theta > 15°$) are colored in blue, moderately misoriented boundaries ($5° < \theta < 15°$) in green and low angle boundaries ($3° < \theta < 5°$) in red. Please note that the scale bar in (a) and (b) is different from that of (c) and (d). This was done in order to provide a clearer view of the microstructure in the latter. (For interpretation of the references to color in this figure legend, the reader is referred to the web version of the article.)

misorientation distribution histograms corresponding to the samples deformed up to strains of 0.10 and 0.15. In the latter there is a higher proportion of boundaries with misorientation angles (θ) ranging from approximately 30° to 65° and a lower proportion of boundaries with θ between 5° and 30°. It seems the newly created high angle boundaries are not formed by a gradual increase in misorientation as, in that case, a higher proportion of boundaries with θ between 5° and 30° should be present in the recrystallized sample than in the sample deformed up to a strain of 0.10. This suggests that discontinuous DRX is the main recrystallization mechanism. Nevertheless, the presence of some (very few) moderately misoriented boundaries (with θ between 5° and 15°), lying perpendicular to the applied stress and thus subdividing the original grains, resulting from dislocation interactions, could also be detected. Two of these boundaries are pointed by white arrows in Fig. 3d.

Fig. 5 illustrates the microstructure and the texture of the sample deformed in tension along the RD up to strains of 0.10 (Fig. 5a and b) and 0.20 (Fig. 5c and d). After a strain of 0.10 the grains remain fairly equiaxed and the average size is 8 μm. Extension, contraction and secondary twinning are apparent to a small extent (Fig. 5b) and thus twin boundaries contribute to the grain refinement. A deformation texture, in which basal planes are parallel to the rolling plane and ⟨10–10⟩ directions are parallel to the loading axis (RD), becomes progressively better defined with increasing deformation. This reveals that the main deformation mechanism is prismatic slip, together with basal slip [4,5,40,41]. At the largest strain level investigated (0.20, Fig. 5c and d) a new maximum appears at the edge of the (0 0 0 1) pole figure, denoting the presence of a larger volume fraction of tensile twins with increasing deformation. This is quite remarkable, as tensile twinning is not a favorable mechanism when testing along the RD. Furthermore, at this high strain, the grain size distribution is bimodal: fine recrystallized grains, approximately 2 μm in size, are embedded in a matrix of larger grains of about 8 μm in diameter. Recrystallized grains are mostly located inside twins or along grain boundaries. Inspection of the boundary map of 5d reveals, additionally, the formation of low to moderately misoriented boundaries within grains, due to dislocation interactions. Together, the stabilization of a deformation texture and the appearance of recrystallized grains mostly near twin or regular grain boundaries, suggest that the DRX mechanism predominant during tensile deformation of the AZ31 alloy along the RD is of a continuous nature, predominantly rotational DRX.

Fig. 6 depicts the microstructure and microtexture evolution corresponding to the sample deformed in compression along the ND up to strains of 0.07 (Fig. 6a), 0.095 (Fig. 6b) and 0.17 (Fig. 6c and d). The basal texture (⟨0 0 0 1⟩ axes parallel to the ND and, thus, to the loading axis) remains basically unchanged with increasing deformation. The values of the average grain sizes for the three strains investigated are 12 μm, 10 μm, and 11 μm, respectively. All these values are lower than the original grain size (13 μm). Since the planes where the EBSD measurements in Fig. 6 were taken are perpendicular to the compression axis, it is expected that, for pure geometrical reasons, in the absence of any recrystallization process, the average grain size along this plane should have increased with deformation. Specifically, it is estimated that the grain size should increase to ~14 μm after a strain of 0.17. Thus, the measured grain size decrease is a sign of the occurrence of DRX. The predominating DRX mechanisms can be evaluated by comparing in Fig. 7 the misorientation distribution histograms of the samples deformed up to

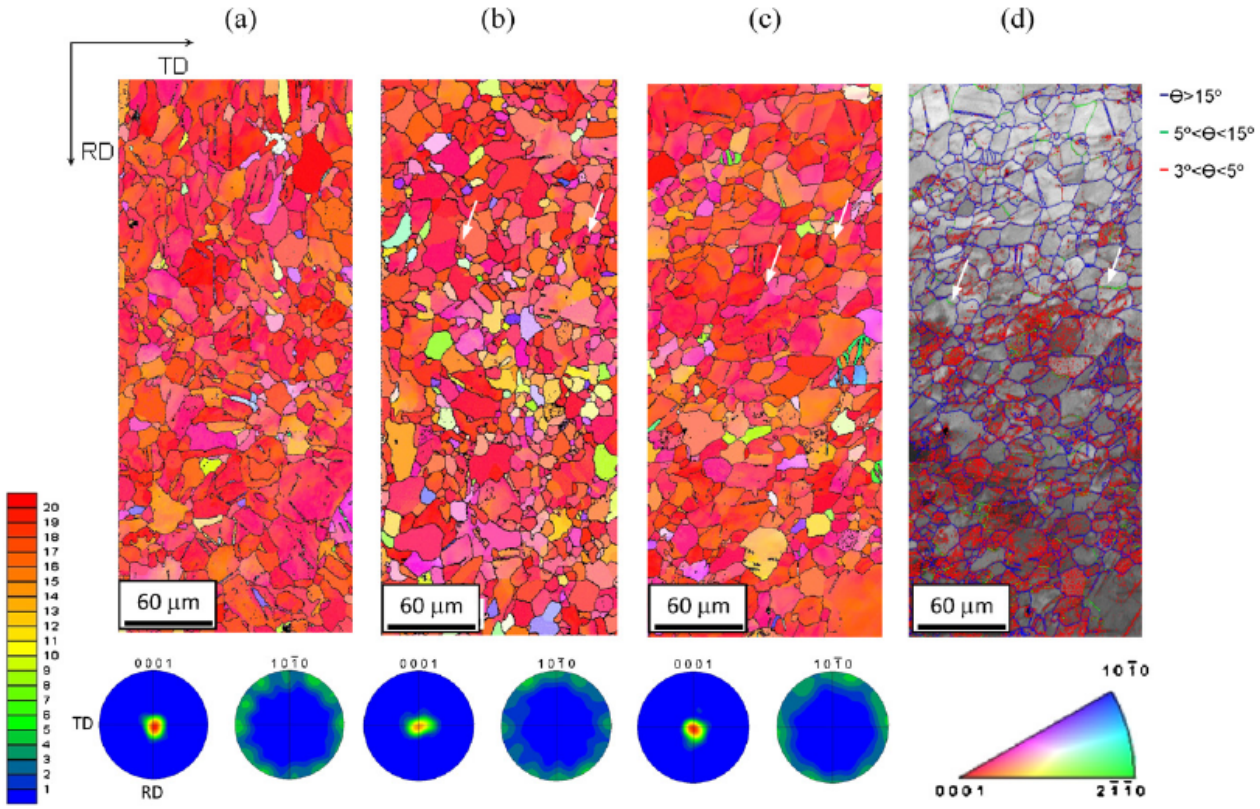

Fig. 6. EBSD inverse pole figure maps in the ND and microtextures corresponding to samples dynamically loaded at 250 °C in compression along ND up to strains of (a) 0.07, (b) 0.095, and (c) 0.17. (d) Boundary map corresponding to the sample strained up to 0.17. High angle boundaries (misorientation, $\theta > 15°$) are colored in blue, moderately misoriented boundaries ($5° < \theta < 15°$) in green and low angle boundaries ($3° < \theta < 5°$) in red. (For interpretation of the references to color in this figure legend, the reader is referred to the web version of the article.)

a strain of 0.095 and 0.17. The latter has a smaller fraction of boundaries with misorientations between 3° and 5°, but the fraction of boundaries in *all* the remaining misorientation ranges up to 60° is higher. This suggests that a combination of discontinuous DRX, which would justify the increase of high angle boundaries with $\theta > 15°–20°$, and grain subdivision by continuous DRX, which would explain increase in boundaries between 5° and ~15°–20° [42], is taking place. Some of the newly formed moderately misoriented boundaries have been highlighted in Fig. 6d with white arrows. A closer inspection of Fig. 6b–d reveals that a significant fraction of the original high angle boundaries become wavy as a consequence of local lattice rotations in those areas. In this figures it is also possible to notice small, recrystallized grains, completely surrounded by high angle boundaries, most likely resulting from a DDRX-type process. They have been pointed out using white arrows.

Altogether, the results described above suggest that the DRX predominating during uniaxial high strain rate deformation of the Mg AZ31 alloy at 250 °C depend on the relative orientation between the loading axis and the crystalline *c*-axes and, in turn, on the predominant deformation mechanisms. In particular, when twinning followed by pyramidal and basal slip are dominant (compression along the RD), recrystallization, mainly by DDRX, takes place readily, leading to a stage of zero hardening. When, on the contrary, prismatic and basal slip are active (tension along the RD), the material exhibits a high resistance to recrystallization and strong hardening. Finally, when pyramidal and basal slip are operative (compression along the ND), DDRX also takes place, in conjunction with CDRX. These differences can be also clearly observed by examining the KAM maps corresponding to samples deformed up to similar strains in compression along the RD (Fig. 8a), in tension along the RD (Fig. 8b), and in compression along the ND (Fig. 8c). It can be clearly noticed that, in the tension test, the dislocation density within grains is significantly higher than in the compression tests, which recrystallize more readily. The map of Fig. 8b provides further proof that the DRX mechanism during tension along the RD up to the measured strain is of a continuous nature, as the intragranular misorientation in the small, recrystallized grains that develop during deformation is also high. (And it should be significantly lower if these grains would have formed by DDRX).

4. Discussion

The results presented above reveal that there is a higher resistance to DRX when testing dynamically in tension along the RD than during compression along the RD and along the ND. These observations can be rationalized as follows.

The influence of texture on DRX at quasi-static rates has been analyzed in a few earlier studies. In a pioneering work on the subject, Kaibyshev et al. [16] reported that the kinetics of DRX in an hot-pressed MA14 Mg rod (Mg–Zn–Zr), with a typical prismatic fiber texture and deformed in compression at 300 °C and $2.8 \times 10^{-3}\ s^{-1}$, were dependent on the crystallographic texture. In particular, they observed that if the compression axis was parallel or perpendicular to the basal planes, DRX took place readily and an almost fully recrystallized structure was obtained at moderate strains. However, when the compression axis was tilted 45° with respect to the basal planes, DRX took place more slowly. In the former, the reported operative slip systems at the strain at which recrystallization started are prismatic, pyramidal ⟨a⟩ and

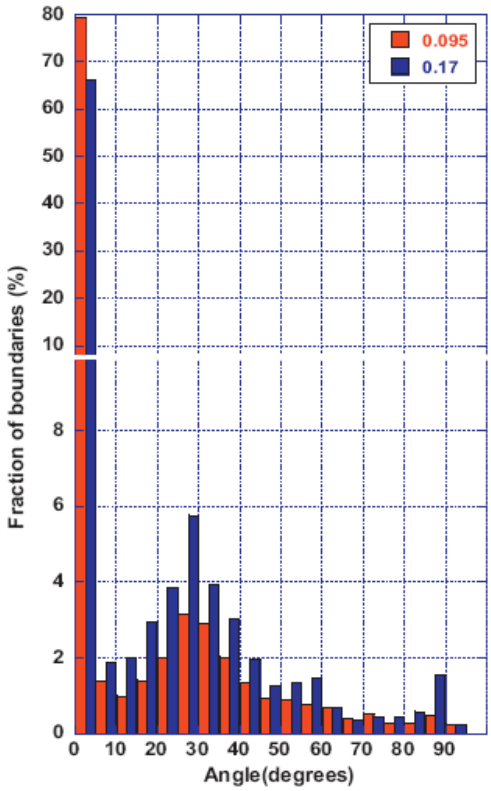

Fig. 7. Misorientation distribution histograms corresponding to the AZ31 sheet alloy compressed along ND at $10^3\,s^{-1}$ and 250 °C up to strains of 0.095 and 0.17.

basal. In the latter, only basal and prismatic slip are found to be active. Thus, Kaibyshev et al. [16] concluded that the kinetics of DRX were accelerated when all three main slip modes (basal, prismatic and pyramidal ⟨a⟩) are active. This, reportedly, is due to the fact that the operation of many slip modes favors the cross-slip of basal dislocations into non-basal planes. These non-basal dislocations have high stacking fault energies ($SFE_{basal} < 50\,mJ\,m^{-2}$; $SFE_{prismatic} = 354\,mJ\,m^{-2}$; $SFE_{pyramidal} = 452\,mJ\,m^{-2}$ [43,44]) and, thus, can easily climb and arrange into new boundaries by the Friedel–Escaig mechanism. Del Valle et al. [19] also observed an enhancement of DRX in AZ31 samples oriented for multiple slip versus others initially oriented only for single (basal) slip. Finally, Barnett [29] reported a delay in DRX in an AZ31 sheet deformed in plane strain under conditions in which prismatic slip would predominate versus others in which ⟨c + a⟩ and basal slip are operative.

Our results at dynamic rates are consistent with the above observations at quasi-static rates and also support the fact that the kinetics of DRX is related to the operative deformation mechanisms. In particular, we observe a higher resistance to recrystallization when prismatic slip and basal slip operate (tension along the RD) than when a combination of ⟨c + a⟩ and basal slip are active (compression along the ND). This can be understood taking into account that pyramidal slip has more independent systems (5) than prismatic slip (2), and that the SFE of pyramidal dislocations is also significantly higher. Together, these two factors favor the occurrence of cross-slip and climb when pyramidal slip is active. We have also observed that the most favorable conditions for DRX at high strain rates are reached during compression along the RD, when extensive tensile twinning is followed by a combination of basal and pyramidal ⟨c + a⟩ slip. Under these conditions DRX takes place homogeneously throughout the microstructure, the final grain size is smaller and the strain hardening is lower than when compressing

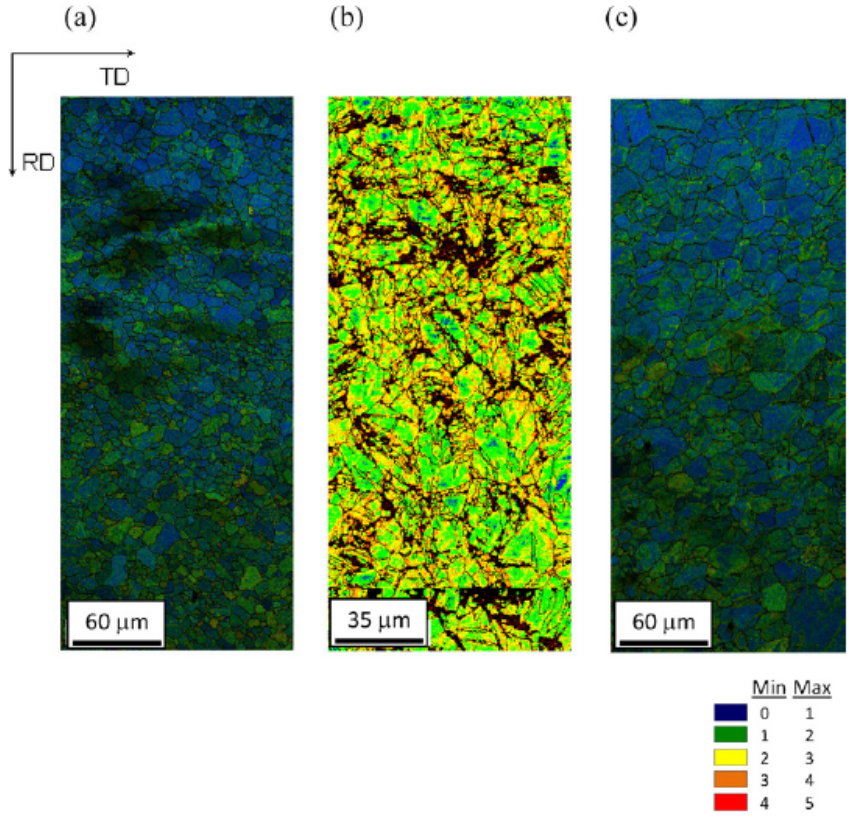

Fig. 8. Kernel average misorientation (KAM) map corresponding to the AZ31 alloy deformed (a) in compression along RD up to a strain of 0.15, (b) in tension along RD up to a strain of 0.20 and (c) in compression along ND up to a strain of 0.17.

along the ND, where only basal and pyramidal ⟨c+a⟩ slip operate from the first stages of deformation. Thus, our results suggest that the operation of twinning during high temperature deformation at dynamic rates in the AZ31 alloy enhances DRX. The beneficial effect of twinning on DRX in Mg alloys as has been observed previously under quasi-static conditions [e.g. 45–49] and it has been attributed to the large stresses accumulated close to twin boundaries, which promote the operation of multiple slip modes.

Fig. 1 reveals that DRX takes place more easily at quasi-static than at dynamic strain rates, resulting in a much more pronounced softening. This may be explained by the easiness of diffusion at low strain rates, as well as by the more pronounced decrease of the CRSS of ⟨c+a⟩ slip with temperature under such conditions [5]. Thus, for example, at 250 °C and 10^{-3} s^{-1}, it is expected that prismatic, ⟨c+a⟩ and basal slip operate, giving rise to the onset of recrystallization. However, at that same temperature and dynamic rates, the CRSS of pyramidal slip is still significantly higher than that of prismatic slip, and therefore only the latter and basal slip are active, resulting in a strong resistance to DRX, as is observed in the current study.

5. Conclusions

The recrystallization mechanisms operative during dynamic deformation of an AZ31 sheet alloy at 250 °C have been investigated as a function of the loading mode and the crystallographic texture. The as-received rolled and annealed sheet, with a typical strong basal texture, has been tested at 10^3 s^{-1} in compression along the RD, in tension along the RD and in compression along the ND. The following conclusions have been drawn from the present study:

1. The DRX mechanisms and kinetics depend on the operative deformation mechanisms and thus vary for different loading modes (tension, compression) as well as for different relative orientations between the loading axis and the c-axes of the grains.
2. The highest resistance to dynamic recrystallization was found when the material was tested in tension along the RD. In this case, in which both prismatic and basal slip operate, the work hardening rate was higher than in the compression tests. Some recrystallized grains do appear at the latest stages of deformation ($\varepsilon \sim 0.20$) as a result of rotational dynamic recrystallization (RDRX). DRX took place more readily under compression along the RD, when twinning, ⟨c+a⟩ and basal slip operate. Recrystallization results in a stage of zero hardening rate. The main recrystallization mechanism is DDRX.
3. DRX at dynamic rates is enhanced by the operation of ⟨c+a⟩ slip, as the existence of a large number of independent systems and the high stacking fault energy of pyramidal dislocations favor cross-slip and climb and, thus, the formation of new high angle boundaries. DRX is also promoted by twinning.

Acknowledgements

The authors would like to thank the vehicle interior manufacturer, Grupo Antolin Ingeniería, S.A., within the framework of the project MAGNO2008-1028-CENIT funded by the Spanish Ministry of Science and Innovation. Funding from the Basque Government through the Manufacturing 0,0 project (within the Etortek Programme) is acknowledged. Assistance from María Jesús Pérez (UPM, Madrid) and Jesús Reales (CENIM, Madrid) with the mechanical testing and from Yu Kyung Shin and V. Kree (HZG, Germany) with the EBSD analysis was appreciated.

References

[1] M. Easton, A. Beer, M. Barnett, C. Davies, G. Dunlop, Y. Durandet, S. Blacket, T. Hilditch, P. Beggs, JOM 60 (2008) 57.
[2] B.L. Mordike, T. Ebert, Mater. Sci. Eng. 302 (2001) 37.
[3] M. Bamberger, G. Dehm, Annu. Rev. Mater. Res. 38 (2008) 505.
[4] S.R. Agnew, Ö. Duygulu, Int. J. Plasticity 21 (2005) 1161.
[5] I. Ulacia, N.V. Dudamell, F. Gálvez, S. Yi, M.T. Pérez-Prado, I. Hurtado, Acta Mater. 58 (2010) 2988.
[6] T. Al-Samman, X. Li, S.G. Chowdury, Mater. Sci. Eng. A 527 (2010) 3450.
[7] A. Chapuis, J.H. Driver, Acta Mater. 59 (2011) 1986.
[8] S.B. Yi, J. Bohlen, F. Heinemann, D. Letzig, Acta Mater. 58 (2010) 592.
[9] M.R. Barnett, Metall. Mater. Trans. 34 (2003) 1799.
[10] N. Stanford, K. Sotoudeh, P.S. Bate, Acta Mater. 59 (2011) 4866.
[11] A.S. Khan, A. Pandey, T. Gnäupel-Herold, R.K. Mishra, Int. J. Plasticity 27 (2011) 688.
[12] B. Hutchinson, M.R. Barnett, A. Ghaderi, P. Cizek, I. Sabirov, Int. J. Mater. Res. 100 (2009) 556.
[13] J.A. Del Valle, O.A. Ruano, Acta Mater. 55 (2007) 455.
[14] S.E. Ion, F.J. Humphreys, S.H. White, Acta Metall. 30 (1982) 1909.
[15] R.O. Kaibyshev, A.M. Galiyev, B.K. Sokolov, Phys. Met. Metallogr. 78 (1994) 209.
[16] R.O. Kaibyshev, B.K. Sokolov, A.M. Galiyev, Texture. Microstruct. 32 (1999) 47.
[17] M.M. Myshlyaev, H.J. McQueen, A. Mwembela, E. Konopleva, Mater. Sci. Eng. A 337 (2002) 121.
[18] J.C. Tan, M.J. Tan, Mater. Sci. Eng. A 339 (2003) 124.
[19] J.A. Del Valle, M.T. Pérez-Prado, O.A. Ruano, Mater. Sci. Eng. A 355 (2003) 68.
[20] M.R. Barnett, A.G. Beer, D. Atwell, A. Oudin, Scr. Mater. 51 (2004) 19.
[21] S.B. Yi, S. Zaefferer, H.G. Brokmeier, Mater. Sci. Eng. A 424 (2006) 275.
[22] T. Al-Samman, G. Gottstein, Mater. Sci. Eng. A 490 (2008) 411.
[23] J.A. Del Valle, O.A. Ruano, Mater. Sci. Eng. A 487 (2008) 473.
[24] E. Martin, J.J. Jonas, Acta Mater. 58 (2010) 4253.
[25] D.K. Sun, C.P. Chang, P.W. Kao, Mater. Sci. Eng. A 527 (2010) 7050.
[26] Z. Liu, S. Bai, S. Kang, Scr. Mater. 60 (2009) 403.
[27] R.D. Doherty, D.A. Hughes, F.J. Humphreys, J.J. Jonas, D. Juul Jensen, M.E. Kassner, W.E. King, T.R. McNelley, H.J. McQueen, A.D. Rollett, Mater. Sci. Eng. A 238 (1997) 219.
[28] F.J. Humphreys, M. Hatherly, Recrystallization and Related Annealing Phenomena, Pergamon, 1995.
[29] M.R. Barnett, J. Light Met. 1 (2001) 11.
[30] K. Ishikawa, H. Watanabe, T. Mukai, Mater. Lett. 59 (2005) 1511.
[31] K. Ishikawa, H. Watanabe, T. Mukai, J. Mater. Sci. 40 (2005) 1577.
[32] H. Watanabe, K. Ishikawa, Mater. Sci. Eng. 523 (2009) 304.
[33] I. Ulacia, C.P. Salisbury, I. Hurtado, M.J. Worswick, J. Mater. Proc. Technol. 211 (2011) 830.
[34] E. El-Magd, M. Abouridouane, J. Phys. IV France 110 (2003) 15.
[35] L.E. Murr, C. Pizaña, Metall. Trans. A 38 (2007) 2611.
[36] D.L. Zou, L. Zhen, Y. Zhu, C.Y. Xu, W.Z. Shao, B.J. Pang, Mater. Sci. Eng. 527 (2010) 3323.
[37] M. Knezevic, A. Levinson, R. Harris, R.K. Mishra, R.D. Doherty, S.R. Kalidindi, Acta Mater. 58 (2010) 6230.
[38] N.V. Dudamell, I. Ulacia, F. Gálvez, S.B. Yi, J. Bohlen, D. Letzig, I. Hurtado, M.T. Pérez-Prado, Acta Mater. 59 (2011) 6949.
[39] A. Fernández, M.T. Pérez-Prado, Y. Wei, A. Jérusalem, Int. J. Plasticity 27 (2011) 1739.
[40] H. Wang, B. Raeisinia, P.D. Wu, S.R. Agnew, C.N. Tome, Int. J. Sol. Struct. 47 (2010) 2905.
[41] Y.B. Chun, C.H.J. Davies, Mater. Sci. Eng. 528 (2011) 3489.
[42] M. Cabibbo, W. Blum, E. Evangelista, M.E. Kassner, M.A. Meyers, Metall. Trans. 39 (2008) 181.
[43] L. Wen, P. Chen, Z.F. Tong, B.Y. Tang, L.M. Peng, W.J. Ding, Eur. Phys. J. B 72 (2009) 397.
[44] A.E. Smith, Surf. Sci. 601 (2007) 5762.
[45] S.B. Yi, I. Schestakow, S. Zaefferer, Mater. Sci. Eng. 516 (2009) 58.
[46] S.Q. Zhu, H.G. Yan, J.H. Chen, Y.Z. Wu, J.Z. Liu, J. Tian, Scr. Mater. 63 (2010) 985.
[47] O. Sitdikov, R. Kaibyshev, T. Sakai, Mater. Sci. Forum 419/422 (2003) 521–526.
[48] O. Sitdikov, R. Kaibyshev, Mater. Trans. 42 (2001) 1928.
[49] A. Galiyev, R. Kaibyshev, G. Gottstein, Acta Mater. 49 (2001) 1199.

PART IV

COMPLEMENTARY STUDIES

4.1. COMPLEMENTARY STUDY I

4.1. *Complementary study I. Mechanical behavior at quasi-static and dynamic rates of a magnesium alloy containing neodymium.*

4.1.1. Introduction.

In this chapter the mechanical behavior of an extruded Mg-1%wtMn-1%wtNd (MN11) alloy during deformation at temperatures ranging from 25°C to 400°C at both quasi-static and dynamic rates is analyzed. Tests are performed along two perpendicular directions in order to evaluate the mechanical anisotropy. The evolution of the microstructure and the texture during deformation is investigated with the aim of elucidating the predominant deformation and recrystallization mechanisms. The behavior of this MN11 alloy is compared throughout the text to that of conventional Mg alloys, such as AZ31.

4.1.2. Materials and Experimental Procedure.

4.1.2.1. Material: initial microstructure.

The material under study is an extruded bar of alloy MN11 (Mg-1%wtMn-0.94%wtNd) fabricated in the Magnesium Innovation Center (MagIC) of the Helmholtz Zemtrum Geesthacht (Germany). The alloy was first gravity cast in order to produce billets for extrusion which were machined up to a diameter of 93 mm. Secondly and before extrusion, the billets were homogenized at 350 ºC during 15 h. Then, indirect extrusion was performed at 300 ºC to fabricate round bars of 17 mm of diameter, which corresponds to an extrusion ratio of 1:30. The extrusion speed used was of 10 m/min. The initial microstructure of the MN11 extruded bar is formed by equiaxed grains with average sizes of 10 µm and a very weak texture. Further considerations about the MN11 alloy can be found in [95].

4.1.2.2. Mechanical testing.

High strain rate tests ($\dot{\varepsilon} \sim 10^3 s^{-1}$) were carried out in compression with the loading axis parallel (PL) and perpendicular (PP) to the extrusion axis (EA) and in tension parallel to the EA. Compression tests were performed in 3x3x4.5 mm^3 prisms with the long axis parallel and perpendicular to the extrusion direction. Tensile tests along ED were performed in dog-bone shaped specimens with a gage length of 12 mm and a width of 4 mm. A Split Hopkinson Pressure Bar (SHPB) machine, provided with a radiant furnace and a high speed camera, was used to carry out these compression dynamic tests. Two nickel superalloy (RENE-41) bars, 1 m in length and 19.3 (incident bar) and 10 (output bar) mm in diameter were machined for this purpose. The compression tests were performed at temperatures ranging from 25ºC (RT) up to 400ºC, at intervals of 50 ºC, until failure and also up to several intermediate strains in order to observe the microstructure and texture evolution of the MN11 alloy with increasing strain level and temperature. With that purpose, the specimens were dynamically loaded to a predefined strain level using a stop-ring technique which restricts the movement of the incident bar (pushed by the impact of the striker bar or projectile) toward the sample. Ring stoppers of specific thickness were machined out of F522 steel. These rings were quenched and tempered in order to have a maximum control of the strain level achieved.

A Split Hopkinson Tension Bar (SHTB) machine, provided with the same radiant furnace and the same high speed camera, was used to carry out tensile dynamic tests. The incident bar used in tensile tests consisted of two parts. The first one, made of steel with 20 mm of diameter and 4100 mm of length and upon which the projectile slide inside the barrel. The second part of the incident bar is located outside the barrel and it is made of RENE-41 with 19.3 mm of diameter and 3850 mm of length.

Both parts were attached with a threaded link. Output bar was made of RENE-41 with 19.3 mm of diameter and 3850 mm of length. In tension the MN11 alloy was tested until failure at room temperature (RT), 200 ºC and 300ºC. Tests were not carried out at 400ºC because it was observed that at this temperature samples crept, i.e. they deformed before the application of an external load.

Quasi-static tests at room temperature (RT), 200ºC and 400ºC and at strain rates of $5x10^{-4}$ s^{-1}, $5x10^{-3}$ s^{-1}, and $5x10^{-2}$ s^{-1} were also carried out in compression until failure with the loading axis parallel and perpendicular to the ED in order to compare the variations in the microstructural evolution with the strain rate. Tests at 400ºC were stopped once a true strain of 0.4 was reached. All quasi-static tests were performed in a conventional universal testing machine (Instron) using the same geometries for the compression specimens described above. Two tests were carried out for each condition.

4.1.2.3. Microstructure examination.

Optical microscopy (OM) was utilized for microstructural examination of selected samples. Surface preparation for OM included grinding with increasingly finer SiC papers, several diamond polishing steps, and surface finishing using a colloidal silica solution. The specimens prepared were additionally chemically etched during 15 s with a solution of 50 ml of ethanol, 0.5 g of picric acid, 0.5 ml of acetic acid, and 1 ml of distilled water.

The microstructure and the microtexture of the samples compressed parallel to the EA and tensile tested along the EA were, additionally, analyzed by electron backscatter diffraction (EBSD) using the TSL-OIM™ software in a Zeiss Ultra 55™ FEG-SEM. Sample preparation for EBSD included grinding with 4000 SiC paper, mechanical polishing

with a 0.05 μm silica suspension and final electro-chemical polishing for 90 s at 33 V using the AC2™ commercial electrolyte at -20ºC approximately. The microstructure is represented by EBSD orientation maps showing the orientation of the EA and the texture by pole figures recalculated from the EBSD orientation data. Additionally, the grain size of various samples was calculated by the linear intercept method in the EBSD orientation maps using only high angle boundaries (misorientations higher than 15°).

The macrotexture of some samples was also measured by the Schulz reflection method in a Philips X´pert-Pro Panalytical X-ray diffractometer furnished with a PW3050/60 goniometer, located at the CAI X-ray Diffraction of the Complutense University in Madrid, Spain. The radiation used was β-filtered Cu Kα. The surface area examined was about 2mm^2. The polar angle ranged from 0° to 75° in steps of 3°. Irradiation time at each step was 2 s. The measured incomplete pole figures were corrected for background and defocusing using the Philips X´pert software. The orientation distribution function (ODF) and the complete pole figures were calculated using the MTex software [124]. Sample preparation for texture measurement included grinding with increasingly finer SiC papers, whose grit size ranged from 320 to 2000.

4.1.3. Results and Discussion.

4.1.3.1. As-extruded and heat treated material.

Figure 4.1 illustrates the microstructure and the texture of the as-extruded MN11 bar. The grain structure is homogeneous and grains are mostly equiaxed, with an average size of 10 μm. The texture, as described previously [95], is significantly weaker than that characteristic of wrought conventional Mg alloys, such as AZ31, but not random. There is a slight tendency for the extrusion axes to cluster

around directions tilted away from the $\langle 10\bar{1}0\rangle$-$\langle 11\bar{2}0\rangle$ boundary of the inverse stereographic triangle.

This texture has been termed “RE texture” [86-99]. Figure 4.2 shows the effect of heat treatments on the microstructure and the texture of the MN11 alloy. In particular, the material was treated at 200°C (Figs. 4.2 a,b) and 400°C (Figs. 4.2 c,d) for 1 h, as this is the time it takes approximately to stabilize the temperature before mechanical tests. In both cases the grain size remains equal to approximately 10 μm. The texture after annealing is still weak and the tilt angle between the extrusion axes and the $\langle 10\bar{1}0\rangle$-$\langle 11\bar{2}0\rangle$ boundary of the inverse stereographic triangle seems to increase slightly.

4.1.3.2. Mechanical behavior at quasi-static rates.

The stress-strain curves corresponding to the MN11 alloy tested in compression at room temperature, 200°C, and 400°C under quasi-static rates ($5x10^{-4}$ s^{-1}, $5x10^{-3}$ s^{-1}, and $5x10^{-2}$ s^{-1}) are depicted in Figs. 4.3 a-f. Tests were performed both along a direction parallel to the EA (PL samples) (Figs. 4.3 a,c,e) as well as in a direction perpendicular to it (PP samples) (Figs. 4.3 b,d,f). Two tests were carried out for each temperature and both stress-strain curves are plotted in Fig. 4.3. Table 4.1 summarizes the yield stresses corresponding to the different tests.

A) Room temperature.

The “concave-up” shape of the curves at room temperature suggests that tensile twinning plays a major role during the first stages of deformation [33]. It is remarkable that, despite the weakness of the initial texture of the MN11 alloy, these curves resemble those corresponding to conventional rolled Mg alloys compressed along the rolling direction (RD) or to conventional extruded alloys compressed

along the EA, where twinning plays a major role at strains smaller than 0.06. Since the texture of the initial material is weak, it can be unambiguously stated that basal slip will also have a contribution to strain.

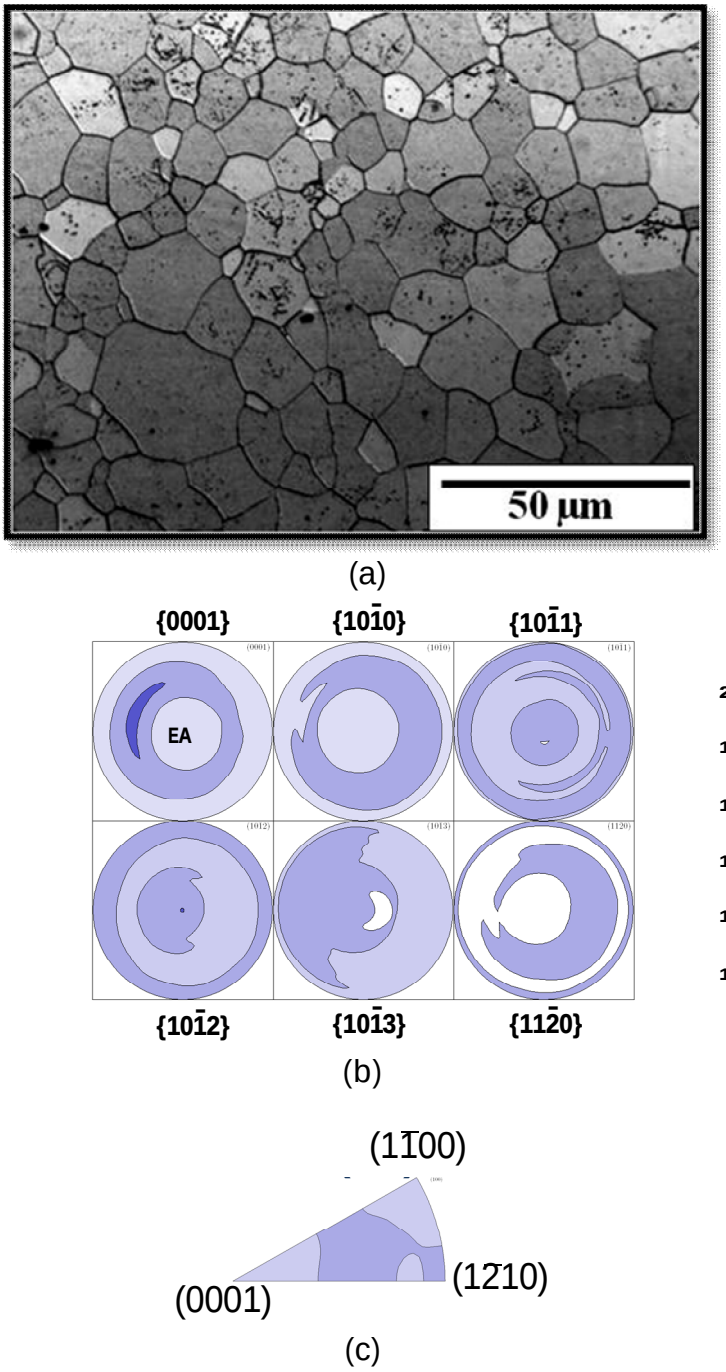

Figure 4.1. Microstructure and texture of the as-extruded MN11 bar. (a) Micrograph obtained by optical microscopy, (b) X-ray pole figures and (c) X-ray inverse pole figure showing the orientation of the extrusion axis (EA). The plane of observation is perpendicular to the extrusion axis (EA).

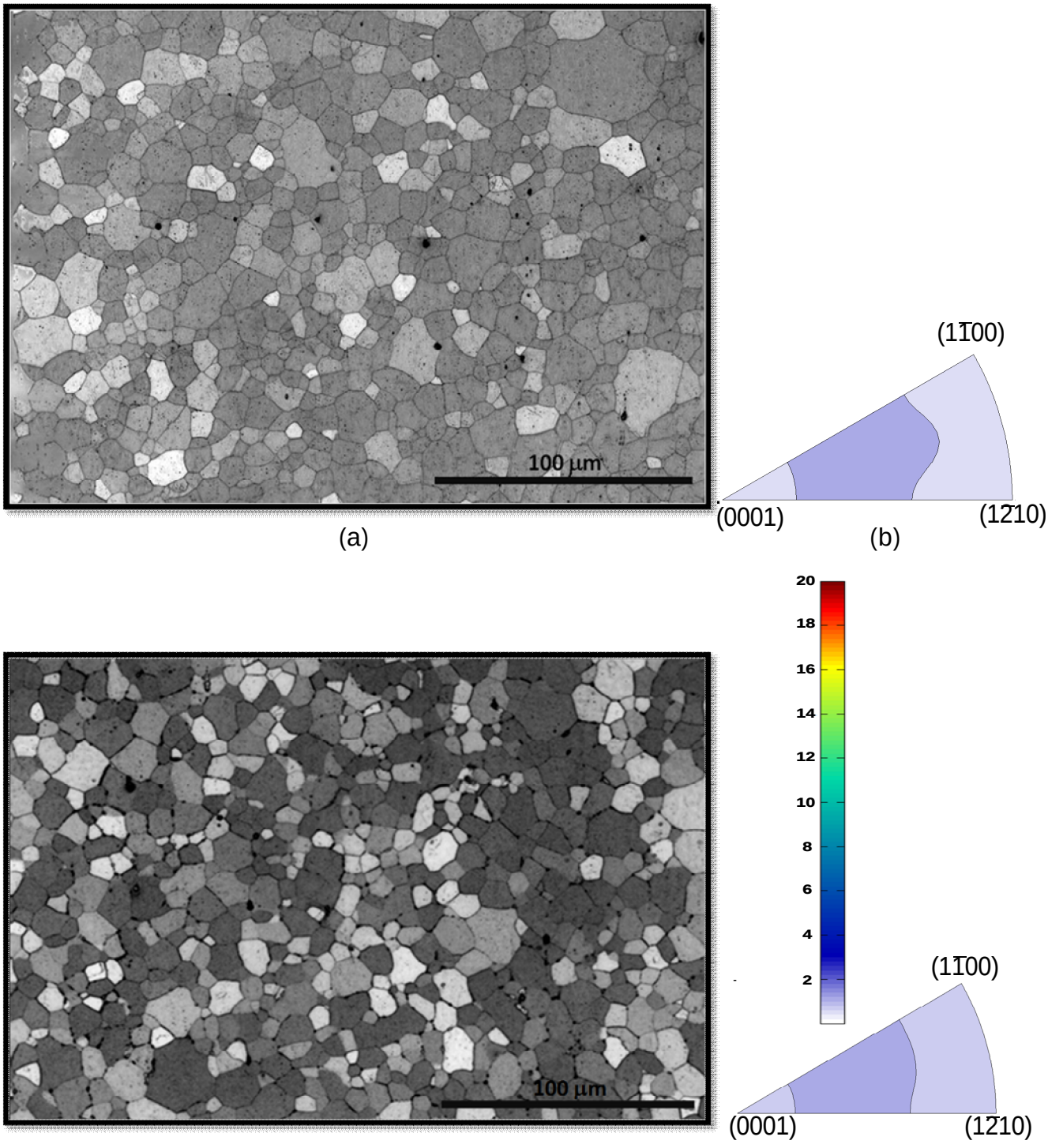

Figure 4.2. Effect of heat treatment on the microstructure and the texture: (a,b) 200 ºC, 1h; (c,d) 400 ºC, 1h. Both samples where heated at 10ºC/min up to the corresponding heat treatment temperature.

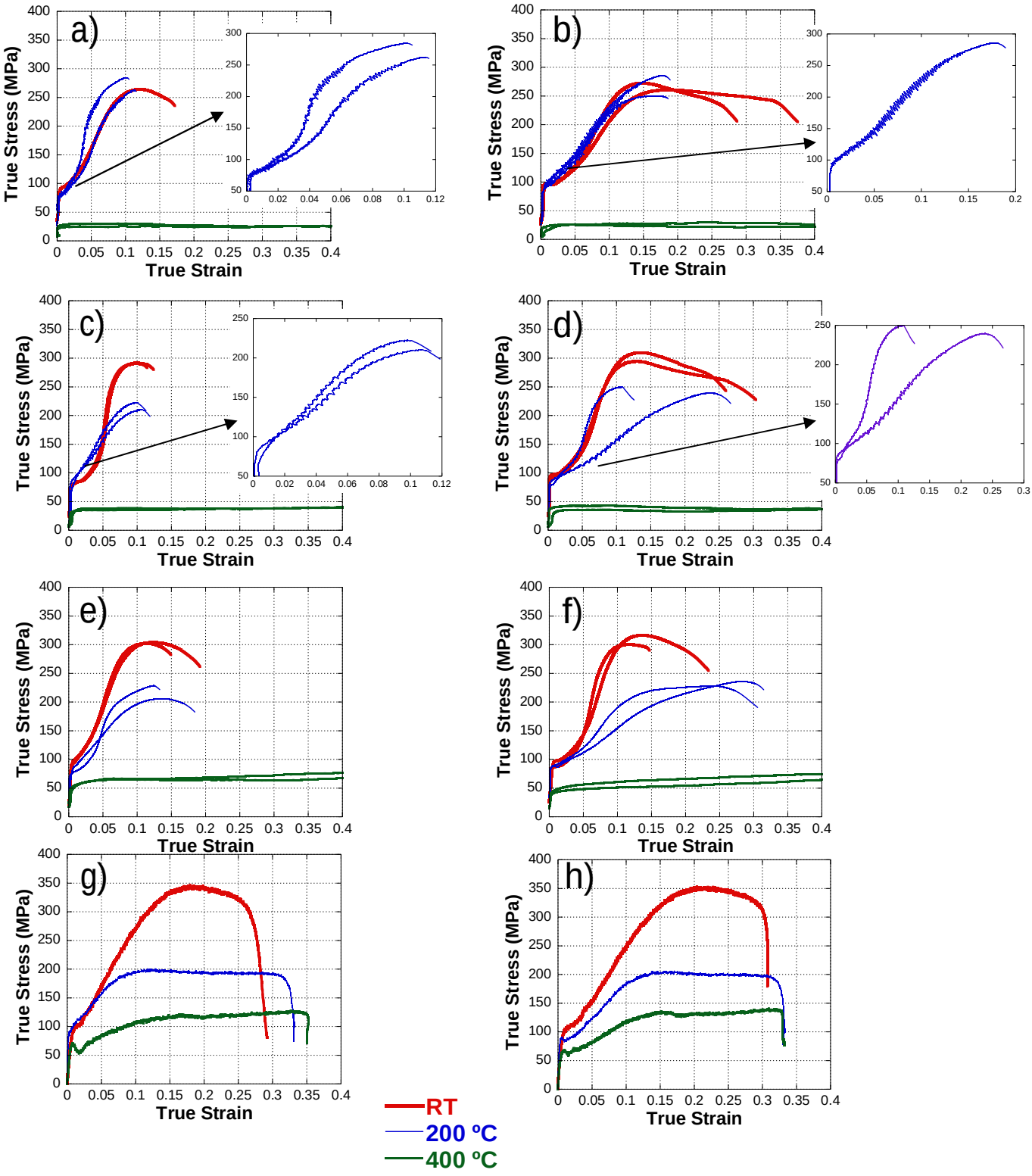

Figure 4.3. Stress-strain curves corresponding to the MN11 alloy deformed in compression at room temperature, 200 ºC and 400 ºC at: (a) $5x10^{-4}$ s^{-1} along the EA, (b) $5x10^{-4}$ s^{-1} perpendicular to the EA, (c) $5x10^{-3}$ s^{-1} along the EA, (d) $5x10^{-3}$ s^{-1} perpendicular to the EA, (e) $5x10^{-2}$ s^{-1} along the EA, (f) $5x10^{-2}$ s^{-1} perpendicular to the EA, (g) 10^{3} s^{-1} along the EA, and (h) 10^{3} s^{-1} perpendicular to the EA.

Table 4.1. Average yield stress values (in MPa). (a) Quasi-static deformation; (b) dynamic deformation.

(a)

	Compression								
	$5x10^{-4}$ s^{-1}			$5x10^{-3}$ s^{-1}			$5x10^{-2}$ s^{-1}		
	RT	**200ºC**	**400ºC**	**RT**	**200ºC**	**400ºC**	**RT**	**200ºC**	**400ºC**
PL	93	81	25	75	87	35	97	82	56
PP	95	91	22	95.5	85	36	92	88	43

(b)

	Compression 10^3 s^{-1}			Tension 10^3 s^{-1}		
	RT	**200ºC**	**400ºC**	**RT**	**200ºC**	**300ºC**
PL	100	99	56	134	134	134
PP	104	86	66			

Significant differences exist between PL and PP tests, particularly at the two lowest strain rates. In particular, in PL tests the strain hardening is larger and the ductility is smaller. These observations may be explained taking into account that, due to the RE texture present in the as-received MN11 alloy, the incidence of twinning is smaller in PP tests.

Figure 4.4 illustrates two inverse pole figures showing the orientation of the compression axis in two different PP tests (i.e., it shows the orientation of two radial directions, <R1> and <R2>, of the extruded bar). First, it can be seen that the orientation of the compression axis is not the same for all radial directions. This would explain the scatter in ductility values observed in PP tests (figure 4.5). Second, the fraction of orientations in the region close to the $\langle 10\bar{1}0\rangle$-$\langle 11\bar{2}0\rangle$ boundary of the stereographic triangles is smaller than in the PL case (figure 4.1 c). This effect is more pronounced in the <R2> direction. Thus, the likelihood of twinning in PP tests is smaller than in PL ones. This is consistent with the lower strain hardening rate observed in the first stages of deformation in PP tests, which is usually attributed to slip/twin and

twin/twin interactions [125]. Consequently, a higher activation of basal slip would justify the higher ductility observed. The differences between PL and PP test are less noticeable at $5x10^{-2}$ s^{-1}, probably because, as the strain rate increases, twinning is enhanced and it takes place in grains with lower Schmid factors, and thus the texture differences become less significant.

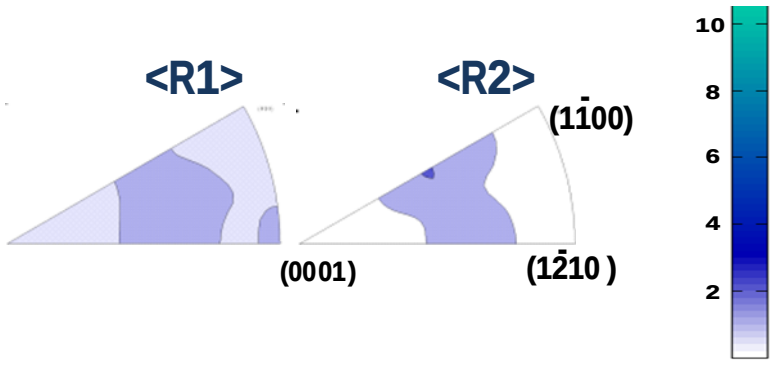

Figure 4.4. Inverse pole figures showing the orientation of two radial directions of the as-received extruded bar of MN11. The two directions have been labeled <R1> and <R2>. Both are perpendicular to the EA.

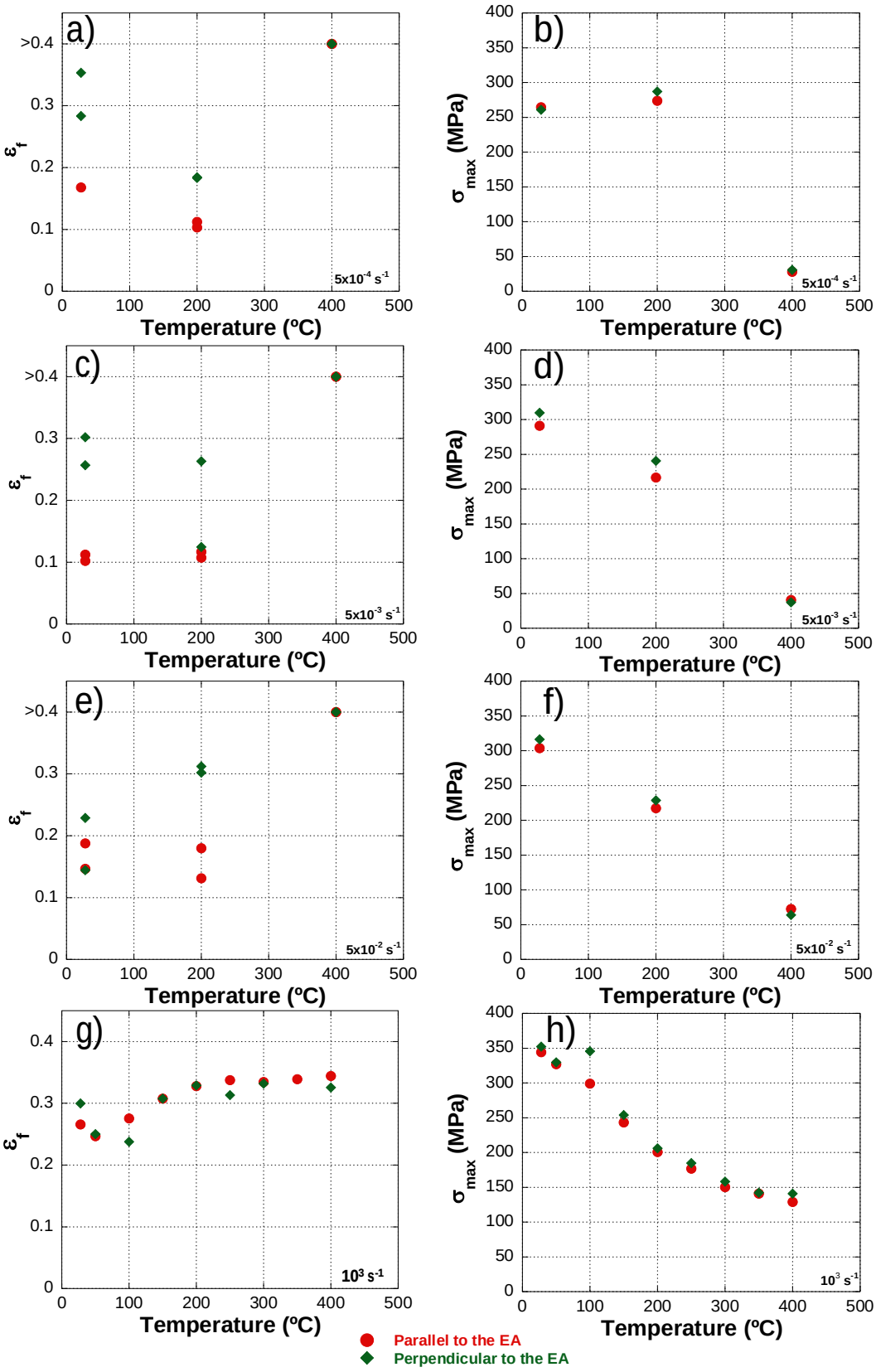

Figure 4.5. Evolution of the strain to failure (ε_f) and the maximum flow stress (σ_{max}) with temperature at different strain rates: a), b) 5x10^{-4} s^{-1}; c),d) 5x10^{-3} s^{-1}; e),f) 5x10^{-2} s^{-1}, g),h) 10^{3} s^{-1}.

B) Elevated temperature.

The variation with temperature of the strain to failure (ε_f) and the maximum strength (σ_{max}) corresponding to all the quasi-static tests are summarized in figure 4.5. As expected, σ_{max} decreases with increasing temperature. No significant scatter in σ_{max} values was observed in the two tests carried out at each temperature and strain rate.

Figures 4.3 and 4.5 suggest that the MN11 alloy presents many manifestations of dynamic strain aging (DSA) [126] at strain rates of $5x10^{-4}$ s^{-1} and $5x10^{-3}$ s^{-1} and at 200°C (named hereafter "DSA" conditions). First, serrations are visible in the stress-strain curves (figures 4.3a-d). Second, the strain rate sensitivity, m, calculated at a strain of 0.1, adopts negative values (Table 4.2). Third, the strain to failure goes through a minimum (Fig. 4.5). Fourth, a larger strain hardening rate is observed at the lowest strain rate (compare Figs. 4.3a and 4.3c). This increased strain hardening rate cannot be related to a higher incidence of twinning, as this mechanism is less frequent as strain rate decreases. The appearance in the MN11 alloy of all the above DSA characteristics reveals a strong interaction between Nd atoms and dislocations.

DSA has been recently reported in Mg alloys with Ce and Gd additions at similar temperatures [97,100]. In these studies, however, not all the DSA characteristics were observed (for example, a decrease in ductility was not reported and serrations were occasionally not visible) and this was attributed to a masking effect of twinning and dynamic recrystallization. In agreement with these reports, DSA characteristics in the MN11 alloy are, in general, slightly less pronounced in PL tests than in PP tests. For example, serrations of larger amplitude and a more pronounced ductility decrease can be noted in figures 4.3b than in

figures 4.3a. Also, a close look at the two curves at 200°C of figures 4.3d reveals that the amplitude of serrations is smaller in the curve with a more "concave-up" shape (and, thus, where twinning plays a more important role). At $5x10^{-2}$ s^{-1} and 200°C the signs of DSA disappear, probably because the waiting time of dislocations at obstacles decreases and solute atoms are no longer able to diffuse fast enough to form atmospheres around them. Compared to the tests at room temperature at the same strain rate ($5x10^{-2}$ s^{-1}), differences in PL and PP tests become more noticeable because the overall incidence of twinning decreases with temperature and, thus, the existing texture differences have an impact in the activation of this mechanism.

Table 4.2. Strain rate sensitivity (m) values corresponding to the different quasi-static testing conditions investigated. Note: In the PP tests, the stress values utilized for the calculation of m are the average values between the two tests performed at each temperature.

	RT		**200°C**		**400°C**	
	$\frac{5x10^{-4}s^{-1}}{5x10^{-3}s^{-1}}$	$\frac{5x10^{-3}s^{-1}}{5x10^{-2}s^{-1}}$	$\frac{5x10^{-4}s^{-1}}{5x10^{-3}s^{-1}}$	$\frac{5x10^{-3}s^{-1}}{5x10^{-2}s^{-1}}$	$\frac{5x10^{-4}s^{-1}}{5x10^{-3}s^{-1}}$	$\frac{5x10^{-3}s^{-1}}{5x10^{-2}s^{-1}}$
PL	0.05	0.015	-0.10	-0.08	0.20	0.20
PP	0.07	0.03	0	-0.06	0.18	0.18

At 400°C the shape of the stress-strain curves is "concave-down" due to the predominance of crystallographic slip. ε_f increases dramatically and tests were stopped at a strain of 0.4. The yield strength increases with increasing strain rate.

4.1.3.3. Mechanical behavior at dynamic rates.

The stress-strain curves corresponding to the MN11 alloy tested in compression at room temperature, 200°C, and 400°C under dynamic conditions (10^3 s^{-1}), both parallel and perpendicular to the EA, are

depicted in figures 4.3g and 4.3h. The values of the stress at a strain of 0.005 ($\sigma_{0.005}$) are summarized in Table 4.1. In dynamic tests it is difficult to measure the true yield stress at the nominal strain rate, since in the early stages of deformation the strain rate increases gradually. Thus, $\sigma_{0.005}$ is used in the present study as a best approximation to this material property.

The shape of the compression stress-strain curves have still a “concave-up” shape, but this shape is significantly less pronounced than at lower strain rates. This is surprising, as it is known that tensile twinning is enhanced in Mg alloys deformed under impact loading at temperatures up to 400°C [56-58,117]. The strain to failure increases slightly with temperature from about 0.27 at RT up to 0.33 at 400°C. The maximum flow stress (σ_{max}) values decrease with increasing temperature. No significant differences were found between the ductility and the maximum flow stress in PL and PP tests at these high strain rates (figures 4.5g and 4.5h). At RT and 200°C the strain to failure in compression is equal or higher under impact loading than at lower strain rates. A yield point effect is observed in the dynamic compression tests at 400°C, probably caused by the migration of solute atoms to dislocation cores during the temperature stabilization treatment prior to testing. Figure 4.6 illustrates the tension stress-strain curves corresponding to tests carried out under dynamic conditions at RT, 200 °C and 300°C. The shape of the curves is now “concave-down”, consistent with the predominance of crystallographic slip during the first stages of deformation. A yield point effect is observed during compression at 400°C and during tension at 300°C, revealing, again, the strong interaction between RE atoms and dislocations.

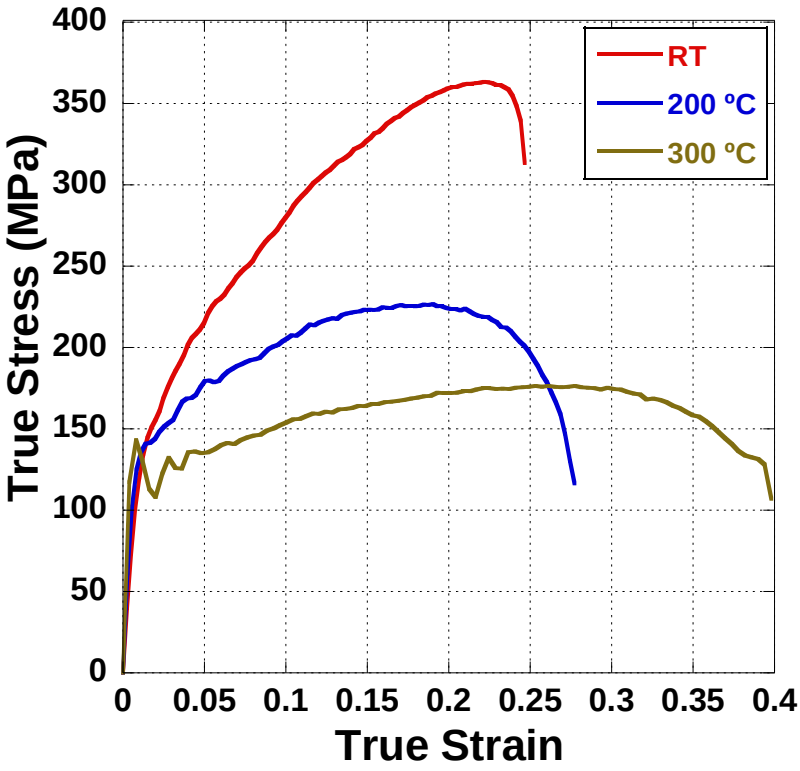

Figure 4.6. Stress-strain curves corresponding to the MN11 alloy deformed in tension parallel to the extrusion axis (EA) at high strain rate at room temperature, 200 ºC and 300 ºC.

4.1.3.4. Microstructural evolution under quasi-static and dynamic conditions.

Figures 4.7, 4.8 and 4.9 depict the microtexture of the MN11 alloy deformed in compression at $5x10^{-3}$ s^{-1} at RT, 200 °C and 400°C (PL samples). At the two lowest temperatures the c-axes tend to align with the EA. This texture is consistent with the occurrence of tensile twinning and basal slip [127]. The appearance of the six-fold symmetry in the prismatic pole figures reveals further the large incidence of twinning and suggests that, in most grains, only one twin variant or a single twin variant pair is active. Similar observations have been reported for an AZ31 rolled sheet deformed in compression along RD [128,129]. The operation of only one twin variant pair promotes the formation of parallel twin boundaries and rapid twin growth [129]. The activation of tensile twinning is also evidenced by the presence of tensile

twin boundaries in Figs. 4.7b and 4.8b. The definition of the six-fold symmetry is less clear at 200 °C, as twinning is less frequent (figure 4.8c). Compression and double twins are not frequent at RT but their incidence increases notably at 200 °C. This is in agreement with previous reports of a decrease in the CRSS of these twinning modes as temperature raises [32]. Finally, a second intensity maximum is also evident at the center of the $(10\bar{1}3)$ pole figure at RT and 200 ºC, suggesting the simultaneous activation of pyramidal slip. No evidence of dynamic recrystallization has been found at 200 °C. At 400 °C the microstructure is completely recrystallized and a very weak texture is obtained. Table 4.3 compares the values of the average grain size measured for each condition (d_M), without taking into account twin boundaries, and a theoretical grain size value (d_T) calculated from the original grain size (10 µm) taking into account the strain attained. It must be noted that all grain size values are calculated and/or measured in a plane perpendicular to the extrusion axis. At RT and 200°C d_M is slightly lower than d_T, revealing the occurrence of grain subdivision as a consequence of dislocation interactions. At 400°C d_M is half the value of d_T, consistent with a significant reduction of grain size due to DRX.

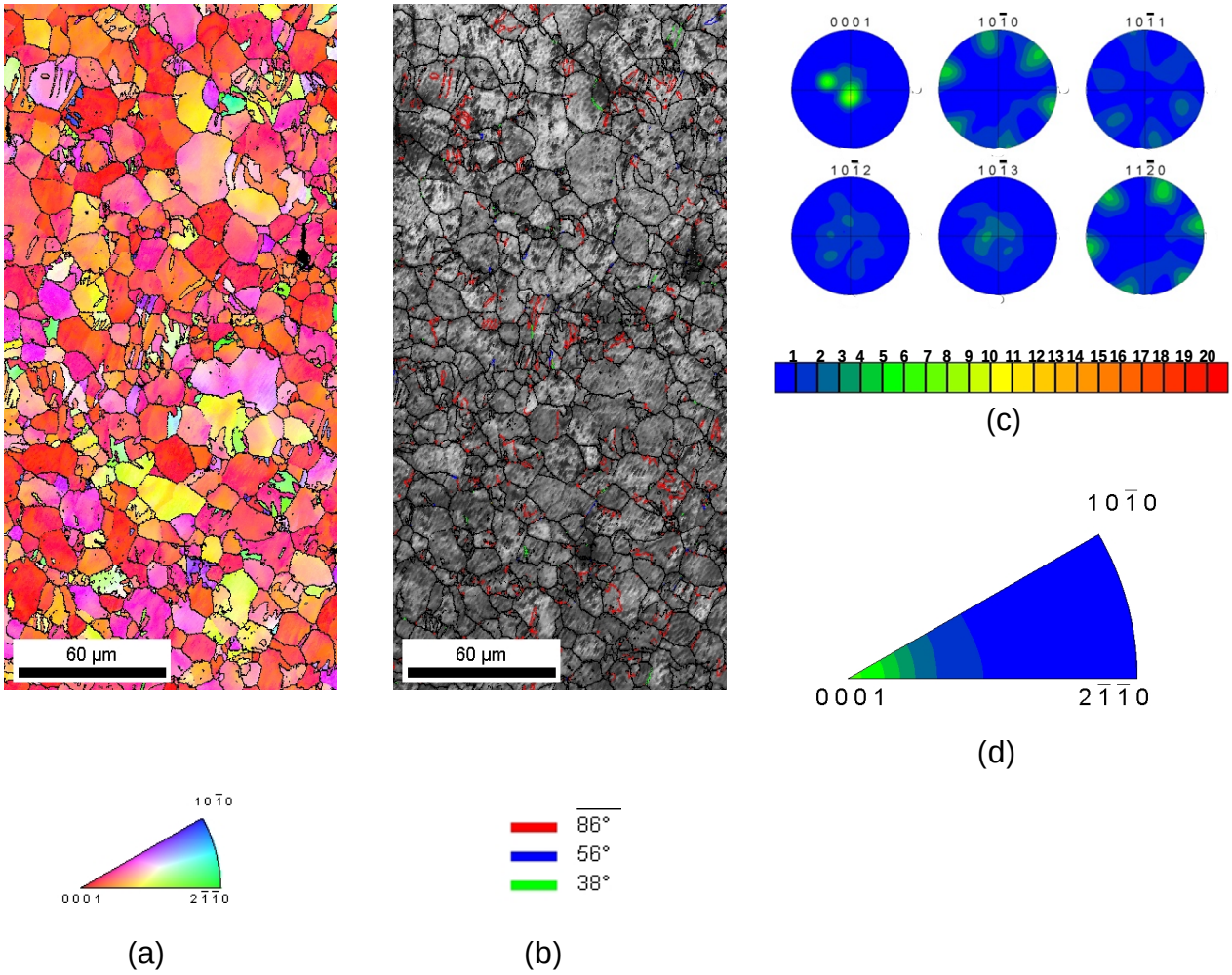

Figure 4.7. Microtexture of the MN11 alloy tested at low strain rate ($5x10^{-3}$ s^{-1}), at room temperature in compression along the EA up to a strain of 0.12 (fracture) (a) EBSD inverse pole figure map showing the orientation of the EA; (b) Twin boundary map (Red: tensile twins; Blue: compression twins; Green: double twins); (c) Pole figures. (d) Inverse pole figure showing the orientation of the EA. The plane shown is perpendicular to the EA.

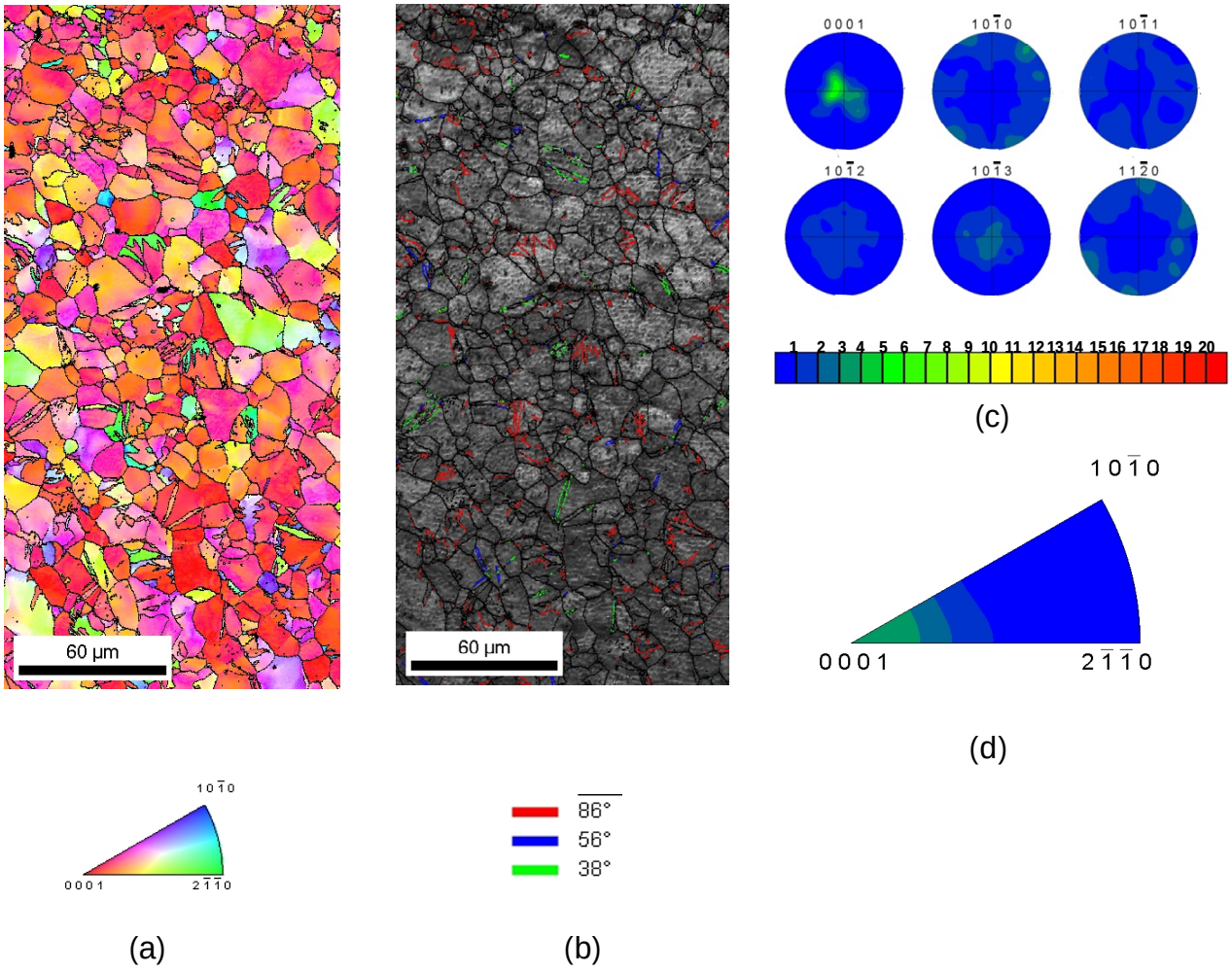

Figure 4.8. Microtexture of the MN11 alloy tested at low strain rate ($5x10^{-3}$ s^{-1}) at 200 ºC in compression along the EA up to a strain of 0.11 (fracture) (a) EBSD inverse pole figure map in the EA; (b) Twin boundary map (Red: tensile twins; Blue: compression twins; Green: double twins); (c) Pole figures. (d) Inverse pole figure showing the orientation of the EA. The plane shown is perpendicular to the EA.

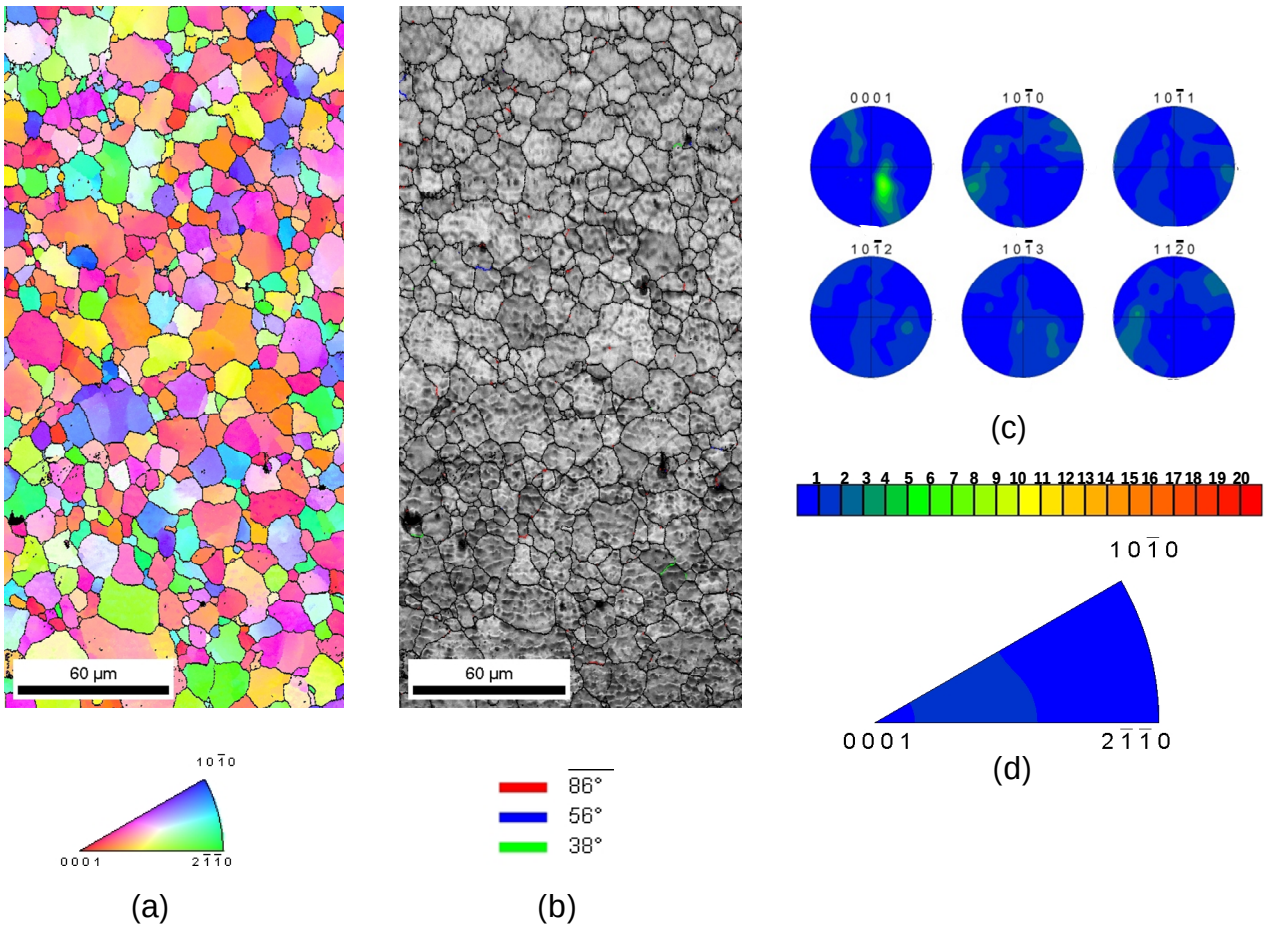

Figure 4.9. Microtexture of the MN11 alloy tested at low strain rate ($5x10^{-3}$ s^{-1}) at 400 ºC in compression along the EA up to a strain of 0.6 (test stopped) (a) EBSD inverse pole figure map in the EA; (b) Twin boundary map (Red: tensile twins; Blue: compression twins; Green: double twins); (c) Pole figures. (d) Inverse pole figure showing the orientation of the EA. The plane shown is perpendicular to the EA.

Figures 4.10 and 4.11 illustrate the evolution of the microtexture of the MN11 alloy (PL sample) with increasing strain during high strain rate (10^3 s^{-1}) compression at RT and at 400°C. The microstructural development at room temperature is similar to that observed under quasi-static conditions. After a true strain of 0.095, the c-axes tend to align with the EA (Fig. 4.10c), consistent with the activation of tensile twinning and basal slip [127]. This texture becomes more intense with increasing strain (Fig. 4.10f). Simultaneously, a six-fold symmetry develops in the prismatic pole figures with increasing strain (figures 4.10f), suggesting that tensile twinning continues to operate up to true strains as high as 0.15. The activation of tensile twinning is also evidenced by the presence of tensile twin boundaries in Figs. 4.10b and 10e. A texture intensity maximum appears also at the center of the $(10\bar{1}3)$ pole figure, revealing the operation of pyramidal slip. At 400°C the six maxima developed with increasing strain in the prismatic pole figures are more poorly defined at 400 °C (figure 4.11f) and compression and double twins are more frequent at 400 °C than at RT (figures 4.11b and 4.11e); finally, at a strain of 0.16 a small number of DRX grains are located at grain or twin boundaries (figures 4.11d), but their volume fraction is too small to have a significant impact on the texture development.

Table 4.3 reveals, again, that, under dynamic conditions, the measured grain sizes (d_M) are smaller than the calculated ones (d_T) and, furthermore, that d_M decreases with strain at all the temperatures investigated. This is consistent with the occurrence of grain subdivision processes due to dislocation interactions. Grain subdivision has been previously reported in an AZ31 alloy under quasi-static and dynamic conditions. Grain subdivision was observed to be favored when dislocations with high stacking fault energy (such as prismatic ones) carried most of the strain. In the MN11 alloy, grain subdivision might be favored by the interaction between basal and pyramidal dislocations.

Table 4.3. Theoretical grain size (d_T) and measured grain size (d_M) for MN11 samples tested in compression and in tension at high and low strain rate at different temperatures. The grain sizes are measured and calculated along a plane perpendicular to the extrusion axis.

	Compression									**Tension**		
	$5x10^{-3}$ s^{-1}			**10^3 s^{-1}**						**10^3 s^{-1}**		
	RT	**200ºC**	**400ºC**	**RT**		**200ºC**		**400ºC**		**RT**	**200ºC**	**300ºC**
	0.12*	0.11*	0.60*	0.095*	0.15*	0.10*	0.16*	0.11*	0.16*	0.25*	0.28*	0.4*
d_T	10.5	10.5	18	10.5	11	10.5	11	10.5	11	9	9	8.5
d_M	7.5	8	9	7.5	6.5	8	6.5	8	7	6.5	5	3

(*fracture, *test stopped)

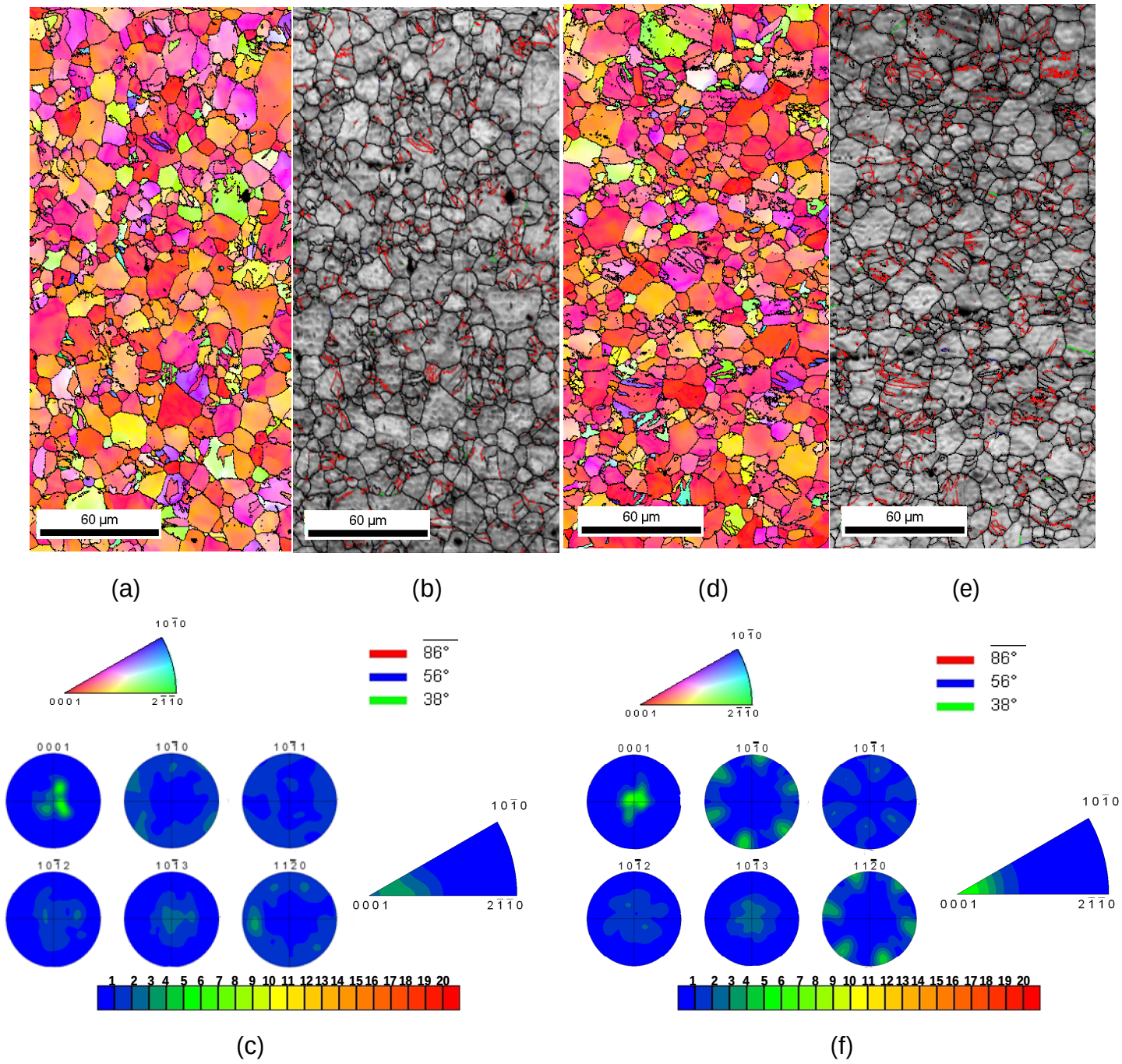

Figure 4.10. Evolution of the microtexture of the MN11 alloy during compression at high strain rate (10^3 s^{-1}) along the EA at RT with increasing strain. (a) ε= 0.095; EBSD inverse pole figure map showing the orientation of the EA; (b) ε= 0.095; Twin boundary map (Red: tensile twins; Blue: compression twins; Green: double twins); (c) ε= 0.095; Pole figures and inverse pole figure showing the orientation of the EA. (d) ε= 0.15; EBSD inverse pole figure map showing the orientation of the EA; (e) ε= 0.15; Twin boundary map (Red: tensile twins; Blue: compression twins; Green: double twins); (f) ε= 0.15; Pole figures and inverse pole figure showing the orientation of the EA. The plane shown is perpendicular to the EA.

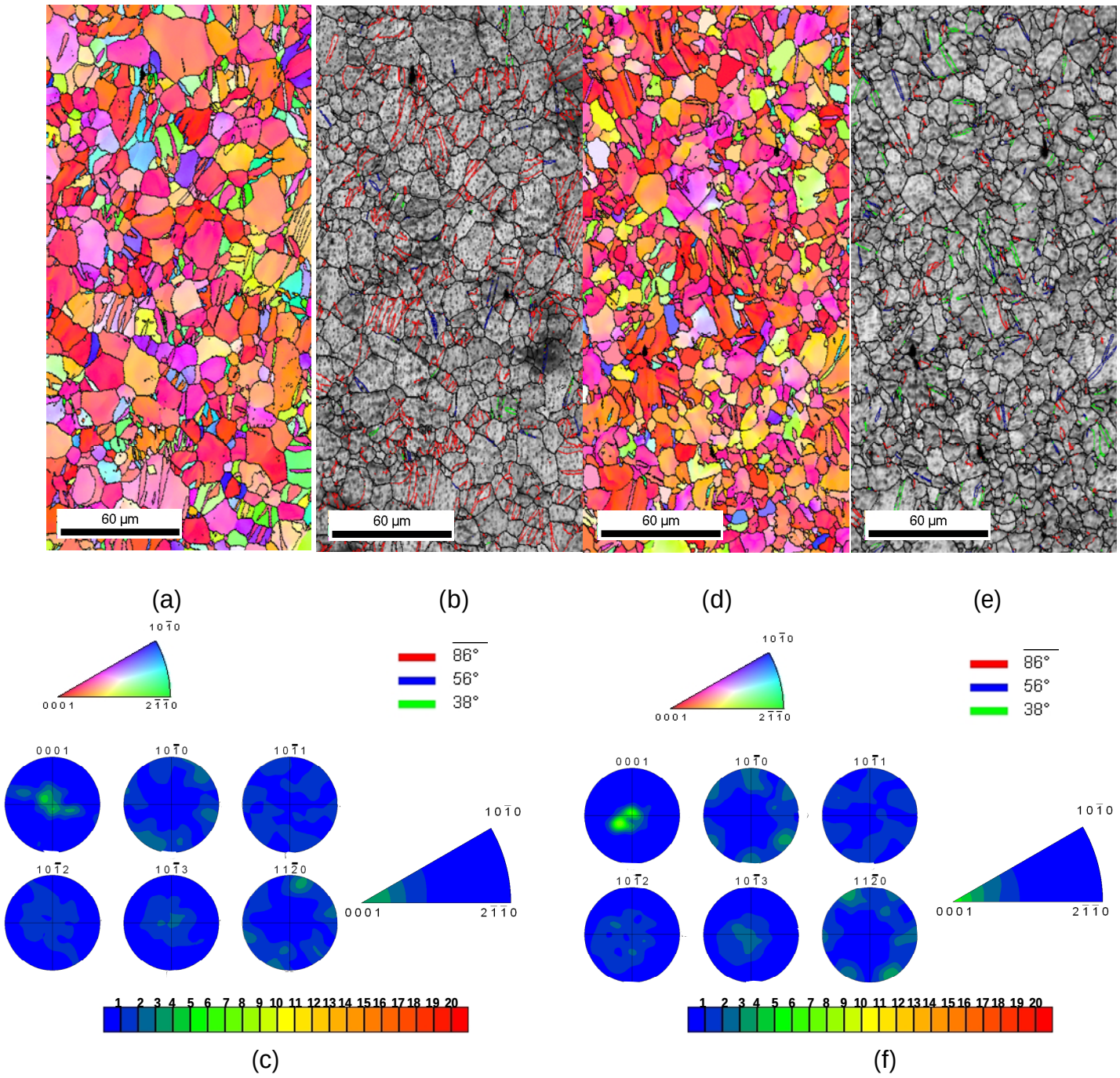

Figure 4.11. Evolution of the microtexture of the MN11 alloy during compression at high strain rate (10^3 s^{-1}) along the EA at 400 ºC with increasing strain. (a) ε= 0.11; EBSD inverse pole figure map showing the orientation of the EA; (b) ε= 0.11; Twin boundary map (Red: tensile twins; Blue: compression twins; Green: double twins); (c) ε= 0.11; Pole figures and inverse pole figures showing the orientation of the EA. (d) ε= 0.16; EBSD inverse pole figure map showing the orientation of the EA; (e) ε= 0.16; Twin boundary map (Red: tensile twins; Blue: compression twins; Green: double twins); (f) ε= 0.16; Pole figures and inverse pole figures showing the orientation of the EA. The plane shown is perpendicular to the EA.

Figures 4.12 and 4.13 illustrate the evolution of the microtexture of the MN11 alloy deformed in tension under dynamic conditions at RT and at 300°C. At both temperatures c-axes tend to align preferentially with the prismatic $\langle 10\bar{1}0 \rangle$ pole figure (figures 4.12c and 4.13c). The c-axes are located along the $\langle 10\bar{1}0 \rangle$-$\langle 11\bar{2}0 \rangle$ boundary, except in the vicinity of the $\langle 11\bar{2}0 \rangle$ pole. Calnan and Clews [127] have predicted that a Mg randomly oriented polycrystal, deformed in tension by basal slip and tensile twinning, should, given enough strain, develop a texture in which all c-axes are parallel to all prismatic directions. The clustering of c-axes around the $\langle 10\bar{1}0 \rangle$ pole in our MN11 alloy is consistent with the additional activation of pyramidal $\{10\bar{1}0\}$ slip [127]. Given the as-received texture of the MN11 alloy, it is logical that the contribution of basal slip is higher in tension than in compression and that, therefore, the shape of the tensile curves is “concave-down”. Figure 4.14 shows the superposition of the inverse stereographic triangle (extrusion axis) corresponding to the as-extruded MN11 alloy and the schematic triangle showing contours of constant resolved shear stress, i.e., of constant Schmid factor for basal slip, reported by Calnan and Clews. The occurrence of grain subdivision at room temperature is evidenced by the lower value of d_M versus d_T (Table 4.3). Finally, at 300°C a significant volume fraction of small DRX grains can be observed to form mainly at grain boundaries, giving rise to a dramatic decrease in d_M with respect to d_T at this temperature (Table 4.3).

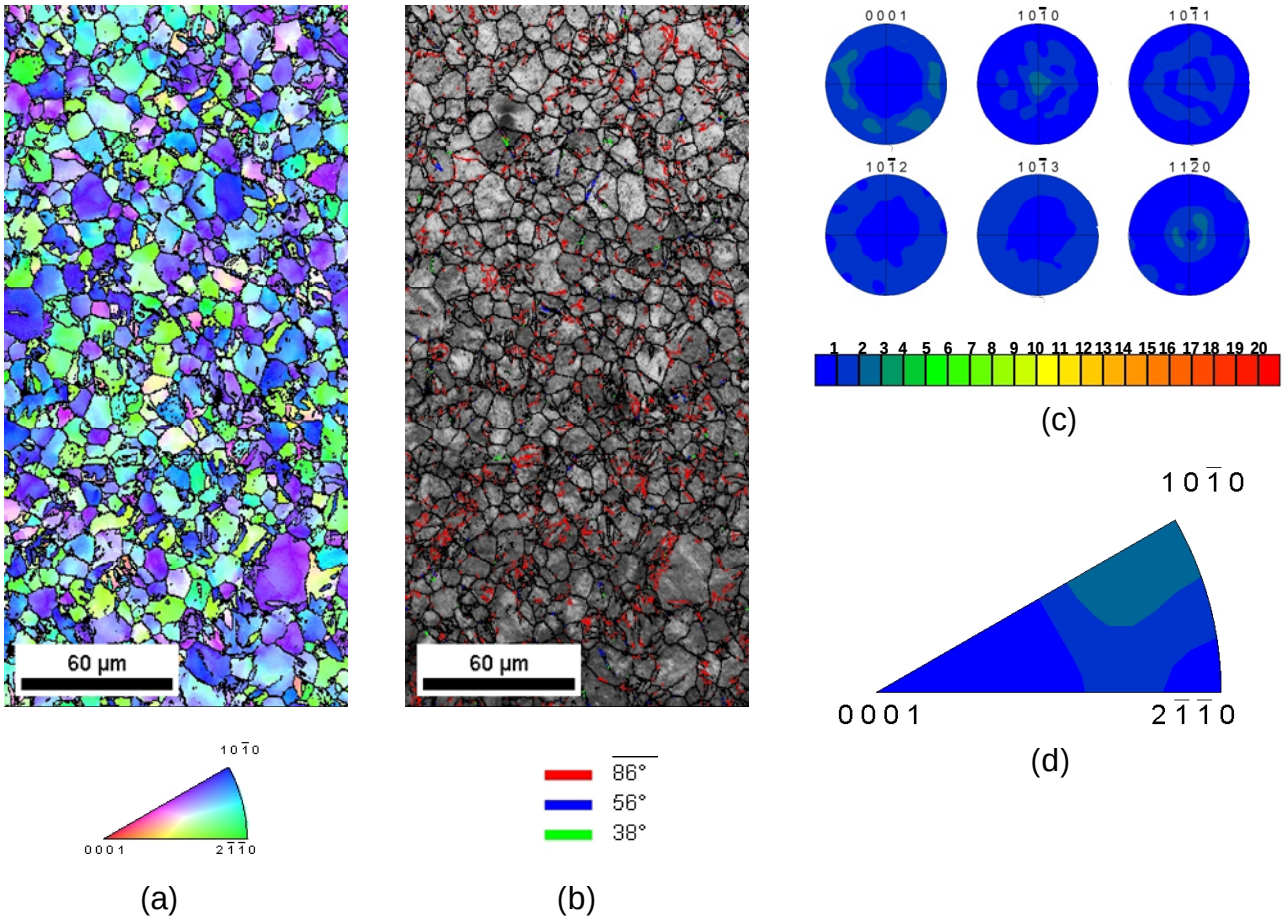

Figure 4.12. Microtexture of the MN11 alloy tested in tension along the EA at high strain rate (10^3 s^{-1}) at RT up to a strain of 0.25 (fracture). (a) EBSD inverse pole figure map showing the orientation of the EA; (b) Twin boundary map (Red: tensile twins; Blue: compression twins; Green: double twins); (c) Pole figures. (d) Inverse pole figure showing the orientation of the EA. The plane shown is perpendicular to the EA.

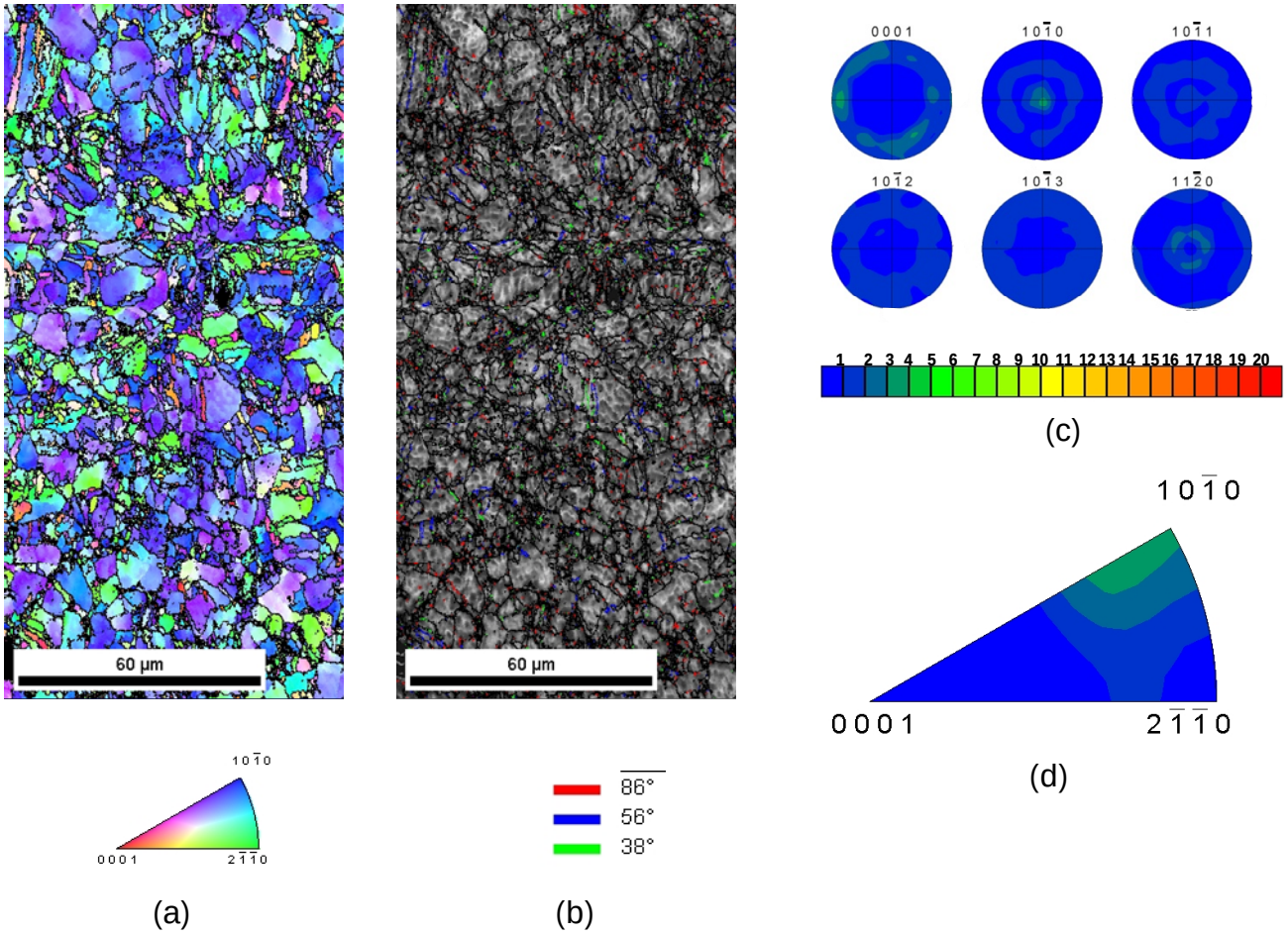

Figure 4.13. Microtexture of the MN11 alloy tested in tension along the EA at high strain rate (10^3 s^{-1}) at 300 ºC up to a strain of 0.40 (fracture). (a) EBSD inverse pole figure map showing the orientation of the EA; (b) Twin boundary map (Red: tensile twins; Blue: compression twins; Green: double twins); (c) Pole figures.; (d) Inverse pole figure showing the orientation of the EA. The plane shown is perpendicular to the EA.

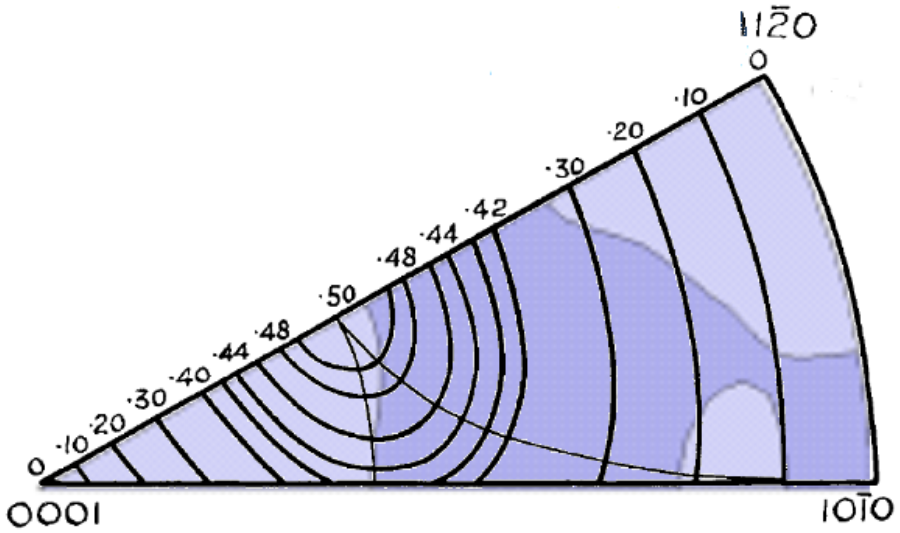

Figure 4.14. Superposition of the inverse stereographic triangle (extrusion axis) corresponding to the as-extruded MN11 alloy and the schematic triangle showing contours of constant resolved shear stress, i.e., of constant Schmid factor for basal slip, reported by Calnan and Clews [127].

4.1.4. Conclusions.

The mechanical behavior of an extruded Mg-based alloy containing Mn and Nd additions (Mg-1%Mn-1%Nd) was investigated at quasi-static and dynamic rates and at temperatures ranging from 25°C to 400°C. Tests were carried out along the extrusion axis and along a direction perpendicular to it. The evolution of the texture and of the nature of the grain boundaries during testing was examined using electron backscattered diffraction (EBSD). The main conclusions of the present work are the following:

- The strong interaction between Nd atoms and dislocations is evidenced by the occurrence of dynamic strain aging (DSA) at 200°C at quasi-static rates and of a yield point phenomenon at 300°C and 400°C at dynamic rates.

- The predominant deformation mechanisms under all the testing conditions investigated are basal slip and tensile twinning. The incidence of each mechanism varies significantly with temperature and strain rate.

- The critical resolved shear strength of basal slip appears to be similar or perhaps higher than that of tensile twinning. This is consistent with a higher yield strength value in tension than in compression and with the pronounced “concave-up” shape of the stress-strain curves observed at quasi-static rates. The increase in the CRSS of basal slip might be attributed to the preferential location of Nd atoms along basal planes.

- Discontinuous dynamic recrystallization takes place during quasi-static compression at 400°C, leading to a weak texture. During dynamic deformation a small fraction of DRX grains are formed at grain or twin boundaries at temperatures higher than 300°C in both tension and compression. Their volume fraction is too small to have a significant impact in the texture development. Grain subdivision by dislocation interaction is observed both under quasi-static and dynamic rates.

4.2. COMPLEMENTARY STUDY II

4.2. complementary study II. Dynamic deformation of high pressure die-cast Mg alloys.

4.2.1. Introduction.

The aim of this work is to investigate the mechanical behavior and the operative deformation mechanisms of die-cast AZ91 and AM60 alloys at impact strain rates under a wide range of temperatures in tension and in compression. The influence of the strain rate on the yield strength, the maximum stress, the elongation to failure and the property variability will be described. A comparison between high strain and low strain properties will be established.

4.2.2. Materials and Experimental Procedure

The alloys utilized for this study are AZ91D and AM60B. They were purchased in the form of ingots. The latter were melted and die-cast into dog-bone mechanical testing specimens of circular cross-section with a gage length of 12 mm and a gage diameter of 4 mm. The liquid metal gate velocity was 8-9 m/s and the solidification pressure 400-500 bar. The liquid alloy temperature was 630°C-670°C and the temperature of the mould 190°C-230°C. The microstructure of the die-cast materials was investigated by optical (OM) and scanning electron microscopy (SEM). Sample preparation for these two techniques included grinding with increasingly finer SiC papers, several diamond polishing steps, and surface finishing using a colloidal silica solution. The specimens prepared for OM were additionally chemically etched during 15 s with a solution of 50 ml of ethanol, 0.5 g of picric acid, 0.5 ml of acetic acid, and 1 ml of distilled water. The macrotextures of the die-cast AZ91 and AM60 alloys were measured by the Schulz reflection method in a Philips X´pert-Pro Panalytical X-ray diffractometer

furnished with a PW3050/60 goniometer. The radiation used was β-filtered Cu Kα. The measured incomplete pole figures were corrected for background and defocusing using the Philips X´pert software. The orientation distribution function (ODF), the complete pole figures and the volume fraction of selected texture components were calculated using the MTex software [124]. Sample preparation for texture measurement included grinding with SiC papers of grit sizes ranged from 320 to 2000.

High strain rate mechanical tests (~10^3 s^{-1}) were carried out using a tensile split Hopkinson bar, equipped with a radiant furnace. Testing temperatures ranged from room temperature to 400°C, at intervals of 50°C. Low strain rate tests were performed at room temperature, 200°C and 400°C at $5x10^{-3}$ s^{-1} in a conventional electromechanical Instron testing machine. Two samples were tested for each condition. The heads of the dog-bone die-cast AZ91 and AM60 coupons were threaded in order to be able to screw them to the grips of the testing machines for tension tests. Cylinders of 6 mm in length were cut out of the gage length of the die-cast dog-bone specimens for the compression tests.

4.2.3. *Results and Discussion*

Fig. 4.15 illustrates the microstructure and the texture of the as-die-cast AZ91 and AM60 alloys. The plane examined is perpendicular to the loading axis of the coupons. Microanalysis at the SEM revealed that the phases present in both alloys alloy are mainly α-Mg (light areas in figure 4.15), and $Al_{12}Mg_{17}$ (dark areas in figure 4.15). A very small fraction of Mg-Al-Mn compounds were also detected. Both materials have a weak texture. The texture of die-cast materials is usually deemed to be completely random. However, here the volume fraction of material with

c-axes tilted more than 45° away from the loading axis ($V_{f>45°}$) in both the AM60 and AZ91 alloys is ~70%.

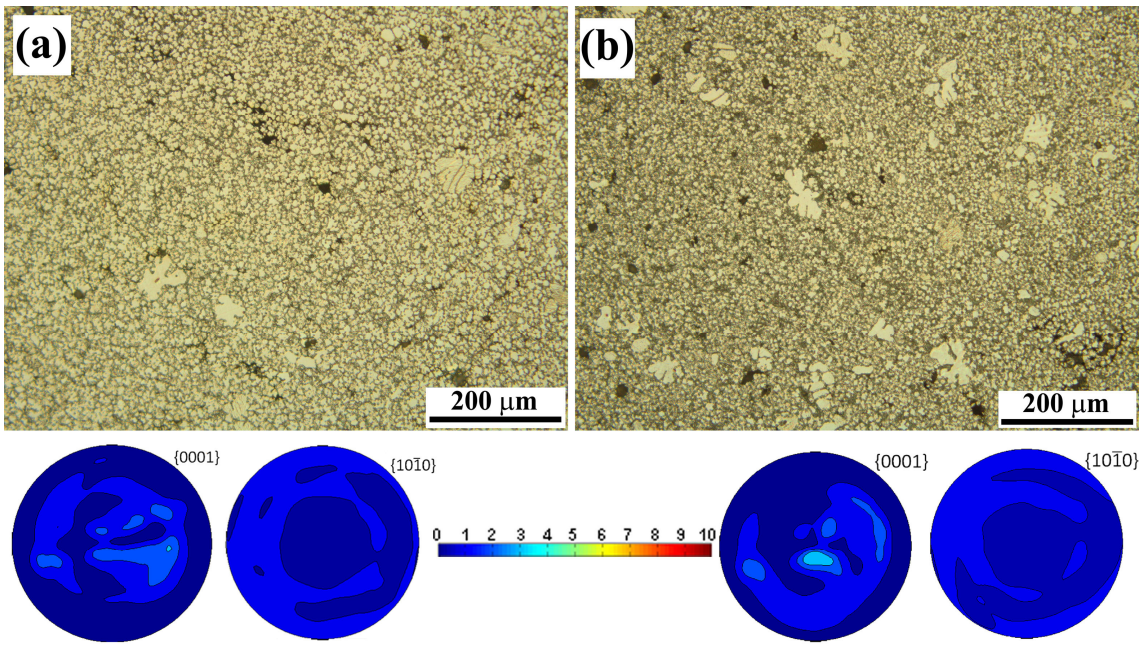

Figure 4.15. Microstructure and macrotexture (X-ray) of the as-received die-cast Mg alloy: (a) AM60, (b) AZ91. The plane examined is perpendicular to the loading axis.

Figure 4.16 summarizes the values of the yield (σ_y) and maximum strengths (σ_{max}), as well as of the strain to failure (ε_f), corresponding to the tests performed in tension (T) and in compression (C) at dynamic and quasi-static rates in both alloys. A note must be made here to state that ε_f in compression corresponds to the strain until the maximum flow stress is reached. In dynamic tests it is difficult to measure the true yield stress at the nominal strain rate, since in the early stages of deformation the strain rate increases gradually. Thus, the stress at a true strain of 0.005 ($\sigma_{0.005}$) is used in the present study as a best approximation to this material property. The two die-cast alloys exhibit an excellent dynamic mechanical behavior. In general, the room temperature yield and maximum strengths are slightly higher in the dynamic tests than at quasi-static rates. With increasing temperature the values of these two magnitudes decrease, but the change is less

pronounced at high strain rate. Thus, the yield and maximum strengths at dynamic rates are significantly higher than those obtained at quasi-static rates at temperatures higher than 200°C. At 400°C and quasi-static rates none of the two alloys experience any work hardening under all the conditions investigated while at dynamic rates a significant amount of work hardening is present. In both alloys the strain to failure increases dramatically with temperature at low strain rates while it remains rather constant at high strain rates. In the AM60 alloy, in the dynamic range, ε_f retains values close to 20% in compression and between 10 and 15% in tension. In the AZ91 alloy the dynamic strain to failure in compression remains in the range between 15% and 20% until 350°C. In tension, it varies between 7% at room temperature and 5% at 400°C. In summary, the two die-cast alloys have a good energy absorption capacity at dynamic rates within all the temperature range investigated. This is because the decrease in the yield and maximum strengths with temperature are not as pronounced as during quasi-static tests and the strain to failure does not change substantially.

A rather large scatter has been found in the tensile ductility of the AM60 alloy in low strain rate tests (figure 4.16d). This is consistent with the results of earlier works [104], which have reported a similar variability of the tensile ductility in a die-cast AM50 alloy deformed in tension at temperatures ranging from 25°C to 120°C. A strong quantitative correlation between the tensile ductility and the area fraction of the porosity in the corresponding fracture surfaces was found. However, the ductility was not reported to be related to the pore volume fraction. Thus, higher ductility values are predicted to be present in tensile specimens with a smaller number of large gas pores and/or of clustered small pores. In [104] the extent of the variability was observed to decrease with temperature. The authors did not report the reason for this decrease but they put forward several possible explanations such as variations in the strain hardening rate with

temperature or plastic relaxation due to the activation of secondary slip systems at high temperatures. In the present work the tensile ductility shows great variability until temperatures as high as 400°C. The differences between the two studies might be due to the use of different solidification conditions, which might result in drastic variations in the porosity distribution. Additionally, no significant variability was found in the tensile ductility of the AZ91 alloy at quasi-static rates (figure 4.16h). It has been reported that the presence of a network of low melting point second phases ($Al_{12}Mg_{17}$) improves the casting properties of the material by suppressing microporosity. Since the AZ91 alloy has a higher alloying content, this effect should be enhanced in this material when compared to the AM60 alloy [130]. Finally, in the dynamic tests the scatter in the tensile ductility is significantly smaller. This might suggest that the formation of adiabatic shear bands, the precursors to failure in most metals at impact strain rates, is rather independent of the porosity distribution.

Figure 4.17 compares the compression stress-strain curves corresponding to the die-cast AM60 (figures 4.17a and 4.17b) and AZ91 (figures 4.17c and 4.17d) specimens tested at dynamic (figures 4.17a and 4.17c) and quasi-static rates (figures 4.17b and 4.17d) and at temperatures ranging from 25°C to 400°C. In both alloys, the low strain rate curves at room temperature have a “concave-up” shape at the early stages of deformation, revealing the activation of tensile twinning and slip. As temperature increases and secondary slip systems become operative, the twinning activity decreases significantly and the shape of the curve changes to “concave-down”. This effect has been observed in numerous occasions. Under dynamic conditions, the curves retain the “concave-up” shape up to temperatures as high as 400°C in the AM60 alloy and 350°C in the AZ91 alloy. This is consistent with the enhancement of twinning at high temperatures observed earlier [56,57].

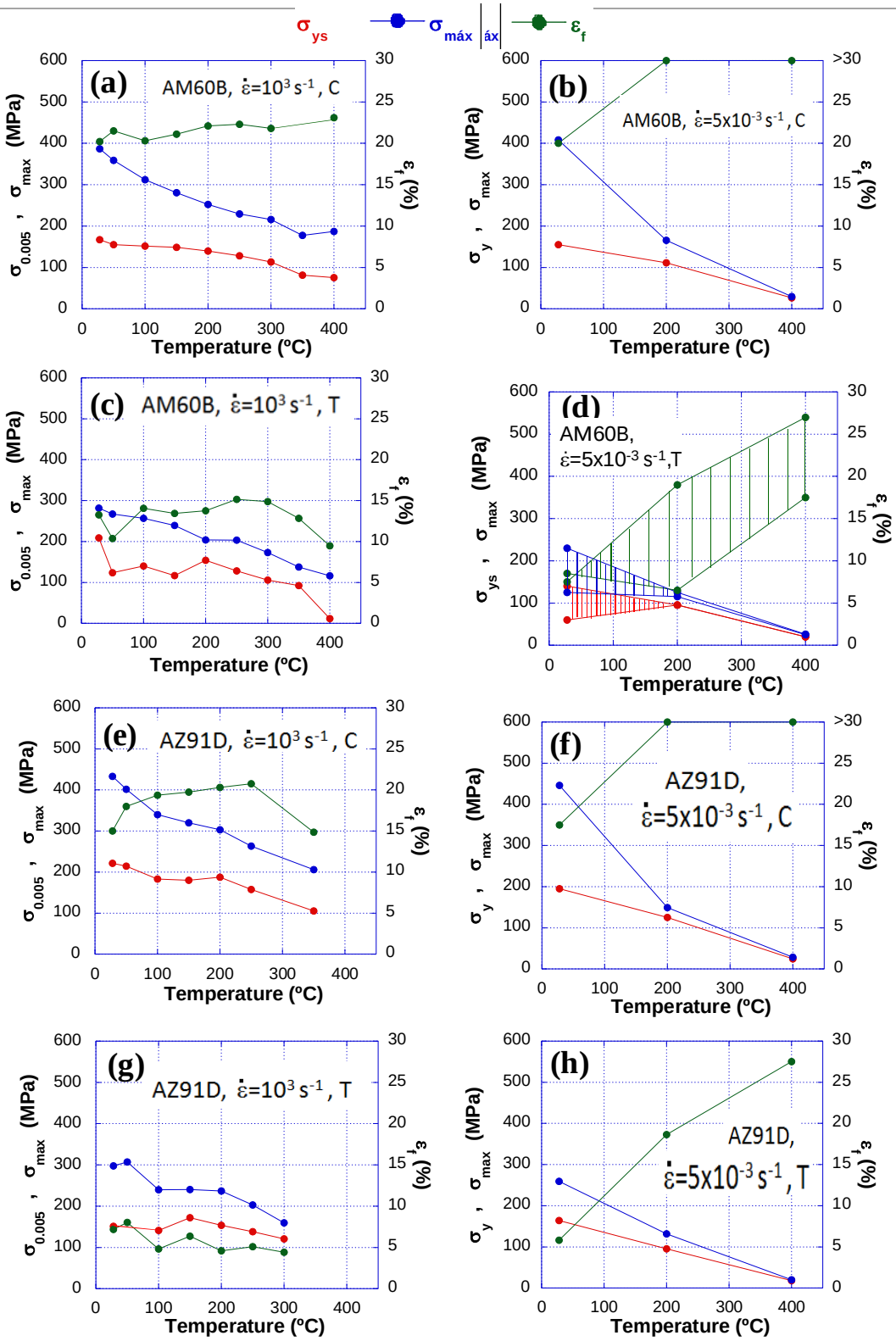

Figure 4.16. Variation of the yield stress ($\sigma_{0.005}$) and of the flow stress (σ_{max}) with temperature during high (10^3 s^{-1}, left column) and low ($5x10^{-3}$ s^{-1}, right column) strain rate tests in die-cast AM60B and AZ91B alloys: (a) AM60B, 10^3 s^{-1} in compression; (b) AM60B, $5x10^{-3}$ s^{-1} in compression; (c) AM60B, 10^3 s^{-1} in tension, (d) AM60B, $5x10^{-3}$ s^{-1} in tension, (e) AZ91D, 10^3 s^{-1} in compression; (f) AZ91D, $5x10^{-3}$ s^{-1} in compression; (g) AZ91D, 10^3 s^{-1} in tension, (h) AZ91D, $5x10^{-3}$ s^{-1} in tension.

It must be noted that the shape of the tension stress-strain curves, both at dynamic and quasi-static rates, was always “concave-down” in both alloys (figure 4.18). Thus, the activity of tensile twinning seems to be higher in compression than in tension tests. This is consistent with the fact that the volume fraction of material with c-axes tilted more than 45° away from the loading axis is higher than the fraction of material with tilt angles smaller than 45° (70% vs. 30%), as twinning is a polar mechanism [45].

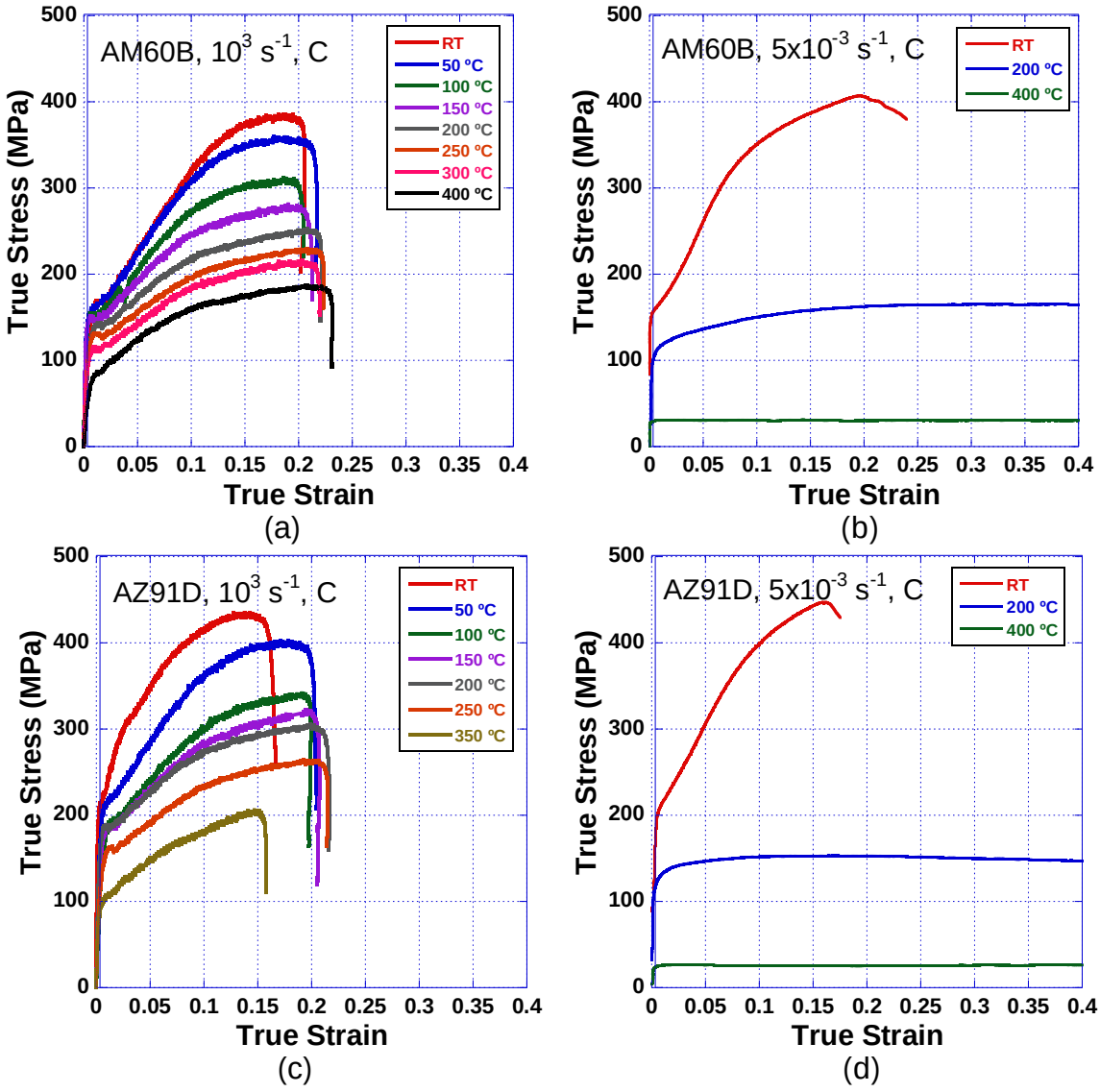

Figure 4.17. True stress-true strain curves corresponding high (10^3 s^{-1}) and low ($5x10^{-3}$ s^{-1}) strain rate tests performed in compression at different temperatures in die-cast Mg alloys : (a) AM60B, 10^3 s^{-1}, (b) AM60B, $5x10^{-3}$ s^{-1} (c) AZ91D, 10^3 s^{-1}, (d) AZ91, $5x10^{-3}$ s^{-1} .

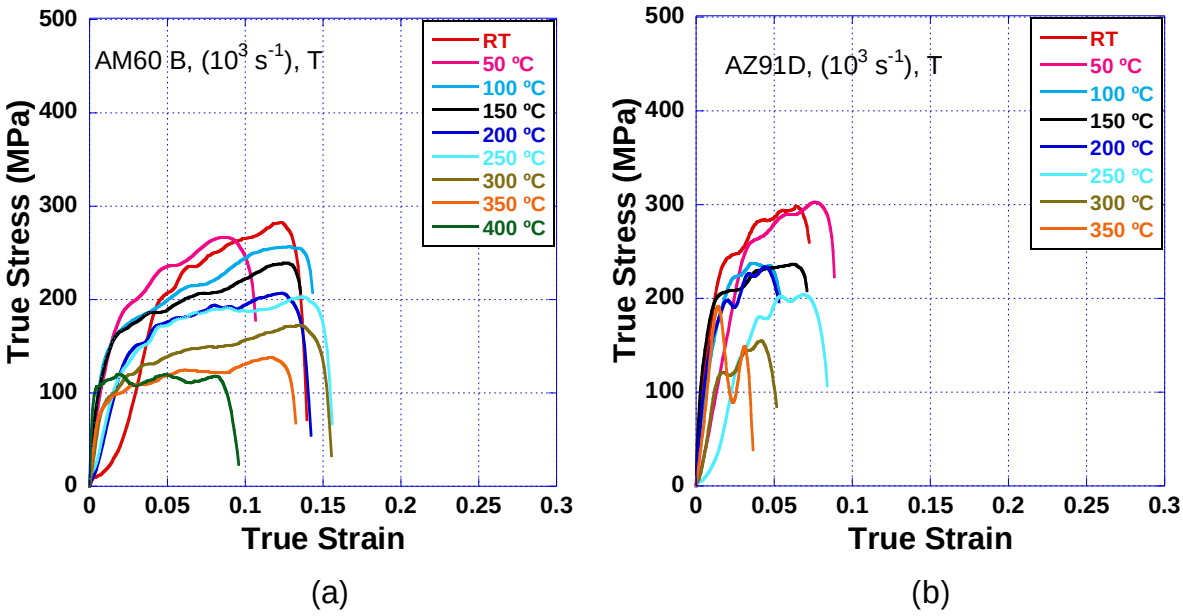

Figure 4.18. True stress-true strain curves corresponding high strain rate (10^3 s^{-1}) tests performed in compression at different temperatures in die-cast Mg alloys : (a) AM60B (b) AZ91D.

4.2.4. Conclusions.

The dynamic behavior of the die-cast AM60 and AZ91 alloys has been investigated in a wide range of temperatures and compared to the quasi-static behavior. The main conclusions of the present work are the following:

- The texture of the die-cast alloys is not random and this results in an anisotropic mechanical behavior.

- It has been found that both alloys possess very good energy absorption capacity, since the yield and maximum strengths do not decrease with increasing temperature as dramatically as at quasi-static rates and the strain to failure values remain fairly constant.

- The absence of any significant variability in the tensile ductility at dynamic rates is attributed to the independence of the adiabatic shear failure mechanism of the porosity distribution.

- Tensile twinning is observed to be enhanced at dynamic rates in compression even at temperatures as high as 400°C.

PART V

GENERAL DISCUSSION

5. GENERAL DISCUSSION

5.1. Strain rate sensitivity of the yield stress in the Mg AZ31 alloy.

It is well known that the crystalline structure influences the strain rate response of metallic materials [131]. For body centered cubic (bcc) metals the strain rate sensitivity is in the yield stress dependence, whereas for face centered cubic (fcc) metals it is mainly in the strain hardening [132] . In the latter, the yield stress is virtually independent of the strain rate and of temperature. Hexagonal close packed metals are known to follow either bcc or fcc behavior. In particular, magnesium alloys with a random texture are reported to follow the fcc pattern [132].

Our results presented in the first research paper (*Ulacia I., N.V Dudamell, et al. Acta Materialia 58 (2010), 2988-2998)* show that the strain rate sensitivity of the yield stress of the AZ31 sheet alloy may follow the fcc or the bcc patterns depending on the initial relative orientation between the tensile/compression axis and the c-axes. A close look at the room temperature data of Figures 4a, 4c, and 4e of the mentioned paper reveals that the yield strength does indeed not vary with strain rate when testing the material in compression along RD (RD-C) due to the preferential activation of twinning, whose CRSS is strain rate insensitive, or when testing the material in compression along ND (ND-C), where pyramidal slip and compression twinning play a major role (fcc pattern). However, there is a significant variation of the yield strength with strain rate when testing the material in tension along in-plane directions (RD-T and TD-T), where prismatic and basal slip predominate (bcc pattern).

5.2. Strain rate dependence of the critical resolved shear stress of non-basal slip systems and of tensile twinning in the Mg AZ31 alloy.

It has been found that the yield stress (σ_y) is related to the CRSS of the various operating deformation mechanisms as $\sigma_y = m\tau_o + mkd^{-\frac{1}{2}}$, where m is the Taylor factor, τ_o is the CRSS for the operative slip systems and k is the microstructural shear stress intensity characterizing the average grain boundary resistance to plasticity spreading between the grains [132]. Thus, analyzing the variation of σ_y with strain rate and temperature (figures 4a,c, and e of the first paper) allows inferring roughly the sensitivity of the CRSS of the operative slip systems to these two parameters. Our results suggest, firstly, that at room temperature the strain rate dependency of the CRSS of prismatic slip systems is higher than that of pyramidal systems. Consistently with earlier findings, twinning is seen to be strain rate independent. Secondly, it appears that the temperature dependence of the CRSS of non-basal slip systems is significantly less pronounced at dynamic strain rates than at quasi-static strain rates. Barnett [32] has calculated the evolution of the CRSS of several Mg deformation mechanisms as a function of the Zener-Hollomon parameter (Z) (table 2.2). The model shows good correlation with experimental data for values of Z between 10^9 s^{-1} and 10^{14} s^{-1} , for temperatures between approximately 180°C and 380°C at 10^{-3} s^{-1} and higher than 380°C at 10^3 s^{-1}. Although this model does not cover well the strain rate/temperature conditions utilized in the present work, it does point toward a higher variation of the CRSS of non-basal slip systems at lower strain rates. Thirdly, at dynamic strain rates the CRSS for {10-12} twinning seems to remain constant with temperature up to 400°C.

Figure 5a of the first research paper (*Ulacia I., N.V Dudamell, et al. Acta Materialia 58 (2010), 2988-2998)* shows that under dynamic conditions the yield stress tension-compression asymmetry and the out-of-plane yield stress anisotropy remain high up to 400°C. This suggests that the CRSS of non-basal slip systems remains higher than that of twinning, even at these high temperatures. Also, the in-plane yield stress anisotropy does not change with temperature, revealing that the CRSS of non-basal slip remains higher than that of basal slip up to temperatures as high as 400°C. Both observations are in full agreement with Barnett´s model prediction [32].

5.3. Influence of strain rate on the twinning activity.

The strain rate has also an important influence on the twinning activity. It is now well known that twinning is enhanced in Mg alloys during dynamic deformation to such an extent that it is present even at very high temperatures (400 ºC) [56-58,117], at which it is absent at low strain rates. A profuse twinning activity at dynamic rates has also been reported in other hexagonal close-packed metals, such as Ti and Zr [133-135]. The results of the second research paper presented (*N.V. Dudamell et al. Acta Materialia 59 (2011), 6949-6962*) additionally reveals that the influence of the strain rate on the AZ31 alloy consists of the enhancement of extension twinning, but that compression and double twinning are not only not enhanced, but are even hindered under dynamic conditions.

In particular, it has been observed that the strain rate enhances extension twin propagation in grains that are favorably oriented for this mechanism to operate, and that it promotes the nucleation of extension twins even in grains that would not be favorably oriented for extension twinning at low strain rates.

The enhancement of extension twinning at high strain rates can be rationalized as follows. Arguments based on variations in the CRSS for twinning with strain rate must be ruled out, as it is well known that this parameter is strain rate and temperature insensitive [32,45]. The choice of twin systems was classically based on the criterion of minimum shear put forward by *Jaswon and Dove* [136] (see also Ref. [45]). This model assumes that the atoms in the twinned area reach their final positions exclusively by pure shear, which excludes atomic translations (shuffles).

The twinning shears associated to extension and compression twinning in Mg (s) are -0.1289 and 0.1377, respectively [45]. These values are very similar, but usually extension twins are abundant and thick, while the compression twins are often observed only in localized regions. Furthermore, this criterion does not explain why extension twinning is preferentially enhanced at high strain rates, since shear is not diffusion assisted. A more sophisticated model for determining the operative twin systems was proposed by Bilby and Crocker [137] (see also Ref. [45]). This model considers twinning as a combination of shear plus individual atomic shuffles. The latter are dependent on both temperature and strain rate [138]. Bilby and Crocker suggested that, besides having a small shear, the operative twin mode should require only simple shuffles. In their theory, the "simplicity" of the atomic shuffles is related to a positive integer parameter (q) associated with each twinning mode, which is the number of lattice invariant planes (K_1) of spacing d traversed by the primitive lattice vector in the shear direction (η_2) [45]. The lower the value of q, the simpler the shuffles involved. For extension twinning $q=4$, while for $\{10\bar{1}1\}$ contraction twinning $q=8$ [45]. Thus, contraction twinning involves more complicated atom shuffling. Since atomic translations (shuffling) are activated thermally, an increase in the strain rate would hinder these

atomic movements – and even more so if they are complex. Therefore contraction twinning is expected to be less favored than extension twinning at high strain rates. This is consistent with our observations.

The enhancement of extension twinning under dynamic conditions is especially dramatic during compression along the ND, where the polarity of twinning is reversed in a rather large number of grains. It is remarkable that an inversion of the polarity of tensile twinning is preferred to an enhancement of compression twinning in grains in which the c-axes are being compressed. The reason for this surprising phenomenon is not entirely clear. Twin polarity is explained in the following way. The shear associated to a specific twinning system (s) is calculated as the ratio between the modulus of the corresponding twinning dislocation (b_{TD}) and the step height, h ($s = \frac{b_{TD}}{h}$) [45]. For twinning modes with q higher than 2, $s \sim \frac{2b_{TD}}{q}$ [45]. b_{TD}, and therefore s, may also be expressed as a function of the c/a ratio (γ). For $\{10\bar{1}2\}$ twins, $s = \frac{2b_{TD}}{q} = \frac{\left(\gamma^2 - 3\right)}{3^{\frac{1}{2}}\gamma}$. The shear thus changes dramatically with the c/a ratio. In Mg, γ is equal to 1.624 and the resulting shear is negative. This makes this twinning mode a tension twin [22,45]. Within this framework, the observation of $\{10\bar{1}2\}$ twins during c-axis compression at dynamic rates implies that the associated twinning shear adopts a positive value. This could only be achieved if the c/a ratio were to increase by approximately 5% during elastic deformation, which is not observed experimentally, or if a different mechanism (other than the propagation of the above-mentioned twinning dislocation) would dominate $\{10\bar{1}2\}$ twinning under the mentioned conditions. Some controversy does indeed exist regarding the fundamental mechanism responsible for $\{10\bar{1}2\}$ twinning in Mg alloys [139-140].

5.4. Influence of the strain rate on grain subdivision.

The strain rate has also influence on dynamic recovery. It is well known that the dislocations generated during shock loading in high stacking fault energy materials arrange in ordered cell structures whose size and misorientation angle depend on the applied pressure and pulse time [131]. Since dislocation reorganization into cell structures requires some thermal activation, usually cells become better developed as the strain rate decreases. In low stacking fault energy metals, however, dislocation rearrangement during dynamic deformation is more sluggish and thus homogeneous dislocation distributions develop.

It has been observed that significant dislocation rearrangement to form new boundaries subdividing the original grains takes place when the AZ31 alloy is tested both at quasi-static and dynamic rates (see Figs. 3, 4 and 8 of the research paper *N.V. Dudamell et al. Acta Materialia 59 (2011), 6949-6962*). However, the misorientation of these GNBs can reach very high angles in AZ31, in some cases exceeding 15º, whereas the typical misorientation of a cell boundary is rarely higher than 1 or 2º. Such highly misoriented GNBs have been observed only in rare cases, such as when deforming severely ($\varepsilon = 1$) pure Al by equal channel angular pressing [141]. It is remarkable that dislocation rearrangement can take place to such an extent at dynamic rates, where thermal activation is very limited. The explanation for this phenomenon might be related to the very high values of the stacking fault energies corresponding to both $\langle c+a \rangle$ and prismatic $\langle 10\bar{1}0 \rangle$ dislocations in Mg alloys, which are activated under all the conditions investigated here, as described in the previous sections. These values are compared in Table 1 of section 3.2.

The phenomenon of grain subdivision is most pronounced in the sample deformed quasi-statically in tension along the RD, resulting in a large reduction of the grain size with increasing deformation (from 13 to 2.5 μm). This can be rationalized as follows. First, the predominant deformation mechanism is the slip of prismatic dislocations, which have high stacking fault energy [143]. Second, prismatic slip predominates during all the deformation stages, and thus carries a large amount of the total strain (not all, as basal slip also takes place to some extent). This is not the case of the compression test along the RD, where twinning carries quite a large portion of the strain during the first stages of deformation, and pyramidal $\langle c+a \rangle$ slip, also with a high stacking fault energy [143], becomes predominant only in the latter stages of deformation. This is not the case of the compression test along ND, since the total strain to failure is small (0.07). The dynamic fracture energy corresponding to the tension test along the RD is higher than that corresponding to the other two tests (see Section 3.1 of the research paper *N.V. Dudamell et al. Acta Materialia 59 (2011), 6949-6962*)). This energy is presumably employed in the formation of a larger fraction of GNBs. Finally, grain subdivision is more pronounced in the test in tension along the RD at quasi-static rates than at dynamic rates due to the easier thermal activation in the former case.

5.5. Dynamic recrystallization at high strain rates.

Crystallographic texture plays a key role on the recrystallization mechanisms of magnesium alloys. With the purpose of going into this matter in depth, the research paper entitled “Influence of texture on the recrystallization mechanisms in an AZ31 Mg sheet alloy at dynamic rates” (*N.V. Dudamell et al. Materials Science and Engineering A 532 (2012), 528-535*) was published. The results reveal that there is a higher resistance to DRX when testing dynamically in tension along the RD

than during compression along the RD and along the ND. These observations can be rationalized as follows.

The influence of texture on DRX at quasi-static rates has been analyzed in a few earlier studies. In a pioneering work on the subject, *Kaibyshev et al*. [72] reported that the kinetics of DRX in an hot-pressed MA14 Mg rod (Mg-0.5wt%Zn-5%Zr), with a typical prismatic fiber texture and deformed in compression at 300°C and 2.8 x 10^{-3} s^{-1}, were dependent on the crystallographic texture. In particular, they observed that if the compression axis was parallel or perpendicular to the basal planes, DRX took place readily and an almost fully recrystallized structure was obtained at moderate strains. However, when the compression axis was tilted 45° with respect to the basal planes, DRX took place more slowly. In the former, the reported operative slip systems at the strain at which recrystallization started are prismatic, pyramidal <a> and basal. In the latter, only basal and prismatic slip are found to be active. Thus, *Kaibyshev et al.* [72] concluded that the kinetics of DRX were accelerated when all three main slip modes (basal, prismatic and pyramidal $\langle a \rangle$) are active. This, reportedly, is due to the fact that the operation of many slip modes favors the cross-slip of basal dislocations into non-basal planes. These non-basal dislocations have high stacking fault energies ($SFE_{basal} < 50\,\text{mJ.m}^{-2}$; $SFE_{prismatic} = 354\,\text{mJ.m}^{-2}$; $SFE_{pyramidal} = 452\,\text{mJ.m}^{-2}$ [142,143]) and, thus, can easily climb and arrange into new boundaries by the Friedel-Escaig mechanism. *Del Valle et al*. [75] also observed an enhancement of DRX in AZ31 samples oriented for multiple slip versus others initially oriented only for single (basal) slip. Finally, *Barnett* [28] reported a delay in DRX in an AZ31 sheet deformed in plane strain under conditions in which prismatic slip would predominate versus others in which $\langle c+a \rangle$ and basal slip are operative.

Our results at dynamic rates are consistent with the above observations at quasi-static rates and also support the fact that the kinetics of DRX is related to the operative deformation mechanisms. In particular, we observe a higher resistance to recrystallization when prismatic slip and basal slip operate (tension along the RD) than when a combination of $\langle c+a \rangle$ and basal slip are active (compression along the ND). This can be understood taking into account that pyramidal slip has more independent systems (5) than prismatic slip (2), and that the SFE of pyramidal dislocations is also significantly higher. Together, these two factors favor the occurrence of cross-slip and climb when pyramidal slip is active. We have also observed that the most favorable conditions for DRX at high strain rates are reached during compression along the RD, when extensive tensile twinning is followed by a combination of basal and pyramidal $\langle c+a \rangle$ slip. Under these conditions DRX takes place homogeneously throughout the microstructure, the final grain size is smaller and the strain hardening is lower than when compressing along the ND, where only basal and pyramidal $\langle c+a \rangle$ slip operate from the first stages of deformation. Thus, our results suggest that the operation of twinning during high temperature deformation at dynamic rates in the AZ31 alloy enhances DRX. The beneficial effect of twinning on DRX in Mg alloys as has been observed previously under quasi-static conditions [eg. 85,144-147] and it has been attributed to the large stresses accumulated close to twin boundaries, which promote the operation of multiple slip modes.

Figure 1 of the research paper mentioned above reveals that DRX takes place more easily at quasi-static than at dynamic strain rates, resulting in a much more pronounced softening. This may be explained by the easiness of diffusion at low strain rates, as well as by the more pronounced decrease of the CRSS of $\langle c+a \rangle$ slip with temperature under such conditions. Thus, for example, at 250°C and 10^{-3} s^{-1}, it is expected

that prismatic, $\langle c+a \rangle$ and basal slip operate, giving rise to the onset of recrystallization. However, at that same temperature and dynamic rates, the CRSS of pyramidal slip is still significantly higher than that of prismatic slip, and therefore only the latter and basal slip are active, resulting in a strong resistance to DRX, as is observed in the current study.

5.6. Influence of Rare Earth (RE) atoms in the incidence of basal slip and twinning at quasi-static rates.

It is well accepted that, in weakly textured Mg alloys with a grain size similar to that of the MN11 studied here (~10 μm), the CRSS of the various slip and twinning systems increase following the order $CRSS_{basal} < CRSS_{\{10\bar{1}2\}twinning} < CRSS_{prismatic} < CRSS_{pyramidal}$ [32,44,47] and, therefore, at room temperature and quasi-static rates, these materials deform mainly by basal slip and, to a smaller extent, by tensile twinning. The incidence of non-basal systems is, comparatively, negligible. The corresponding stress-strain curves have either a “concave-down” shape or a very subtle “concave-up” shape, depending on the relative twinning activity [104,148]. Our results reveal that the predominant deformation mechanisms during room temperature quasi-static deformation of the MN11 alloy are also tensile twinning and basal slip. However, the pronounced “concave-up” shape of the stress-strain curves indicates that tensile twinning is the main contributor to strain during the first stages of deformation [149]. We propose that this dramatically enhanced activity of tensile twinning may be due to the fact that, in this MN11 alloy, the critical resolved shear stress of basal slip is higher than that of tensile twinning. The increase in the CRSS of basal slip could be caused by the preferential location of Nd atoms along basal slip planes. Indeed, we have observed that there is a strong interaction between Nd atoms and dislocations, evidenced by the observation of DSA at 200°C

at quasi-static rates and of yield point phenomena at 300°C and 400°C at dynamic rates. The strong interaction could be due to the large radius of the Nd atoms (181 pm), comparable to that of other potent Mg strengtheners such as Ce (182.5 pm) and Gd (180.2 pm) [97]. As the testing temperature increases to 200°C the activity of twinning decreases, as thermal activation promotes diffusion of the Nd atoms, resulting in a decrease of the CRSS for basal slip.

Our results also reveal the activation of pyramidal slip during room temperature quasi-static deformation. This is evidenced, first, by the appearance of an intensity maximum at the center of the $(10\bar{1}3)$ pole figure after compression straining, which suggests $\langle c+a \rangle$ slip is active and, second, by the occurrence of grain subdivision during deformation. The formation of high angle boundaries by the progressive increase of misorientation of dislocation arrays was observed to be favored when dislocations with high stacking fault energy (such as prismatic or pyramidal ones) carried most of the strain. Galiyev et al. [85] have reported that the creation of a 3D network of high angle grain boundaries in Mg alloys is favored by the mutual interaction of dislocations of two different Burgers vectors ($\langle a \rangle$ and $\langle c+a \rangle$). The fact that grain subdivision takes place readily in the MN11 alloy, reveals, thus, the interaction between basal and pyramidal $\langle c+a \rangle$ dislocations and constitutes, therefore, further evidence of the activation of non-basal slip.

In conventional, weakly textured, Mg alloys, deformed at room temperature and quasi-static rates, the contribution of non-basal slip systems to strain is very minor, since the CRSS of basal slip is at least an order of magnitude smaller than those of non-basal slip. However, an enhanced activation of non-basal slip has been reported in several Mg alloys containing RE elements [87-88,96-98]. The origin of this

increased activity is still not clear. Chino et al. [87-88,96] and Sandlöbes et al. [96] suggested that the stacking fault energies of certain types of dislocations changed by the addition of Ce and Y, respectively, thus altering the critical resolved shear stresses of $\langle a \rangle$ and $\langle c+a \rangle$ slip. Robson et al. [98] carried out VPSC modeling to simulate the behavior of a Mg–6Y–7Gd–0.5wt% Zr alloy and found that the best fit was obtained when the relative CRSS of prismatic slip was significantly reduced with respect to that of a conventional alloy such as AZ31. Our results are consistent with these studies, in that they suggest an increased activity of non-basal slip with the addition of Nd but suggest, instead, that this is due to an increase of the CRSS of basal slip.

5.7. Influence of Rare Earth (RE) atoms in the incidence of basal slip and twinning under dynamic deformations.

The analysis of the mechanical behavior as well as of the microstructural evolution of this MN11 alloy deformed at high strain rates also reveals that the main deformation mechanisms are basal slip and tensile twinning. The additional contribution of pyramidal slip is also evidenced by the appearance of the texture intensity maxima at the center of the $(10\bar{1}3)$ pole figure in the samples deformed in compression and by the clustering of orientations near the $\langle 10\bar{1}0 \rangle$ pole in the samples deformed in tension.

The incidence of slip and twinning is different in compression and in tension tests, as evidenced by the “concave-up” shape of the compression stress-strain curves and the “concave-down” shape of the tension curves, which reveal that basal slip is a more important contributor to strain in tension and, in turn, twinning is enhanced in compression. This can be attributed to geometrical reasons as illustrated in figure 4.14, in which the inverse pole figure (extrusion

axis) of the as-received MN11 alloy has been superimposed to a schematic triangle showing the contours of constant resolved shear stress, i.e., constant Schmid factor, for basal slip. The contour corresponding to a Schmid factor of 0.5 denotes the orientations tilted 45° with respect to the $\langle 10\bar{1}0\rangle$-$\langle 11\bar{2}0\rangle$ boundary and with respect to the $\langle 0001\rangle$ pole. In compression, twinning would be favored in those grains in which the extrusion axis is parallel to the $\langle 10\bar{1}0\rangle$-$\langle 11\bar{2}0\rangle$ boundary and the likelihood of twinning will gradually decrease until it becomes zero in grains tilted 45° from this boundary due to the twinning polarity. Figure 4.14 shows that a large fraction of grains have orientations within the area of the triangle where twinning is favored (darker blue areas). However, in tension, twinning is favored in those grains in which the extrusion axis is parallel to the $\langle 0001\rangle$ boundary and, again, the likelihood of twinning decreases gradually until it becomes zero in grains tilted 45° from this boundary due to the twinning polarity. As can be seen in figure 4.14, twinning is thus not favored in tension in this MN11 alloy, even when the CRSS of basal slip would increase significantly.

Table 4.1 reveals that the yield strength in tension at room temperature and 10^3 s^{-1} is significantly higher than the compression yield strength under the same temperature and strain rate conditions (134 MPa vs. 100 MPa). Since basal slip appears the to be the main contributor to strain in tension, this difference in yield strengths is, again, consistent with an increase of the CRSS of basal slip due to the addition of Nd.

PART VI

CONCLUSIONS (CONCLUSIONES)

6. CONCLUSIONS

This doctoral thesis constitutes a study of the mechanical properties as well as on the deformation and recrystallization mechanisms of the commercial magnesium alloy Mg- Mg-3%wtAl-1%wtZn (AZ31) at high strain rates. Additionally, the effect of rare earth alloying additions on the mechanical behavior and on the incidence of the different deformation mechanisms has been analyzed at high and quasi-static strain rates. Finally, this study has been extended to two commercial alloys, Mg-9%wtAl-1%wtZn (AZ91D) and Mg-6%wtAl-0.5%wtMn (AM60B), processed by high pressure die casting, as this is currently the most relevant processing technology for Mg alloys. The main conclusions from this research work are the following:

6.1. In the AZ31 alloy, at high strain rates, the yield stress asymmetry as well as the in-plane and out-of-plane yield stress anisotropies retain relatively high values even at the highest temperatures investigated (400°C).

6.2. The rate of decrease of the CRSS of non-basal slip systems with temperature is much smaller at high strain rates than at low strain rates in the AZ31 Mg alloy. The CRSS of non-basal systems is still significantly higher than that of twinning and of basal systems at 400°C. At room temperature, the strain rate dependency of the CRSS of prismatic slip systems seems to be higher than that of pyramidal slip systems.

6.3. Tensile twinning is enhanced at high strain rates and remains the predominant deformation mechanism at the early stages of deformation in compression tests along the RD of an AZ31 Mg sheet even at very high temperatures (400°C). Compression and double twinning, however, have

been found to be basically strain-rate insensitive. The choice of tensile twinning at high strain rates may be attributed to the simpler atom shuffles involved.

6.4. The polarity of twinning may be inverted at dynamic rates. In particular, $\{10\bar{1}2\}$ twinning, which is well known to be a tension twin in the AZ31 alloy, has been observed to take place in grains in which the c-axes are compressed during dynamic compression along the normal direction.

6.5. Grain subdivision by the formation of geometrically necessary boundaries takes place readily in the AZ31 alloy during both quasi-static and dynamic deformation. The extent to which grain subdivision takes place depends on the relative orientation between the applied stress and the c-axes of the crystallites. This phenomenon is most pronounced in the sample tested in tension along RD since prismatic dislocations, which have high stacking fault energy, carry most of the strain up until failure. Grain subdivision is enhanced at low strain rates due to the easiness of thermal activation.

6.6. The DRX mechanisms and their kinetics depend on the operative deformation mechanisms and thus vary for different loading modes (tension, compression) as well as for different relative orientations between the loading axis and the c-axes of the grains. The highest resistance to dynamic recrystallization was found when the AZ31 Mg sheet was tested in tension along the RD, i.e., when prismatic slip predominates. Under these conditions, some recrystallized grains do appear at the latest stages of deformation (ε~0.20) as a result of rotational dynamic recrystallization (RDRX). DRX took place more readily under compression along the

RD, when twinning, $\langle c+a \rangle$ and basal slip operate. In this case, the main recrystallization mechanism is discontinuous dynamic recrystallization (DDRX).

6.7. The addition of rare earth elements (Nd) results in significant changes in the predominant deformation and recrystallization mechanisms. In particular, in the MN11 alloy, the critical resolved shear strength of basal slip increases to values similar or perhaps higher than that of tensile twinning. The increase in the CRSS of basal slip might be attributed to the preferential location of Nd atoms along basal planes.

6.8. The AZ91 and AM60 alloys, processed by high pressure die casting, possess good energy absorption capacity at high strain rates since the yield and maximum strengths do not decrease with increasing temperature as dramatically as at quasi-static rates and the strain to failure values remain fairly constant. The absence of any significant variability in the tensile ductility of these alloys at dynamic rates of, is attributed to the independence of the adiabatic shear failure mechanism of the porosity distribution.

6. CONCLUSIONES

En esta tesis doctoral se han estudiado las propiedades mecánicas así como los mecanismos de deformación y recristalización de la aleación comercial de magnesio Mg-3%pAl-1%pZn (AZ31) a alta velocidad de deformación. Así mismo, se ha analizado el efecto de la adición de tierras raras en el comportamiento mecánico y en la actividad de diferentes mecanismos de deformación en condiciones dinámicas y cuasiestáticas. Finalmente, se ha investigado el comportamiento mecánico en condiciones dinámicas en dos aleaciones comerciales, Mg-9%pAl-1%pZn (AZ91D) and Mg-6%pAl-0.5%pMn (AM60B), procesadas mediante colada por inyección a alta presión, la tecnología de procesado más importante para aleaciones de Mg. Las principales conclusiones de la presente tesis doctoral son las siguientes:

6.1. En la aleación AZ31, a altas velocidades de deformación, la asimetría en el límite elástico y las anisotropías del límite elástico en el plano y fuera del plano retienen valores relativamente altos incluso a las temperaturas más altas investigadas (400 ºC).

6.2. La tensión crítica de cizalla resuelta (*CRSS*) de los sistemas de deslizamiento no basales disminuye con la temperatura más lentamente a altas velocidades de deformación que a velocidades cuasi-estáticas para la aleación de Mg AZ31. Así, la *CRSS* de los sistemas no basales es aún significativamente mayor que la del maclado y la de los sistemas basales a 400ºC a velocidades de impacto. A temperatura ambiente, la dependencia de la *CRSS* de los sistemas de deslizamiento prismáticos con la velocidad de

deformación parece ser mayor que la de los sistemas de deslizamiento piramidales.

6.3. El maclado de extensión se favorece a altas velocidades de deformación y permanece como mecanismo de deformación predominante durante los primeros estadios de deformación en ensayos de compresión a lo largo de *RD* de una chapa laminada de aleación de Mg AZ31 incluso a temperaturas muy altas (400 ºC). Sin embargo la actividad del maclado de compresión y la del maclado secundario parecen no ser tan sensibles a la velocidad de deformación. La preferencia del maclado de extensión a altas velocidades de deformación se puede atribuir a que este mecanismo conlleva un menor reajuste atómico que los otros dos.

6.4. La polaridad del maclado de extensión se puede invertir a altas velocidades de deformación. En particular, éste se ha observado en algunos granos en los cuales se produce una deformación de compresión a lo largo del eje “c” durante ensayos de compresión dinámica a lo largo de la dirección normal de laminación para una chapa de aleación AZ31.

6.5. El proceso de subdivisión de granos debida a la formación de fronteras geométricamente necesarias tiene lugar en la aleación AZ31 deformada tanto en condiciones dinámicas como cuasiestáticas. El grado de subdivisión de los granos depende de la orientación relativa entre la carga aplicada y el eje “c” de los cristales. Así, este fenómeno es más pronunciado en muestras ensayadas en tensión a lo largo de la dirección de laminación (*RD*) debido a que el mecanismo de deformación predominante hasta la fractura es el deslizamiento prismático y a que las dislocaciones que se deslizan en planos prismáticos tienen alta energía de

falla de apilamiento. La subdivisión de grano se favorece a bajas velocidades de deformación debido a que, en estas condiciones se favorecen los procesos de deslizamiento cruzado, que se activan térmicamente.

6.6. Los mecanismos de recristalización dinámica (*DRX*) y su cinética dependen de los mecanismos de deformación operativos y, así, varían según sea el modo de carga (tensión, compresión) y la orientación relativa entre el eje de carga y el eje “c” de los granos. La mayor resistencia a la recristalización dinámica fue hallada cuando el material se ensayó en tracción a lo largo de *RD*, es decir, cuando predomina el deslizamiento prismático. En estas condiciones, algunos granos recristalizados aparecen en los últimos estadios de la deformación ($\varepsilon \sim 0.20$) como resultado de la recristalización dinámica rotacional (*RDRX*). La recristalización dinámica se produce más fácilmente cuando la aleación AZ31 se deforma en compresión a lo largo de la dirección de laminación, es decir, cuando se activan el maclado, el deslizamiento <c+a> y el deslizamiento basal. En este caso, el mecanismo de recristalización predominante es recristalización dinámica discontinua (*DDRX*).

6.7. La adición de elementos de tierras raras (Nd) da lugar a un cambio significativo de los mecanismos de deformación y de recristalización predominantes. En particular, en la aleación MN11, la tensión crítica de cizalla resuelta del deslizamiento basal aumenta hasta alcanzar valores comparables a los del maclado de extensión. El incremento en la *CRSS* del deslizamiento basal se puede atribuir a la ubicación preferencial de los átomos de Nd a lo largo de los planos basales.

6.8. Las aleaciones AZ91 y AM60, procesadas mediante colada por inyección a alta presión, poseen buena capacidad de absorción de energía a altas velocidades de deformación ya que el límite elástico y la tensión máxima no disminuyen cuando aumenta la temperatura tan drásticamente como a velocidades cuasi-estáticas y los valores de deformación a fractura permanecen prácticamente constantes. La poca variabilidad de la elongación a fractura de estas aleaciones a alta velocidad de deformación se puede atribuir a la independencia de los mecanismos de fallo de cizalla adiabática de la distribución de la porosidad.

PART VII

FURTHER WORK

7. FURTHER WORK.

This work has raised new questions and has motivated numerous opportunities for further research in magnesium alloys. Some areas of further work currently contemplated are listed below:

- Study of the incidence of different twinning modes and of the occurrence of specific recrystallization mechanisms at dynamic rates in Mg as a function of alloy composition and grain size.
- Analysis of the deformation and recrystallization mechanisms of Mg alloys with different amounts of selected rare earth elements under a wide range of temperatures and strain rates. Various alloys will be processed using different extrusion conditions including several extrusion ratios at selected temperatures. The dependency of the critical resolved shear stresses of basal slip and twinning on the processing conditions and on the alloy composition will be investigated.
- Investigation of the relationship between the processing conditions, the microstructure and the mechanical behavior of high pressure die cast alloys. An attempt will be made to quantify mechanical properties such as the hardness and the yield stress as a function of the grain size, the distribution of the beta phase and the porosity distribution.

PARTE VIII

REFERENCES

8. REFERENCES

[1] UTTLEY C. *"The elements: Magnesium"*. Marshal Cavendish Corporation. Nueva York. (2000). Pp. 4.

[2] EASTON M, BEER A, BARNETT M, DAVIES C, DUNLOP G, DURANDET Y, BLACKET S, HILDITCH T, BEGGS P. "*Magnesium Alloy Applications in Automotive Structures*" JOM 2008;60:57.

[3] MORDIKE B.L., EBERT T. "*Magnesium Alloy Applications in Automotive Structures*" . Mater Sci Eng 2001;302:37.

[4] DOEGE E, DRÖDER K., JANSSEN ST. "*Deformation of Magnesium*". En: Magnesium Alloys and Technologies. Kainer KU [Ed.] Wiley-VCH. Geesthacht. 2003. (285 p.) Pp. 73.

[5] BAMBERGER M, DEHM G. "*Trends in the Development of New Mg Alloys*". Annu Rev Mater Res 2008; 38:505.

[6] WATARAI H. "*Trend of research and Development for Magnesium Alloys"*. Science & Technology Trends. 2006;18:84

[7] MANI G., FELDMAN M.D., PATEL D., MAULI AGRAWAL C. "*Coronary stents: A materials perspective*". Biomat. 2007; 28:1689

[8] AVEDESIAN, M. "*Magnesium and Magnesium Alloys"*. American Society for Metals. United States of America. 1999. (314 p.) Pp. 7-15, 258-263.

[9] CALLISTER W., "*Introducción a la Ciencia e Ingeniería de los Materiales"* Vol.1. Ed. Reverté. Barcelona (2009). (459 p.) Pp. 37

[10] FRIEDRICH H E.; MORDIKE, B L (Eds.) "*Magnesium Technology: metallurgy, design data, applications*". Ed. Springer. (2006), XXII. (677 p.) Pp. 146

[11] GEHRMANN R., FROMMERT M.M., GOTTSTEIN G. "*Texture effects on plastic deformation of magnesium*". Mater Sci Eng 2005;395:338.

[12] AL-SAMMAN T, GOTTSTEIN G. "*Room temperature formability of a magnesium AZ31 alloy: Examining the role of texture on the deformation mechanisms*". Mater Sci Eng 2008;488:406.

[13] KIM W.J., HONG S.I., KIM Y.S., MIN S.H., JEONG H.T., LEE JD. "*Texture development and its effect on mechanical properties of an AZ61 Mg alloy fabricated by equal channel angular pressing*". Acta mater 2003; 51:3293

[14] WANG Y.N., HUANG J.C. "*Texture analysis in hexagonal materials*". Mater Chem and Phys 2003; 81:11

[15] GRAFF S. "*Micromechanical modeling of the deformation of HCP Metals*". Ed. GKSS. Geesthacht (2008). (117p.) Pp. 1-3

[16] MAYAMA T, AIZAWA K, TADANO Y, KURODA M. "*Influence of twinning deformation and lattice rotation on strength differential effect in polycrystalline pure magnesium with rolling texture*" Comp. Mat. Sci 2009; 47: 448

[17] COULING S.L.,PASHAK J.F., STURKEY L. "*Unique deformation and aging characteristics of certain magnesium-based alloys*". Trans ASM 1959;51:94.

[18] KOCKS U.F., WESTLAKE D.G "*The Importance of Twinning for the Ductility of CPH Polycrystals*". Trans AIME 1967;239:1107.

[19] Kelley EW, Hosford WF. "*Deformation characteristics of textured magnesium*" Trans AIME 1968;242:654.

[20] COURET A, CAILLARD D. "*An in situ study of prismatic glide in magnesium—II. Microscopic activation parameters*". Acta metal 1985;33:1455.

[21] CHIN GY, MAMMEL WL. "*Competition among basal, prism, and pyramidal slip modes in HCP metals*". Metall Trans 1970;1:357.

[22] YOO MH. "*Slip, twinning and fracture of in hexagonal closed-packed metals*" Metall Trans 1981;12A:409.

[23] VAGARALI SS, LANGDON TG. "*Deformation mechanisms in h.c.p. metals at elevated temperatures—I. Creep behavior of magnesium*" Acta Metall 1981;29:1969.

[24] ZELIN MG, YANG HS, VALIEV RZ, MUKHERJEE AK. "*Interaction of high temperature deformation mechanisms in a magnesium alloy with mixed fine and coarse grains*". Metall Trans 1992;23:3135.

[25] MUNROE N, TAN X. "*Orientation dependence of slip and twinning in HCP metals*". Scripta Mater 1997;36:1383.

[26] AGNEW SR, YOO MH, TOMÉ CN. "*Application of texture simulation to understanding mechanical behavior of Mg and solid solution alloys containing Li or Y*". Acta mater 2001;49:4277.

[27] WATANABE H, TSUTSUI H, MUKAI T, KOHZU M, TANABE S, HIGASHI K. "*Deformation mechanism in a coarse-grained Mg–Al–Zn alloy at elevated temperatures*" Int J Plasticity 2001;17:387.

[28] Barnett MR. "*Influence of deformation conditions and texture on the high temperature flow stress of magnesium AZ31*". J Light Metals 2001;1:167.

[29] AGNEW S.R., TOMÉ C.N., BROWN D.W., HOLDEN T.M., VOGEL S.C. "*Study of slip mechanisms in a magnesium alloy by neutron diffraction and modeling*". Scripta Mater 2003; 48:1003.

[30] GALIYEV A, SITDIKOV O, KAIBYSHEV R. "*Deformation behavior and controlling mechanisms for plastic flow of magnesium and magnesium alloy*". Mater Trans 2003; 44:426.

[31] KOIKE J, KOBAYASHI T, MUKAI T, WATANABE H, SUZUKI M, MARUYAMA K, HIGASHI K. "*The activity of non-basal slip systems and dynamic recovery at room temperature in fine-grained AZ31B magnesium alloys*" Acta mater 2003;51:2055.

[32] BARNETT MR. *"A Taylor model based description of the proof stress of magnesium AZ31 alloy during hot working,"* Metall Mater Trans 2003; 34:1799.

[33] BARNETT M.R., KESHAVARZ Z., BEER A.G., ATWELL D. "*Influence of grain size on the compressive deformation of wrought Mg–3Al–1Zn*". Acta Mater 2004; 52:5093.

[34] AGNEW SR, DUYGULU Ö. "*Plastic anisotropy and the role of non-basal slip in magnesium alloy AZ31B*". Int J Plasticity 2005;21:1161.

[35] DEL VALLE J.A., PÉREZ-PRADO M.T., RUANO O.A. "*Deformation mechanisms responsible for the high ductility in a Mg AZ31 alloy analyzed by electron backscattered diffraction*". Metall Mater Trans 2005; 36:1427.

[36] KESHAVARZ Z., BARNETT M.R. "*EBSD analysis of deformation modes in Mg–3Al–1Zn*". Scripta mater 2006;55:915.

[37] MEZA-GARCÍA E., DOBROŇ P., BOHLEN J., LETZIG D., CHMELIK F., LUKÁČ P., KAINER K.U. "*Deformation mechanisms in an AZ31 cast magnesium*

alloy as investigated by the acoustic emission technique".Mater Sci Eng 2007; 462: 297.

[38] BARNETT M.R. "*Twinning and the ductility of magnesium alloys: Part I: "Tension" twins*". Mater Sci Eng 2007;464:1.

[39] DEL VALLE J.A., RUANO O.A. "*Separate contributions of texture and grain size on the creep mechanisms in a fine-grained magnesium alloy*". Acta mater 2007;55:455.

[40] CHINO Y., KIMURA K., MABUCHI M. "*Twinning behavior and deformation mechanisms of extruded AZ31 Mg alloy*". Mater Sci Eng 2008;486:481.

[41] JAIN A., DUYGULU O., BROWN D.W., TOMÉ C.N., AGNEW S.R. "*Grain size effects on the tensile properties and deformation mechanisms of a magnesium alloy, AZ31B,* sheet*".* Mater Sci Eng 2008;486:545.

[42] HUTCHINSON B, BARNETT MR, GHADERI A, CIZEK P, SABIROV I. "*Deformation modes and anisotropy in magnesium alloy AZ31*". Int J Mat Res 2009;100:556.

[43] BALL E.A., PRANGNELL P.B. "*Tensile-compressive yield asymmetries in high strength wrought magnesium alloys*". Scripta Metall Mater 1994;31:111.

[44] LOU X.Y., LI M., BOGER R.K., AGNEW S.R., WAGONER R.H. "*Hardening evolution of AZ31B Mg sheet*". Int J Plasticity 2007; 23:44.

[45] CHRISTIAN J.W., MAHAJAN S. "*Deformation Twinning*". Prog Mater Sci 1995;39:1.

[46] BARNETT M.R. "*Twinning and the ductility of magnesium alloys: Part II: "Contraction" twins*". Mater Sci Eng 2007;464:8.

[47] CHAPUIS A., DRIVER J.H. "*Temperature dependency of slip and twinning in plane strain compressed magnesium single crystals*". Acta Mater 2011; 59:1986.

[48] HUTCHINSON B., BARNETT M.R. "*Effective values of critical resolved shear stress for slip in polycrystalline magnesium and other hcp metals*". Scripta Mater 2010;63:737.

[49] WONSIEWICZ B.C., BACKOFEN W.A. "*Plasticity of magnesium crystal*". Trans AIME. 1967; 239:1422.

[50] HARTT W.H., REED-HILL R.E. " *Internal deformation and frature of second order [1011]-[1112] twins in magnesium*". Trans AIME. 1968; 242:1127.

[51] HARTT W.H., REED-HILL R.E. "*Irrational habit of second-order (1011)-(1012) twins in magnesium*". Trans AIME. 1967; 239:1511.

[52] NAVE M.D., BARNETT M.R., "*Microstructures and textures of pure magnesium deformed in plane-strain compression*". Scripta Mater 2004; 51:881.

[53] BARNETT M.R., NAVE M.D., BETTLES C.J. "*Deformation microstructures and textures of some cold rolled Mg alloys*". Mater Sci Eng 2004; 386:205.

[54] CIZEK P., BARNETT M.D. "*Characteristics of the contraction twins formed close to the fracture surface in Mg-3Al-1Zn alloy deformed in tension*". Scripta Mater 2008; 59:959.

[55] KNEZEVIC M., LEVINSON A., HARRIS R., MISHRA R.K., DOHERTY R.D., KALIDINDI S.R. "*Deformation twinning in AZ31: Influence on strain hardening and texture evolution*". Acta Mater 2010; 58:6230

[56] ISHIKAWA K, WATANABE H, MUKAI T. "*High strain rate deformation behavior of an AZ91 magnesium alloy at elevated temperatures*". Mat Lett 2005;59:1511.

[57] ISHIKAWA K., WATANABE H., MUKAI T. "*High temperature compressive properties over a wide range of strain rates in an AZ31 magnesium alloy*". J Mat Sci 2005;40:1577.

[58] WATANABE H, ISHIKAWA K. "*Effect of texture on high temperature deformation behavior at high strain rates in a Mg–3Al–1Zn alloy*". Mater Sci Eng 2009;523:304.

[59] ULACIA I., SALISBURY C.P., HURTADO I., WORSWICK M.J. "*Tensile characterization and constitutive modeling of AZ31B magnesium alloy sheet over wide range of strain rates and temperatures*" J Mater Proc Technol 2011; 211:830.

[60] EL-MAGD E, ABOURIDOUANE M. "*Influence of Strain Rate and temperature on the compressive ductility of Al, Mg and Ti alloys*". J. Phys IV France. 2003;110:15.

[61] MURR L.E., PIZAÑA C. "*Dynamic recrystallization: The dynamic deformation regime*". Metall Trans A 2007; 38:2611

[62] ZOU D.L., ZHEN L., ZHU Y., XU C.Y., SHAO W.Z., PANG B.J. "*Deformed microstructure and mechanical properties of AM60B magnesium alloy under hypervelocity impact at a velocity of 4 km s−1*". Mater Sci Eng 2010; 527:3323.

[63] RITTEL D., WANG Z.G. "*Thermo-mechanical aspects of adiabatic shear failure of AM50 and Ti6Al4V alloys*". Mech Mater 2008; 40: 629.

[64] WAN G, WU BL, ZHAO YH, ZHANG YD, ESLING C. "*Strain-rate sensitivity of textured Mg–3.0Al–1.0Zn alloy (AZ31) under impact deformation*". Scripta mater 2011; 65:461-464.

[65] WU BL, WAN G, ZHANG YD, ESLING C. "*Twinning characteristics in textured AZ31 alloy under impact loading along specified direction*". Mat Lett 2010; 64:636-639.

[66] TUCKER M.T., HORSTEMEYER M.F., GULLETT P.M., EL KADIRI H., WHITTINGTON W.R. "*Anisotropic effects on the strain rate dependence of a wrought magnesium alloy*". Scripta mater 2009;60:182.

[67] STANFORD N., SOTOUDEH K., BATE P.S. "*Deformation mechanisms and plastic anisotropy in magnesium alloy AZ31*". Acta Mater 2011; 59:4866.

[68] KHAN A.S., PANDEY A., GNÄUPEL-HEROLD T., MISHRA R.K. "*Mechanical response and texture evolution of AZ31 alloy at large strains for different strain rates and temperatures*". Int J Plas 2011; 27:688

[69] AL-SAMMAN T., LI X., CHOWDURY S.G. "*Orientation dependent slip and twinning during compression and tension of strongly textured magnesium AZ31 alloy*" Mater Sci Eng A 2010; 527:3450.

[70] ION S.E., HUMPHREYS F.J., WHITE S.H. "*Dynamic recrystallisation and the development of microstructure during the high temperature deformation of magnesium*" Acta metall 1982; 30:1909.

[71] KAIBYSHEV R., GALIYEV A.M., SOKOLOV B.K, "*Effect of grain size on the plastic deformation and dynamic recrystallization of a magnesium alloy*".Phys Met Metallog 1994; 78:209.

[72] KAIBYSHEV R., SOKOLOV B., GALIYEV A. "*The Influence of Crystallographic Texture on Dynamic Recrystallization*".Textures and Microstructures. 1999;32:47.

[73] MYSHLYAEV M.M., MCQUEEN H.J., MWEMBELA A., KONOPLEVA E. "*Twinning, dynamic recovery and recrystallization in hot worked Mg–Al–Zn alloy*". Mater Sci Eng 2002;337:121.

[74] TAN J.C., TAN M.J. "*Dynamic continuous recrystallization characteristics in two stage deformation of Mg–3Al–1Zn alloy sheet*" Mater Sci Eng A 2003; 339:124

[75] DEL VALLE J.A., PÉREZ-PRADO M.T., RUANO O.A. "*Texture evolution during large-strain hot rolling of the Mg AZ61 alloy* ". Mat Sci Eng 2003; 355:68.

[76] BARNETT M.R., BEER A.G., ATWELL D., OUDIN A. "*Influence of grain size on hot working stresses and microstructures in Mg–3Al–1Zn*". Scripta Mater 2004; 51:19

[77] YI S., ZAEFFERER S., BROKMEIER H.G. "*Mechanical behavior and microstructural evolution of magnesium alloy AZ31 in tension at different temperatures*" Mater Sci Eng A 2006; 424:275.

[78] AL-SAMMAN T., GOTTSTEIN G. "*Dynamic recrystallization during high temperature deformation of magnesium*".Mater Sci Eng 2008;490:411.

[79] DEL VALLE J.A., RUANO O.A. "*Influence of texture on dynamic recrystallization and deformation mechanisms in rolled or ECAPed AZ31 magnesium alloy*". Mater Sci Eng 2008;487:473.

[80] MARTIN E., JONAS J.J. "*Evolution of microstructure and microtexture during the hot deformation of Mg–3% Al*". Acta mater 2010; 58:4253.

[81] SUN K., CHANG C.P., KAO P.W. "*Microstructural study of strain localization in hot compressed Mg–3Al–1Zn alloy*" . Mater Sci Eng A 2010; 527:7050.

[82] LIU Z., BAI S., KANG S. "*Low-temperature dynamic recrystallization occurring at a high deformation temperature during hot compression of twin-roll-cast Mg–5.51Zn–0.49Zr alloy*". Scripta mater 2009; 60:403.

[83] DOHERTY R.D., HUGHES D.A., HUMPHREYS F.J., JONAS J.J., JUUL JENSEN D., KASSNER M.E., KING W.E., MCNELLEY T.R., MCQUEEN H.J., ROLLETT A.D. "*Current issues in recrystallization: a review*" . Mater Sci Eng A 1997; 238:219.

[84] HUMPHREYS F.J., HATHERLY M. "*Recrystallization and related annealing phenomena*". Pergamon, 1995.

[85] GALIYEV A., KAIBYSHEV R., GOTTSTEIN G. "*Correlation of plastic deformation and dynamic recrystallization in magnesium alloy ZK60*". Acta mater 2001;49:1199.

[86] BOHLEN J., NÜRNBERG M.R., SENN J.W., LETZIG D., AGNEW S. "*The texture and anisotropy of magnesium–zinc–rare earth alloy sheets*". Acta Mater 2007; 55:2101.

[87] CHINO Y., KADO M., MABUCHI M." *Compressive deformation behavior at room temperature – 773 K in Mg–0.2 mass%(0.035at.%)Ce alloy*". Acta Mater 2008;56:387.

[88] CHINO Y., KADO M., MABUCHI M. "*Enhancement of tensile ductility and stretch formability of magnesium by addition of 0.2 wt%(0.035 at%)Ce*". Mater Sci Eng 2008;494:343.

[89] MISHRA R.K., GUPTA A.K., RAMA RAO P., SACHDEV A.K., KUMAR A.M., LUO A.A."*Influence of cerium on the texture and ductility of magnesium extrusion*". Scripta mater 2008;59:562.

[90] MACKENZIE L.W.F., PEKGULERYUZ M.O. "*The recrystallization and texture of magnesium–zinc–cerium alloys*" Scripta Mater 2008;59:665.

[91] COTTAM R., ROBSON J., LORIMER G., DAVIS B. "*Dynamic recrystallization of Mg and Mg–Y alloys: Crystallographic texture development*". Mater Sci Eng 2008;485:375.

[92] STANFORD N., ATWELL D., BEER A., DAVIS C. AND BARNETT M.R. "*Effect of microalloying with rare-earth elements on the texture of extruded magnesium-based alloys*" Scripta Mater 2008; 59:772.

[93] STANFORD N. "*Micro-alloying Mg with Y, Ce, Gd and La for texture modification—A comparative study*". Mater Sci Eng 2010; 527:2669.

[94] STANFORD N., ATWELL D., BARNETT R. "*The effect of Gd on the recrystallisation, texture and deformation behavior of magnesium-based alloys*". Acta Mater 2010; 58:6773.

[95] BOHLEN J., YI S., LETZIG D., KAINER K.U. "*Effect of rare earth elements on the microstructure and texture development in magnesium–manganese alloys during extrusion*". Mater Sci Eng A 2010; 527:7092.

[96] SANDLÖBES S., ZAEFFERER S., SCHESTAKOW I., YI S., GONZÁLEZ-MARTÍNEZ R. "*On the role of non-basal deformation mechanisms for the ductility of Mg and Mg–Y alloys*". Acta Mater 2011; 59:429.

[97] JIANG L., JONAS J.J., MISHRA R. "*Effect of dynamic strain aging on the appearance of the rare earth texture component in magnesium alloys*". Mater Sci Eng 2011;528:6596.

[98] ROBSON J.D., TWIER A.M., LORIMER G.W., ROGERS P. "*Effect of extrusion conditions on microstructure, texture, and yield asymmetry in Mg–6Y–7Gd–0.5 wt%Zr alloy*"Mater Sci Eng 2011;528:7247

[99] AL-SAMMAN T., LI X. "*Sheet texture modification in magnesium-based alloys by selective rare earth alloying*" Mater Sci Eng 2011; 528:3809.

[100] STANFORD N., SABIROV I., SHA G., LA FONTAINE A., RINGER S.P., BARNETT M.R. "*Effect of Al and Gd solutes on the strain rate sensitivity of magnesium alloys*. Metall Mater Trans 2010;41:734.

[101] ZHU S.M., NIE J.F. "*Serrated flow and tensile properties of a Mg–Y–Nd alloy*". Scripta Mater 2004;50:51.

[102] AGNEW S.R., SENN J.W., HORTON J.A."*Mg Sheet Metal Forming: Lessons Learned from deep drawing Li and Y Solid-Solution Alloys*". JOM 2006;58:62.

[103] STANFORD N., SHA G., XIA J., RINGER S.P., BARNETT M.R. "*Solute segregation and texture modification in an extruded magnesium alloy containing gadolinium*" Scripta Mater 2011;65:919.

[104] LEE S.G., PATEL G.R., GOKHALE A.M., SREERANGANATHAN A., HORSTEMEYER M.F. "*Variability in the tensile ductility of high-pressure die-cast AM50 Mg-alloy*". Scripta Mater 2005; 53:851-856.

[105] WEILER J.P., WOOD J.T. "*Modeling fracture properties in a die-cast AM60B magnesium alloy: I-Analytical failure model*". Mater Sci Eng 2009; 527:25-31.

[106] WEILER J.P., WOOD J.T. "*Modeling fracture properties in a die-cast AM60B magnesium alloy: II-The effects of the size and location of porosity determined using finite element simulations*". Mater Sci Eng 2009; 527:32-37.

[107] LEE C.D. "*Dependence of tensile properties of AM60 magnesium alloy on microporosity and grain size*". Mater Sci Eng 2007; 454-455:575-580.

[108] WEILER J.P., WOOD J.T., KLASSEN R.J., MAIRE E., BERKMORTEL R., WANG G. "*Relationship between internal porosity and fracture strength of die-cast magnesium AM60B alloy*". Mater Sci Eng 2005; 395:315-322.

[109] WEI Y.H., HOU L.F., YANG L.J., XU B.S., KOZUKA M., ICHINOSE H. "*Microstructures and properties of die casting components with various thicknesses made of AZ91D alloy*". J Mater Proc Tech 2009; 209:3278-3284.

[110] PRAKASH D.G.L., REGENER D., VORSTER W.J.J. "*Effect of position on the tensile properties in high-pressure die cast Mg alloy*". J Alloys Comp 2009; 470:111-116.

[111] SONG J., XIONG S.M., LI M., ALLISON J. "*The correlation between microstructure and mechanical properties of high-pressure die-cast AM50 alloy*". J Alloys Comp 2009; 477:863-869.

[112] DØRUM C., HOPPERSTAD O.S., BERSTAD T., DISPINAR D. "*Numerical modelling of magnesium die-castings using stochastic fracture parameters*". Eng Fract Mech 2009; 76:2232-2248.

[113] MAYER H., PAPAKYRIACOU M., ZETTL B., STANZL-TSCHEGG S.E. "*Influence of porosity on the fatigue limit of die cast magnesium and aluminium alloys"*. Int J Fatigue 2003; 35:245-256.

[114] LEE SG, GOKHALE AM, PATEL GR, EVANS M. "*Effect of process parameters on porosity distributions in high-pressure die-cast AM50 Mg-alloy*". Mater Sci Eng 2006; 427:99-111.

[115] LEE SG, GOKHALE AM. "*Formation of gas induced shrinkage porosity in Mg-alloy high-pressure die-castings*". Scripta Mater 2006; 55:387-390.

[116] SONG QW, BEGGS P, EASTON M. "*Compressive strain-rate sensitivity of magnesium–aluminum die casting alloys*". Materials & Design 2009; 30:642-648.

[117] WATANABE H., ISHIKAWA K., MUKAI T. "*High strain rate deformation behavior of Mg–Al–Zn alloys at elevated temperatures*". Key Eng Mater 2007;340-341:107

[118] MUKAI T., MOHRI T., MABUCHI M., NAKAMURA M., ISHIKAWA K., HIGASHI K. "*Experimental study of a structural magnesium alloy with high absorption energy under dynamic loading*". Scripta mater 1998;39:1249.

[119] MUKAI T., YAMANOI M., YIGASHI K. "*ductility enhancement in magnesium alloys under dynamic loading*". Mater Sci Forum 2000;350-351:97.

[120] YOKOHAMA T. "*Impact Tensile Stress–strain Characteristics of Wrought Magnesium Alloys*". Strain 2003;39:167.

[121] SHU D.W., ZHOU W., MA G.W. "*Tensile Mechanical Properties of AM50A Alloy by Hopkinson Bar*". Key Eng Mater 2007;340-341:247.

[122] EL-MAGD E., ABOURIDOUANE M. "*Characterization, modelling and simulation of deformation and fracture behavior of the light-weight wrought alloys under high strain rate loading*". Int J Impact Eng 2006;32:741.

[123] LI B., JOSHI S., AZEVEDO K., MA E., RAMESH K.T., FIGUEIREDO R.B., LANGDON T.G. "*Dynamic testing at high strain rates of an ultrafine-grained magnesium alloy processed by ECAP*". Mater Sci Eng 2009;517:24.

[124] Hielscher R., Mtex Software, TU Chemnitz, Germany.

[125] Fernández A., Pérez-Prado M.T., Jérusalem A. "*Continuum modeling of the response of a Mg alloy AZ31 rolled sheet during uniaxial deformation*" . Int J Plast 2011; 27:1739-1757

[126] ROBINSON J.M., SHAW M.P. "*Microstructure and mechanical influences on dynamic strain aging phenomena*". Int Mater Rev 1994; 39(3):113-122.

[127] Calnan E.A., Clews C.J.B. "*The development of deformation textures in metals Part III. Hexagonal structures*". Phil Mag. Ser. 7 1951; 42(331):919-931

[128] JÉRUSALEM A, FERNÁNDEZ A, PÉREZ-PRADO MT. "*Modelización del maclado* $\{10\bar{1}2\}$ *de una chapa laminada de Mg-3%Al-1%Zn*" Rev. Metal. Madrid. 2010;46:133.

[129] HONG S.G., PARK S.H., LEE C.S. "*Role of $\{10\bar{1}2\}$ twinning characteristics in the deformation behavior of a polycrystalline magnesium alloy*" Acta mater 2010; 58:5873-5885.

[130] POLMEAR I.J. "*Light Alloys*". Ed. Edward Arnold, London, UK, 1989, p.190

[131] MEYERS M.A. "*Dynamic behavior of materials*". JJohn Wiley & Sons, New York, 1994.

[132] ARMSTRONG R.W., WALLEY S.M. "*High strain rate properties of metals and alloys*" Int Mater Rev 2008;53:105-128.

[133] PADILLA H.A., SMITH C.D., LAMBROS J., BEAUDOIN A.J., ROBERTSON I.M., "*Effects of Deformation Twinning on Energy Dissipation in High Rate Deformed Zirconium*" Metall Mater Trans 2007; 38A:2916-2927.

[134] GURAO N.P., KAPOOR R, SUWAS S. "*Deformation behaviour of commercially pure titanium at extreme strain rates*" Acta Mater 2011; 59: 3431-3446

[135] NEMAT-NASSER S., GUO W.G., CHENG J.Y. "*Mechanical properties and deformation mechanisms of a commercially pure titanium*" Acta Mater 1999; 47:3705-3720.

[136] JASWON M. A.; DOVE D. B. "*Twinning properties of lattice planes*". Acta Cryst 1956; 9:621-626

[137] BILBY B.A., CROCKER A.G. "*The Theory of the Crystallography of Deformation Twinning*" Proc Roy Soc 1965; 288:240-255

[138] SERRA A., BACON D.J. "*Modelling the motion of $\{11\bar{2}2\}$ twinning dislocations in the HCP metals*" Mater Sci Eng A 2005; 400–401: 496-498.

[139] LI B., MA E. "*Atomic Shuffling Dominated Mechanism for Deformation Twinning in Magnesium*". Phys Rev Lett 2009; 103:035503.

[140] SERRA A., BACON D.J., POND R.C., Comment on "*Atomic Shuffling Dominated Mechanism For Deformation Twinning In Magnesium*" Phys Rev Lett 2010; 104:029603.

[141] CABIBBO M., BLUM W., EVANGELISTA E., KASSNER M.E. AND MEYERS M.A., "*Transmission Electron Microscopy Study of Strain-Induced Low- and High-Angle Boundary Development in Equal-Channel Angular-*

Pressed Commercially Pure Aluminum" Metall. and Mater. Trans. 39, pp. 181-189, 2008.

[142] WEN L., CHEN P., TONG Z.F., TANG B. Y., PENG L.M., DING W.J., "*A systematic investigation of stacking faults in magnesium via first-principles calculation*". Eur Phys J B 2009; 72:397-403.

[143] SMITH A.E., "*Surface, interface and stacking fault energies of magnesium from first principles calculations*". Surface Sci 2007; 601: 5762-5765

[144] YI S., SCHESTAKOW I., ZAEFFERER S. "*Twinning-related microstructural evolution during hot rolling and subsequent annealing of pure magnesium*". Mater Sci ·ng 2009; 516:58-64.

[145] ZHU S.Q., YAN H.G., CHEN J.H., WU Y.Z., LIU J.Z., TIAN J. "*Effect of twinning and dynamic recrystallization on the high strain rate rolling process*". Scripta Mater 2010; 63:985-988.

[146] SITDIKOV O., KAIBYSHEV R., SAKAI T. "*Dynamic Recrystallization Based on Twinning in Coarse-Grained Mg*". Mater Sci Forum 2003; 419-422: 521-526

[147] SITDIKOV O., KAIBYSHEV R. "*Dynamic recrystallization in pure magnesium*" Mater Trans 2001; 42:1928-1937.

[148] RAEISINIA B., AGNEW S.R. "*Using polycrystal plasticity modeling to determine the effects of grain size and solid solution*

[149] BARNETT MR, NAVE MD, GHADERI A. "*Yield point elongation due to twinning in a magnesium alloy*" Acta mater 2012;60:1433-1443.

PART IX

APPENDICES

9. APPENDICES.

This appendix comprises, first, the stress-strain curves of several tests that were finally not included in the manuscript (section 9.1). In particular, data are presented for AM60 samples machined out of an automotive component processed by die casting and AM60 and AZ91 samples machined out of ingots processed by gravity casting. Additionally, it includes the tabulated mechanical properties corresponding to all the tests carried out (section 9.2). This information is thought useful for anyone wishing to know the mechanical response of several Mg alloys under a wide range of testing conditions.

9.1. Stress-strain curves

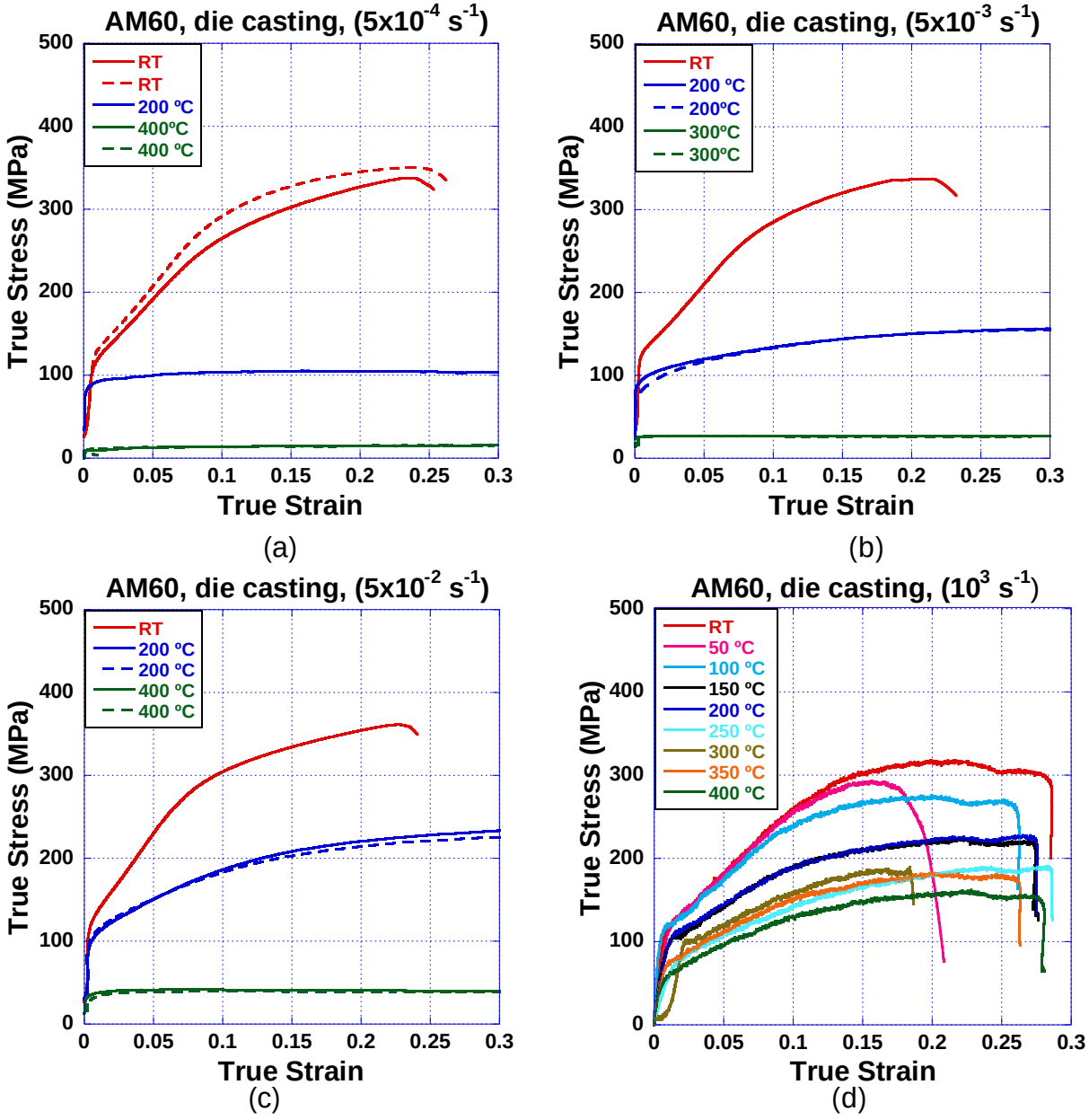

Figure 9.1. True stress – true strain curves corresponding to an AM60 automotive part processed by die casting and tested in compression at different strain rates: a) $5x10^{-4}$ s^{-1}, b) $5x10^{-3}$ s^{-1}, c) $5x10^{-2}$ s^{-1}, d) 10^{3} s^{-1}.

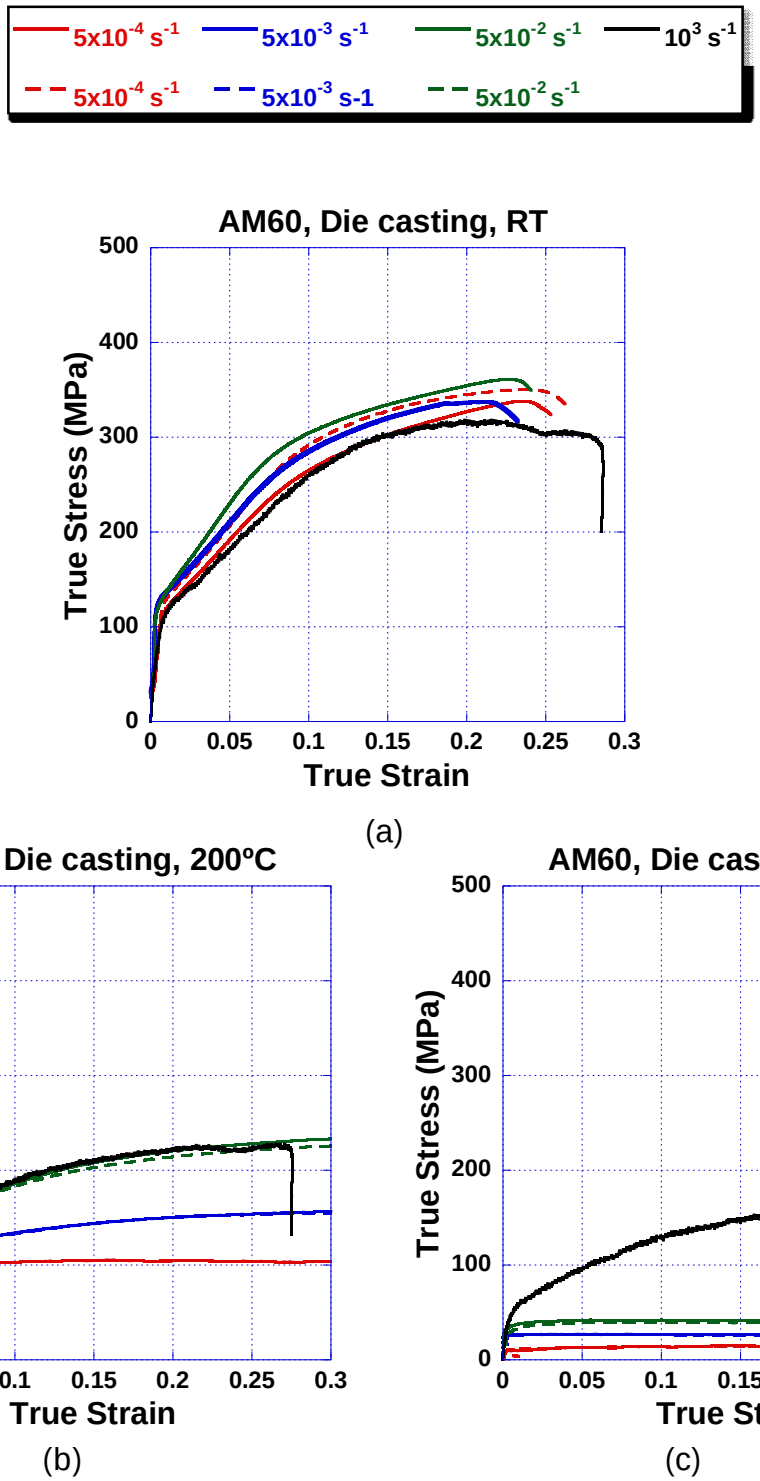

Figure 9.2. True stress – true strain curves corresponding to samples of an AM60 automotive part processed by die casting and tested in compression at different temperatures: a) RT, b) 200 ºC and c) 400 ºC.

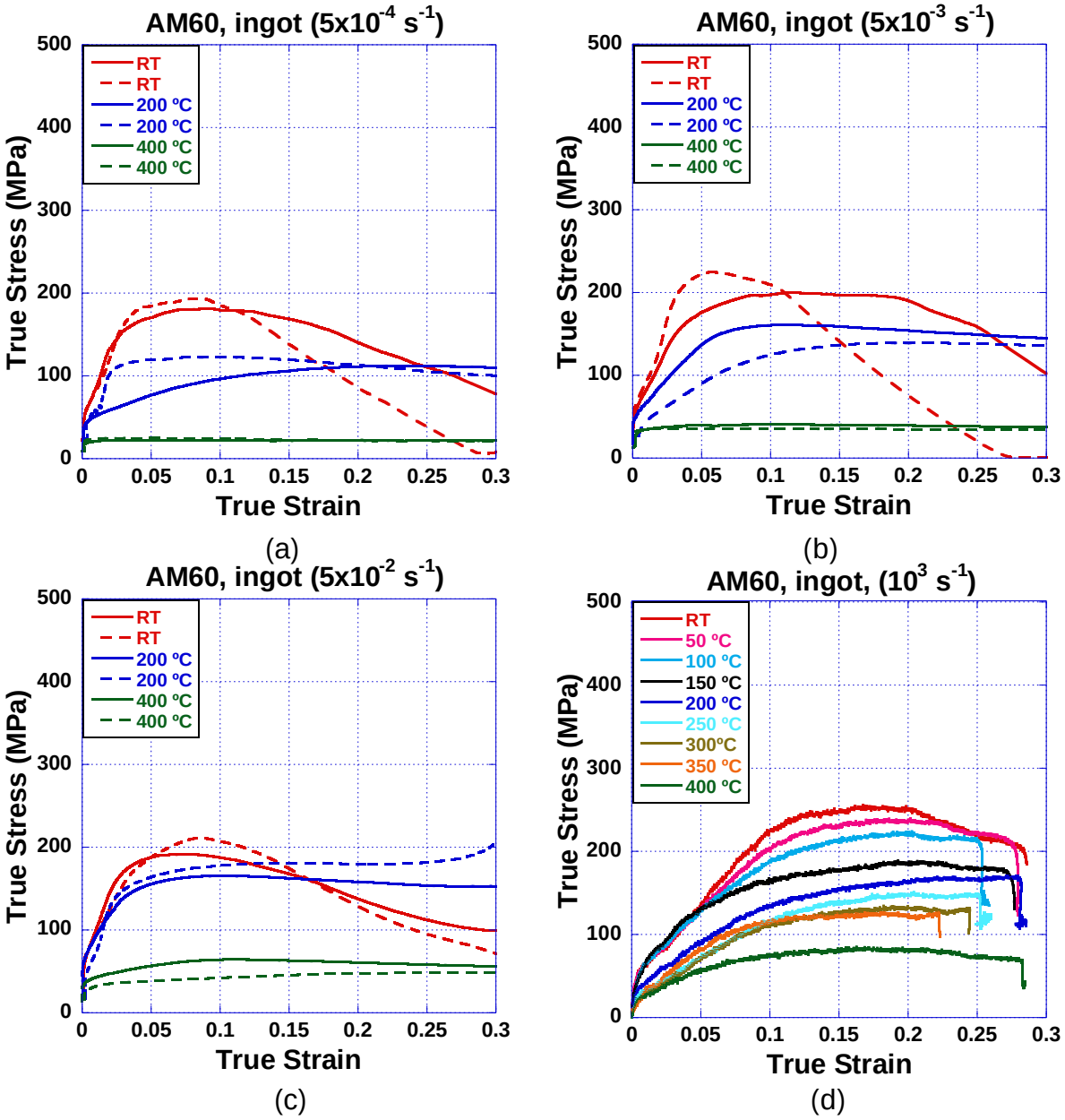

Figure 9.3. True stress – true strain curves corresponding to an AM60 ingot alloy tested in compression at different strain rates: a) $5x10^{-4}$ s^{-1}, b) $5x10^{-3}$ s^{-1}, c) $5x10^{-2}$ s^{-1}, d) 10^{3} s^{-1}.

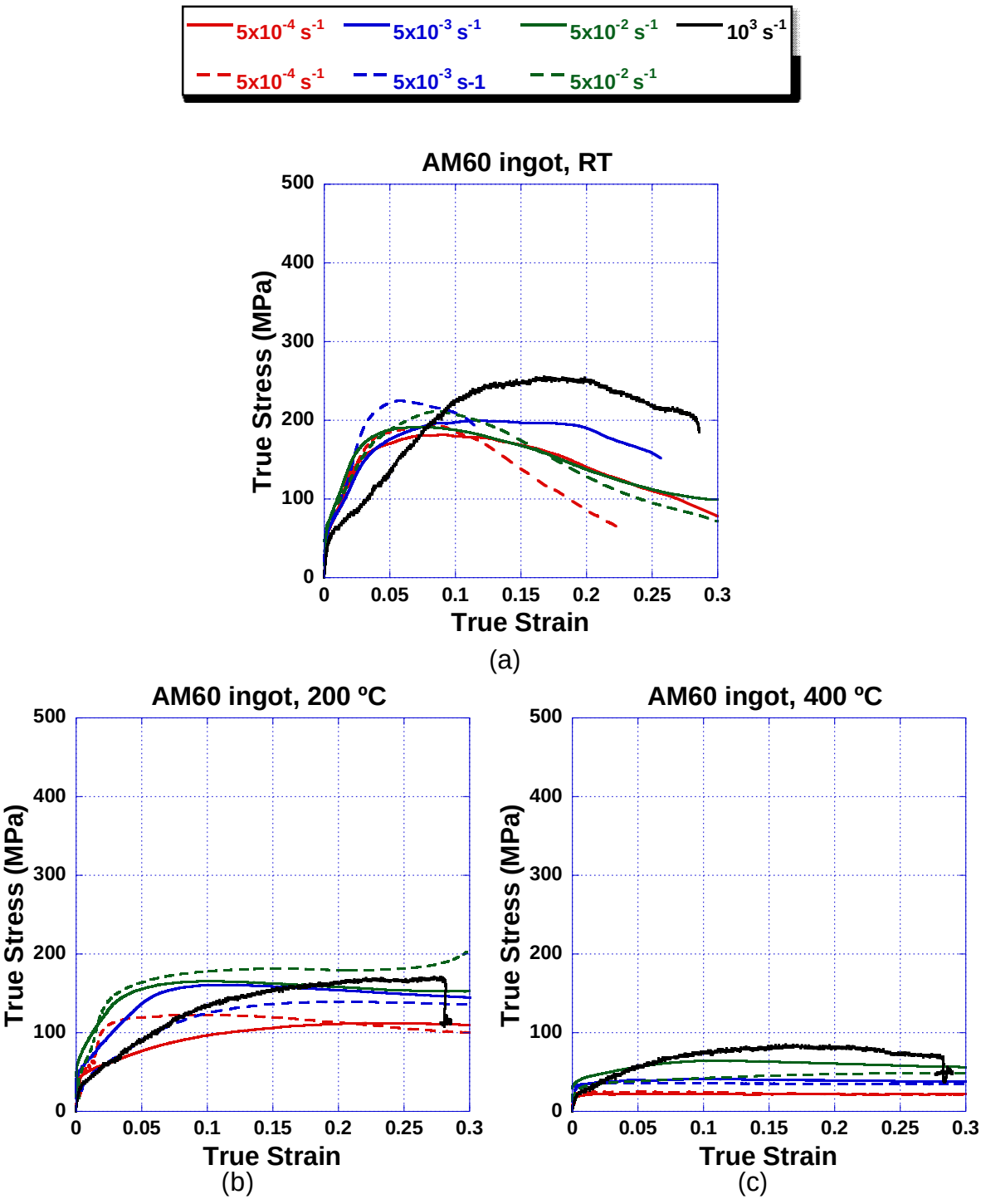

Figure 9.4. True stress – true strain curves corresponding to an AM60 ingot alloy tested in compression at different temperatures: a) RT, b) 200 ºC and c) 400 ºC.

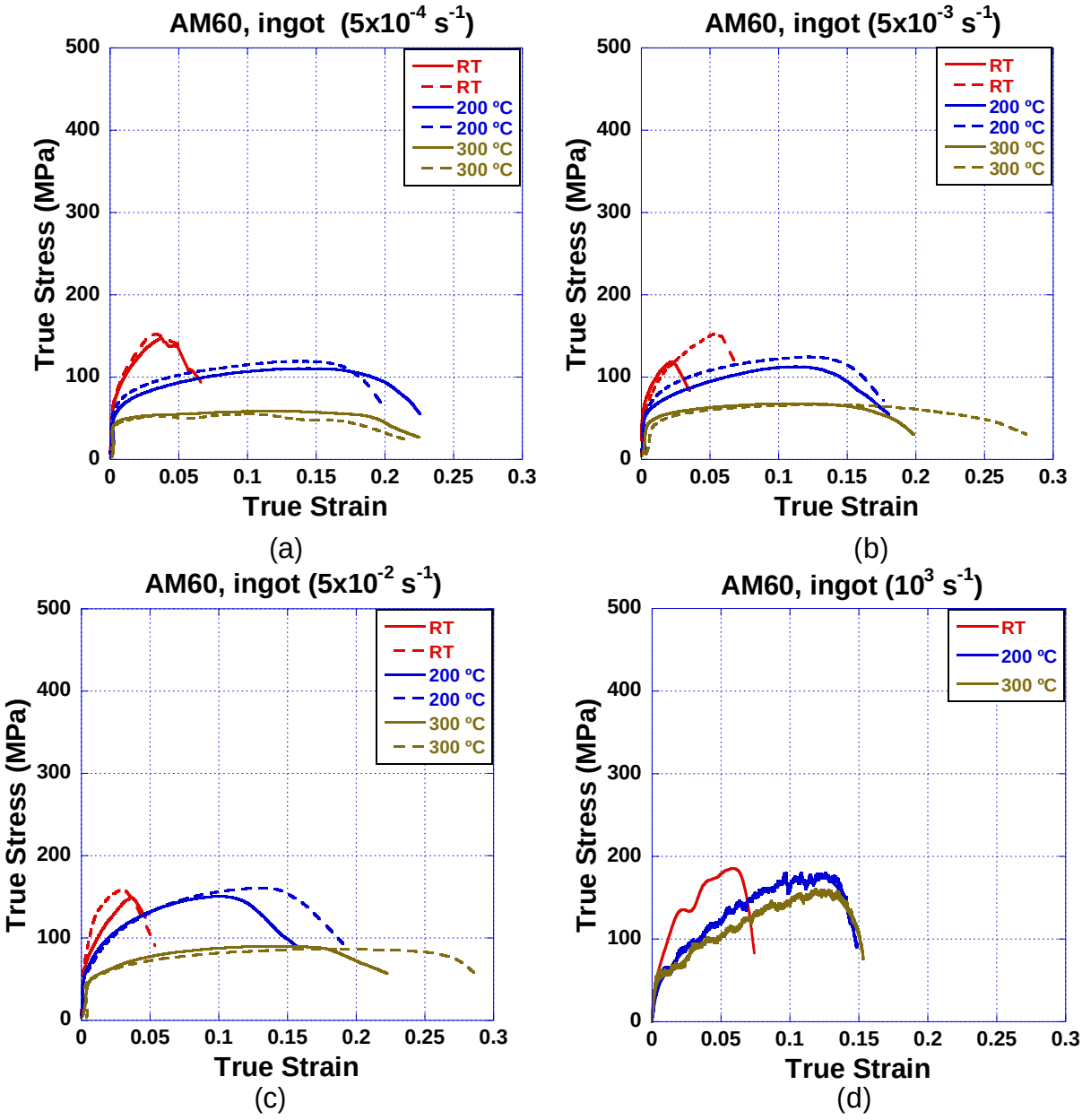

Figure 9.5. True stress – true strain curves corresponding to an AM60 ingot alloy processed by gravity casting and tested in tension at different strain rates: a) $5x10^{-4}$ s^{-1}, b) $5x10^{-3}$ s^{-1}, c) $5x10^{-2}$ s^{-1}, d) 10^{3} s^{-1}.

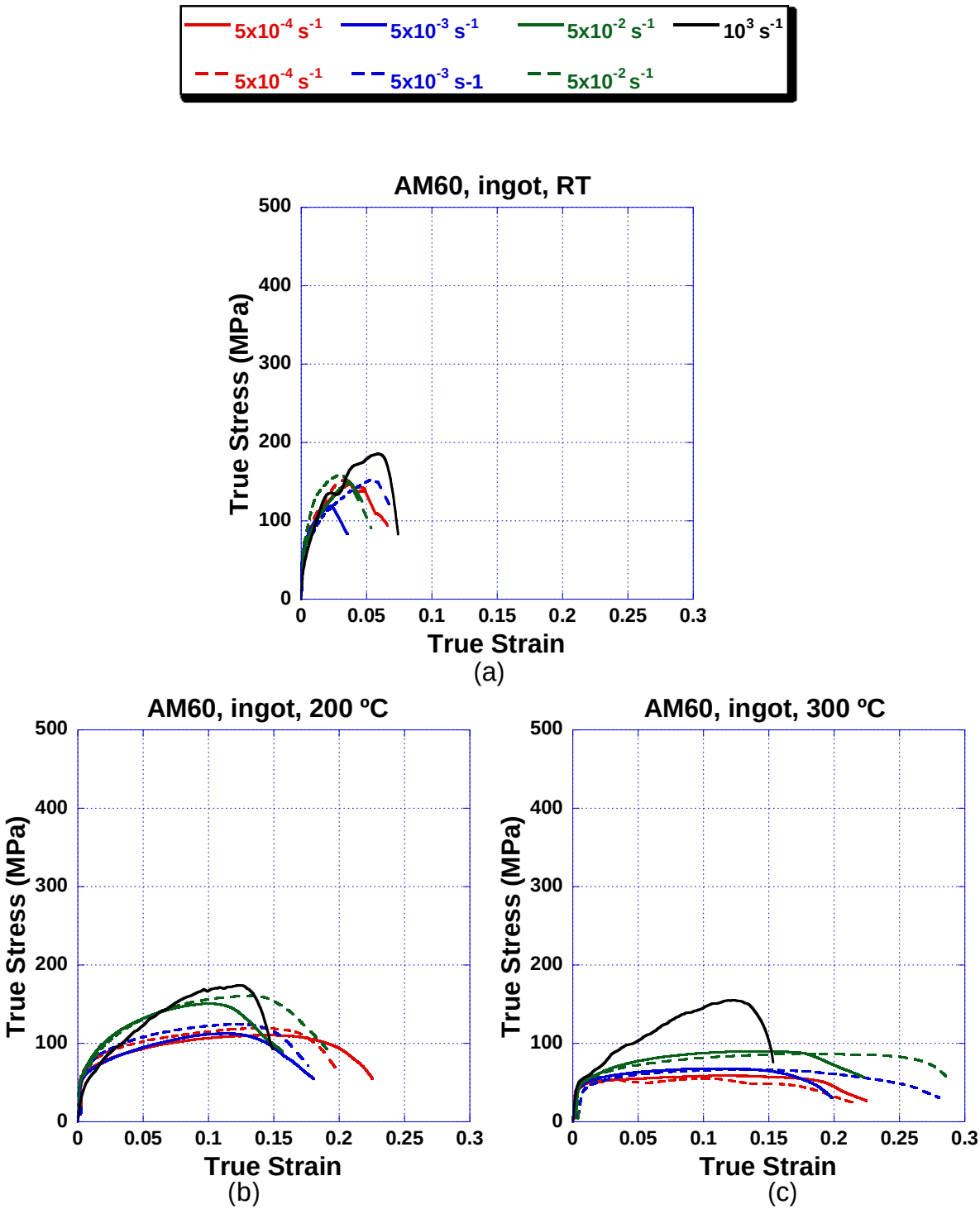

Figure 9.6. True stress – true strain curves corresponding to an AM60 ingot alloy processed by gravity casting and tested in tension at different temperatures: a) RT, b) 200 ºC and c) 300 ºC.

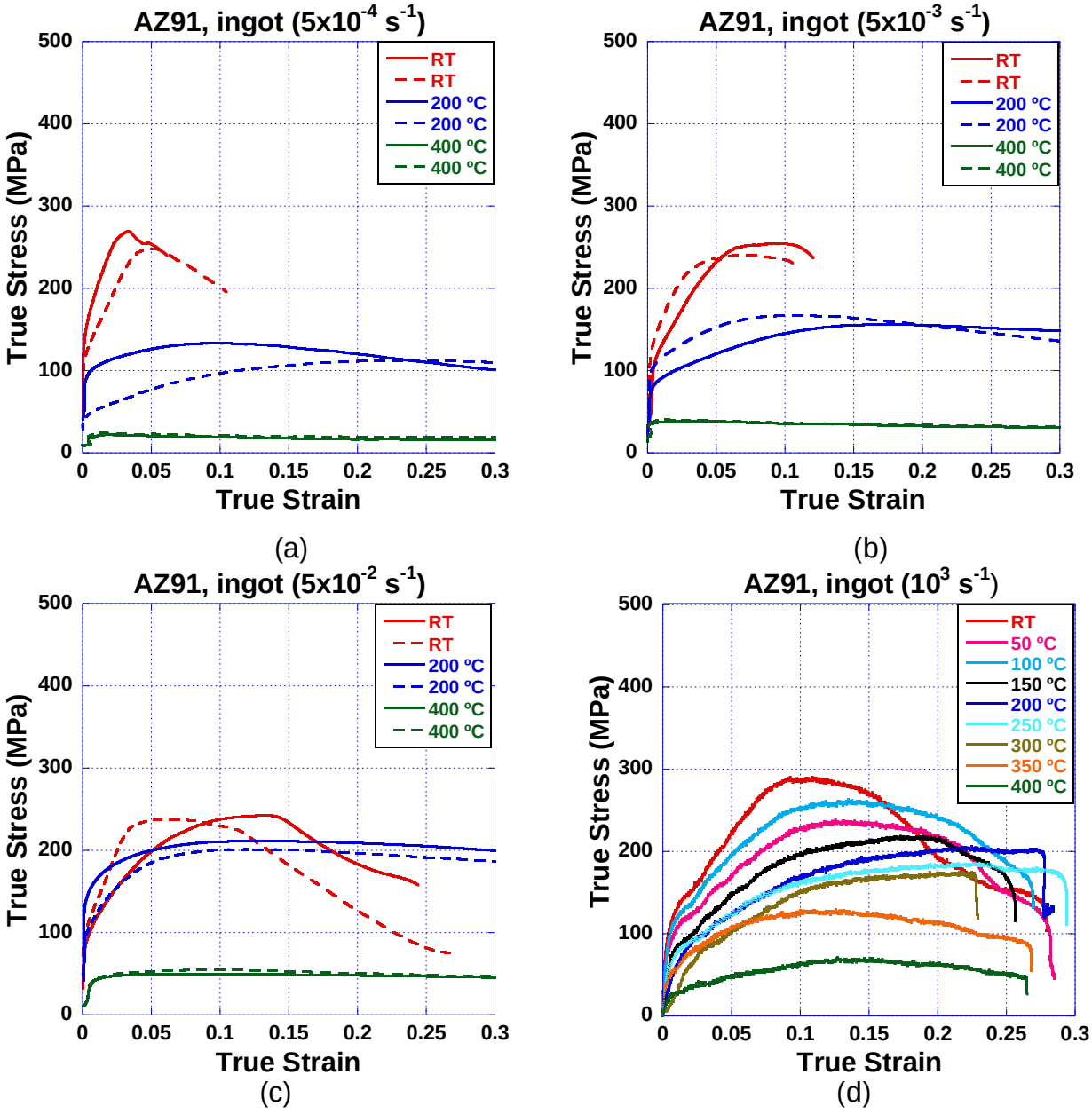

Figure 9.7. True stress – true strain curves corresponding to an AZ91 ingot alloy processed by gravity casting and tested in compression at different strain rates: a) $5x10^{-4}$ s^{-1}, b) $5x10^{-3}$ s^{-1}, c) $5x10^{-2}$ s^{-1}, d) 10^{3} s^{-1}.

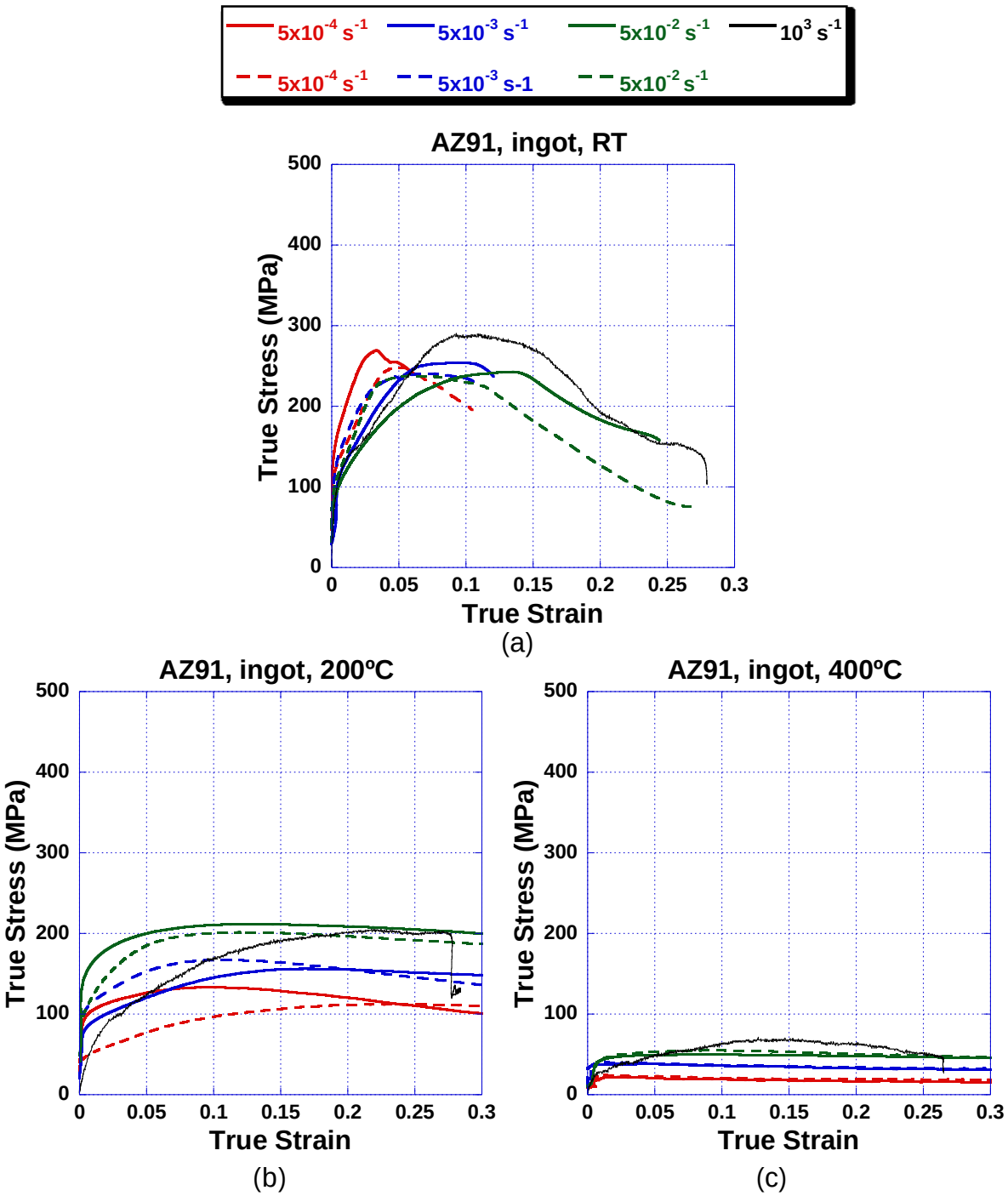

Figure 9.8. True stress – true strain curves corresponding to an AZ91 ingot alloy tested in compression at different temperatures: a) RT, b) 200 ºC and c) 400 ºC.

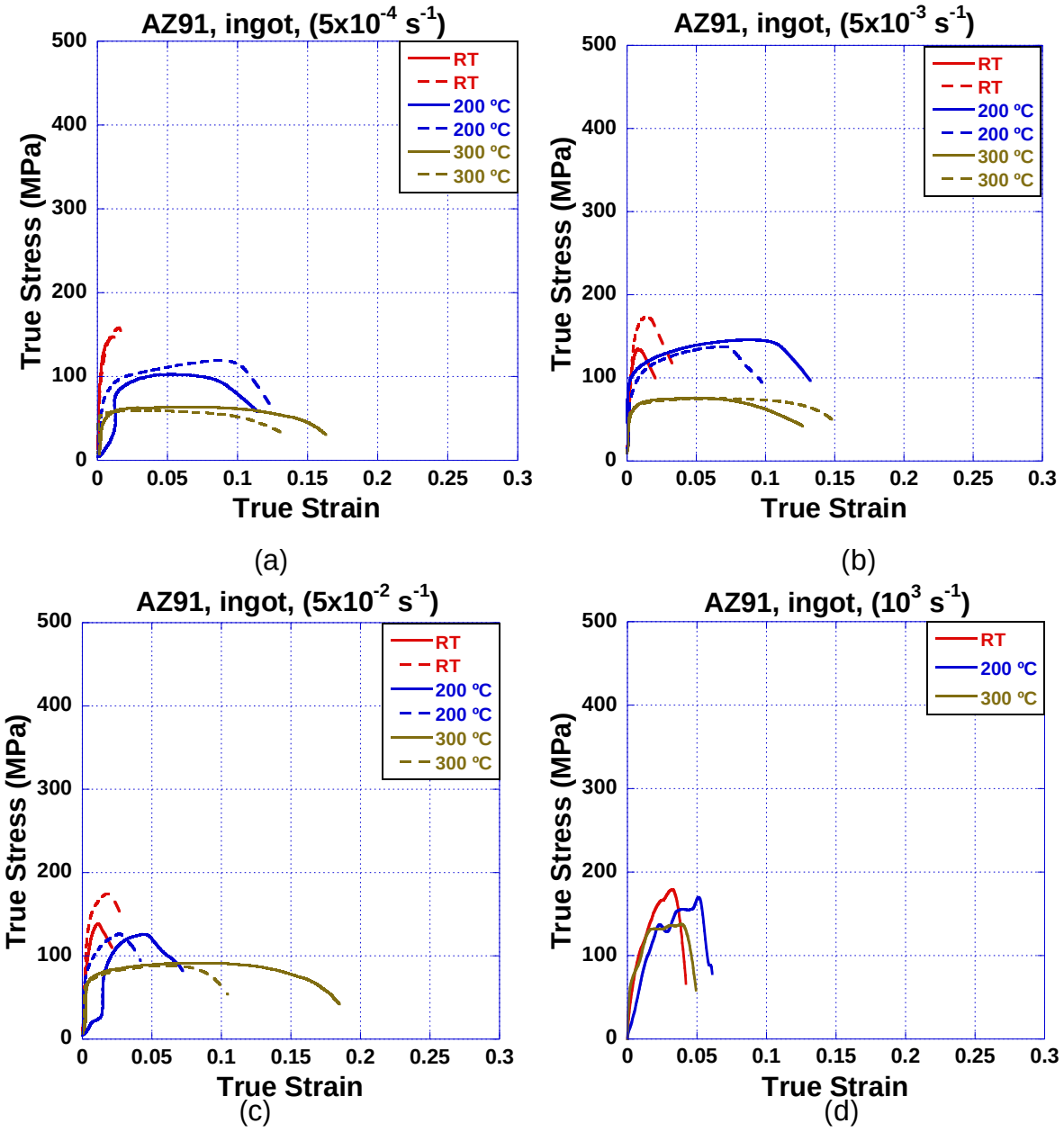

Figure 9.9. True stress – true strain curves corresponding to an AZ91 ingot alloy processed by gravity casting and tested in tension at different strain rates: a) $5x10^{-4}$ s^{-1}, b) $5x10^{-3}$ s^{-1}, c) $5x10^{-2}$ s^{-1}, d) 10^{3} s^{-1}.

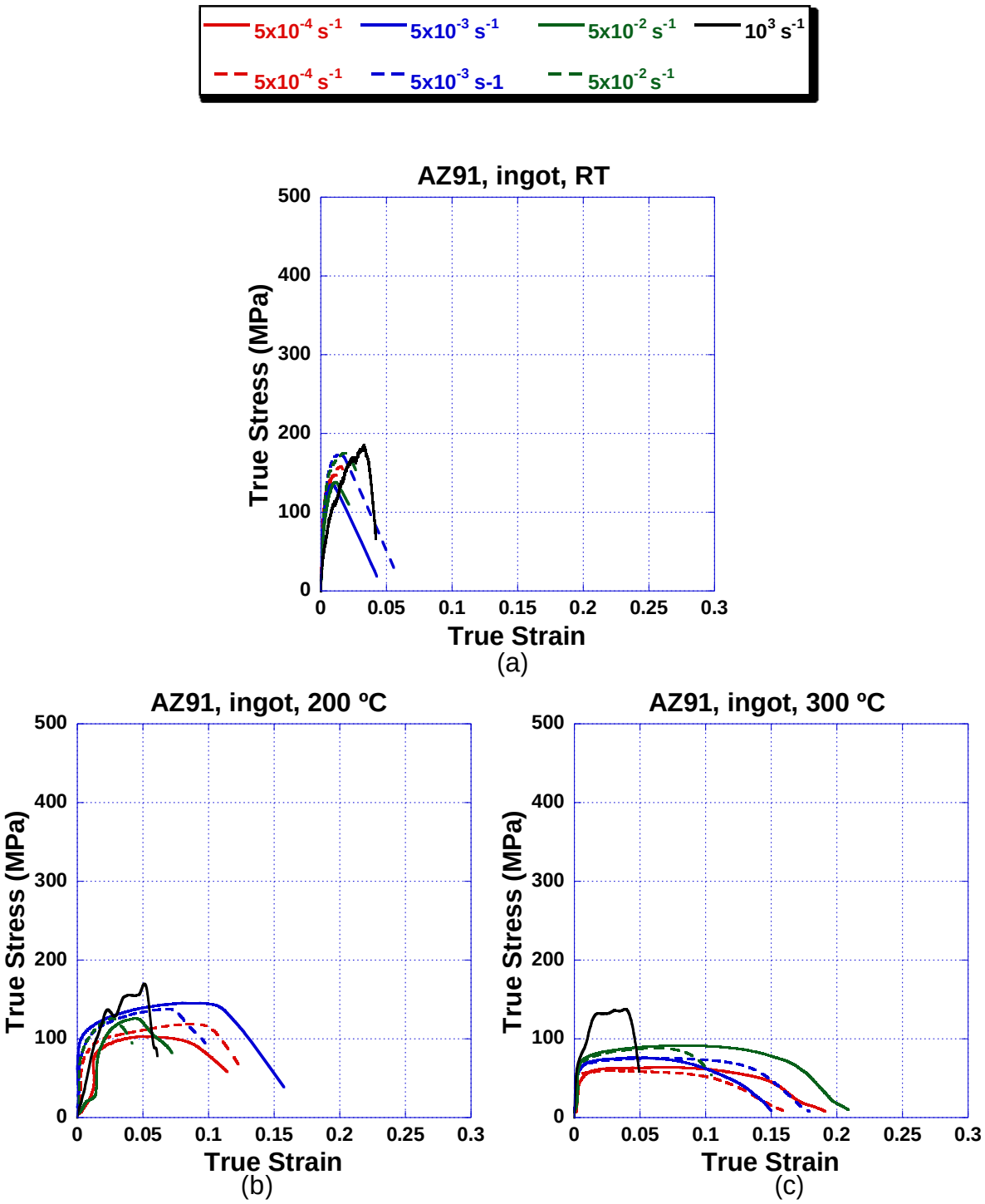

Figure 9.10. True stress – true strain curves for corresponding to an AZ91 ingot alloy processed by gravity casting and tested in tension at different temperatures: a) RT, b) 200 ºC and c) 300 ºC.

9.2 Mechanical properties data

Table 9.1. Mechanical Properties of the AZ31 Mg alloy

	Alloy: **AZ31**. Fabrication Process: Rolling and Annealing. (Compression tests along rolling direction (RD) and normal direction (ND))						
$\dot{\varepsilon}$ (s^{-1})	T (ºC)	$\sigma_{0.005}$ (MPa) RD	$\sigma_{0.005}$ (MPa) ND	σ_{max} (MPa) RD	σ_{max} (MPa) ND	ε_f RD	ε_f ND
$5x10^{-4}$	RT	64	276	334	320	0.16	0.06
	200	75	100	90	122	0.60*	0.44*
	400	15	19	21	21	0.70*	0.68*
$5x10^{-3}$	RT	64	230	338	329	0.135	0.06
	200	75	125	152	176	0.47*	0.45*
	400	24	30	26	33	0.74*	0.68*
$5x10^{-2}$	RT	62	278	350	333	0.09	0.04
	200	65	214	233	241	0.53*	0.40*
	400	31	41	37	51	0.78*	0.55*
10^3	RT	65	279	408	393	0.25	0.47
	50	65	230	393	366	0.23	0.40
	100	50	238	331	331	0.25	0.36
	150	52	233	276	265	0.26	0.38
	200	52	185	229	229	0.27	0.35
	250	53	172	208	215	0.29	0.39
	300	62	150	192	196	0.22	0.37
	350	45	126	174	167	0.26	0.37
	400	46	126	175	159	0.22	0.39

*Test stopped

Table 9.2. Mechanical Properties of the MN11 Mg alloy.

	Alloy: **MN11**. Fabrication Process: extrusion. (Tests parallel to the extrusion axis)												
$\dot{\varepsilon}$ (s^{-1})	T (ºC)	$\sigma_{0.005}$ (MPa) Compression		$\sigma_{0.005}$ (MPa) Tension		σ_{max} (MPa) Compression		σ_{max} (MPa) Tension		ε_f Compression		ε_f Tension	
$5x10^{-4}$	RT	93	---	---	---	264	---	---	---	0.17	---	---	---
	200	81	81	---	---	263	284	---	---	0.12	0.10	---	---
	400	23	28	---	---	25	30	---	---	0.40*	0.50*	---	---
$5x10^{-3}$	RT	69	80	---	---	290	290	---	---	0.11	0.12	---	---
	200	88	86	---	---	211	222	---	---	0.12	0.11	---	---
	400	34	37	---	---	44	42	---	---	0.60*	0.60*	---	---
$5x10^{-2}$	RT	100	95	---	---	304	302	---	---	0.19	0.15	---	---
	200	89	76	---	---	206	229	---	---	0.18	0.13	---	---
	400	56	56	---	---	73	83	---	---	0.50*	0.50*	---	---
10^3	RT	100	---	134	---	346	---	363	---	0.29	---	0.25	---
	50	88	---	---	---	326	---	---	---	0.33	---	---	---
	100	80	---	---	---	297	---	---	---	0.33	---	---	---
	150	93	---	---	---	243	---	---	---	0.31	---	---	---
	200	99	---	134	---	201	---	226	---	0.33	---	0.19	---
	250	92	---	---	---	177	---	---	---	0.34	---	---	---
	300	68	---	134	---	151	---	176	---	0.34	---	0.40	---
	350	51	---	---	---	140	---	---	---	0.34	---	---	---
	400	56	---	---	---	127	---	---	---	0.33	---	---	---

*Test stopped

Table 9.3. Mechanical Properties of the MN11 Mg alloy.

	Alloy: **MN11**. Fabrication Process: extrusion. (Tests perpendicular to the extrusion axis)						
$\dot{\varepsilon}$ (s^{-1})	T (ºC)	$\sigma_{0.005}$ (MPa)		σ_{max} (MPa)		ε_f	
		Compression		Compression		Compression	
$5x10^{-4}$	RT	95	95	271	260	0.29	0.38
	200	85	97	250	285	0.19	0.19
	400	22	23	25	30	0.65*	0.66*
$5x10^{-3}$	RT	97	94	294	310	0.30	0.14
	200	87	82	250	239	0.13	0.27
	400	39	34	43	41	0.60*	0.60*
$5x10^{-2}$	RT	86	97	300	316	0.15	0.23
	200	88	89	235	227	0.31	0.30
	400	43	42	80	80	0.60*	0.6*
10^3	RT	104	---	351	---	0.31	---
	50	108	---	328	---	0.25	---
	100	101	---	345	---	0.25	---
	150	94	---	252	---	0.31	---
	200	86	---	205	---	0.33	---
	250	85	---	184	---	0.32	---
	300	77	---	157	---	0.34	---
	350	62	---	143	---	0.22	---
	400	66	---	140	---	0.33	---

*Test stopped

Table 9.4. Mechanical Properties of the AM60 Mg alloy.

	Alloy: **AM60**. Fabrication Process: Die Casting (tensile coupon)												
$\dot{\varepsilon}$ (s^{-1})	T (ºC)	$\sigma_{0.005}$ (MPa) Compression		$\sigma_{0.005}$ (MPa) Tension		σ_{max} (MPa) Compression		σ_{max} (MPa) Tension		ε_f Compression		ε_f Tension	
$5x10^{-4}$	RT	77	---	149	---	193	---	238	---	0.23	---	0.08	---
	200	98	94	90	91	110	108	102	101	0.82*	0.53*	0.18	0.10
	400	9	13	7	6	19	22	9	8	0.80*	0.60*	0.28	0.53
$5x10^{-3}$	RT	161	---	73	149	406	---	124	230	0.24	---	0.09	0.07
	200	117	116	98	96	166	165	123	113	0.71*	0.72*	0.20	0.10
	400	30	29	22	22	31	30	22	23	0.6*	0.60*	0.28	0.18
$5x10^{-2}$	RT	162	159	153	152	390	398	251	265	0.22	0.24	0.09	0.12
	200	124	---	117	113	230	---	163	161	0.64*	---	0.18	0.16
	400	45	49	40	38	46	51	41	40	0.60*	0.75*	0.21	0.26
10^3	RT	169	---	208	---	386	---	281	---	0.21	---	0.14	---
	50	160	---	128	---	359	---	267	---	0.22	---	0.11	---
	100	151	---	133	---	311	---	263	---	0.20	---	0.14	---
	150	148	---	116	---	282	---	239	---	0.21	---	0.14	---
	200	139	---	145	---	253	---	207	---	0.22	---	0.14	---
	250	129	---	128	---	230	---	203	---	0.22	---	0.16	---
	300	113	---	105	---	216	---	172	---	0.22	---	0.16	---
	350	85	---	95	---	177	---	137	---	0.14	---	0.13	---
	400	85	---	108	---	186	---	120	---	0.23	---	0.10	---

*Test stopped

Table 9.5. Mechanical Properties of the AM60 Mg alloy.

	Alloy: **AM60**. Fabrication Process: Die Casting (automotive part)						
$\dot{\varepsilon}$ (s^{-1})	T (ºC)	$\sigma_{0.005}$ (MPa) Compression		σ_{max} (MPa) Compression		ε_f Compression	
$5x10^{-4}$	RT	122	133	337	350	0.25	0.26
	200	89	---	104	---	0.57*	---
	400	9	11	16	15	0.65*	0.65*
$5x10^{-3}$	RT	133	---	336	---	0.23	---
	200	95	83	160	156	0.43*	0.39*
	400	26	25	27	26	0.68*	0.73*
$5x10^{-2}$	RT	132	---	361	---	0.24	---
	200	107	110	246	236	0.46*	0.47*
	400	35	33	41	39	0.66	0.66*
10^3	RT	117	---	316	---	0.29	---
	50	125	---	292	---	0.21	---
	100	115	---	273	---	0.26	---
	150	102	---	223	---	0.27	---
	200	105	---	225	---	0.28	---
	250	75	---	189	---	0.29	---
	300	99	---	187	---	0.19	---
	350	76	---	180	---	0.26	---
	400	55	---	161	---	0.28	---

*Test stopped

Table 9.6. Mechanical Properties of the AM60 Mg alloy.

	Alloy: **AM60**. Fabrication Process: gravity casting.												
$\dot{\varepsilon}$ (s^{-1})	T (ºC)	$\sigma_{0.005}$ (MPa)		$\sigma_{0.005}$ (MPa)		σ_{max} (MPa)		σ_{max} (MPa)		ε_f		ε_f	
		Compression		Tension		Compression		Tension		Compression		Tension	
$5x10^{-4}$	RT	71	72	85	88	181	193	147	152	0.22	0.34	0.07	0.05
	200	48	60	65	71	112	122	110	119	0.47*	0.38*	0.23	0.20
	300	---	---	47	45	---	---	58	55	---	---	0.22	0.22
	400	20	24	---	---	23	25	---	---	0.79*	0.83*		
$5x10^{-3}$	RT	70	78	82	74	200	224	118	152	0.26	0.12	0.04	0.07
	200	60	49	61	70	160	138	112	124	0.39*	0.44*	0.18	0.18
	300	---	---	48	46	---	---	67	66	---	---	0.20	0.28
	400	34	34	---	---	41	35	---	---	0.76*	0.65*	---	---
$5x10^{-2}$	RT	85	81	83	100	191	211	148	159	0.4*	0.4*	0.05	0.05
	200	81	70	71	64	165	181	150	160	0.4*	0.4*	0.16	0.19
	300	---	---	54	51	---	---	90	86	---	---	0.22	0.29
	400	41	30	---	---	64	48	---	---	0.65*	0.65*	---	---
10^3	RT	45	---	73	---	253	---	158	---	0.29	---	0.07	---
	50	57	---	---	---	239	---	---	---	0.28	---	---	---
	100	64	---	---	---	224	---	---	---	0.25	---	---	---
	150	55	---	---	---	188	---	---	---	0.28	---	---	---
	200	39	---	60	---	169	---	173	---	0.28	---	0.15	---
	250	30	---	---	---	151	---	---	---	0.25	---	---	---
	300	24	---	57	---	134	---	154	---	0.24	---	0.15	---
	350	40	---	---	---	126	---	---	---	0.22	---	---	---
	400	26	---	---	---	85	---	---	---	0.28	---	---	---

*Test stopped

Table 9.7. Mechanical Properties of the AZ91 Mg alloy.

	Alloy: **AZ91**. Fabrication Process: Die Casting (tensile coupon)												
$\dot{\varepsilon}$ (s^{-1})	T (ºC)	$\sigma_{0.005}$(MPa)		$\sigma_{0.005}$ (MPa)		σ_{max} (MPa)		σ_{max} (MPa)		ε_f		ε_f	
		Compression		Tension		Compression		Tension		Compression		Tension	
$5x10^{-4}$	RT	221	217	186	184	486	447	250	234	0.19	0.17	0.05	0.04
	200	106	109	91	97	113	115	98	105	0.34*	0.34*	0.14	0.17
	400	9	9	3	4	16	16	4	5	0.34*	0.34*	0.54	0.58
$5x10^{-3}$	RT	214	206	189	187	446	444	254	261	0.17	0.19	0.06	0.06
	200	128	132	113	116	144	152	132	130	0.60*	0.60*	0.19	0.20
	400	25	26	19	19	26	30	20	19	0.60*	0.60*	0.30	0.28
$5x10^{-2}$	RT	210	209	189	188	445	431	248	241	0.18	0.18	0.06	0.05
	200	148	162	138	134	220	231	184	168	0.65*	0.62*	0.13	0.13
	400	44	44	37	36	44	49	37	37	0.6*	0.70*	0.32	0.21
10^3	RT	221	---	157	---	436	---	298	---	0.17	---	0.06	---
	50	214	---	259	---	402	---	302	---	0.20	---	0.09	---
	100	191	---	127	---	342	---	238	---	0.20	---	0.05	---
	150	186	---	157	---	322	---	236	---	0.21	---	0.07	---
	200	187	---	136	---	306	---	233	---	0.22	---	0.05	---
	250	157	---	143	---	264	---	203	---	0.22	---	0.08	---
	300	---	---	126	---	---	---	154	---	---	---	0.05	---
	350	107	---	189	---	206	---	191	---	0.16	---	0.04	---
	400	94	---	---	---	148	---	---	---	0.24	---	---	---

*Test stopped

Table 9.8. Mechanical Properties of the AZ91 Mg alloy.

	Alloy: **AZ91**. Fabrication Process: gravity casting.												
$\dot{\varepsilon}$ (s^{-1})	T (^oC)	$\sigma_{0.005}$ (MPa)		$\sigma_{0.005}$ (MPa)		σ_{max} (MPa)		σ_{max} (MPa)		ε_f		ε_f	
		Compression		Tension		Compression		Tension		Compression		Tension	
$5x10^{-4}$	RT	180	135	139	135	268	248	147	158	0.06	0.10	0.01	0.02
	200	100	48	86	85	133	112	102	118	0.54*	0.46*	0.11	0.12
	300	---	---	56	56	---	---	63	59	---	---	0.16	0.13
	400	21	24	---	---	21	24	---	---	0.80*	0.80*	---	---
$5x10^{-3}$	RT	129	150	133	156	254	241	134	174	0.12	0.11	0.02	0.03
	200	86	111	107	95	155	166	145	137	0.53*	0.50*	0.13	0.10
	300	---	---	66	66	---	---	75	75	---	---	0.13	0.15
	400	36	39	---	---	37	40	---	---	0.80*	0.80*	---	---
$5x10^{-2}$	RT	106	119	120	153	242	237	138	174	0.24	0.27	0.02	0.03
	200	157	114	97	93	211	201	126	126	0.60*	0.50*	0.06	0.04
	300	---	---	75	70	---	---	91	88	---	---	0.18	0.10
	400	43	44	---	---	50	54	---	---	0.61*	0.73*	---	---
10^3	RT	115	---	83	---	289	---	179	---	0.28	---	0.04	---
	50	96	---	---	---	237	---	---	---	0.29	---	---	---
	100	110	---	---	---	262	---	---	---	0.27	---	---	---
	150	79	---	---	---	218	---	---	---	0.26	---	---	---
	200	62	---	114	---	205	---	169	---	0.28	---	0.06	---
	250	65	---	---	---	186	---	---	---	0.29	---	---	---
	300	69	---	80	---	175	---	138	---	0.23	---	0.05	---
	350	55	---	---	---	128	---	---	---	0.27	---	---	---
	400	28	---	---	---	70	---	---	---	0.26	---	---	---

*Test stopped

LIST OF FIGURES

PAG.

PART II. INTRODUCCIÓN. EL MAGNESIO

Figure 2.1. Tabla periódica de los elementos 17

Figure 2.2. Densidades de algunos metales estructurales 18

Figure 2.3. Aplicaciones de las aleaciones de magnesio en automóviles 21

Figure 2.4. Aplicaciones de las aleaciones de magnesio para la fabricación de dispositivos biomédicos, electrónicos y material deportivo 22

Figure 2.5. Estructura cristalina hexagonal compacta (HCP): representación de la celdilla unidad mediante esferas reducidas 23

Figure 2.6. Tipos de textura que se desarrollan en los materiales procesados mediante tres procesos de fabricación: colada, laminación más un recocido posterior y extrusión 25

Figure 2.7. Sistemas de deslizamiento de las aleaciones de magnesio 27

Figure 2.8. Sistemas de maclado más comunes en las aleaciones de magnesio 28

Figure 2.9. Variación de la *CRSS de los distintos sistemas de deslizamiento y maclado* con la 35

PART III. RESEARCH PAPERS

3.1 Mechanical behavior and microstructural evolution of a Mg AZ31 sheet at dynamic strain rates

Figure 3.1.1. Microstructure and microtexture of the as-received Mg AZ31-O alloy obtained by EBSD 47

Figure 3.1.2. Schematic illustrating the relative orientation of the tension and compression axes with respect to the c-axes and the sheet reference system (RD, TD, ND) 47

Figure 3.1.3. True stress-true strain curves corresponding to HSR (10^3 s^{-1}) tests performed at room temperature and at 250°C.: (a) RD-T versus RD-C; (b) RD-T versus TD-T; (c) RD-C versus ND-C 48

PAG.

Figure 3.1.4. Variation of the true stress at ε=0.005 ($\sigma_{0.005}$) and of the flow stress (σ_{max}) with temperature during HSR (10^3 s^{-1}, closed symbols) and LSR (10^{-3} s^{-1}, open symbols) strain rate tests 49

Figure 3.1.5. (a) Variation of the yield stress tension-compression asymmetry ($\sigma_{0.005\,(RD-T)}/\sigma_{0.005(RD-C)}$), the yield stress in-plane anisotropy ($\sigma_{0.005(TD-T)}/\sigma_{0.005(RD-T)}$) and the yield stress out-of-plane anisotropy ($\sigma_{0.005(ND-C)}/\sigma_{0.005(RD-C)}$) with temperature at both high strain rates (HSR) and low strain rates (LSR). (b) Modulus-compensated flow stress (σ_{max}/G) as a function of temperature corresponding to tests performed in tension along in-plane directions (RD-T/TD-T) and in compression along RD and ND (RD-C and ND-C) at both high strain rate (HSR) and low strain rate (LSR) 50

Figure 3.1.6. EBSD inverse pole figure maps in the ND and textures measured in the samples loaded in tension at HSR under the following conditions: a) room temperature, tension along RD; b) room temperature, tension along TD; c) 250ºC, tension along RD. d)Kernel average misorientation map at the area c) 52

Figure 3.1.7. Microstructure and microtexture of the AZ31 sheet deformed in tension along RD at 10^{-3} s^{-1} and 250ºC. a) EBSD inverse pole figure maps in the ND and b) Kernel Average misorientation map of the same area 53

Figure 3.1.8. Discrete orientations of the recrystallized grains in the sample deformed at high strain rates (RD-T at 10^3 s^{-1} and 250ºC) 54

PAG.

3.2 Twinning and grain subdivision during dynamic deformation of Mg AZ31 sheet alloy at room temperature

Figure 3.2.1. Texture of the as-received sheet alloy 59

Figure 3.2.2. Room temperature stress-strain curves corresponding to the AZ31 alloy deformed at a high strain rate (10^3 s^{-1}) and a quasi-static strain rate in (a) compression along the RD; (b) tension along the RD; and (c) compression along the ND. Images of the specimen after fracture, taken in real time with a high speed camera, are included next to each plot. The strains to failure corresponding to each tests, ε_f, are indicated by arrows 60

Figure 3.2.3. EBSD inverse pole figure maps in the ND and microtextures measured in the samples deformed quasi-statically at room temperature in compression along the RD up to strains of (a) 0.05 and (b) 0.13. (c) Twin boundary map corresponding to the sample strained up to 0.13 62

Figure 3.2.4. EBSD inverse pole figure maps in the ND and microtextures measured in the samples dynamically loaded at room temperature in compression along the RD up to strains of (a) 0.05, (b) 0.10 and (c) 0.13. (d) Boundary map corresponding to the sample strained up to 0.13 63

Figure 3.2.5. Misorientation distribution histograms corresponding to AZ31 compressed at dynamic strain rates along the RD at room temperature up to strains of 0.05, 0.10 and 0.13 64

Figure 3.2.6. Texture of the AZ31 alloy deformed to failure at room temperature in tension along the RD at a strain rate of 10^{-3} s^{-1}. Direct pole figures, measured by neutron diffraction 64

PAG.

Figure 3.2.7. EBSD inverse pole figure maps in the ND and direct pole figures, measured by neutron diffraction, corresponding to the samples dynamically loaded at room temperature in tension along the RD up to strains of (a) 0.10 and (b) 0.20. (c) Twin boundary map corresponding to the sample deformed to 0.20 65

Figure 3.2.8. Boundary maps corresponding to the AZ31 alloy deformed in tension along the RD: (a) at a high strain rate up to a strain of 0.10; (b) at a high strain rate up to a strain of 0.20; (c) at a low strain rate up to failure (failure strain approximately equal to 0.20). (d) Twin boundary map corresponding to the sample deformed at a low strain rate until failure 66

Figure 3.2.9. (a) EBSD inverse pole figure map in the ND, macrotexture (X-ray) and microtexture (EBSD) corresponding to the AZ31 alloy dynamically loaded at room temperature in compression along the ND up to a strain of 0.05; (b) twin boundary map corresponding to the same sample; (c) EBSD inverse pole figure map in the ND, macrotexture (X-ray) and microtexture (EBSD) corresponding to the AZ31 alloy dynamically loaded at room temperature in compression along the ND up to a strain of 0.10 67

3.3 Influence of texture on the recrystallization mechanisms in an AZ31 Mg sheet alloy at dynamic rates

Figure 3.3.1. Stress-strain curves corresponding to the Mg AZ31 alloy deformed at high strain rate (10^3 s^{-1}, solid line) and at quasi-static strain rates (10^{-3} s^{-1}, dotted line) at 250 ºC in (a) compression along RD; (b) tension along RD; and (c) compression along NDThe images below each graph show the corresponding specimen before testing (upper image) and after dynamic deformation up to a true strain of approximately 0.25 (lower image) 73

Figure 3.3.2. Work hardening behavior corresponding to the AZ31 sheet alloy deformed at 250°C and 10^3 s^{-1}. 74

PAG.

Figure 3.3.3. EBSD inverse pole figure maps in the ND and microtextures corresponding to samples dynamically loaded at 250ºC in compression along RD up to strains of (a) 0.06, (b) 0.10, and (c) 0.15. (d) Boundary map corresponding to the sample strained up to 0.15 74

Figure 3.3.4. Misorientation distribution histograms corresponding to the AZ31 sheet alloy compressed along RD at 10^3 s^{-1} and 250 ºC up to strains of 0.10 and 0.15 75

Figure 3.3.5. EBSD inverse pole figure maps in the ND and microtextures corresponding to samples dynamically loaded at 250ºC in tension along RD up to strains of (a) 0.10, and (c) 0.20. (b) Twin boundary map corresponding to the sample deformed up to a strain of 0.10. (d) Boundary map corresponding to the sample strained up to 0.20 76

Figure 3.3.6. EBSD inverse pole figure maps in the ND and microtextures corresponding to samples dynamically loaded at 250ºC in compression along ND up to strains of (a) 0.07, (b) 0.095, and (c) 0.17. (d) Boundary map corresponding to the sample strained up to 0.17 77

Figure 3.3.7. Misorientation distribution histograms corresponding to the AZ31 sheet alloy compressed along ND at 10^3 s^{-1} and 250 ºC up to strains of 0.095 and 0.17 78

Figure 3.3.8. Kernel average misorientation (KAM) map corresponding to the AZ31 alloy deformed (a) in compression along RD up to a strain of 0.15, (b) in tension along RD up to a strain of 0.20 and (c) in compression along ND up to a strain of 0.17 78

PART IV. ADDITIONAL AND COMPARATIVE STUDIES

Figure 4.1. Microstructure and texture of the as-extruded MN11 bar. (a) Micrograph obtained by optical microscopy, (b) X-ray pole figures and (c) X-ray inverse pole figure showing the orientation of the extrusion axis (EA). The plane of observation is perpendicular to the extrusion axis (EA). 87

PAG.

Figure 4.2. Effect of heat treatment on the microstructure and the texture: (a,b) 200 ºC, 1h; (c,d) 400 ºC, 1h. Both samples where heated at 10ºC/min up to the corresponding heat treatment temperature. 88

Figure 4.3. Stress-strain curves corresponding to the MN11 alloy deformed in compression at room temperature, 200 ºC and 400 ºC at: (a) $5x10^{-4}$ s^{-1} along the EA, (b) $5x10^{-4}$ s^{-1} perpendicular to the EA, (c) $5x10^{-3}$ s^{-1} along the EA, (d) $5x10^{-3}$ s^{-1} perpendicular to the EA, (e) $5x10^{-2}$ s^{-1} along the EA, (f) $5x10^{-2}$ s^{-1} perpendicular to the EA, (g) 10^{3} s^{-1} along the EA, and (h) 10^{3} s^{-1} perpendicular to the EA. 89

Figure 4.4. Inverse pole figures showing the orientation of two radial directions of the as-received extruded bar of MN11. The two directions have been labeled <R1> and <R2>. Both are perpendicular to the EA. 91

Figure 4.5. Evolution of the strain to failure (ε_f) and the maximum flow stress (σ_{max}) with temperature at different strain rates: a), b) $5x10^{-4}$ s^{-1}; c),d) $5x10^{-3}$ s^{-1}; e),f) $5x10^{-2}$ s^{-1}, g),h) 10^{3} s^{-1}. 92

Figure 4.6. Stress-strain curves corresponding to the MN11 alloy deformed in tension parallel to the extrusion axis (EA) at high strain rate at room temperature, 200 ºC and 300 ºC. 96

Figure 4.7. Microtexture of the MN11 alloy tested at low strain rate ($5x10^{-3}$ s^{-1}), at room temperature in compression along the EA up to a strain of 0.12 (fracture) (a) EBSD inverse pole figure map showing the orientation of the EA; (b) Twin boundary map (Red: tensile twins; Blue: compression twins; Green: double twins); (c) Pole figures. (d) Inverse pole figure showing the orientation of the EA. The plane shown is perpendicular to the EA. 98

Figure 4.8. Microtexture of the MN11 alloy tested at low strain rate ($5x10^{-3}$ s^{-1}) at 200 ºC in compression along the EA up to a strain of 0.11 (fracture) (a) EBSD inverse pole figure map in the EA; (b) Twin boundary map (Red: tensile twins; Blue: compression twins; Green: double twins); (c) Pole figures. (d) Inverse pole figure showing the orientation of the EA. The plane shown is perpendicular to the EA. 99

PAG.

Figure 4.9. Microtexture of the MN11 alloy tested at low strain rate ($5x10^{-3}$ s^{-1}) at 400 ºC in compression along the EA up to a strain of 0.6 (test stopped) (a) EBSD inverse pole figure map in the EA; (b) Twin boundary map (*Red*: tensile twins; Blue: compression twins; Green: double twins); (c) Pole figures. (d) Inverse pole figure showing the orientation of the EA. The plane shown is perpendicular to the EA. 100

Figure 4.10. Evolution of the microtexture of the MN11 alloy during compression at high strain rate (10^3 s^{-1}) along the EA at RT with increasing strain. (a) ε= 0.095; EBSD inverse pole figure map showing the orientation of the EA; (b) ε= 0.095; Twin boundary map (Red: tensile twins; Blue: compression twins; Green: double twins); (c) ε= 0.095; Pole figures and inverse pole figure showing the orientation of the EA. (d) ε= 0.15; EBSD inverse pole figure map showing the orientation of the EA; (e) ε= 0.15; Twin boundary map (Red: tensile twins; Blue: compression twins; Green: double twins); (f) ε= 0.15; Pole figures and inverse pole figure showing the orientation of the EA. The plane shown is perpendicular to the EA. 103

Figure 4.11. Evolution of the microtexture of the MN11 alloy during compression at high strain rate (10^3 s^{-1}) along the EA at 400 ºC with increasing strain. (a) ε= 0.11; EBSD inverse pole figure map showing the orientation of the EA; (b) ε= 0.11; Twin boundary map (Red: tensile twins; Blue: compression twins; Green: double twins); (c) ε= 0.11; Pole figures and inverse pole figures showing the orientation of the EA. (d) ε= 0.16; EBSD inverse pole figure map showing the orientation of the EA; (e) ε= 0.16; Twin boundary map (Red: tensile twins; Blue: compression twins; Green: double twins); (f) ε= 0.16; Pole figures and inverse pole figures showing the orientation of the EA. 104

Figure 4.12. Microtexture of the MN11 alloy tested in tension along the EA at high strain rate (10^3 s^{-1}) at RT up to a strain of 0.25 (fracture). (a) EBSD inverse pole figure map showing the orientation of the EA; (b) Twin boundary map (Red: tensile twins; Blue: compression twins; Green: double twins); (c) Pole figures. (d) Inverse pole figure showing the orientation of the EA. 106

PAG.

Figure 4.13. Microtexture of the MN11 alloy tested in tension along the EA at high strain rate (10^3 s^{-1}) at 300 ºC up to a strain of 0.40 (fracture). (a) EBSD inverse pole figure map showing the orientation of the EA; (b) Twin boundary map (Red: tensile twins; Blue: compression twins; Green: double twins); (c) Pole figures.; (d) Inverse pole figure showing the orientation of the EA. 107

Figure 4.14. Superposition of the inverse stereographic triangle (extrusion axis) corresponding to the as-extruded MN11 alloy and the schematic triangle showing contours of constant resolved shear stress, i.e., of constant Schmid factor for basal slip, reported by Calnan and Clews [127] 108

Figure 4.15. Microstructure and macrotexture (X-ray) of the as-received die-cast Mg alloy: (a) AM60, (b) AZ91. The plane examined is perpendicular to the loading axis. 113

Figure 4.16*.* Variation of the yield stress ($\sigma_{0.005}$) and of the flow stress (σ_{max}) with temperature during high (10^3 s^{-1}, left column) and low ($5x10^{-3}$ s^{-1}, right column) strain rate tests in die-cast AM60B and AZ91B alloys: (a) AM60B, 10^3 s^{-1} in compression; (b) AM60B, $5x10^{-3}$ s^{-1} in compression; (c) AM60B, 10^3 s^{-1} in tension, (d) AM60B, $5x10^{-3}$ s^{-1} in tension, (e) AZ91D, 10^3 s^{-1} in compression; (f) AZ91D, $5x10^{-3}$ s^{-1} in compression; (g) AZ91D, 10^3 s^{-1} in tension, (h) AZ91D, $5x10^{-3}$ s^{-1} in tension. 116

Figure 4.17*.* True stress-true strain curves corresponding high (10^3 s^{-1}) and low ($5x10^{-3}$ s^{-1}) strain rate tests performed in compression at different temperatures in die-cast Mg alloys : (a) AM60B, 10^3 s^{-1}, (b) AM60B, $5x10^{-3}$ s^{-1} (c) AZ91D, 10^3 s^{-1}, (d) AZ91, $5x10^{-3}$ s^{-1} . 117

Figure 4.18*.* True stress-true strain curves corresponding high strain rate (10^3 s^{-1}) tests performed in compression at different temperatures in die-cast Mg alloys : (a) AM60B (b) AZ91D. 118

PART IX. APPENDICES

Figure 9.1. True stress – true strain curves corresponding to an AM60 automotive part processed by die casting and tested in compression at different strain rates: a) $5x10^{-4}$ s^{-1}, b) $5x10^{-3}$ s^{-1}, c) $5x10^{-2}$ s^{-1}, d) 10^3 s^{-1}. 160

PAG.

Figure 9.2. True stress – true strain curves corresponding to samples of an AM60 automotive part processed by die casting and tested in compression at different temperatures: a) RT, b) 200 ºC and c) 400 ºC. 161

Figure 9.3. True stress – true strain curves corresponding to an AM60 ingot alloy tested in compression at different strain rates: a) $5x10^{-4}$ s^{-1}, b) $5x10^{-3}$ s^{-1}, c) $5x10^{-2}$ s^{-1}, d) 10^{3} s^{-1}. 162

Figure 9.4. True stress – true strain curves corresponding to an AM60 ingot alloy tested in compression at different temperatures: a) RT, b) 200 ºC and c) 400 ºC. 163

Figure 9.5. True stress – true strain curves corresponding to an AM60 ingot alloy processed by gravity casting and tested in tension at different strain rates: a) $5x10^{-4}$ s^{-1}, b) $5x10^{-3}$ s^{-1}, c) $5x10^{-2}$ s^{-1}, d) 10^{3} s^{-1}. 164

Figure 9.6. True stress – true strain curves corresponding to an AM60 ingot alloy processed by gravity casting and tested in tension at different temperatures: a) RT, b) 200 ºC and c) 300 ºC. 165

Figure 9.7. True stress – true strain curves corresponding to an AZ91 ingot alloy processed by gravity casting and tested in compression at different strain rates: a) $5x10^{-4}$ s^{-1}, b) $5x10^{-3}$ s^{-1}, c) $5x10^{-2}$ s^{-1}, d) 10^{3} s^{-1}. 166

Figure 9.8. True stress – true strain curves corresponding to an AZ91 ingot alloy tested in compression at different temperatures: a) RT, b) 200 ºC and c) 400 ºC. 167

Figure 9.9. True stress – true strain curves corresponding to an AZ91 ingot alloy processed by gravity casting and tested in tension at different strain rates: a) $5x10^{-4}$ s^{-1}, b) $5x10^{-3}$ s^{-1}, c) $5x10^{-2}$ s^{-1}, d) 10^{3} s^{-1}. 168

Figure 9.10. True stress – true strain curves for corresponding to an AZ91 ingot alloy processed by gravity casting and tested in tension at different temperatures: a) RT, b) 200 ºC and c) 300 ºC. 169

LIST OF TABLES

PÁG.

PART II. INTRODUCCIÓN. EL MAGNESIO

Tabla 2.1. Comparación de las propiedades físicas del Mg puro con las de otros metales estructurales 19

Tabla 2.2 Valores de la *CRSS* para los diferentes sistemas de deslizamiento y maclado en Mg según Barnett [32]. 33

PART III. RESEARCH PAPERS

3.2 Twinning and grain subdivision during dynamic deformation of Mg AZ31 sheet alloy at room temperature.

Table 3.2.1. Comparison of the stacking fault energies corresponding to non-basal and basal dislocations in Mg with those of other metals 69

PART IV. ADDITIONAL AND COMPARATIVE STUDIES

Table 4.1. Average yield stress values (in MPa). (a) Quasi-static deformation; (b) dynamic deformation. 90

Table 4.2. Strain rate sensitivity (m) values corresponding to the different quasi-static testing conditions investigated. Note: In the PP tests, the stress values utilized for the calculation of m are the average values between the two tests performed at each temperature. 94

Table 4.3. Theoretical grain size (d_T) and measured grain size (d_M) for MN11 samples tested in compression and in tension at high and low strain rate at different temperatures. The grain sizes are measured and calculated along a plane perpendicular to the extrusion axis. 102

PART IX. APPENDICES

Table 9.1. Mechanical Properties of AZ31 Mg alloy 170

Table 9.2. Mechanical Properties of MN11 Mg alloy. 171

Table 9.3. Mechanical Properties of MN11 Mg alloy. 172

Table 9.4. Mechanical Properties of AM60 Mg alloy. 173

PAG.

Table 9.5. Mechanical Properties of AM60 Mg alloy. 174

Table 9.6. Mechanical Properties of AM60 Mg alloy. 175

Table 9.7. Mechanical Properties of AZ91 Mg alloy. 176

Table 9.8. Mechanical Properties of AZ91 Mg alloy. 177